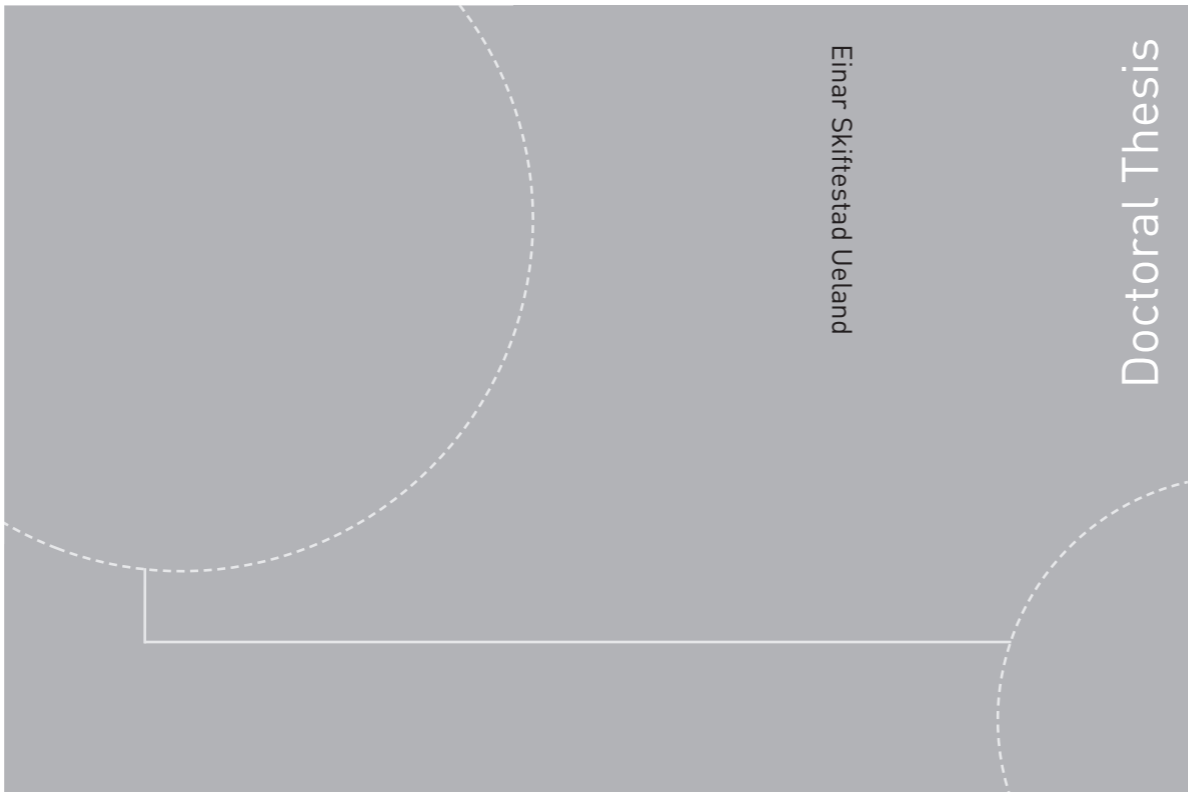


Doctoral theses at NTNU, 2021:284

Einar Skiftestad Ueland

Load Control for Real-time Hybrid Model Testing using Cable-Driven Parallel Robots



Einar Skiftestad Ueland

Doctoral Thesis

ISBN 978-82-326-6885-4 (printed ver.)
ISBN 978-82-326-6727-7 (electronic ver.)
ISSN 1503-8181 (printed ver.)
ISSN 2703-8084 (electronic ver.)

NTNU
Norwegian University of
Science and Technology
Faculty of Engineering
Department of Marine Technology

Doctoral theses at NTNU, 2021:284

 **NTNU**
Norwegian University of
Science and Technology

 **NTNU**
Norwegian University of
Science and Technology

 **NTNU**
Norwegian University of
Science and Technology

Einar Skiftestad Ueland

Load Control for Real-time Hybrid Model Testing using Cable-Driven Parallel Robots

Thesis for the degree of Philosophiae Doctor

Trondheim, September 2021

Norwegian University of Science and Technology
Faculty of Engineering
Department of Marine Technology



Norwegian University of
Science and Technology

NTNU

Norwegian University of Science and Technology

Thesis for the degree of Philosophiae Doctor

Faculty of Engineering
Department of Marine Technology

© Einar Skiftestad Ueland

ISBN 978-82-326-6885-4 (printed ver.)
ISBN 978-82-326-6727-7 (electronic ver.)
ISSN 1503-8181 (printed ver.)
ISSN 2703-8084 (electronic ver.)

Doctoral theses at NTNU, NTNU, 2021:284



Printed by Skipnes Kommunikasjon AS

Preface

This thesis is submitted by Einar Skiftestad Ueland in partial fulfillment of the requirements for the degree of philosophiae doctor (PhD) at the Norwegian University of Science and Technology (NTNU). The research work presented in this thesis was conducted during the period of August 2016 to August 2020. The work is a part of the Norwegian Centre of Excellence, Centre for Autonomous Marine Operations and Systems (NTNU AMOS). It is part of the Research Council of Norway funding scheme, grant no.254845 *Real-Time Hybrid Model Testing for Extreme Marine Environments*. The work has been performed at Centre for Autonomous Marine Operations and Systems (NTNU AMOS) at the Department of Marine Technology (IMT). Professor Roger Skjetne (NTNU, Department of Marine Technology) has been the main supervisor and Associate Professor Thomas Sauder (Sintef Ocean and NTNU) has been the co-supervisor.

Acknowledgments

I would like to thank my main supervisor, Professor Roger Skjetne for his continued support and valuable feedback throughout the thesis period. His extensive knowledge combined with his attention to detail is impressive. He has given me the freedom to pursue my own ideas while supporting me in making strategic decisions and following up my research.

Thomas took on the role of my co-supervisor after completing his own PhD. His level of academic rigour and intuitive understanding of research questions impress me. Thomas is an integral part of the ReaTHM testing research team at NTNU and Sintef Ocean, and his support and guidance have been highly valuable. For that I am grateful.

I would like to thank the ReaTHM testing research team at NTNU and Sintef Ocean for their support, and collaboration. Being able to build on their developments has been crucial in ensuring the successful completion of this work. Thanks also to Torgeir Wahl for helping out in the Marine Cybernetics laboratory, and Ole Erik Vinje assistance in the workshop.

Thanks also to my friends and colleagues at NTNU including Henrik, Senthuran, Andreas, Erlend (x2), Henrik, Stian (x2), Mikkel, Albert, Ida, Astrid, Emil, Børge, Stefan and many more for providing a pleasant and social working environment.

I would like to thank my friends and family for their support and company throughout this period. They have provided a pleasant distraction from work. In this regard, I am especially grateful for my four nephews and nieces (all born while I undertook this PhD), who are generally enjoyable to spend time with.

Beyond acquiring professional and academic skills, I have learned a lot about myself through this thesis. Working on the doctoral project has sometimes, or perhaps even often, been fraught with frustration. However, now that I am at the finish line, I am happy with the result. With that, I once again want to thank everyone who supported me on this journey, both named and unnamed – you helped me through it.

Trondheim, August 23, 2021

Einar Skiftestad Ueland

Abstract

Real-time hybrid model testing (ReaTHM testing) is a method for emulating ocean structures that combines numerical methods with traditional hydrodynamic model testing. This is done by partitioning the ocean structure under consideration into numerical and physical substructures that are coupled in real-time through measurement and control interfaces, for high fidelity emulation of the original ocean structure. The method can be classified as an extension of traditional hydrodynamic model testing since it considers experimental testing of down-scaled models in basin laboratories, and as a subset of hybrid testing since it replaces parts of the down-scaled structure with numerical simulated models.

The developments presented in this thesis is aimed at ReaTHM testing where the numerically computed load vector is calculated based on measurements of the experimental displacements and thereby actuated onto the physical substructure via a configuration of distributed cabled winches. The experimental platform, together with the actuators, thus constitutes a cable-driven parallel robot.

This PhD project's overall goal is to further improve the ReaTHM testing methodology as part of a research effort to make it a well documented, accepted, and valued practise that accurately identifies and predicts the behaviour of ocean structures in realistic marine environments.

One of the major challenges in this regard is to ensure that load actuation is performed with minimal errors and without significant degradation of emulation performance. To this end, the focus of this work is to identify and mitigate issues associated with the actuation of the numerically calculated load vector onto the experimental test platform and to enable more accurate and robust load control.

The thesis is organised as a collection of articles. The two conference articles identify and quantify sources of error in load actuation. They serve as the basis for the subsequent journal articles that address specific load actuation challenges and associated good practise control methods.

In the first journal article, novel methods for determining each actuator's appropriate target cable forces are proposed. These methods guarantee continuous differentiability of the resulting cable forces. The article also shows that an implementation of Newton's method specialised for the resulting optimisation problem can be used for practical real-time applications. The results are beneficial for ReaTHM testing because of the method's flexibility, and because it is expected that smoother cable force trajectories can be more accurately tracked.

The second journal article proposes a procedure for optimal actuator placement that is particularly suitable for ReaTHM testing, for which no such guidelines exist

at the time of writing.

The third and final journal article demonstrates how position-controlled servomotors connected to drums via clocksprings can be used for accurate actuator force control. Associated controllers that compensate for both delays and motion-induced forces are proposed. The study emphasises developments for ReaTHM testing by focusing on relevant use cases, force magnitudes, and frequency ranges.

For development, problem identification, method validation, and demonstration, the work in this thesis is emphasised by extensive experimental testing. Experiments are presented using both a readily accessible 1 degree of freedom setup for basic testing and development and a more complex ReaTHM test setup of a moored barge in a basin laboratory in which the cabled winches are tasked with actuating loads in three degrees of freedom (surge, sway and yaw). The thesis does not use ReaTHM testing to determine realistic ocean structures' behaviour, which is the intended end-use of the overall methodology. Instead, simpler test cases are considered to understand, develop, and improve control functions at a more fundamental level.

Contents

Contents	v
List of Figures	vii
List of Tables	ix
Nomenclature	xi
I Main Report	1
1 Introduction	3
1.1 Experimental and Numerical Methods in Ocean Engineering	5
1.2 Real-time Hybrid Model Testing in Ocean Engineering	9
1.3 Summary of Previous Work	14
1.4 Research Objectives	19
1.5 List of Publications and Main Contributions	21
1.6 Structure of the Thesis	23
2 Modelling and Design of CDP-based ReaTHM Test Setups	25
2.1 Overall Architecture and Examples	25
2.2 Detailed Architecture and Modelling	29
2.3 Sources of Errors in ReaTHM Testing	38
2.4 Experimental Setups and Campaigns Developed in the Present Project	40
3 Summary of Enclosed Articles	49
3.1 Error Sources and Error Quantification	49
3.2 Improvements in Force Allocation Method	53
3.3 Improved Procedure for Placement of Actuators	55
3.4 Improvements in Cable Force Control	57
4 Conclusions and Recommended Future Work	65
4.1 Conclusions	65
4.2 Recommended Future Work	67

References	69
II Collection of Articles	77
Article 1 – C-1	79
Article 2 – C-2	93
Article 3 – J-1	101
Attachment to Article 3	111
Article 4 – J-2	119
Article 5 – J-3	145
III Previous PhD Theses Published at the Department of Marine Technology	163

List of Figures

1.1	Hydrodynamic model testing of various ocean structures.	4
1.2	ReaTHM testing using CDPDR for a moored barge	11
1.3	A motivating example – ReaTHM testing of a moored barge.	12
1.4	Actuator technologies used in hybrid testing.	15
1.5	Different ReaTHM testing applications.	17
2.1	The ReaTHM testing method.	26
2.2	ReaTHM testing recoupling strategy of systems considered in this thesis	29
2.3	Experimental test setup of ReaTHM testing using CDPDR.	30
2.4	Schematic diagram of a ReaTHM testing setup	31
2.5	Schematic representation of the used cabled actuator.	32
2.6	The ReaTHM testing loop.	34
2.7	A CDPDR platform, with one cable highlighted	35
2.8	Cable to drum configurations.	36
2.9	ReaTHM testing loop, highlighting the numerical substructure.	37
2.10	ReaTHM testing loop partitioned into four operations.	39
2.11	The ReaTHM testing loop highlighting four control loop procedures. . .	39
2.12	Schematic diagram of the 1-DOF setup.	41
2.13	Pictures of the 1-DOF setup.	42
2.14	Additional configurations of the 1-DOF setup.	43
2.15	Image from ReaTHM testing of a moored barge.	43
2.16	Schematic diagram of the moored barge ReaTHM testing setup	45
2.17	Picture of ReaTHM testing of a vessel in the MC-Lab.	45
2.18	Schematic representation of the barge in two experimental configurations.	46
2.19	Basin wall mountings for the actuators.	46
3.1	ReaTHM testing loop – C-1.	50
3.2	Effect of 1 <i>ms</i> time delay – C-1.	50
3.3	Schematic representation of ReaTHM testing of a moored barge – C-2.	52
3.4	Force tracking performance in decay tests – C-2.	52
3.5	Motivating example – J-1.	54
3.6	Solver evaluation times from extensive numerical simulations. – J-1. . .	54
3.7	Moored barge with the horizontal required workspace indicated – J-2 . .	56
3.8	Optimal actuator placement that minimise the cost function – J-2 . . .	56
3.9	Actuator transmission system model – J-3.	58
3.10	Force tracking performance – J-3.	58

3.11	Proposed new actuator configuration	60
3.12	Model of the new actuator	61
3.13	Simulated trajectories	63
3.14	A ReaTHM testing setup with the proposed new actuators	64
4.1	ReaTHM testing performed by research partners in SINTEF Ocean	68

List of Tables

2.1	Sources of load actuation errors	40
2.2	Overview over load actuation error source coverage in the enclosed papers	41
2.3	Cable exit points and cable attachment anchors for the moored barge	46
2.4	Overview of the experimental platform coverage in the enclosed papers	47

Nomenclature

List of Abbreviations

C-1	Conference article 1
C-2	Conference article 2
CDPR	Cable-driven parallel robot
CFD	Computational fluid dynamics
DAQ	Data acquisition
DOF	Degrees of freedom
HIL	Hardware-in-the-loop
J-1	Journal article 1
J-2	Journal article 2
J-3	Journal article 3
MC-Lab	Marine Cybernetics Laboratory – a test basin located at NTNU
NTNU	Norwegian University of Science and Technology
PID	Proportional, derivative and integral (feedback controller)
ReaTHM	Real-time hybrid model (testing)

List of Symbols

λ	Scaling ratio between full-scale and model-scale spacial dimensions
u	Fluid velocity
L	Characteristic structural length
ν_w	Kinematic viscosity
g	Gravitational constant
ρ	Fluid density
E	Elastic modulus

f_e	Vortex shedding frequency
T	Wave period
$\boldsymbol{\omega}_{\text{num}}$	Environmental loads acting on the numerical substructure
$\boldsymbol{\omega}_{\text{ph}}$	Environmental loads acting on the physical substructure
$(\cdot)_{\text{p}}$	Subscript indicating that the variable applies to the full-scale structure
$(\cdot)_{\text{m}}$	Subscript indicating that the variable applies to the model-scale structure
S_{num}	Numerical substructure
S_{ph}	Physical substructure
$(\hat{\cdot})$	Notation indicating that the variable (\cdot) is estimated
$\{\mathbf{a}\}$	Earth-fixed coordinate system
$\{\mathbf{b}\}$	Platform fixed coordinate system
O^a	The stationary origin of $\{\mathbf{a}\}$
O^b	The moving body-fixed origin of $\{\mathbf{b}\}$
m	Number of controlled degrees of freedom
n	Number of cabled actuators connected to the experimental platform
$\mathbf{f} = (f_1, f_2, \dots, f_n)$	Cable forces
$\mathbf{f}_{\text{min}} = (f_{\text{min},1}, f_{\text{min},2}, \dots, f_{\text{min},n})$	Minimum cable forces
$\mathbf{f}_{\text{max}} = (f_{\text{max},1}, f_{\text{max},2}, \dots, f_{\text{max},n})$	Maximum cable forces
$\mathbf{f}^* = (f_1^*, f_2^*, \dots, f_n^*)$	Optimal cable forces
$\mathbf{f}_c = (f_{c,1}, f_{c,2}, \dots, f_{c,n})$	Target cable forces
$\mathbf{f}_m = (f_{m,1}, f_{m,2}, \dots, f_{m,n})$	Measured cable forces
$\hat{\mathbf{f}} = (\hat{f}_1, \hat{f}_2, \dots, \hat{f}_n)$	Estimated cable forces
$g(\mathbf{f})$	Cable cost function
\mathbf{w}_I	Non-delayed numerically calculated load vector
τ_n	Lumped delay of the numerically calculated load vector
$\bar{\mathbf{w}}_I$	Numerically calculated load vector incorporating the delay τ_n
$\mathbf{w}_{\text{ref}} \in \mathbb{R}^m$	Target reference load vector
\mathbf{w}	Resulting cable load vector (note that in the CDPR community \mathbf{w} is often used differently to instead refer to the externally acting wrench)
$\mathbf{W} \in \mathbb{R}^{m \times n}$	Kinematic mapping from \mathbf{f} to \mathbf{w} (in the CDPR community also referred to as the structure matrix \mathbf{A}^T)
$\mathbf{p} := (x, y, z)$	Platform position

$\Theta := (\phi, \theta, \psi) \in \mathbb{S}_1^3$ Platform orientation
 $\eta := (\mathbf{p}, \Theta) \in \mathbb{R}^3 \times \mathbb{S}_1^3$ Platform pose vector
 \mathbf{v}_v Body-fixed linear velocity
 $\boldsymbol{\omega}_v$ Body-fixed angular velocity
 $\boldsymbol{\nu} := (\mathbf{v}_v, \boldsymbol{\omega}_v) \in \mathbb{R}^6$ Body-fixed linear and angular velocity vector
 $\mathbf{R} \in \mathbb{R}^{3 \times 3}$ Euler angle rotation matrix, using the zyx convention
 $\mathbf{R}_x \in \mathbb{R}^{3 \times 3}$ Euler angle rotation matrix about the x-axis
 $\mathbf{R}_y \in \mathbb{R}^{3 \times 3}$ Euler angle rotation matrix about the y-axis
 $\mathbf{R}_z \in \mathbb{R}^{3 \times 3}$ Euler angle rotation matrix about the z-axis
 $\mathbf{T} \in \mathbb{R}^{3 \times 3}$ Euler angle velocity transformation matrix, using the zyx Euler angle convention
 A_i The i^{th} cable exit point
 \mathbf{p}_{ai} The position of the i^{th} cable exit point A_i
 E_i The i^{th} cable attachment anchor
 \mathbf{p}_{ei} The position of the i^{th} cable attachment anchor E_i
 \mathbf{r}_i^b The cable lever arm of the i^{th} cable attachment anchor
 $\{\mathbf{p}_a\} := (\mathbf{p}_{a1}, \mathbf{p}_{a2}, \dots, \mathbf{p}_{an})$ All cable exit points of a CDPR configuration
 $\{\mathbf{r}^b\} := (\mathbf{r}_1^b, \mathbf{r}_2^b, \dots, \mathbf{r}_n^b)$ All cable attachment points of a CDPR configuration
 \mathbf{u}_i Unit vector denoting direction of the i^{th} cable force
 $\mathbf{M}_A \in \mathbb{R}^{6 \times 6}$ Added mass matrix
 $\mathbf{M}_{RB} \in \mathbb{R}^{6 \times 6}$ Rigid body mass matrix
 $\mathbf{C}_{RB} \in \mathbb{R}^{6 \times 6}$ Coriolis–centripetal matrix (corresponding to rigid body mass)
 $\mathbf{C}_A \in \mathbb{R}^{6 \times 6}$ Coriolis–centripetal matrix (corresponding to added mass)
 $\mathbf{D} \in \mathbb{R}^{6 \times 6}$ Damping matrix
 $\boldsymbol{\nu}_r \in \mathbb{R}^6$ Relative current velocity vector
 $\boldsymbol{\tau} \in \mathbb{R}^6$ Thrust vector
 $\mathbf{g}_r(\boldsymbol{\eta}) \in \mathbb{R}^6$ Hydrostatic restoring vector
 τ_{cs} Delay between the commanded and resulting motor shaft angle
 k_p, k_i, k_d PID feedback controller gains
 r Drum effective radius
 ζ Cable elongation
 θ_0 Spring equilibrium offset

s_l	Stroke length (voice coil actuator)
B	Magnetic flux density (voice coil actuator)
L	Length of conductor (voice coil actuator)
N	Number of conductors (voice coil actuator)
m_c	Voice coil mass (voice coil actuator)
m_{vc}	Coil mass (voice coil actuator)
m_{ch}	Housing mass (voice coil actuator)
x_e	Relative voice coil displacement (voice coil actuator)
x_1	Coil displacement (voice coil actuator)
x_2	Housing displacement (voice coil actuator)
x_w	Unwound cable length due to change of θ_w (voice coil actuator)
I_w	Drum inertia with respect to x_w (voice coil actuator)
f_v	Interface force (voice coil actuator)
$k_v(x_e)$	Current to force mapping (voice coil actuator)
f_w	Cable force resulting from spring compression (voice coil actuator)

Difference in Notation Between the Attached Papers and the Main Report

There are some differences in notation between the attached papers and the main report due to: 1) differing target audiences between certain papers and the main report (marine hydrodynamical model testing versus robotics), and 2) evolution and standardisation that has taken place throughout the PhD process. The main differences are listed below.

- Whereas the main report uses the term *load-vector* to reference generalized load vectors, [J-1](#) and [J-2](#) use the term *wrench* to mean the same. The former is in line with expected terminology in hydrodynamical model testing, whereas the latter is used to emphasise that the load vectors is actuated by cables (e.g., from *cable-wrench*) and in line with literature on CDPR.
- In article [C-2](#), \mathbf{T} is used for the kinematic mapping \mathbf{W} .
- Article [C-1](#) has several discrepancies in notation relative to the rest of the PhD, reflecting that it was written early in the PhD project.

Part I

Main Report

Chapter 1

Introduction

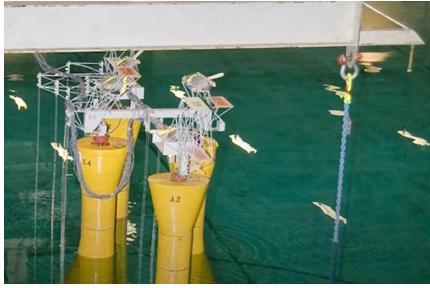
The construction of the Troll A platform (Figure 1.1b) – famously the heaviest structure ever moved by man, Hywind Scotland – the world’s first commercial floating offshore wind farm (Figure 1.1d), a new innovative semi-submersible design for offshore aquaculture farms (Figure 1.1f) – capable of holding 1.5 million salmon [1], and new types of modern ships (Figure 1.1h) – more energy-efficient, and resilient to harsh weather conditions. These serve as examples of different maritime innovations for which model testing has played an important role. That is, prior to their commissioning, their behaviour was evaluated using down-scaled models in basin laboratories subject to realistic laboratory-generated environmental conditions. See column 1 of Figure 1.1.

In the maritime industry, the design, construction, and commissioning of new ocean structures are often large projects that are time-consuming, tedious, and costly¹. Hence, model testing is often a comparatively inexpensive step compared to the cost of full-scale commissioning and operation. It is recognised as an essential tool for identifying and verifying behaviour under operational conditions, for safety validation, for stability assessment, for risk assessment, to improve operational capabilities, for design refinement, and for optimisation. We anticipate model testing to play an important role also in the further development of the various ocean industry segments, which together have a significant economic impact (particularly in Norway) and which are each undergoing rapid technological development:

Aquaculture is an expanding industry that produces more than one million tonnes of fish for food each year in Norway [5]. New fish farms are increasingly deployed in less sheltered areas that are more exposed to the environment [6]. Development is necessary to ensure safety, endurance, and fish well-being under harsher conditions.

Offshore oil and gas continues to play an important role in the economy, especially for Norway, where it accounted for nearly 50 percent of total exports in 2019 [7]. Environmental concerns, falling oil prices and depletion of easily accessible re-

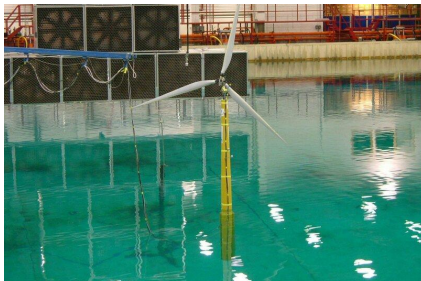
¹For example, the Dogger Bank offshore wind farm, which will supply electrical power to 4.5 million UK homes [2] has a projected investment cost of £9000 million (approximately 107000 million NOK) between 2020 and 2026 [3], whereas investment cost for the recent giant Norwegian oil field Johan Sverdrup reached 68400 million NOK in 2018, with projected future investment costs of 72940 million NOK [4].



(a)



(b)



(c)



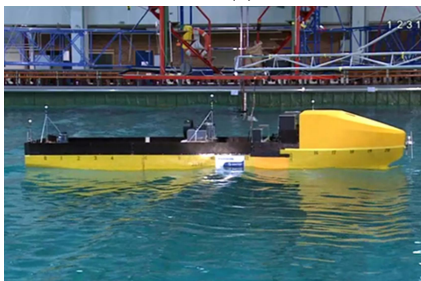
(d)



(e)



(f)



(g)



(h)

Column 1) Hydrodynamic model test Column 2) Corresponding ocean structure

Figure 1.1: Hydrodynamic model testing of ocean structures from different industrial segments. Courtesy SINTEF Ocean, SalMar, Equinor, and DOF Group. (a-b) Oil platform. (c-d) Floating wind turbine. (e-f) Ocean fish farm. (g-h) Offshore construction vessel.

sources have led to high demand for technology development to remain competitive while mitigating climate impacts [8].

Offshore wind is experiencing explosive growth. In 2019, 502 new offshore wind turbines (3623 MW) were connected to the European electricity grid [9]. With a projected capacity of 240-450 GW, the European Commission sees offshore wind as a crucial factor for achieving its 2050 carbon neutrality target [10]. The average rated power of wind turbines, distance to shore, and the size of wind farms are all increasing [9]. These developments necessitate technological advances, especially if the industry is to become a cost-effective source of energy.

1.1 Experimental and Numerical Methods in Ocean Engineering

In this thesis, we use the term *ocean structure* broadly to encompass both permanent structures such as oil platforms or offshore wind turbines and non-permanent structures such as vessels. Traditionally, we distinguish between three families of methods for predicting the behaviour and characteristics of new ocean structures operating in realistic sea conditions:

Experimental methods that empirically determine the behaviour of ocean structures through physical tests. Experimental tests of ocean structures are typically conducted in basin facilities using down-scaled models subjected to controlled environmental loads – to study behaviour under realistic conditions. We refer to this testing as traditional hydrodynamic model testing, or as model testing for short.

Analytical methods that directly use the governing physical equations to find solutions and characteristic behaviour. Although they lead to exact solutions, the necessary assumptions and simplifications typically limit analytical approaches' accuracy and versatility when studying complex ocean structures.

Numerical methods that use a wide range of algorithms and computational techniques to model and simulate ocean structures. Numerical methods often discretise the problem into smaller elements, with each element described by a set of partial differential equations and boundary conditions. These elements are then assembled into a system of algebraic differential equations that are solved with numerical integrators.

The three approaches are in practice interlinked and are typically all part of the development of ocean structures. For example, when analysing a new design, analytical calculations may be used to gain insight into the flow's nature or to provide estimates of stability, dynamic behaviour, and performance. In parallel, numerical modelling can be used to determine detailed performance characteristics and to optimise the design. Finally, experimental testing can be performed late in the design process to evaluate the behaviour and performance of the final design candidates with high fidelity. In this thesis, *fidelity* refers to the ability of the method to predict and mimic the target ocean structure's behaviour.

1.1.1 Hydrodynamic Model Testing

Traditional hydrodynamic model testing using down-scaled models is a well-established tool to replicate realistic ocean structures operating conditions, and to identify and predict their full-scale behaviour and characteristics. In this section, we cover the basics of this method. We refer to [11, 12 (Ch 10), 13, 14 (Ch 2)] for a more comprehensive overview.

For model testing to accurately predict the full-scale behaviour of a structure, the following three similarity laws between model-scale and full-scale systems should be satisfied to a high degree [15, Ch 13]:

- *Geometric similarity*, which requires that the model-scale prototype has the same shape as the full-scale target test structure. This is achieved by asserting a constant scale ratio λ between linear dimensions. Consequently, the area is scaled quadratically, whereas the volume is scaled cubically.
- *Kinematic similarity*, which requires constant scaling between kinematics. This means that the relationships between full-scale and model-scale magnitudes of velocities and accelerations are both given by constant scaling ratios.
- *Dynamic similarity*, which requires constant scaling of forces. This means that the relationship between full-scale and model-scale forces acting on the system (including inertia loads) is constant, with loads acting in the same direction.

If these three similarity conditions are met, test data from model testing can, in principle, be scaled to full-scale without distortion. The rationale for this can be outlined as: 1) *geometric similarity* ensures that the two structures have a similar shape 2) *kinematic similarity* ensures that they operate in similar fluid flows, and 3) *dynamic similarity* ensures that the interaction between the fluids and the structure produces similar loads in similar directions and ensures that the relationship between model-scale and full-scale of all load components (including inertia) can be expressed by a constant scaling ratio. Using Newton's equations of motion, the two systems can then be approximated as equivalent, scaled, dynamic systems, subject to the same governing equations.

Geometric similarity is satisfied by design. *Kinematic similarity* can be achieved with relatively high accuracy in modern laboratory basins. However, complete kinematic similarity is challenging because wavemakers can generate parasitic waves, and since the velocity profile and turbulence intensity of the flow might not be fully controlled. *Dynamic similarity* is fundamentally difficult to satisfy because the resulting forces from different physical phenomena scale differently. As explained below, there are a number of different dimensionless scaling numbers that, if equal at both scales, ensure dynamic similarity for the corresponding physical phenomena [15, Ch 13].

Let u , L , ν_w , and g denote fluid velocity, characteristic structural length (for example diameter of a cylinder subjected to hydrodynamic loads), kinematic viscosity, and the gravitational constant, respectively. Two particularly important scaling numbers are:

- *Reynolds number* (uL/ν_w), which describes the ratio between inertial and viscous forces.

- *Froude number* (u^2/gL), which describes the ratio between inertia and gravitational forces.

Furthermore, let ρ , E , f_e , T be the fluid density, the elastic modulus (for structures subject to deformation), the vortex shedding frequency, and the wave period, respectively. Depending on test specific factors, the following scaling numbers may be important:

- *Keulegan-Carpenter number* (uT/L), which describes the ratio between drag and inertial forces in oscillating flows.
- *Cauchy number* ($\rho u^2/E$), which describes the ratio between inertial and elastic forces.
- *Strouhal number* ($f_e L/u$), which describes the ratio between forces associated with oscillating flow mechanisms and inertial forces (for structures moving relative to a flowing fluid, with build-up and subsequent shedding of vortices).

Of particular importance for model testing is the scaling conflict between the Reynold- and Froude number [11]. Except in some cases where the Reynolds number is particularly important [16], hydrodynamic model tests are in practice performed with matching Froude number. This ensures that the propagation of surface waves (mainly driven by gravitational and inertial forces) is correctly described at the model-scale.

As discussed in for example [15, Ch 13], one may mitigate distortions in Reynold scaling by inducing turbulence to the flow, maximising the model-scale size, perturbing the incoming flow, roughening up the surface, or correcting for it when analysing the results.

Whereas the resulting Reynolds number distortions are typically considered acceptable for hydrodynamic loads, this is not true for wind loads [17] where viscous loads dominate. This is critical when both hydrodynamic and aerodynamic loads are important, which is the case for offshore wind turbines [17].

With the subscripts $(\cdot)_m$ and $(\cdot)_p$ denoting model-scale and full-scale parameters, respectively, the established practice of requiring matching Froude number implies

$$(u_p^2/gL_p) = (u_m^2/gL_m). \quad (1.1)$$

Since spatial lengths are scaled by λ (geometric similarity) and velocity is the change in position over time, the time variable is scaled by $\lambda^{1/2}$ to satisfy (1.1). Importantly, this means that model testing is performed on a different time scale relative to the full-scale emulated scenario, depending on the scaling ratio λ . For example, a scaling ratio of $\lambda = 1/60$, means that an interval of 1 second in model-scale corresponds to a time interval of $\lambda^{-1/2} \approx 7.75$ seconds in the full-scale emulated scenario.

1.1.2 Numerical Emulation of Ocean Structures

Recent technological advances in hardware and software have revolutionised the study of ocean structures. Markedly, these developments have enabled significant use of computational fluid dynamics (CFD) solvers [18].

CFD solvers operate by solving the Navier-Stokes equations on a discretised mesh of the fluid. These are fundamental governing equations describing fluid flow,

capturing viscous, gravitational, and inertial flow effects [19]. Multipurpose physics engineering software (such as ANSYS [20] or OpenFOAM [21]) that combine structural finite element models (FEM) and CFD models is now nearing maturity, enabling relative ease of use of CFD solvers. Moreover, these types of programs are continuously improving to describe the fluid flow better [22]. Complex nonlinear simulations of ocean structures with the inclusion of viscous effects are now within reach, which in practice was not feasible in previous decades [23].

Other numerical solvers are based on potential flow theory, in which the fluid is assumed to be incompressible, inviscid, and irrotational. With these assumptions, the flow can be represented in the form of a velocity potential that can determine fluid pressure and velocities [24]. By linearising the potential flow boundary value problem, these methods can solve the resulting problem, for example, using boundary element methods [25]. Even though potential flow methods use a less complex flow model, they are highly valuable because the computational effort is orders of magnitude less than for CFD solvers.

1.1.3 Model Testing as a Complement to Numerical Methods

Given the recent improvements of numerical methods, we believe it is appropriate to explain why per 2021, and presumably in the foreseeable future, model testing is an integral part of testing and validating ocean structures, as opposed to solely relying on numerical models.

Although CFD solvers can achieve high fidelity under the right conditions, they currently have a number of technological and practical limitations: 1) it may be challenging to configure simulations properly, including defining boundary conditions, meshing strategy, parameters, and input variables; 2) they require excessive use of computational resources, which severely limits the scope of the simulation and achievable fidelity with current technological limitations [22]; and 3) CFD solvers rely on a number of assumptions and simplifications (such as in how to set up turbulence models). These are potential sources of error that cause uncertainty in how well the true model is represented².

While alternative methods such as linear potential flow solvers are much faster, they typically ignore important effects such as wave breaking, viscosity, turbulence, skin friction, and flow separation. This is particularly problematic for complex hull shapes and for problems with high Froude numbers.

For these reasons, the prevailing opinion in the literature is that CFD solvers (and other numerical methods) will not replace experimental methods anytime soon [22]. This is especially true for complex physical phenomena, including complex free surface effects, viscous effects, coupling effects between system components, slamming, and high amplitude or breaking waves. We can summarise the motivations for using experimental model testing as a complement to numerical methods as follows:

- To discover, understand, and model new phenomena and effects.

²For example, in the recent work [22], the authors warn that they have encountered numerous erroneous CFD solutions that look good at first sight but that on closer inspection do not match the expected flow behaviour.

- To investigate cases that are difficult to analyse with numerical methods.
- To assess ocean structures' operational characteristics, capabilities, and limitations, including structural loading, manoeuvrability, stability or behaviour under limiting conditions. This is often done late in the design process to verify and extend the previous analysis.
- To evaluate new innovative designs or new complex operations, where unexpected and unanticipated behaviour may occur.
- To tune numerical models by incorporating experimental results. For example, experimental testing is important to establish the drag and damping coefficients of the famous Morison equations [26].
- To rapidly and robustly verify system performance when time is a limiting factor.

1.2 Real-time Hybrid Model Testing in Ocean Engineering

To overcome the inherent limitations of each method, experimental and numerical methods for ocean structure analysis can be integrated into the same test by using the hybrid testing framework:

Definition: Hybrid testing

A family of methods for analysing and predicting the behaviour of a system that combines: 1) computer-emulated numerical substructures, and 2) experimentally tested physical substructures. Control and measurement interfaces couple the substructures with the goal of realistically emulating of the original, unpartitioned system.

The fundamental assumptions in hybrid testing are that: 1) the numerical substructure can be modelled with sufficiently high fidelity using numerical methods, 2) the physical substructure can be modelled with sufficiently high fidelity using experimental methods, and 3) the substructures can be recoupled without significant loss of fidelity. Whereas the physical substructure typically covers complex phenomena that are difficult to model numerically, the numerical substructure typically covers phenomena that are difficult to capture in the experimental testing campaign. Thus, the testing enables emulation of systems where neither purely numerical simulation nor purely physical model testing is feasible within satisfactory performance levels.

In this thesis, we are concerned with real-time hybrid model testing, which is a subset of hybrid testing applied to the analysis of ocean structures and defined in this thesis as follows:

Definition: Real-time hybrid model testing (ReaTHM testing)

A subset of hybrid testing with real-time recoupling applied to ocean structure emulation, in which the physical substructure is a down-scaled model of an ocean substructure tested in a basin laboratory with adherence to engineering principles employed in conventional hydrodynamic model testing.

In this context, *real-time* refers to the real-time constraints required in connecting the numerical and physical models – to ensure correct behaviour of rate-dependent factors, and *model testing* refers to the relationship to traditional hydrodynamic model testing. For short, we use the denomination ReaTHM³ testing to mean the same.

ReaTHM testing can be classified both as an extension of traditional hydrodynamic model testing in that it considers experimental testing of down-scaled models in basin laboratories and as a subset of hybrid testing in that it replaces parts of the down-scaled model with a numerical substructure that is recoupled with the physical substructure.

A set of different ReaTHM testing configurations for coupling the numerical and physical substructures are in principle possible, which has implications for how the actuation and measurement interfaces are configured. The developments presented in this thesis is aimed at ReaTHM testing where the physical substructure is load driven based on actuation of numerically calculated loads, whereas the numerical substructure is displacement driven based on measurements or estimates of position, velocities and accelerations. Moreover, the loads are actuated using cable-driven parallel robots (CDPR) [27, 28, 29, 30, 31]:

Definition: Cable-driven parallel robot (CDPR)

A type of parallel manipulator setup in which a mobile platform is actuated by cabled winches configured in parallel topology.

That is, in this thesis, we study *ReaTHM testing using CDPR*:

Definition: ReaTHM testing using CDPR

ReaTHM testing where the loads computed within the numerical substructure are actuated onto the experimental physical substructure using a configuration of cabled winches configured in parallel topology.

This definition is closely related to the title of the present thesis. Whereas the first part of the thesis title, *load control*, refers to the transfer and subsequent actuation of forces and moments from the numerical substructure onto the physical substructure, the latter part of the title indicates that the system under consideration is *ReaTHM testing using cable-driven parallel robots*. See Figure 1.2, which shows an example of ReaTHM testing using CDPR, highlighting the tensioned

³ReaTHM[®] is a registered trademark of SINTEF.

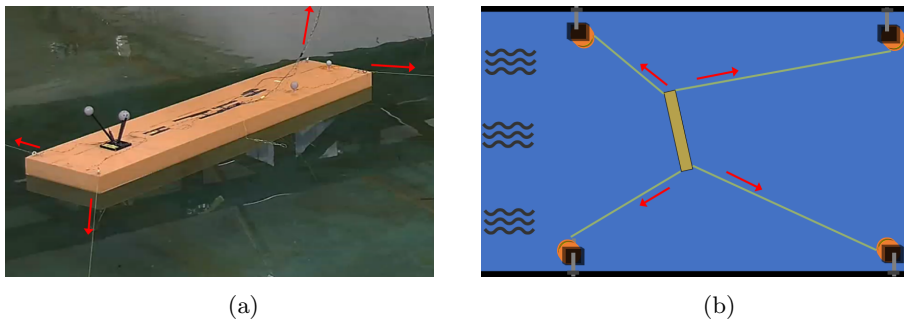


Figure 1.2: ReaTHM testing using C DPR for a moored barge. Red arrows mark the direction of the actuated force through each cable. a) Image of the thesis laboratory setup. b) Schematic overview.

cables that actuate loads onto the floating experimental platform. Conversely, in non-marine C DPR applications, the platform is typically suspended in the air by the cabled actuators; see for example [32].

To ensure that ReaTHM testing can robustly mimic the full-scale behaviour of ocean structures, technological and scientific challenges arise that require multidisciplinary knowledge combining several research areas, including control engineering, hydrodynamics, experimental testing, co-simulation, load actuation, and optimisation.

1.2.1 Motivating Example – ReaTHM testing of a Moored Barge

Consider now the feasibility of performing hydrodynamic model testing of the moored barge shown in Figure 1.3a, which is to be operated⁴ at a water depth of 2900 m and to be experimentally tested using a scaling ratio of $1/60$. With conventional model testing, this necessitates a basin laboratory with a depth of 48 m and a large basin diameter to accommodate for the spreading of the mooring lines. The spatial requirements are far beyond existing basin capabilities. Experimental alternatives such as passive truncation methods and outdoor testing have significant drawbacks due to accuracy and modelling challenges as well as longer test execution times. See discussion in [33, Ch 4]. Moreover, accurate representation of the mooring lines at the model-scale can be challenging even without depth limitations. In summary, it is not practically feasible to test this system using traditional model-scale testing. Conversely, purely numerical models of the barge are not sufficiently accurate for validating the system since they do not adequately capture the complex interactions between the barge and the waves.

ReaTHM testing provides a resolution that enables experimental testing of the barge. As illustrated in Figure 1.3b, using ReaTHM testing, the system is first partitioned into: 1) the mooring lines (numerical substructure), which are

⁴The example is inspired by a floater that is to operate at the Stones field (Gulf of Mexico), described in [33, Ch 4].

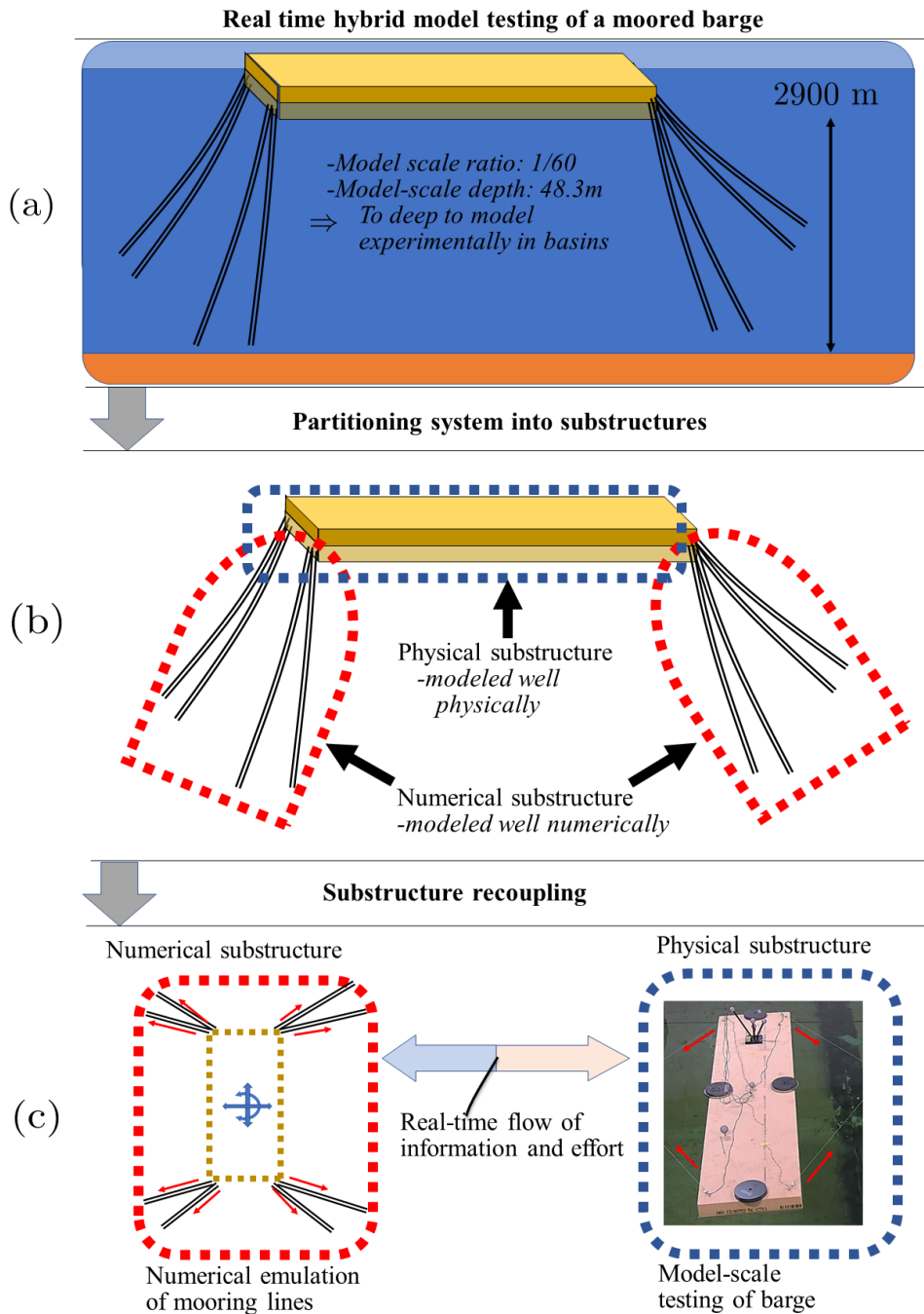


Figure 1.3: A motivating example – ReaTHM testing of a moored barge. (a) Test case description. (b) System partitioning. (c) Emulation of recoupled system.

modelled using numerical methods, and 2) the barge (physical substructure), where complex wave-to-structure interactions take place, which is kept experimentally. In the testing campaign, the two substructures are recoupled in real-time through the measurement and actuation interfaces, as shown in Figure 1.3c. If each substructure can be emulated with high fidelity and the interface only introduces limited errors, the original system should also be emulated with high fidelity.

1.2.2 Motivations for ReaTHM Testing

The motivation for performing ReaTHM testing is fundamentally the same as for performing conventional model testing. That is, to capture complex behaviour and phenomena of ocean structures in realistic conditions that would be difficult to capture without experimental testing.

The following is an overview of the types of motivations one may have for conducting ReaTHM testing instead of traditional hydrodynamic model testing.

Spatial infrastructure limitations. This is the case when the down-scaled model does not fit into existing laboratory basins due to fixed physical and geometric facility constraints. Reducing the model-scale ratio beyond established practices is not an acceptable alternative since: 1) smaller scaling ratios (corresponding to smaller models) reduce test fidelity [34], and 2) it eventually becomes difficult to generate high quality waves for realistic ocean conditions, and the physical phenomena observed at the model-scale will no longer translate to the corresponding full-scale test case. See also the discussion on ill-conditioning in [35]. ReaTHM testing is proposed to overcome this problem for cases where space-consuming parts of the system can be numerically modelled with high fidelity, and the remaining experimental setup fits in the laboratory basin.

Scaling law conflicts. This is the case when two or more physical phenomena, that require different, incompatible scaling regimes for mapping between full-scale and model-scale are important for the dynamics of the system. Of particular note is the aforementioned Froude-Reynolds scaling conflict that arises because wave loads and aerodynamic loads require different scaling regimes; see Section 1.1.1. ReaTHM testing is proposed as a method to overcome this conflict for cases where one of the conflicting physical phenomena can be managed numerically. A prominent example is the use of ReaTHM testing to evaluate offshore wind turbines [17, 36]. Here, ReaTHM testing overcomes the Froude-Reynolds scaling conflict by numerically calculating the wind associated aerodynamic loads [37].

Technology and fidelity limitations. This is the case when installation, modelling, and fidelity limitations make conventional model testing infeasible or too costly. Examples include testing in limiting conditions that are difficult or dangerous to implement with a fully physical model (such as fault conditions for mooring systems or blade seize scenarios for offshore wind turbines [36]), and the modelling of complex mooring systems (even if the basin depth is large enough). The latter is particularly the case when unconventional materials are used, such as elastomeric mooring lines [38].

Cost reduction, versatility, and effectivity. This is the case when it is preferable to perform ReaTHM testing, even if it is feasible to emulate the system fully experimentally. For example, this may be the case for cost savings, to rapidly prototype different configurations (for example varying anchor systems) or to increase the determinism of loads acting on the physical substructure (for example, to test dynamic positioning performance subject to deterministic environmental loads).

1.3 Summary of Previous Work

1.3.1 Hybrid Testing

In conventional hybrid testing, the physical and numerical substructures are reconnected using numerical time-stepping techniques without real-time requirements. This implies that all rate- and time-dependent effects must be simulated or neglected. See, for example [39]. Conventional hybrid testing for emulating the dynamics and the properties of the coupled system was first performed in 1969 when a cantilever beam connected to an analogue computer was studied [40].

Much of the earlier work and development on the method was within civil engineering to analyse structural responses to earthquake loads [39, 41]. Here, the physical substructure captures complex structural behaviour, including plastic deformation and hysteresis, which is difficult to model numerically. See, for example [42], which considers a bridge pier subject to earthquake loads.

Real-time hybrid testing [43] is an extension of conventional hybrid testing in which substructures are connected in real-time, enabling the capture of rate-dependent effects such as damping or inertia. See [44, 45] for early publications on real-time hybrid testing, and [46] for an outline of the historical development from conventional hybrid testing to real-time hybrid testing. Real-time hybrid testing enables realistic emulation of a wide range of complex nonlinear systems and has been employed in numerous fields. Depending on the research community and field, the technique is also referred to as *real-time hybrid substructure testing* [47], *real-time dynamic substructuring* [48], *model-in-the-loop testing* [49], *cyber-physical testing* [50], and *ReaTHM testing*. The latter is the suggested name when the method is used for hydrodynamic model testing.

See [51] for a discussion of sources of errors in hybrid testing, including truncation errors, handling of rotational degrees of freedom, interface continuity, rigid body modes, joint dynamics, time delay, and experimental errors. In [52] a discussion on the effect that the interface errors have on the coupled system is given. See [53] and references therein for a comprehensive review of hybrid testing from a civil engineering perspective.

Actuation In hybrid testing, actuators apply the numerically calculated loads or displacements onto the physical substructure. Depending on the application and coupling strategy, a series of configurations with different actuator technologies are possible, as illustrated in Figure 1.4.

For civil engineering applications, servohydraulic actuators are favoured, particularly for position control of the physical substructure [54, 55]; see Figure 1.4a.

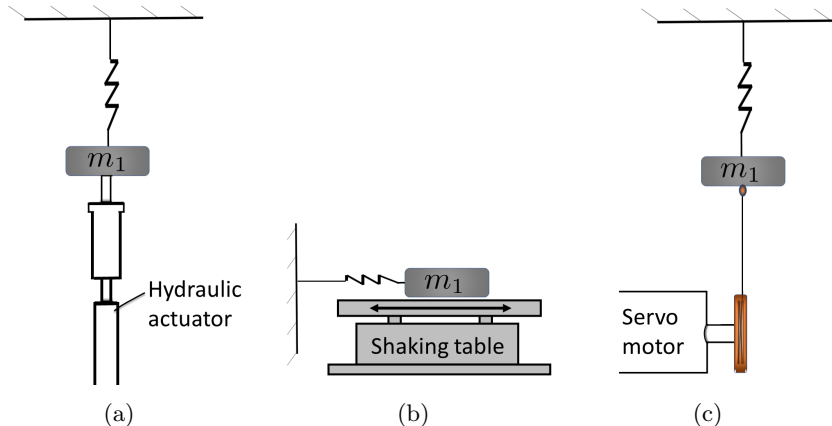


Figure 1.4: Different actuator technologies used in hybrid testing – applied to a setup similar to the 1 degree of freedom experimental setup considered later in this thesis. (a) Servo hydraulic actuator. (b) Shaking table. (c) Actuated cabled winch.

These have the advantage of providing high power and position tracking capabilities. However, they typically have limited stroke length and may have complex actuator dynamics associated with the internal hydraulic flow. See [43] for a comprehensive analysis of their use.

Shaking tables are popular to simulate earthquake loads in seismic engineering [56, 57]. While traditionally being used to prescribe ground accelerations, shaking tables can also be accommodated to hybrid testing [58]; see Figure 1.4b.

In [59], shaking tables and hydraulic actuators are combined and connected to the physical substructure at different interface locations.

In ReaTHM testing, where we typically actuate lower forces over a larger workspace range, neither servohydraulic actuators nor shaking tables have proven suitable. Instead, we use an actuated winch [60, 61] for force control, as illustrated in Figure 1.4c. It consists of a cabled pulley connected to a servomotor via a clockspring, and might be characterized as a type of series elastic actuator [62]. The actuated winches maintain satisfactory force actuation capabilities also under significant end effector motion, which is useful in ReaTHM testing, where the down-scaled models exhibit significant motion.

Related Fields A closely related test framework with extensive literature [63, 64, 65] is hardware-in-the-loop (HIL) testing. Here, control systems are tested by keeping some control loop components on real hardware (physical substructure), while other processes or components are simulated (numerical substructure). Roughly HIL testing can be distinguished from ReaTHM testing as follows: 1) whereas ReaTHM testing typically tests the structural or dynamic behaviour of a physical system, HIL testing is typically used to emulate and test the behaviour of control systems. Thus, emphasis on reproducing the exact dynamics is typically less in the latter. 2) Whereas ReaTHM testing requires external actuators to excite the

physical system, in HIL testing all actuators (if any) are typically a part of the system being emulated.

Despite their differences, use of the terms may overlap, and hybrid testing is sometimes referred to as a subclass of HIL-testing. See, for example [60] and [66].

Another related emulation framework with an extensive body of literature is the study of *co-simulations* [67], which considers the coupling of two independently emulated numerical systems. Although different in that it does not include an experimentally tested substructure, the field addresses issues relevant to hybrid testing such as substructure partitioning and recoupling. This is particularly the case if the co-simulation study considers explicitly connected systems. See, for example [68].

1.3.2 ReaTHM Testing – Literature Overview

ReaTHM testing was initially proposed for experimental testing of floating offshore structures with mooring lines that are difficult to incorporate experimentally [69, 70, 71]. Due to technical limitations of both hardware and software, the early publications were conceptual, without real-world experimental testing.

Developments in computer technology, greater availability of numerical modelling tools, and advances in actuator technology have recently made experimental use of ReaTHM testing feasible. For instance, complex numerical models can now be run in real-time on inexpensive computers [72]. In parallel with technological developments, there is a renewed interest in ReaTHM testing. In particular, for emulation of offshore wind turbines [36] and deepwater installations [73], which are applications that are becoming increasingly important [35].

These developments have led to a willingness to invest in the necessary research and equipment over the last decade. *SINTEF Ocean*, one of the leading model basin operators, now has commercial ReaTHM testing capabilities in its basin laboratories. Other leading basin operators such as *Marin* and research centres such as *CENER* have also shown interest in the method. See [74] (from *SINTEF Ocean*), [75] (from *Marin*), and [76] (from *CENER*) for references including images and description of ReaTHM testing from their respective laboratory basins.

Several studies [73, 50] suggest simulating the mooring lines numerically only below a given truncation point and to let the mooring system above the truncation point be emulated experimentally; see Figure 1.5a. In [38] it is noted how risers and other flexible subsea structures may be tested similarly. Experimental ReaTHM testing campaigns using truncated mooring systems are not found in relevant literature beyond conceptual and theoretical studies. Instead, experimental ReaTHM testing campaigns have kept the entire mooring system numerically, with the actuation of numerically calculated horizontal mooring loads directly onto the ocean structure [77]; see Figure 1.5b.

In recent years, ReaTHM testing has emerged as a solution to overcome the Froude-Reynold scaling conflict between aerodynamical and hydrodynamic loads that arise in the testing of offshore wind turbines [66, 36, 60, 78]. In these ReaTHM testing applications, the numerical substructure is a full-scale numerical aerodynamic model, and the turbine fundament is tested experimentally; see Figure 1.5c.

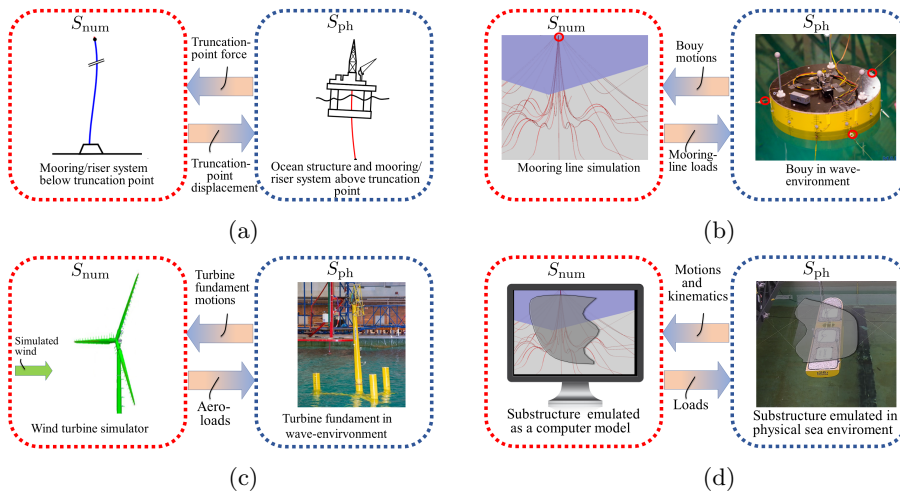


Figure 1.5: Different ReaTHM testing applications. Figures are adapted from the author’s and research partner’s work. (a) Active truncation of a slender structure [50]. (b) Circular moored buoy [72]. (c) Floating wind turbine [36]. (d) General setup overlaid on ReaTHM testing of a moored ship [C-2].

Although several recoupling strategies in principle are possible within the ReaTHM testing framework, publications considering experimental ReaTHM testing are in practice limited to the coupling strategy where the numerical substructure computes a global load vector on displacement measurements, which in turn is actuated onto the physical substructure; see Figure 1.5d. Moreover, the resulting load vector has typically been actuated using a configuration of distributed cabled winches, such that the experimental setup constitutes a CDPR. An exception to the use of CDPR setups is [79], where a ducted fan actuates the numerically calculated loads.

The International Towing Tank Conference presents guidelines and recommendations for ReaTHM testing of offshore wind turbines in [17] and the same for moored floating offshore structures in [38]. Similarly, [77] and [36] are publications that outline a design methodology for ReaTHM testing.

In developing new ReaTHM testing concepts, several publications propose to perform preliminary ReaTHM testing co-simulation studies [77, 80, 50]. These are purely numerical simulations where also experimental components (physical substructure, environmental loads, actuators and sensors) are emulated numerically. This facilitates the development of safety procedures, coupling strategies, improvement of control systems, and detailed sensitivity studies. The latter is comprehensively studied in [80] and [50], which present a sophisticated approach for assessing error sensitivity and fidelity of ReaTHM systems, given assumptions on the statistical distribution of the relevant parameters.

Research and development of ReaTHM testing have thus far been conducted primarily to develop the overall methodology. However, the method is approaching maturity. In recent years, there have been examples where the primary purpose of

a ReaTHM testing campaign was to obtain new empirical data on the behaviour of ocean structures. For example, see [81] and [82].

Other envisioned applications of the method include testing of liquid sloshing in tanks on ships, dynamic positioning systems, and aquaculture farms [35]. As per the motivations listed in Section 1.2.2, many other applications are possible.

1.3.3 Research on ReaTHM Testing at NTNU and SINTEF Ocean

Although there has been a growing interest in ReaTHM testing over the past decade, at the time of writing, the method is still in a developmental phase without widespread commercial use. A limiting factor for using and researching the method is that significant investment and basin laboratory facilities are needed to conduct ReaTHM testing. Only a limited number of actors and projects have these capabilities. One of the most prominent projects in this regard is the Hybrid KPN project which is a research project in close collaboration between the Norwegian University of Science and Technology (NTNU), SINTEF Ocean, Equinor, SaMar, and ABB. The author's PhD programme is part of this project. Judging by the number of academic publications, this project (together with affiliated projects at NTNU and SINTEF Ocean) is the leading driver for research on ReaTHM testing as of 2021. Consequently, it is the source of a substantial number of the references we cite when describing state of the art for ReaTHM testing in Section 1.3.2. That is, [74, 36, 77, 50, 72, 35, 72, 83, 80, 60].

The Hybrid KPN project had access to several basin laboratories (both small and large) designed for hydrodynamic model testing, located in Trondheim, Norway, near NTNU and SINTEF Ocean. One of the main goals of the project was to make ReaTHM testing a well tested and validated method that predicts ocean structure behaviour at a level of fidelity comparable to traditional hydrodynamic testing. As the method matures, the vision is that ReaTHM testing will be accepted and valued by the ocean industry and regularly performed in ocean laboratories as a new best practice. The project was launched in its current form in 2016. Since the project start, ReaTHM testing has been further developed through both laboratory experiments and theoretical studies.

ReaTHM testing will play a key role in the Ocean Space Centre, which is a planned large Norwegian national centre for education, research and technology development for the marine industry [84]. Both SINTEF Ocean and NTNU are key stakeholders in this centre. It is expected that research and best practices from the Hybrid KPN project will contribute to the successful use of ReaTHM testing in the new centre.

Prior to this thesis, no less than three PhD projects on ReaTHM testing were completed at NTNU in collaboration with SINTEF Ocean. To contrast these PhD projects with the present work, we present a summary of each:

- The thesis of Valentin Chabaud (2016) [60] examines in detail ReaTHM testing of floating wind turbines. As this work was performed early in the project, much of its emphasis is on describing and developing the necessary fundamental concepts and best practices for ReaTHM testing. The study includes

consideration of error sources, control system development, data processing, and specific issues related to the development of ReaTHM testing for offshore floating wind turbines.

- The thesis of Thomas Sauder (2018) [33] considers how various sources of error affect the achieved fidelity of ReaTHM testing. It develops and demonstrates new sophisticated mathematical methods for fidelity analysis and discusses them in the context of active truncation of slender marine structures.
- The thesis of Stefan Vilsen (2019) [35] considers ReaTHM testing on moored ocean structures. It emphasises the feasibility and implications of incorporating complex numerical models into ReaTHM testing and develops a comprehensive yet straightforward design method for ReaTHM testing.

This thesis builds upon and extends the research and best practices developed in the above theses. However, its focus is different. In comparison, it focuses more on issues related to the actuation of forces and moments (loads) onto the physical substructure. Whereas the above theses mainly considered ReaTHM testing with complex numerical models, to emulate full-scale ocean structures, this thesis considers experimental testing using more simplified numerical substructures to investigate the method at a more fundamental level.

While [33] relies mainly on mathematical modelling, proofs, and simulations, [35] and [60] include extensive experimental work. Particularly relevant to this thesis is the experimental work of [35], which, like this thesis, covers experimental ReaTHM testing of a moored system. Whereas [35] actuates forces in two degrees of freedom using a complex mooring model, we actuate forces in three degrees of freedom using a simple linear mooring model, emphasising issues related to load control. Since the experimental work presented in [35] and [60], we have further developed the actuators and experimental architecture in collaboration with the research team. The related development, including the corresponding control systems, actuator design, and procedures, is elaborated in this thesis.

1.4 Research Objectives

The overall objective of this PhD project was to further improve the ReaTHM testing methodology as a step toward making it a documented, accepted, and valued practise that accurately identifies and predicts the behaviour of ocean structures in realistic hydrodynamic environments. One of the main challenges in this regard, and a major focus of this work, is to ensure that load actuation is performed robustly with minimal errors and without significant degradation of emulation performance.

The research presented in this thesis is underlined by five main objectives which are explained below.

Research Objective 1

Investigate, identify, and mitigate errors associated with load actuation in ReaTHM testing using CDPR setups, including the development of good practice control methods.

When addressing Research objective 1, we emphasise four distinct sources of error associated with load actuation: 1) delay-induced force errors, 2) force allocation errors, 3) force estimation errors, and 4) target force tracking errors. Further description of these errors is given in Table 2.1 after the detailed system architecture and modelling is presented. We will place a different emphasis on each source of error, depending on the state of the art and the potential for novel developments and improvements. For example, whereas we cover target force tracking extensively, we place less emphasis on force estimation errors since the latter is highly dependent on the specific sensor characteristics, which are generally well covered in other sources [85, 86].

Research objectives 2-4 are related to Research objective 1 and address specific challenges with load actuation and associated good practice control methods.

Research objective 2 addresses force allocation, which is the process of distributing the target cable forces such that they sum up to the numerically calculated load vector.

Research Objective 2

Study and further develop methods for force allocation on CDPR setups. The methods shall be applicable to ReaTHM testing in that the resulting target cable forces have beneficial properties and are robustly output by the solver in real-time.

Research objective 3 addresses the placement of actuated winches, with the goal of providing accurate and robust load actuation.

Research Objective 3

Study and develop a procedure for placement of actuators on cable-driven parallel robot setups that is optimal for ReaTHM testing.

Research objective 4 addresses accurate target force tracking using actuated winches.

Research Objective 4

Study and propose methods for accurate force control onto moving objects using actuated winches with emphasis on the use case of ReaTHM testing.

Experimental testing is important to develop and validate good practice control methods. Particularly, since ReaTHM testing is a recently developed method, there is limited experimental and theoretical documentation and limited rigorously established practices. We, therefore, direct considerable effort to experimental testing and related developments. With this, we state our fifth and final research objective.

Research Objective 5

Conduct experiments to identify, understand, and mitigate problems, to validate proposed methods, and to contribute to the development of procedures for ReaTHM testing using CDPR setups

The thesis does not use ReaTHM testing to determine the behaviour of realistic ocean structures, which is the intended end use of the method once it is mature. Instead, simpler test cases are considered to understand, develop, and improve the method at a fundamental level.

1.5 List of Publications and Main Contributions**Article 1 – Conference Paper [C-1]**

[87] E. S. Ueland and R. Skjetne.

Effect of time delays and sampling in force actuated real-time hybrid testing; a case study.

Proc. of the IEEE Oceans Conference, Anchorage, 2017.

<https://ieeexplore.ieee.org/abstract/document/8232196>

- ★ Contribution 1: Using simulations, we show how time delay and sampling in the ReaTHM testing loop significantly affect the fidelity of the emulated system. For the simulated test case, results are quantified in both the frequency domain and the time domain.

Article 2 – Conference Paper [C-2]

[88] E. S. Ueland, R. Skjetne, and S. A. Vilsen.

Force actuated real-time hybrid model testing of a moored vessel; A case study investigating force errors.

Proc. of the 11th IFAC Conference on Control Applications in Marine Systems, Robotics, and Vehicles CAMS, 2018.

[10.1016/j.ifacol.2018.09.472](https://doi.org/10.1016/j.ifacol.2018.09.472)

- ★ Contribution 2: Supported by experimental data, we identify, discuss, and partly quantify four sources of error related to load actuation in ReaTHM testing.
- ★ Contribution 3: The presented experiment constitute a first proof of concept of ReaTHM testing of ship-shaped vessels.

Article 3 – Journal Paper [J-1]

[89] E. S. Ueland, T. Sauder, R. Skjetne.

Optimal Force Allocation for Overconstrained Cable-Driven Parallel Robots: Continuously Differentiable Solutions With Assessment of Computational Efficiency

IEEE Transactions on Robotics, 2020.
[10.1109/TRO.2020.3020747](https://doi.org/10.1109/TRO.2020.3020747)

- ★ Contribution 4: We analyse the optimal force allocation problem for CDPR and propose a new cost function for the standard version of the problem that ensures \mathcal{C}^1 continuity of target cable forces.
- ★ Contribution 5: We propose a new cost function for the slacked version of the problem. This ensures that the error remains close to zero when desired. We derive an upper bound on the error under certain assumptions.
- ★ Contribution 6: Through extensive numerical simulations, we conjecture that a solver based on Newton's method is feasible for use in real-time applications.

Article 4 – Journal Paper [J-2]

[90] E. S. Ueland, T. Sauder, R. Skjetne.
Optimal Actuator Placement for Real-time Hybrid Model Testing using Cable-driven Parallel Robots
Journal of Marine Science and Engineering, 2021
[10.3390/jmse9020191](https://doi.org/10.3390/jmse9020191)

- ★ Contribution 7: We propose a procedure for actuator placement that: 1) ensures that the numerically calculated loads are applicable throughout the testing campaign – which is a prerequisite to carry out ReaTHM testing, and 2) maximises load actuation accuracy – which is important to ensure high fidelity ReaTHM testing.

Article 5 – Journal Paper [J-3]

[91] E. S. Ueland, T. Sauder, R. Skjetne.
Force Tracking using Actuated Winches with Position controlled Motors for use in Hydrodynamic Model Testing.
IEEE Access, 2021
[10.1109/ACCESS.2021.3083539](https://doi.org/10.1109/ACCESS.2021.3083539)

- ★ Contribution 8: We demonstrate that a force actuation system based on a position controlled servomotor fitted with a clockspring, a drum, and a force sensor at the end effector can be used for accurate cable force control onto moving objects. Here, we propose a feedforward force control term that uses online estimates of the clockspring characteristics for better performance. Furthermore, control terms are proposed to deal with time delays and model disturbances which, if not compensated for, introduce force errors that correlate with end effector motions.
- ★ Contribution 9: We experimentally validate the proposed design and methods.

1.6 Structure of the Thesis

This thesis has three parts; Part I) the main report, 2) Part II) a collection of articles, and Part III) a list of previously published theses at the Department of Marine Technology at the Norwegian University of Science and Technology.

The thesis is organised as follows:

- ▷ Chapter 1 describes the background and motivation for developing ReaTHM testing, research questions, contributions, and structure of the thesis.
- ▷ Chapter 2 describes the assumptions, modelling, methods and experimental design of the ReaTHM testing systems considered in this thesis.
- ▷ Chapter 3 summarises the novelty, methods and results of the enclosed articles.
- ▷ Chapter 4 concludes the thesis and provides recommendations for future work.

Chapter 2

Modelling and Design of CDPR-based ReaTHM Test Setups

2.1 Overall Architecture and Examples

Using Figure 2.1 as a reference, we below present a method overview of ReaTHM testing, which divides the method into three phases: 1) identification and planning, 2) setup and configuration, and 3) verification and testing.

The section is based on the design procedures and recommendations presented in [77, 36, 38, 17], and on research, developments, and lessons learned from this PhD project.

2.1.1 Identification and Planning

Before commencing a ReaTHM testing campaign, a thorough evaluation of the test purpose and requirements is important. Key test criteria considered at this stage are:

- *Test objectives*: The full-scale behaviour and characteristics that one wishes to determine through ReaTHM testing. For example, these can be motions in rough seas, stresses, the structural loading at critical points, or wave drift forces.
- *Load cases*: The environmental conditions, including wave and current profiles, under which the structural behaviour is to be evaluated.
- *Quantities of interest*: The set of test quantities that should be observed, directly or indirectly, to enable the engineer to assess the behaviour of the structure under consideration in relation to the test objectives. These can be localised quantities, such as the strain at critical sections of the structure or the water column height at a particular location. They may also be global behaviours such as the motions of the structure.
- *Accuracy targets*: The test accuracy specifications for the various quantities of interest.

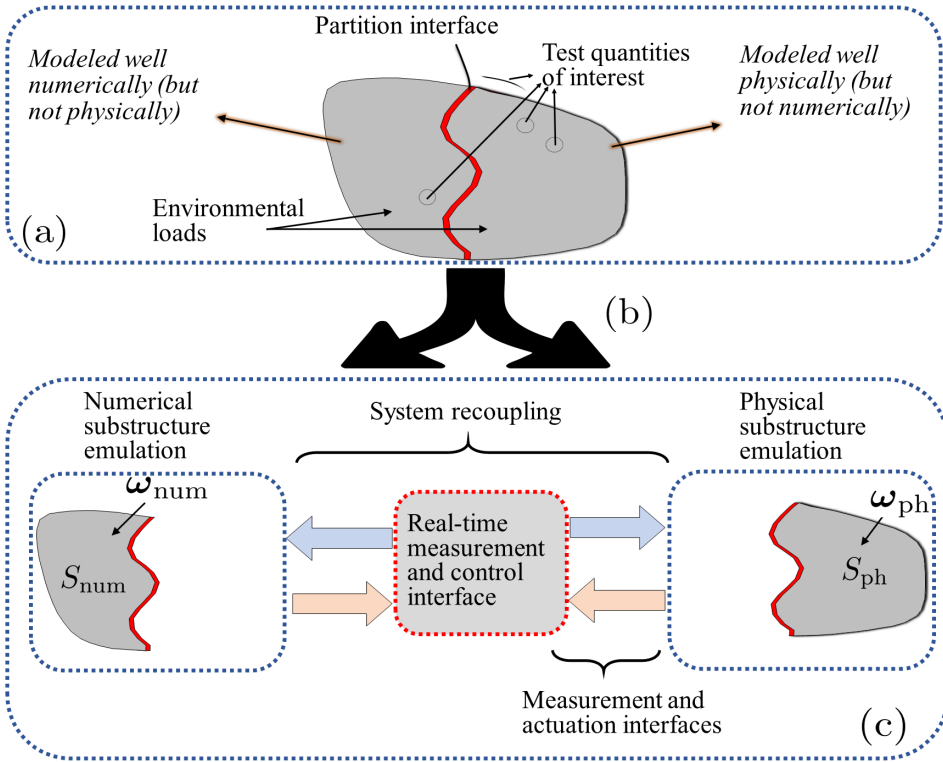


Figure 2.1: The ReaTHM testing method – highlighting important elements. (a) The target system for emulation. (b) System partitioning. (c) Emulation of recoupled system.

These criteria are all important inputs when configuring a ReaTHM testing setup. For example, accuracy targets, load cases, and test objectives determine whether a substructure can be numerically emulated within acceptable performance levels. They also relate to testability, as introduced for HIL testing in [65]. Testability can loosely be defined as the extent to which a test objective can be met, requiring controllability and observability of the corresponding quantities of interest.

2.1.2 ReaTHM testing Setup and Configuration

System Partitioning

The target ocean structure is partitioned into physical and numerical substructures. The partitioning interface location is chosen based on a number of considerations, including: 1) which parts of the system and physical phenomena must be modelled physically, and which can be modelled numerically, 2) limitations of laboratory facilities and actuation technology, and 3) the desired recoupling method.

Substructure Emulation

Each substructure should be accurately emulated according to established practices, as described next.

The *physical substructure emulation* is performed adhering to engineering practices used in traditional hydrodynamic model testing. That is, a down-scaled version of the ocean structure is tested in a laboratory basin and subjected to controlled environmental loads, with experiments designed to satisfy the relevant similarity laws. In addition, actuators are attached to the test platform, responsible for transferring the numerically calculated interface quantities.

The *numerical substructure* is typically emulated using a full-scale numerical model. This model can be, for example, a nonlinear finite element program running on a separate, dedicated computer [72]. There are three crucial requirements for the numerical substructure emulation:

1. The numerical substructure must be emulated with sufficiently high fidelity.
2. The numerical model must produce updated solutions in each control cycle. Since the physical emulation is Froude-scaled, the numerical models must run in Froude real-time; see Section 1.1.1.
3. The numerical solver must be adapted for coupling with a physical substructure by allowing real-time information flow at the interface. In practice, adaptation of established solvers may be required to facilitate this [72].

Modern basins have specialised wave flaps and current generators that can generate highly controlled hydrodynamic environments that mimic real-world sea conditions at model-scale. These conditions, in turn, interact with the structure in the form of hydrodynamic *environmental loads*. Depending on the test specifications, some environmental loads may be captured by the numerical substructure if this does not compromise test performance beyond acceptable accuracy targets. Reference [36] argues that this is the case for aerodynamic loads in ReaTHM testing of offshore wind turbines.

System Recoupling

The system recoupling control logic is determined by the *real-time measurement and control interface*, which specifies the control inputs of the actuators and the input variables for the numerical substructure. It must ensure that information flows between the substructures in real-time with a high degree of interface consistency and without amplification of errors.

The *measurement and actuation interfaces* are the physical actuators and sensors connected to the physical substructure that: 1) measure the states of the physical substructure, such that the corresponding effect can be transferred to the numerical substructure, and 2) transfer the numerically calculated interface components to the physical substructure. To ensure high performance in these interfaces, attention should be paid to advantageous placement and configuration of actuators and sensors, depending on test objectives, load cases, quantities of interest, and accuracy goals.

2.1.3 Verification and Testing

To evaluate system performance, robustness, and sensitivity, and to identify safety issues, both [77] and [83] recommend performing *co-simulation studies* prior to testing on new ReaTHM testing setups, if relevant numerical models are available.

After the preliminary co-simulation study and once the setup is installed in the basin, a series of preliminary *verification tests* should be performed to develop and verify the experimental setup. To the degree possible, we recommend performing verification tests using automated testing strategies as part of an integrated deployment procedure for ReaTHM testing setups. We recommend the following steps:

1. Verify expected behaviour using a simple linear numerical substructure with predictable behaviour and without waves.
2. Assess the performance of the actuation and measurement interface relative to benchmark references.
3. If applicable, compare free decay test in which the ocean structure freely dampens out from initial offset both with and without connected actuators.
4. Evaluate the repeatability of the setup.
5. Evaluate and tune actuators.
6. Verify that procedures such as test initialisation, automated testing, and emergency shutdown behave as intended.

With verification tests satisfactory performed, the *testing campaign* can commence. Here, the quantities of interest are investigated subject to specified laboratory-generated environmental conditions according to test objectives, load cases and in line with best practices for traditional hydrodynamic model testing.

2.1.4 Examples from the Literature

Next, we summarise two examples of ReaTHM testing from the literature, emphasising concepts discussed in this section.

Example 1 (Figure 1.5b) [77]

This reference describes ReaTHM testing of a *moored buoy*. ReaTHM testing is performed to overcome basin depth limitations by partitioning the system into: 1) a physical substructure that is the floating buoy, and 2) a numerical substructure which is the full-scale mooring system simulated in RIFLEX [92]. The test objective is to identify effects corresponding to viscous drag and eddy making near the body's surface. Quantities of interest are the rigid body dynamics, damping coefficients, and the top-tension in the mooring lines. The buoy positions are input to the numerical substructure, whereas the numerically calculated loads are actuated onto the physical substructure in two degrees of freedom, using three cabled winches. Platform positions are estimated using gyro, accelerometers, and optical sensors. In the system verification phase, a simple linear isotropic stiffness model is used instead of the complex RIFLEX model. Moreover, load tracking and repeatability are assessed using simple decay and displacement tests. Finally, the subsequent

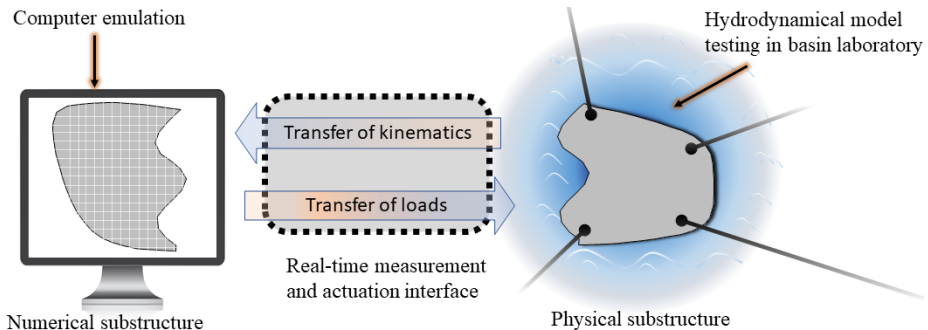


Figure 2.2: ReaTHM testing recoupling strategy of systems considered in this thesis.

testing campaign identifies linear and quadratic damping coefficients of the moored buoy.

Example 2 (Figure 1.5c) [36, 74]

These references describe ReaTHM testing of a 5MW moored *floating wind turbine*. ReaTHM testing is performed to overcome the Froude-Reynold conflict by partitioning the system into: 1) a physical substructure that is a floating offshore wind turbine subject to laboratory-generated waves, and 2) a numerical substructure which is the full-scale wind turbine exposed to simulated wind in AeroDyn [93]. The test objective is to evaluate system performance in conditions representative of the Northern North Sea. Quantities of interest are the rigid body dynamics, mooring line tensions and loads at the tower/floater interface. The turbine fundament motions are input to the numerical substructure, whereas the numerically calculated loads are actuated onto the physical substructure in 5 degrees of freedom, using six cabled winches. Platform positions are estimated using gyro, accelerometers, and optical sensors. In the system verification phase, initial decay tests are performed with and without actuators, comparing the quantities of interest. Moreover, load tracking, repeatability, and delays are assessed. Finally, results from an extensive experimental campaign are presented, where the wind turbine is found to have a significant impact on the system's natural periods and damping.

2.2 Detailed Architecture and Modelling

2.2.1 General Assumptions

In this thesis, we aim at developing methods and procedures for ReaTHM testing setups that satisfy the following assumptions:

- The target ocean structure is partitioned into a computer-emulated numerical substructure and an experimentally tested, down-scaled physical substructure, hereafter also referred to as the experimental platform. The experimentally measured displacements are input to the numerical substructure, and

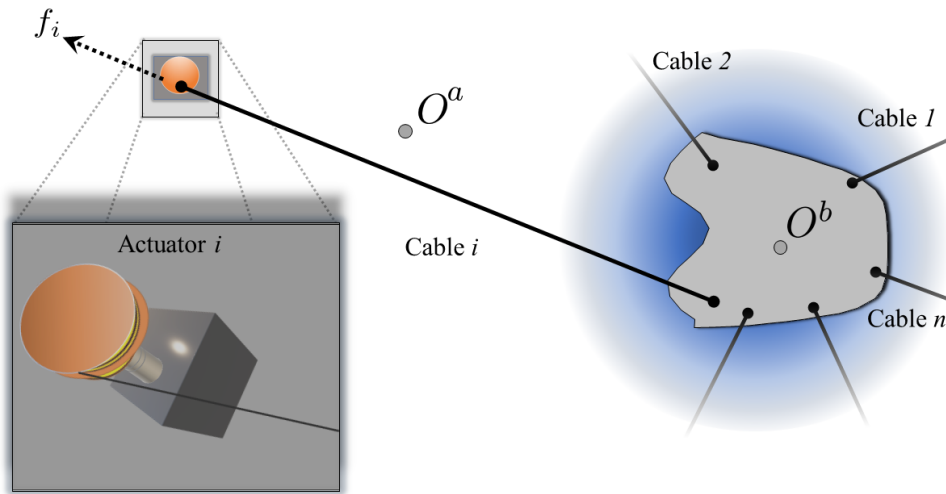


Figure 2.3: Experimental test setup with the platform (down-scaled physical substructure) connected to n actuated cables (only one of the actuators is sketched).

the numerically calculated loads are actuated onto the physical substructure; see Figure 2.2.

- The physical substructure is rigid with respect to load actuation such that the interface forces can be assembled to a global load vector that can be actuated distributively without disturbing the dynamics of the physical substructure.
- We actuate forces through n cables, each connected to the platform at one end, and tensioned by an actuated winch at the other. In this way, the experimental platform and actuators constitute a CDPR; see Figure 2.3.
- We control the platform in $m \leq 6$ spatial and rotational degrees of freedom (DOF). Moreover, if $m > 1$, then the CDPR is overconstrained such that $n > m$.
- Each cable forms a straight line and exerts a pull force on the platform in the cable direction. Constraints are imposed on each actuator; minimum pull forces $\mathbf{f}_{\min} = (f_{\min,1}, f_{\min,2}, \dots, f_{\min,n})$ are set to prevent the cable from going slack, and maximum pull forces $\mathbf{f}_{\max} = (f_{\max,1}, f_{\max,2}, \dots, f_{\max,n})$ are set based on actuator and cable limitations.
- The ReaTHM testing experimental architecture is functionally equivalent to that described in Section 2.2.2.
- The ReaTHM testing loop is functionally equivalent to that described in Section 2.2.3

2.2.2 Experimental Architecture

Figure 2.4 shows the ReaTHM testing experimental architecture used in this thesis. We next elaborate on the components indicated in the figure.

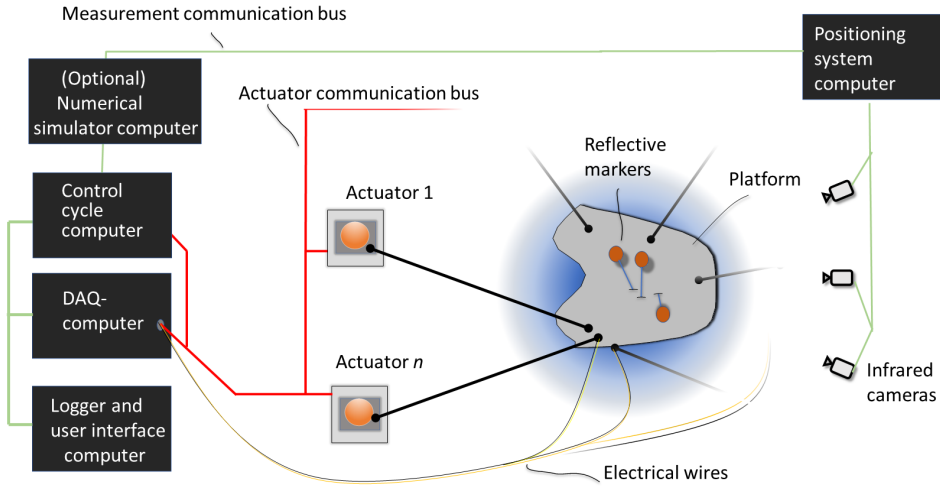


Figure 2.4: Schematic diagram of a ReaTHM testing setup and associated instrumentation, highlighting two of the n actuators.

Actuators

Figure 2.5 schematically illustrates a single actuator. It is composed of the following components¹.

- The *cable*, which is a thin braided polymer line, mass-produced for high-performance fishing applications. The stretched cable has one end wound onto the drum and the other end attached to the platform via the strain gauge.
- The *servomotor*, which is an industrial grade motor with integrated internal encoders, drive-level position control, and associated electronics. It allows high bandwidth, is fast and accurate, and has robust internal vendor-configured control software for motor shaft control.
- The *drum* which winds and unwinds the cable, enabling force control with large end effector motions. A rotary encoder measures the drum angle of rotation.
- The *clockspring* which is a flat spiral spring with its inner end attached to the motor shaft, and its outer end attached to the drum. The clockspring coils do not touch each other under compression, resulting in low friction and a nearly linear deflection-to-torque characteristic.

¹The resulting actuators have been developed by the research team over time and in several iterations. For confidentiality reasons, product-specific details of the actuator are not discussed. This includes component product names and certain technological or mechanical solutions that do not significantly impact the actuator model. For the same reason, we do not provide a picture of the actuator itself.

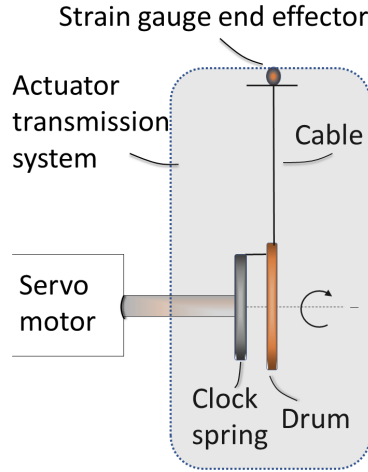


Figure 2.5: Schematic representation of the cabled actuator. During testing, n such actuators are connected in parallel topology to the experimental test platform.

- The *strain gauge end effector*, which is a full bridge six-wire strain gauge that outputs a current proportional to its tension. The strain gauge constitutes the end effector that connects the cable to the physical test platform.

Due to the compliance of the clock spring, the high-performance of the servomotor, and the high precision encoders, the proposed actuator is suitable for force control onto moving objects. For a more comprehensive description of the actuator, we refer to [J-3], where a corresponding force model of the actuator is presented along with a discussion of the design in relation to comparative literature.

Miscellaneous

- The *platform* is the experimental structure that shall mimic the target physical substructure. The platform is connected to the actuated winches and tested in basin laboratories subject to laboratory-generated hydrodynamic conditions. The platform is generally designed and produced according to engineering practices for traditional hydrodynamic model testing.
- *Reflective markers* are attached to the moving platform.
- *Infrared cameras* continuously measure the distance to the *reflective markers* based on the reflection of infrared light.

Computers

- The *control cycle computer* manages the control logic and transmits new setpoints to the actuator at the end of each control cycle.
- The *data acquisition (DAQ) computer* captures the measured values and passes them through the loop. The DAQ computer may employ simple filters or transformations before passing the signals to the rest of the loop.

- The *logger and user interface computer* connects the user to the control loop during operation. In addition to enabling user supervision, it logs data sampled by the DAQ computer.
- The *numerical simulator computer*. ReaTHM testing setups employed by research partners often use an external computer to run complex numerical models. See, for example [35]. This thesis only considers simple numerical models run on the control cycle computer and, therefore, does not employ this computer.
- The *positioning system computer*. The data sampled by the cameras is passed to the positioning system computer installed with proprietary Qualisys tracking manager software [94], which uses triangulation to continuously estimate the pose of the experimental platform with high accuracy.

Communication

- *Electrical wires* connect each force sensor to the DAQ computer. The end effector tensions are estimated based on the current-magnitude in these wires. Whereas the force sensors move with the experimental platform, the DAQ computer is stationary, meaning that there is relative movement between the end points of the electrical wires. The electrical wiring is light, and careful alignment minimises the force introduced through the wiring. A practical alternative to moving wires is to install a DAQ computer on the experimental platform. This can then be connected to the main loop, either by a single cable or by wireless communication. With this in mind, this thesis does not further elaborate on potential issues of the electrical wiring, or, alternatively, the wireless communication.
- *Communication buses* connect the computers and actuators. We separate between three communication buses: 1) the *actuator communication bus*, which communicates between the controller, the servomotor, and the encoders, 2) the *measurement communication bus*, which routes the pose estimates and measurements between computers in the loop, and 3) the *logger and DAQ bus*, which routes the signals from the DAQ computer to the other computers in the loop.

2.2.3 The ReaTHM Testing Loop

Figure 2.6 depicts the ReaTHM testing loop examined in this thesis, with relevant loop components highlighted and annotated. It can be partitioned into a higher-level outer control loop which couple the two substructures (left side of Figure 2.6) and a lower-level inner control loop responsible for actuating forces in each cable (right side of Figure 2.6). In the following, each element of the control loop is described, including the relevant modelling.

Resulting Load Vector

In considering the experimental setup, we refer to two reference frames, $\{a\}$ and $\{b\}$; O^a is the stationary origin of the local Earth-fixed coordinate frame $\{a\}$ in

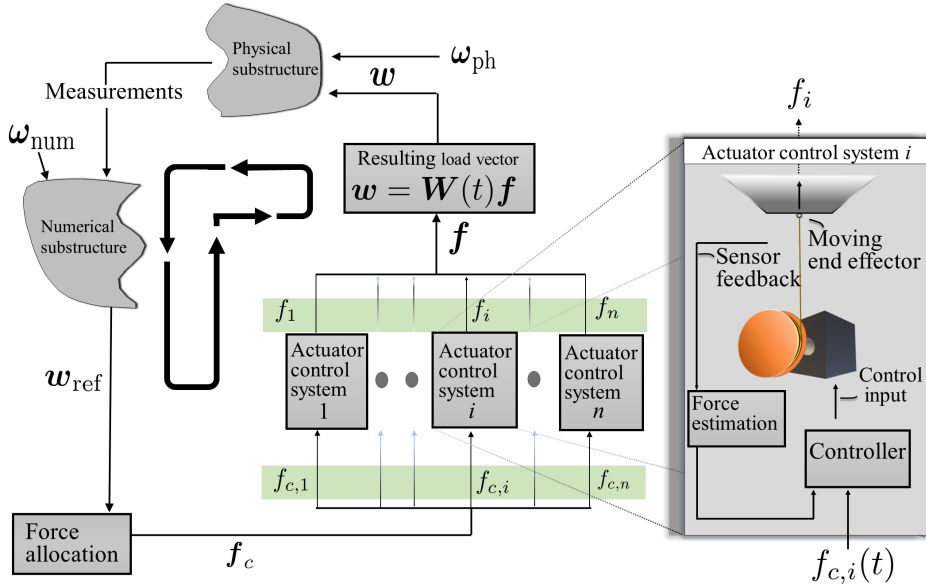


Figure 2.6: The ReaTHM testing loop highlighting the signal flow and loop components. Adapted from [J-3].

the basin, and O^b is the moving origin of the platform's body-fixed frame $\{b\}$; see Figure 2.3. Accordingly, vectors that are decomposed into $\{a\}$ or $\{b\}$ are given the superscripts letters a or b , respectively (if the superscript letter is omitted, and the vector has not been previously defined, it is decomposed into the $\{a\}$ frame). Using Figure 2.7 as a reference, this section outlines the geometric relationship between the cable force vector $\mathbf{f} = (f_1, f_2, \dots, f_n) \in \mathbb{R}^n$ and the cable load vector $\mathbf{w} \in \mathbb{R}^m$.

The position and orientation $\{b\}$ relative to $\{a\}$ are denoted by $\mathbf{p} := \mathbf{p}^a = (x, y, z) \in \mathbb{R}^3$ and $\boldsymbol{\Theta} := (\phi, \theta, \psi) \in \mathcal{S}_1^3$, where $\mathcal{S}_1 = [-\pi, \pi]$ (this thesis represent orientation by the zyx Euler angle convention [95, Ch 2.2.1]). These are represented in the body pose vector $\boldsymbol{\eta} := (\mathbf{p}, \boldsymbol{\Theta}) \in \mathbb{R}^3 \times \mathcal{S}_1^3$. The body-fixed linear and angular velocities are denoted by \mathbf{v}_v^b and $\boldsymbol{\omega}_v^b$, respectively. These are combined to form the body's linear and angular velocity vector $\boldsymbol{\nu} := (\mathbf{v}_v^b, \boldsymbol{\omega}_v^b)$. For each actuator $i \in \{1, \dots, n\}$, let $\mathbf{p}_{ai} := \mathbf{p}_{ai}^a$ be the fixed position of the i^{th} cable exit point A_i . Similarly, let the constant body-fixed lever arm from O^b to the i^{th} cable attachment anchor E_i (on the platform) be denoted \mathbf{r}_i^b .

The Euler angle rotation matrix $\mathbf{R}(\boldsymbol{\Theta})$ and the angular velocity transformation matrix $\mathbf{T}(\boldsymbol{\Theta})$ map vectors and angular velocities from $\{b\}$ to $\{a\}$:

$$\mathbf{R}(\boldsymbol{\Theta}) = \mathbf{R}_z(\psi)\mathbf{R}_y(\theta)\mathbf{R}_x(\phi), \quad (2.1)$$

with,

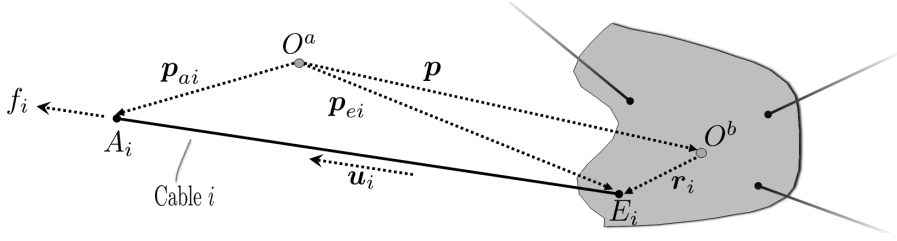


Figure 2.7: A CDPR platform, with one cable highlighted. (from [J-1]).

$$\mathbf{R}_x = \begin{bmatrix} 1 & 0 & 0 \\ 0 & \cos(\phi) & -\sin(\phi) \\ 0 & \sin(\phi) & \cos(\phi) \end{bmatrix}, \quad \mathbf{R}_y = \begin{bmatrix} \cos(\theta) & 0 & \sin(\theta) \\ 0 & 1 & 0 \\ -\sin(\theta) & 0 & \cos(\theta) \end{bmatrix}, \quad \mathbf{R}_z = \begin{bmatrix} \cos(\psi) & -\sin(\psi) & 0 \\ \sin(\psi) & \cos(\psi) & 0 \\ 0 & 0 & 1 \end{bmatrix}. \quad (2.2)$$

and

$$\mathbf{T}(\Theta) = \begin{bmatrix} 1 & \sin(\phi)\tan(\theta) & \cos(\phi)\tan(\theta) \\ 0 & \cos(\phi) & -\sin(\phi) \\ 0 & \frac{\sin(\phi)}{\cos\theta} & \frac{\cos(\phi)}{\cos(\theta)} \end{bmatrix}. \quad (2.3)$$

Accordingly, $\mathbf{r}_i(t) = \mathbf{r}_i^a = \mathbf{R}(\Theta)\mathbf{r}_i^b$, $\dot{\mathbf{p}}^a = \mathbf{R}(\Theta)\mathbf{v}_v^b$, and $\dot{\Theta} = \mathbf{T}(\Theta)\boldsymbol{\omega}_v^b$. It follows that the absolute position of E_i is $\mathbf{p}_{ei} := \mathbf{p}_{ei}^a = \mathbf{p} + \mathbf{R}(\Theta)\mathbf{r}_i^b$. From each actuator i , a force \mathbf{f}_i is acting on the platform at E_i , directed along the straight line $\mathbf{p}_{ai} - \mathbf{p}_{ei}$, whose direction is denoted by the unit vector $\mathbf{u}_i := \frac{\mathbf{p}_{ai} - \mathbf{p}_{ei}}{|\mathbf{p}_{ai} - \mathbf{p}_{ei}|}$. The relationship between the cable force vector \mathbf{f} and the cable load vector \mathbf{w} applied by the cables is described by $\mathbf{w}(t) = \mathbf{W}(t)\mathbf{f}(t)$, where

$$\mathbf{W}(t) = [\mathbf{q}_1(t) \quad \mathbf{q}_2(t) \quad \dots \quad \mathbf{q}_n(t)], \quad \text{with } \mathbf{q}_i(t) = \begin{bmatrix} \mathbf{u}_i(t) \\ \mathbf{r}_i(t) \times \mathbf{u}_i(t) \end{bmatrix}. \quad (2.4)$$

Since the pose $\boldsymbol{\eta}(t)$ varies with time, it follows that $\mathbf{u}_i(t) = \mathbf{u}_i(\boldsymbol{\eta}(t))$ and $\mathbf{r}_i(t) = \mathbf{r}_i(\boldsymbol{\eta}(t))$ are time-varying signals, and hence also $\mathbf{W}(t) = \mathbf{W}(\boldsymbol{\eta}(t))$.

The cable can be guided to the drum via a fuse, resulting in constant \mathbf{p}_{ai} . In cases without a fuse, the cable always forms a tangent to the drum. In this case, \mathbf{p}_{ai} depends on the position of the end effector relative to the actuator; see Figure 2.8a. Assuming that the drum and the cable are oriented in the xy-plane, \mathbf{p}_{ai} is determined, with reference to Figure 2.8b, as follows:

$$\mathbf{p}_{ai} = \mathbf{p}_{ai,0} + (\Delta x_a, \Delta y_a, 0) \quad (2.5a)$$

$$\Delta x_a = \frac{r^2 \Delta x \mp \Delta y r l}{d^2}, \quad \Delta y_a = \frac{r^2 \Delta y \pm \Delta x r l}{d^2}, \quad (2.5b)$$

$$d = \sqrt{\Delta x^2 + \Delta y^2}, \quad l = \sqrt{d^2 - r^2}, \quad (2.5c)$$

where $(\Delta x_a, \Delta y_a)$ is the decomposed vector from the cable attachment point \mathbf{p}_{ai} to the drum centre of rotation $\mathbf{p}_{ai,0}$, Δx and Δy is the decomposed horizontal

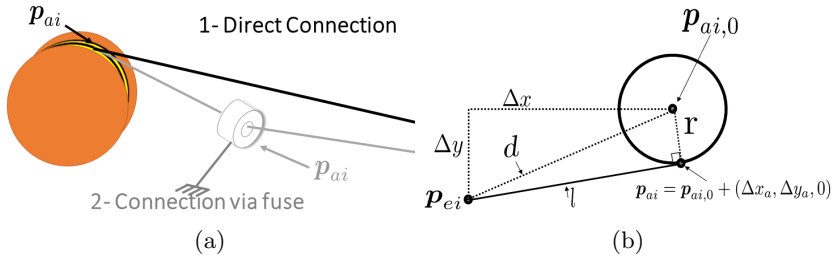


Figure 2.8: Cable to drum configurations. (a) Attachment with and without fuse. (b) Geometry when the cable attachment point is tangential to the cable-drum.

distance from \mathbf{p}_{ei} to $\mathbf{p}_{ai,0}$, and r is the effective drum radius. Furthermore, the signs of (2.5) are $(+, -)$ when the drum is wound in the clockwise direction and $(-, +)$ when the drum is wound in the counterclockwise direction. If the drum is not in the same plane as the cable, further rotations are required in addition to (2.5).

To describe a complete actuator configuration of a CDPR setup, we use the notation $\{\mathbf{p}_a\} := (\mathbf{p}_{a1}, \mathbf{p}_{a2}, \dots, \mathbf{p}_{an})$ and $\{\mathbf{r}^b\} := (\mathbf{r}_1^b, \mathbf{r}_2^b, \dots, \mathbf{r}_n^b)$.

Physical Substructure

The physical substructure is a down-scaled model of the corresponding target substructure, scaled according to Froude-scaling practices presented in Section 1.1.1. If the down-scaled model is a floating ocean structure, a simplified model of its dynamics, following [95] is

$$\mathbf{M}_{RB}\dot{\boldsymbol{\nu}} + \mathbf{C}_{RB}(\boldsymbol{\nu})\boldsymbol{\nu} + \mathbf{M}_A\dot{\boldsymbol{\nu}}_r + \mathbf{C}_A(\boldsymbol{\nu}_r)\boldsymbol{\nu}_r + \mathbf{D}(\boldsymbol{\nu}_r)\boldsymbol{\nu}_r + \mathbf{g}_r(\boldsymbol{\eta}) = \boldsymbol{\omega}_{ph} + \mathbf{w}, \quad (2.6)$$

where the coefficients are assumed to be independent of the wave excitation frequency, $\boldsymbol{\nu}_r$ is the body-fixed velocity relative to the local current, \mathbf{M}_{RB} and \mathbf{M}_A are the inertia matrices (due to rigid body mass and added mass), $\mathbf{C}_{RB}(\boldsymbol{\nu})$ and $\mathbf{C}_A(\boldsymbol{\nu}_r)$ are the corresponding Coriolis and centripetal matrices, $\mathbf{D}(\boldsymbol{\nu}_r)$ is the non-linear damping matrix, $\mathbf{g}_r(\boldsymbol{\eta})$ is the hydrostatic restoring force, \mathbf{w} is the cable load vector, and $\boldsymbol{\omega}_{ph}$ is the environmental forces acting on the ocean structure except those mentioned above.

Numerical Substructure

Consider now Figure 2.9. The numerical substructure receives the platform pose estimates $\hat{\boldsymbol{\eta}}$ and its derivatives from the camera-based pose tracking system described in Section 2.2.2. Since the numerical substructure is generally emulated in full-scale, whereas the physical substructure is emulated in model-scale, the inputs and outputs of the numerical solver are up-scaled and down-scaled, respectively (using Froude-scaling). With the assumption of rigidity, the numerically calculated force at each interface location is assembled into a global load vector that is to be actuated onto the physical substructure. The undelayed version of this load vector is denoted \mathbf{w}_I .

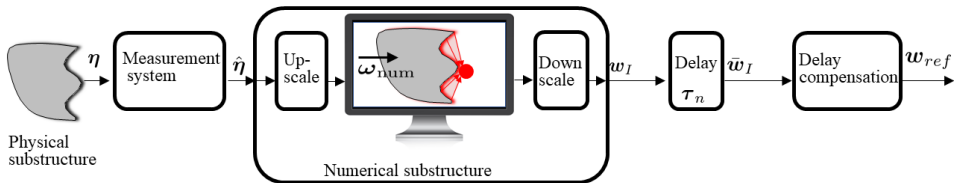


Figure 2.9: A part of the ReaTHM testing loop highlighting the numerical substructure (from pose to reference cable load vector).

Delay and Delay Compensation

Measurement delays, communication delays, processing times, and sampling times cause delays in the control loop; see [87, 72] and [C-1]. We model the time it takes for a motion in the experimental platform to be reflected in the numerically calculated load vector as a lumped delay τ_n . In the case of jitter, buffering, and inconsistent synchronisation of the control loop, τ_n may vary with time. The numerically calculated cable load vector that incorporates τ_n is denoted by $\bar{\mathbf{w}}_I(t) = \mathbf{w}_I(t + \tau_n)$.

We compensate for the delay by predicting the load vector forward in time. This is performed using forward extrapolation based on polynomial fitting, which should be accurate given the short prediction horizon, frequent sampling, and bounded frequencies of \mathbf{w}_I . After delay compensation, the resulting cable load vector is referred to as the *reference cable load vector*, denoted by \mathbf{w}_{ref} .

An alternative approach to polynomial fitting is to use model-based prediction methods, such as described in [43]. This requires accurate models of the experimental platform, which is inherently difficult to obtain in ReaTHM testing (since this is yet to be identified).

Force Allocation

Force allocation is the problem of finding the optimal cable forces $\mathbf{f}^* = (f_1^*, f_2^*, \dots, f_n^*)$ on an overconstrained CDPR setup such that they sum up to the reference cable load vector \mathbf{w}_{ref} . We find \mathbf{f}^* as the value of \mathbf{f} that minimises the cable cost function $g(\mathbf{f})$ subject to cable constraints $\mathbf{f}_{\min} \preceq \mathbf{f} \preceq \mathbf{f}_{\max}$ and the kinematic mapping $\mathbf{W}(\boldsymbol{\eta})\mathbf{f} = \mathbf{w}_{\text{ref}}$,

$$\mathbf{f}_c = \mathbf{f}^* = \underset{\mathbf{f}'}{\operatorname{argmin}} \{g(\mathbf{f}') : \mathbf{f}' \in \mathbb{R}^n, \hat{\mathbf{W}}(\boldsymbol{\eta})\mathbf{f}' = \mathbf{w}_{\text{ref}}, \mathbf{f}_{\min} \preceq \mathbf{f}' \preceq \mathbf{f}_{\max}\}, \quad (2.7)$$

where \mathbf{f}' is any cable tension vector \mathbf{f} satisfying the constraints and $\hat{\mathbf{W}}(\boldsymbol{\eta})$ is our best estimate of \mathbf{W} . Note that although \mathbf{f}^* and \mathbf{f}_c refer to different processes in the ReaTHM testing loop (the solution to the optimal force allocation problem and the commanded target forces, respectively), they differ only in name.

The force allocation problem is comprehensively studied in [J-1], which also presents a slacked version of the problem that allows small penalised errors in the resulting load vector.

Force Estimation

The i^{th} cable force measurement $f_{i,m}$ is computed based on the magnitude of the current u_i flowing through the force gauge i , which is assumed to be linearly proportional to the cable force f_i . After calibration and conversion of current-to-force it is modelled using

$$f_{i,m} = (1 + \alpha)f_i + \beta + \epsilon_i, \quad \text{for } i=1, \dots, n \quad (2.8)$$

where α is a scaling error, β is bias, and ϵ_i is Gaussian noise. The force sensors are sensitive to temperature variations [35], such that the coefficients α and β may drift over time. With scaling and calibration, we expect high-performance force measurements such that both α and β are close to zero. See also [C-2]. The force measurements are filtered. The force estimates, after filtering, $\mathbf{f}_m = (f_{m1}, f_{m2}, \dots, f_{mn})$ are denoted $\hat{\mathbf{f}} = (\hat{f}_1, \hat{f}_2, \dots, \hat{f}_n)$.

Target Force Tracking

In the inner control loop, the goal is for the applied cable force \mathbf{f} to accurately and robustly track the commanded forces \mathbf{f}_c , despite significant end effector motions. With the actuator compliance and the high bandwidth of the inner loop compared to the bandwidth of the outer loop, this thesis uses the concept of successive loop closure [96, Ch 6] and considers the inner loop and the outer loop independently. Consequently, the control of each actuator is treated as an independent control problem, assuming that the results are applicable to multiple cables in parallel topology; see [J-3]. For each actuator i , the resulting inner loop control objective is to control the estimated force \hat{f}_i to match the commanded force $f_{c,i}$ accurately. That is, to minimise the tracking error $\tilde{f}_i = \hat{f}_i - f_{c,i}$. Challenges associated with force tracking include disturbances caused by end effector motions, delays, and varying actuator spring characteristics.

2.3 Sources of Errors in ReaTHM Testing

When recoupling the numerical and physical substructures, the goal is to achieve a high degree of *interface consistency*, which refers to the following two conditions:

- *Force equilibrium* – the interface forces should be equal in magnitude and opposite in direction.
- *Kinematic compatibility* – the interface kinematics (position, velocity and acceleration) should be equal.

In general, the original system can be considered to be well mimicked if: 1) both the numerical and physical substructures are emulated with high fidelity, 2) we achieve a high degree of interface consistency, and 3) errors and disturbances are damped over time (as opposed to being amplified).

As shown in Figure 2.10, the ReaTHM testing loop can be divided into four operations, each of which may be associated with its own sources of error:

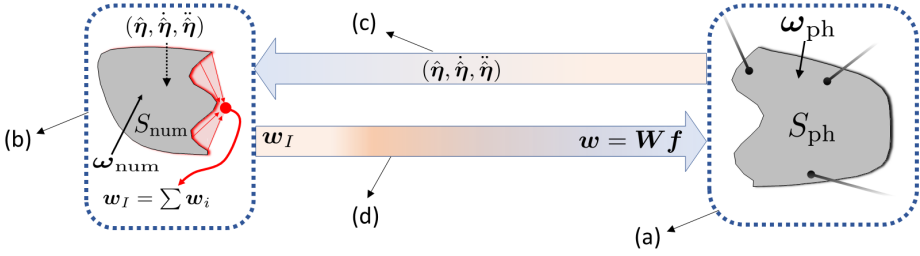


Figure 2.10: ReaTHM testing loop partitioned into four operations. (a) Emulation of the physical substructure. (b) Emulation of the numerical substructure. (c) Flow of kinematics from the physical substructure to the numerical substructure. (d) Flow of forces from the numerical substructure to the physical substructure.

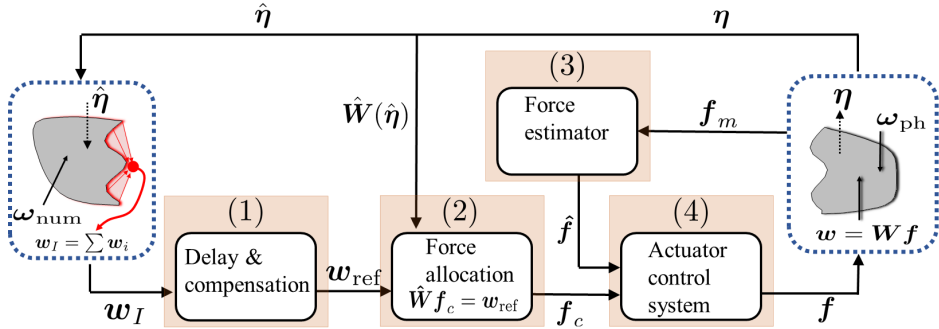


Figure 2.11: The ReaTHM testing loop highlighting four control loop procedures used for actuation of the numerically calculated load vector.

- (a) *Emulation of the physical substructure.* The sources of error associated with this operation are similar to those associated with hydrodynamic model testing. That is, errors may occur due to imperfections in geometric similarity (imperfect model), imperfections in kinematic similarity (deviation from specified current and wave fields), and imperfections in *dynamic similarity* (for example, due to mismatch in Reynolds number between model-scale and full-scale).
- (b) *Emulation of the numerical substructure.* The sources of error associated with this operation include simplifications in modelling, inaccurate or erroneous assumptions, use of approximations, incomplete capture of nonlinear effects, discretisation and linearisation. See also the discussion in Section 1.1.3. Due to real-time constraints, the numerical substructure may need to be simplified to ensure that solutions are returned within each control cycle, which may degrade performance further.
- (c) *Transfer of kinematics from the physical substructure to the numerical substructure.* Due to imperfect sensor measurements, estimation errors, and de-

Table 2.1: Sources of load actuation errors (in O^a).

Error type	Load actuation error	Explanation
(1) Delay-induced force errors:	$\mathbf{w}_{\text{ref}} - \mathbf{w}_I$	After delay compensation, some error is expected to remain between \mathbf{w}_I and \mathbf{w}_{ref} . Both due to inaccurate estimation of the delay τ_n and due to extrapolation errors.
(2) Force allocation errors:	$(\mathbf{W} - \hat{\mathbf{W}})\mathbf{f}_c$	$\hat{\mathbf{W}}$ generally deviates from the true mapping \mathbf{W} due to mischaracterisation of true actuator placement, mischaracterisation of reference frames, inaccuracies, and delays in pose estimates.
(3) Force estimation errors:	$\mathbf{W}(\mathbf{f} - \hat{\mathbf{f}})$	The estimated forces $\hat{\mathbf{f}}$ do not exactly match the true forces \mathbf{f} due to filtering, estimation errors, and measurement inaccuracies.
(4) Target force tracking errors:	$\mathbf{W}(\hat{\mathbf{f}} - \mathbf{f}_c)$	The estimated forces $\hat{\mathbf{f}}$ deviate from the target forces \mathbf{f}_c due to tracking errors in the actuator force controller. These errors are related to actuator dynamics, reaction times, and actuator control.

lays, there are errors in the kinematics sampled by the numerical substructure. That is, there are kinematic compatibility errors associated with this operation.

- (d) *Transfer of loads from the numerical substructure to the physical substructure.* Load actuation onto the physical substructure is imperfect. That is, there are force equilibrium errors associated with this operation.

Of the above four operations and their associated errors, this thesis, in line with the stated research objectives, are mainly concerned with operation (d) and associated good practice control methods.

Figure 2.11 schematically illustrates the four control loop procedures of operation (d) from the undelayed load vector \mathbf{w}_I to the applied load vector \mathbf{w} . As identified, discussed and partly quantified in [C-2], each of the four procedures is associated with errors that impact the applied load vector. These errors, which are listed in Table 2.1, correspond to the four errors that are emphasised for Research Objective 1; see Section 1.4. An overview of where each item is covered in the enclosed articles is listed in Table 2.2. As reflected in the table, we do not cover each of these errors in equal depth. Instead, we focus on developments where we see fit according to the current state of the art. Whereas articles [C-1] and [C-2] emphasise identification and quantification of load actuation errors, articles [J-1], [J-2], and [J-3] address specific issues and good practice control methods aimed at improving robustness and performance of load actuation in ReaTHM testing.

2.4 Experimental Setups and Campaigns Developed in the Present Project

As part of the thesis work, experiments were carried out using both a readily accessible 1-DOF setup suitable for fundamental testing and development, and a

Table 2.2: Overview over load actuation error source coverage in the enclosed papers².

	[C-1]	[C-2]	[J-1]	[J-2]	[J-3]
(1) Delay-induced force errors:	✓	✓			
(2) Force allocation errors:		✓	Related	Related	
(3) Force estimation errors:		✓			
(4) Target force tracking errors:		✓	Related	Related	✓

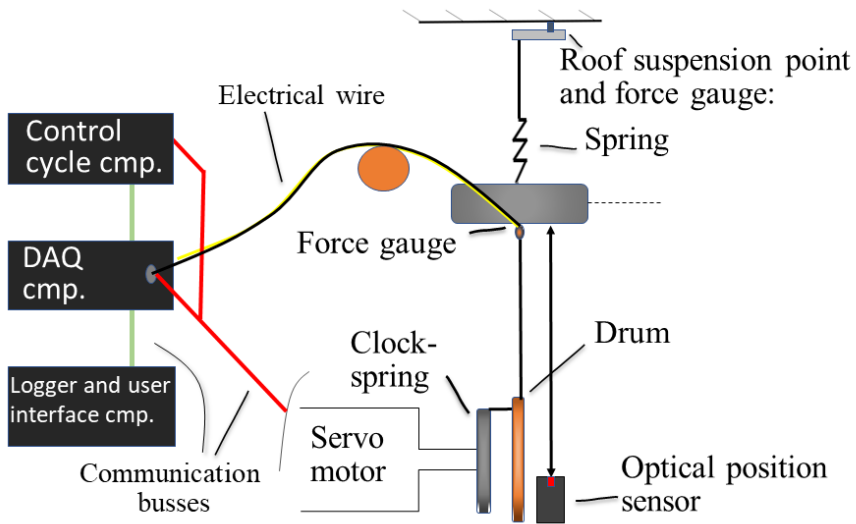


Figure 2.12: Schematic diagram of the 1-DOF setup and associated instrumentation.

more complex ReaTHM testing setup, as described next.

2.4.1 Setup 1 – A Simple 1 Degree of Freedom Platform

This setup, referred to as the 1-DOF setup, is illustrated schematically in Figure 2.12, and by pictures in Figure 2.13. The test platform consists of a mass connected to a roof suspension point by linear springs. Cable forces are applied to the platform from below along the same vertical axis, meaning that the platform is effectively a 1-DOF system (one translational degree of freedom). We used this

²The grey *related* designation indicates that the corresponding error is not considered explicitly. That is, [J-1] is listed as related to Error 2 since it considers force allocation, and to Error 4 since the resulting target force trajectories are smoother, which should improve force tracking performance. Similarly, [J-2] is listed as related to Error 2 and Error 4, since the optimisation procedure for actuator placement should reduce these errors.

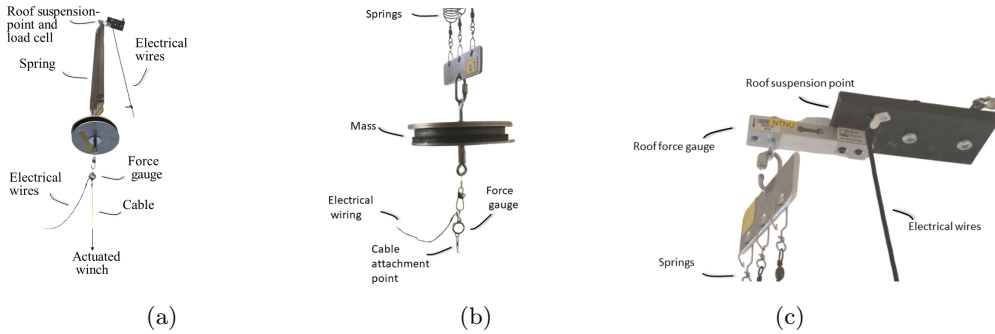


Figure 2.13: Pictures of the 1-DOF setup. The servomotor equipped with spring and drum is not shown for confidentiality reasons. (a) Experimental setup seen from below. (b) Mass fixed between end effector and springs. (c) Roof suspension point with load cell.

setup because it is easy to model, monitor, install, reconfigure, and use, yet capable of providing wide-ranging force and end effector trajectories. Apart from the components already described in Section 2.2.2, the setup consists of the following:

- The *mass*, which is composed of interchangeable metal discs, and to which the end effector is attached from below; see Figure 2.13b.
- The *spring*, which consists of interchangeable linear springs that are tensioned between the mass and the roof suspension point.
- The *roof force gauge*, which is a double bending beam load cell; see Figure 2.13c. Since the load cell is of a different technology than the strain gauge, it serves as a redundant sensor to monitor that the main force strain gauge remains well-behaving.
- The *optical position sensor* which measures the position of the mass. It serves as a redundant sensor to monitor the mass position.

Configurations

In experimental testing, the 1-DOF setup was used with two different actuator configurations, as illustrated in Figure 2.14:

- The *fixed end effector configuration* which is illustrated in Figure 2.14a. Here the end effector is directly attached to the fixed roof suspension point, enabling force control with a constant end effector position.
- The *dynamic end effector configuration*, which is illustrated in Figure 2.14b. Here, the mass is excited by a second actuator (Actuator 2). The primary actuator (Actuator 1) is operated in force control mode. This enables testing of force tracking performance under controlled dynamic end effector trajectories.

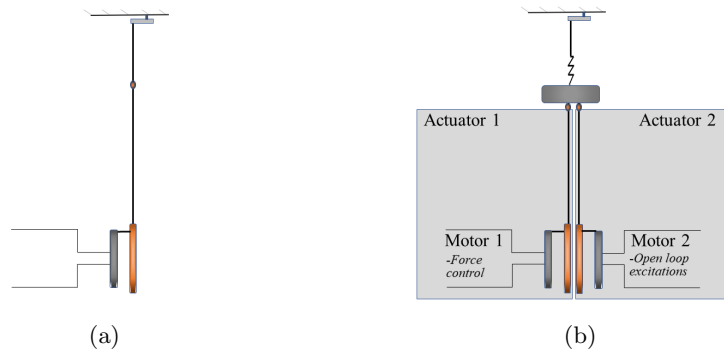


Figure 2.14: Additional configurations of the 1-DOF setup. (a) Fixed end effector configuration. (b) Dynamic end effector configuration.

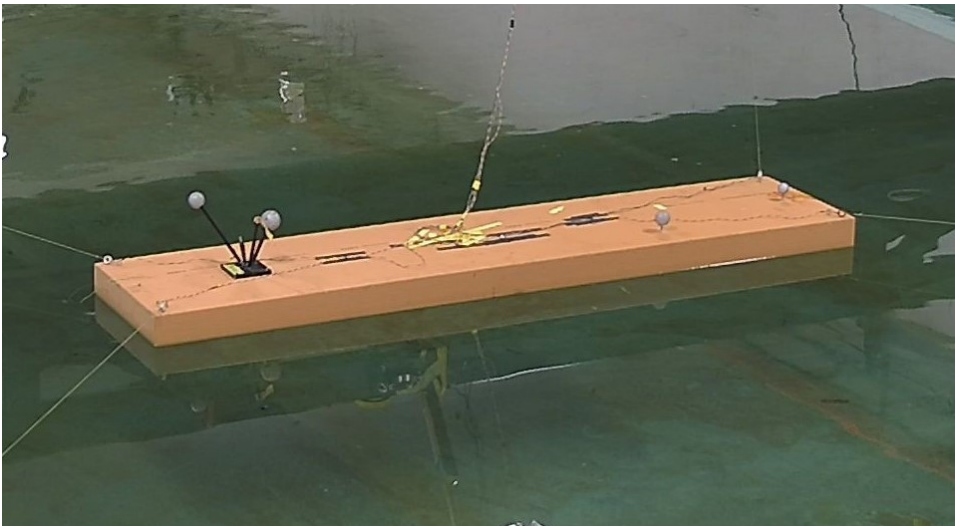


Figure 2.15: Image from ReaTHM testing of a moored barge (from thesis work, fall 2017).

2.4.2 Setup 2 – A Moored Vessel/Barge Installed in a Basin Laboratory

During this PhD project, we conducted ReaTHM-testing in the *Marine Cybernetics Laboratory* (MC-Lab) which is a basin facility with length-width dimensions $40m \times 6.45m$, equipped with both a towing carriage and a wavemaker. Whereas the nearby ocean laboratories, operated by SINTEF Ocean, require extensive personnel, costs, and resources to operate, the smaller MC-Lab is suitable for test campaigns smaller in scope.

Figure 2.15 shows the MC-Lab installed with the experimental setup from one of our ReaTHM testing campaigns, and Figure 2.16 illustrates the same schematically. In the latter, 13 elements are highlighted:

- (1)-(10) Elements as described in Section 2.2.1: (1) actuator, (2) reflective markers, (3) infrared cameras, (4) DAQ computer, (5) control cycle computer, (6) logger and user-interface computer, (7) positioning system computer (8) electrical wires, (9) actuator communication bus, and (10) measurement communication bus.
- (11) The experimental platform is a barge with length-width dimensions $2m \times 0.45m$, as illustrated in Figure 2.15. The same configuration was briefly tested using a ship of similar dimensions; see Figure 2.17. However, given the work’s developmental nature, we chose to limit testing to the latter as not to jeopardise the vessel’s expensive equipment.
- (12) A pole is extended over the vessel from the basin bridge to guide and align the electrical wiring for minimal motion-induced disturbances.
- (13) Actuator mountings are installed to fasten the actuators to the basin walls.

Configurations

Experimental testing with the moored barge was performed with the two actuator configurations shown in Figure 2.18 and detailed in Table 2.3:

- In *configuration 1*, illustrated in Figure 2.18a, a crossed cable configuration with the drum oriented in the xy -plane was used. In practice, this required a cable guide to ensure that the cable was always properly wound onto the drum.
- In *configuration 2*, illustrated in Figure 2.18b, an uncrossed cable configuration with the drum aligned in the xz -plane was used. This configuration allowed more flexibility in the placement of the actuators and eliminated the need for the cable guide. See discussion in Section 2.2.3. Since cable guide friction is a source of non-modelled forces, removing the cable guide is expected to increase force tracking performance.

The two configurations required different actuator mountings as shown in Figure 2.19. Whereas the mounting in Figure 2.19a already was used earlier in the research project [35], the mounting in Figure 2.19b had to be designed and fabricated for use in *Configuration 2*.

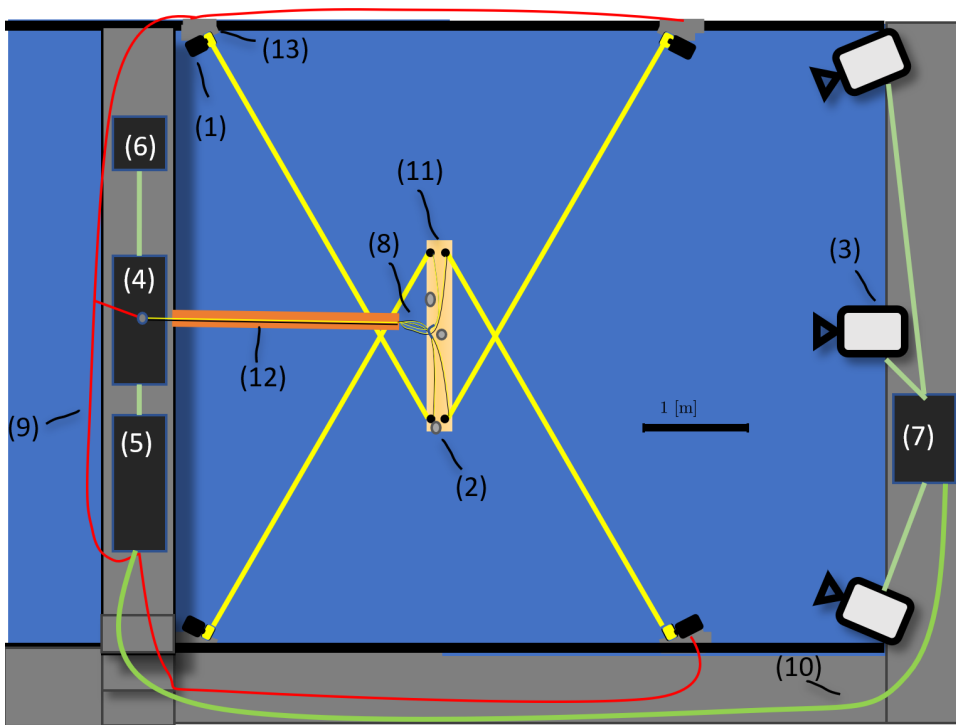


Figure 2.16: Schematic representation of the moored barge ReaTHM testing setup and associated instrumentation.

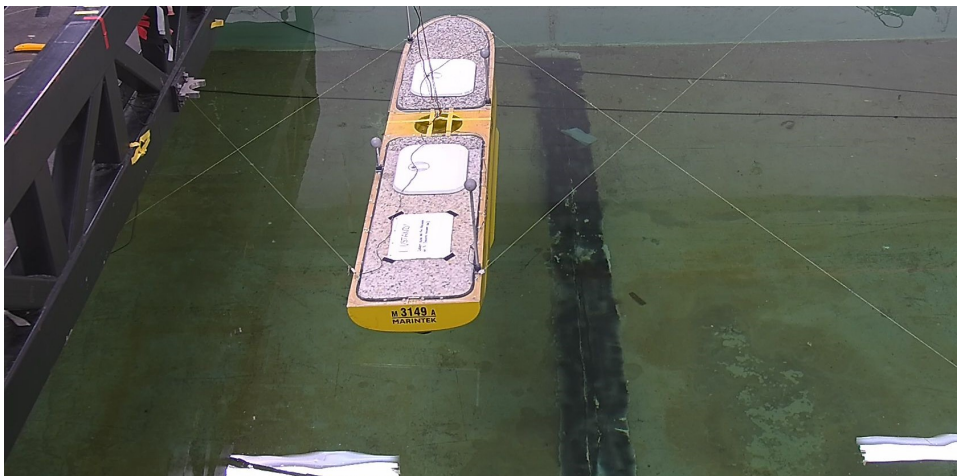


Figure 2.17: Picture of ReaTHM testing of a vessel in the MC-Lab (from thesis work, fall 2017).

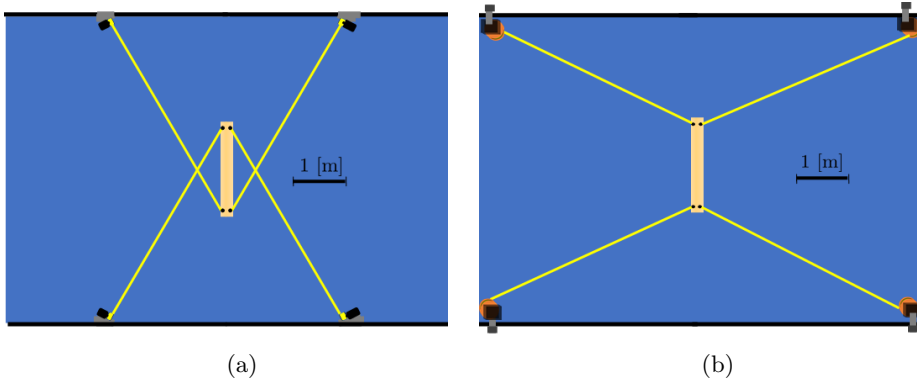


Figure 2.18: Schematic representation of the barge and actuator configuration in the two different experimental campaigns. (a) Configuration 1. (b) Configuration 2.

Table 2.3: Cable exit points and cable attachment anchors for the different configuration of the moored barge

Config. 1: $\{p_a\}$				Config. 2: $\{p_a\}$				Config. 1 and Config. 2: $\{r^b\}$						
	1	2	3	4		1	2	3	4		1	2	3	4
x	2.6	2.6	-2.6	-2.6	x	4.07	4.07	-4.07	-4.07	x	0.18	0.18	-0.18	-0.18
y	-3.25	3.25	-3.25	3.25	y	3.05	-3.18	3.18	-3.05	y	0.95	-0.95	0.95	-0.95
z	-0.02	0.02	-0.02	0.02	z	0	0	0	0	z	0	0	0	0

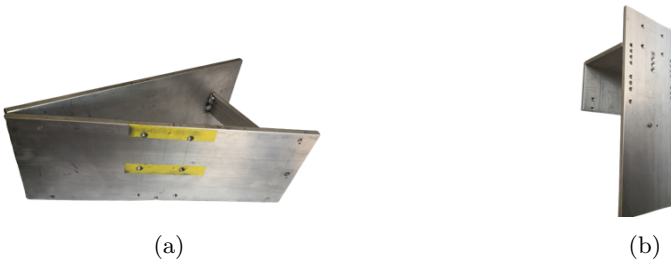


Figure 2.19: Basin wall mountings for the actuators. (a) Mounting used in Configuration 1. (b) Mounting used in Configuration 2.

Table 2.4: Overview of the experimental platform coverage in the enclosed papers³.

	[C-1]	[C-2]	[J-1]	[J-2]	[J-3]
Ship-shaped platform:		✓	Partial	✓	
1-DOF setup:	✓				✓
Includes experiments:		✓	Partial		✓

2.4.3 Experimental Campaigns of the Thesis

The two experimental setups were used extensively throughout the project work. See Table 2.4 for an overview of experimental setup coverage in the various enclosed articles.

Testing using the 1-DOF Setup

The 1-DOF setup was used throughout the project period and was essential to develop and improve control logic and to prepare for more extensive experimental campaigns in the MC-Lab. It enabled rapid prototyping of actuators, software, hardware, control system, and the ReaTHM testing loop as a whole. In addition, its simplicity makes it ideal for studying fundamental aspects of ReaTHM testing. Examples of developments made with the setup include the introduction of encoders to track the actuator clock spring deflection and the force controller developments presented in [J-3].

We used two different iterations of the setup:

Spring 2017-Fall 2018. This was the first version of the setup using an earlier iteration of the actuator. Due to lower performance, the experimental results are less interesting and not included in the published work. However, the setup was essential to the development of the overall system, including software solutions, hardware configurations, and controllers.

Fall 2019-Spring 2020. With the experience gained from the previous iteration, the setup was reinstalled with the latest version of the actuators. This setup is the one shown in Figure 2.13c. Experimental results and developments from this setup are described in [J-3].

Testing using the Moored Barge

We conducted two extensive ReaTHM testing campaigns with the moored barge in the MC-Lab. In addition to applying ReaTHM testing to a new type of structure (that is, ship-shaped vessel), the main goals of the tests were to further develop the control system, develop and validate procedures and best practices, and to identify and understand limitations and issues of the method. The experimental campaigns aimed at developing ReaTHM testing at a fundamental level rather than quantifying the responses of a real-world moored system. For this purpose, simple horizontal linear mooring models were used to calculate the mooring loads in three degrees of freedom (surge, sway and yaw) as described in as described in

³The grey *partial* designation indicates that the corresponding experimental setup is a minor element of the study.

[C-2]. These loads were then actuated onto the barge using four cabled winches. If the goal were, instead, to accurately reproduce the real-world mooring system, one would typically use a high fidelity numerical simulation tool for the mooring system. See, for example [72].

Fall 2017. Using Configuration 1, this testing campaign examined the behaviour of the moored barge in decay tests. That is, tests in which the barge is released from an initial offset from the mooring line equilibrium point. The setup was also used to assess performance under actuation of harmonic loads with varying frequency. The tests identified linear hydrodynamic damping coefficients, problems related to load actuation, and the influence of the actuation system on the damping. The results of the campaign are described in [C-2].

Spring 2019. Using Configuration 2, this testing campaign investigated decay tests as well as the estimated load actuation error of the system with the barge in different poses of its workspace. The setup used the latest iteration of the actuator system and a version of the force allocation procedures developed in [J-1]. However, practical and technical issues, unrelated to the considered research methods, impaired the quality and scope of testing. For this reason, elaboration on these results is not prioritised in this thesis, beyond the brief excerpts presented in [J-1].

Chapter 3

Summary of Enclosed Articles

This chapter summarises each of the enclosed articles, by outlining their novelties, methods used and results. The article summaries are organised into four topics: 1) error sources and error quantification, 2) improvements in force allocation method, 3) improved procedure for placement of actuators, and 4) improvements in cable force control. For the latter, we have included an extension to article [J-3], not published elsewhere.

3.1 Error Sources and Error Quantification

[C-1] – Effect of Time Delays and Sampling in Force Actuated Real-time Hybrid Testing; a Case Study

Problem Description and Novelty This paper presents a study in which ReaTHM testing is used to emulate a double mass-damper-spring system. The study emphasises how delays and sampling at different points in the control loop (see Figure 3.1) reduce fidelity, i.e., the systems ability to replicate the trajectories of the ideal unpartitioned system.

Methodology The study is carried out by means of co-simulation, where both the numerical substructure and the experimental test components are modelled numerically. The emulated trajectories of the moving mass given delays and sampling in the ReaTHM testing loop are compared with the ideal benchmark trajectories to evaluate the emulation performance (both in the frequency domain and in the time domain).

Results The paper shows that the effect of short time delays can be well approximated by a first-order Taylor series. This, in turn, is used to show how the delays alter the system matrices describing the partitioned mass-damper-spring setup. The paper shows that the force feedforward delay introduces negative damping, while the position feedforward delay introduces positive damping. The latter's effect is most significant due to the relatively high stiffness of the actuator transmission system. Consequently, energy is damped out of the system under motion. It is shown how even small delays can significantly affect the trajectories when the system is

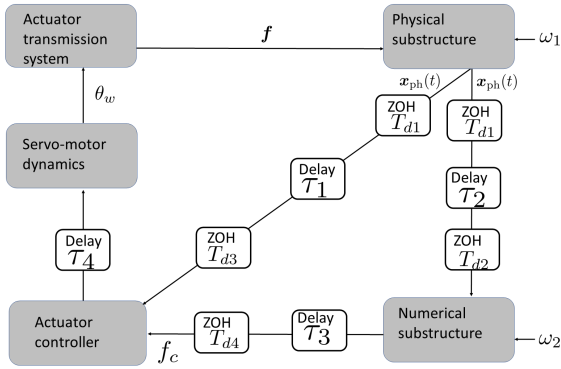


Figure 3.1: The ReaTHM testing loop used in C-1 with sampling (zero-order-hold elements T_{d1}, \dots, T_{d4}), and delays (τ_1, \dots, τ_4) indicated.

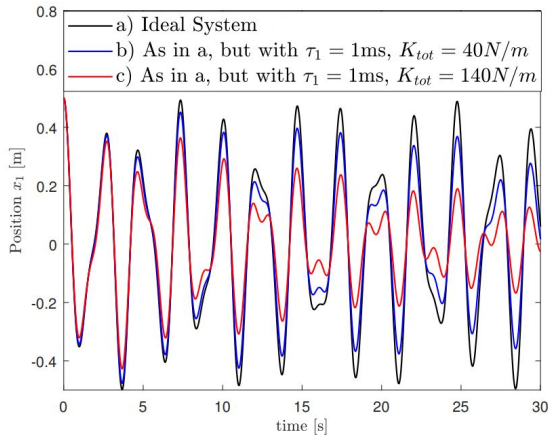


Figure 3.2: Effect of 1 ms delay on the mass trajectories in equally initialised decay tests. In simulation (a) an ideal actuator response was used whereas in simulation (b) and (c) a non-ideal, delayed actuator response was used. K_{tot} is the actuator transmission system stiffness. Coupled with delay, the stiffness introduces artificial damping to the system.

not excited – since the error accumulates over time. See Figure 3.2. When the system is harmonically excited, the effect of delays is found to be large for excitations near the systems natural frequency and small otherwise.

[C-2] – Force Actuated Real-Time Hybrid Model Testing of a Moored Vessel: A Case Study Investigating Force Errors

Problem Description and Novelty This paper considers ReaTHM testing of a moored barge. Assuming no modelling errors of the numerical substructure, the study aims at determining what distinguishes the loads acting on the physical substructure in ReaTHM testing from the ideal loads that would act on it in the real unpartitioned target system.

Supported by experiments, the study identifies, discusses, and partly quantifies issues related to load actuation in ReaTHM testing. The results are significant because they provide a straightforward and comprehensive overview of the types of load actuation errors that can occur in ReaTHM testing, not found elsewhere.

The presented experiment also constitute a first proof of concept of ReaTHM testing of ship-shaped vessels.

Methodology The paper considers a ReaTHM testing campaign of a moored barge in which the barge is kept experimentally, and the mooring system is emulated numerically. Based on the position of the barge, the numerically emulated mooring system outputs a load vector that in turn is actuated onto the barge; see Figure 3.3. As the work aims to investigate load actuation at a fundamental level, the numerical substructure is chosen as a horizontal linear mooring model with target forces proportional to the excursion in position and heading, rather than a more realistic, complex mooring model.

The experimental analysis chiefly considers decay tests in which the vessel decays from an initial offset towards the mooring system centre of origin, with an emphasis on load tracking performance.

Results Four sources of load actuation errors are identified, and partially quantified:

1. *Delay-induced force errors.* The paper experimentally verifies that a delay in the actuation of the numerically calculated load vector effectively introduces negative damping to the system. By varying an artificially introduced delay, the paper demonstrates that time delays affect the system in the form of negative damping that is linearly proportional to velocities. The paper suggests polynomial forward prediction to overcome the error.
2. *Force allocation errors.* The paper identifies how the estimated kinematic mapping may deviate from its real value. Complementary, it expresses load actuation sensitivity to changes in the geometric parameters of the kinematic mapping. The paper concludes that larger basin facilities combined with standardised actuator positioning can reduce force allocation errors.
3. *Force estimation errors.* These are errors between the forces estimated based on sensor measurements and the actual forces and are divided into random errors and biases. The random errors are handled by filtering. An experimental procedure is proposed to recalibrate the sensors to ensure minimum relative bias of the force sensors.

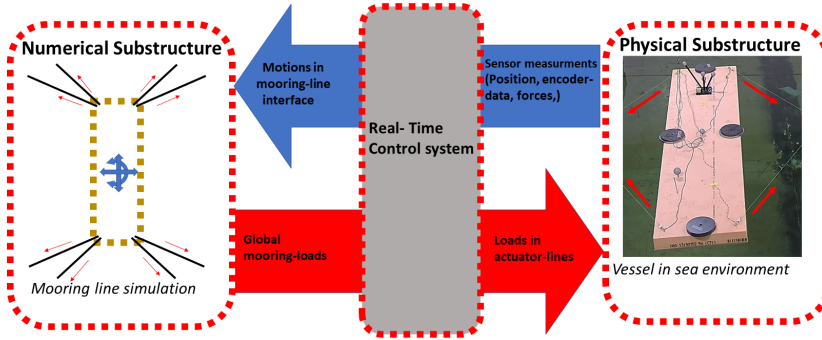


Figure 3.3: ReaTHM testing of a moored barge performed in [C-2]. Image on the right is from the experimental testing campaign.

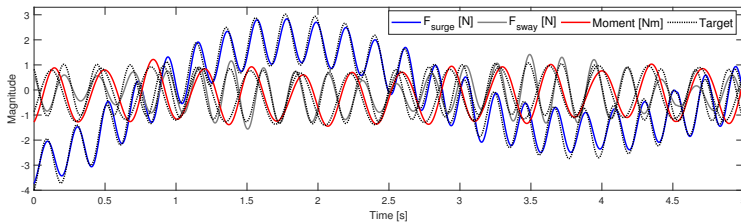


Figure 3.4: Force tracking performance in decay tests, demonstrated in [C-2]. The target load vector is the mooring line force combined with a harmonic excitation force.

4. *Target force tracking error.* This is the error between the estimated force and the target force. To further improve force tracking performance, the paper proposes to focus on improvements of the communication flow – to reduce resulting effective delays and jitter, improvements of the actuator design – to reduce the effect of actuator dynamics, better control design – to increase responsiveness and track the target forces more accurately, and compensation of delays and dynamics – to reduce motion-induced errors.

Overall, the experimental testing demonstrates encouraging force tracking performance of the presented ReaTHM testing setup.

3.2 Improvements in Force Allocation Method

[J-1] – Optimal Force Allocation for Overconstrained Cable-Driven Parallel Robots: Continuously Differentiable Solutions with Assessment of Computational Efficiency

Problem Description and Novelty This paper considers the *force allocation* problem of distributing a set of lower and upper bounded pull forces in the individual cables on an overconstrained C DPR setup such that the resulting forces and moments match the desired reference cable load vector. Figure 3.5 illustrates the paper’s central motivating example, along with the resulting force trajectories using traditional approaches. Two problems are highlighted in the figure: *A*) the standard formulation cannot handle cases where load feasibility is lost, and *B*) the p -norm cost functions might result in non-smooth forces.

The paper’s key contributions include a method for generating continuously differentiable actuator forces and a method that permits penalised errors in the resulting load vector, thereby increasing the C DPRs capabilities in practice. In addition, real-time feasibility is shown for a variety of configurations. This improves on current practices, where iterative methods are often disregarded due to real-time concerns.

Methodology The paper considers two versions of the force allocation problem: 1) the standard version, where the resulting load vector should exactly match the reference load vector, and 2) the slacked version, where some penalised errors are allowed.

The paper presents the mathematical basis for the proposed methods, including the formulation of theorems and propositions. The proposed cost functions and properties of the resulting force trajectories are analysed in detail. The real-time feasibility of the proposed methods is evaluated by applying their solvers to a substantial number of random configurations and trajectories.

Results Under relevant assumptions, the paper shows that the resulting cable forces are C^1 continuous. Figure 3.6 illustrates the computation time and the number of Newton iterations used by the solver for different configurations. As can be seen, the computation times always remain less than 0.3 milliseconds. By evaluating the method on a vast number of cases, which are assumed to challenge the algorithm for most relevant applications, the paper conjectures that the proposed method and solver is feasible for use in real-time applications.

For the slacked version of the solver, an upper bound on the cable load vector error is provided under some assumptions.

The presented methods are flexible in dealing with different problem configurations (varying number of cables, p -norms and actuator configurations) and enable intuitive tuning of the cost function, overcoming some of the challenges of existing methods.

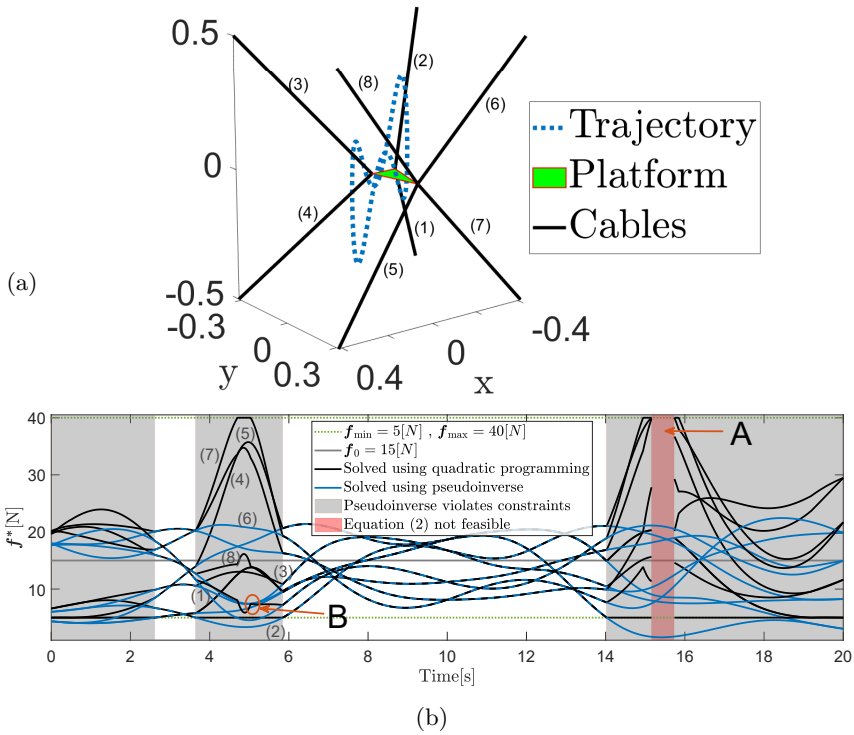


Figure 3.5: Motivating example in J-1. (a) Trajectory and configuration. (b) Resulting forces as a function of time. Two distinct issues are identified (A and B).

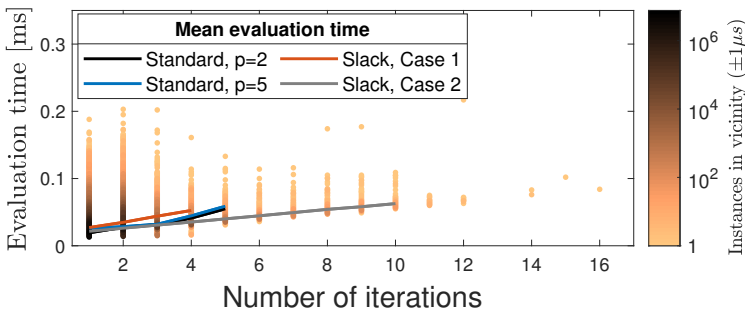


Figure 3.6: Scatterplots of the solver evaluation times as a function of iterations. Data gathered through extensive numerical simulations performed in [J-1].

3.3 Improved Procedure for Placement of Actuators

[J-2] – Optimal Actuator Placement for Real-time Hybrid Model Testing using Cable-driven Parallel Robots

Problem Description and Novelty This paper considers the problem of optimal placement of actuators for ReaTHM testing using CDPR. The paper’s key contribution is an actuator placement procedure that: 1) ensures that the numerically calculated loads are applicable throughout the testing campaign – which is a prerequisite to carry out a successful ReaTHM testing campaign, and 2) maximises load actuation accuracy – which is important to ensure high fidelity ReaTHM testing. The resulting procedure for placement of actuators is optimal in the sense that it minimises the proposed cost function.

The content of the paper is novel, as no other such guidelines currently exist.

Methodology The paper highlights differences between CDPR used for ReaTHM testing and more typical non-marine CDPR applications. It argues that the performance measures used in typical CDPR applications are not appropriate for ReaTHM testing – as this application requires accurate load control despite platform motions. In contrast, more typical applications require accurate kinematic control despite external loads acting on the platform.

With this in mind, a new performance measure is proposed, which is a linear combination of terms all aimed at accurate load actuation (that is, force distribution quality, target load vector sensitivity, motion sensitivity and kinematic mapping sensitivity). An associated actuator placement procedure is presented that minimises the proposed cost function and ensures that the expected numerical loads are always feasible.

The proposed procedure includes a problem specification phase in which constraints and parameters are specified. Recommendations for problem specification are first discussed at a general level, then for a test case represented in Figure 3.7.

Results Figure 3.8a shows the resulting global cost function value as a function of actuator placement for the investigated test case. The optimal placement is indicated in the figure both with non crossed cable configuration (black mark) and crossed cables (grey mark). The corresponding actuator placements are shown in Figure 3.8a. Although there are multiple trade-offs, captured by the global performance measure function, the general trend is that the procedure tends to align the cable attack angles in the DOFs that are highly prioritised by the performance measure weighting parameters.

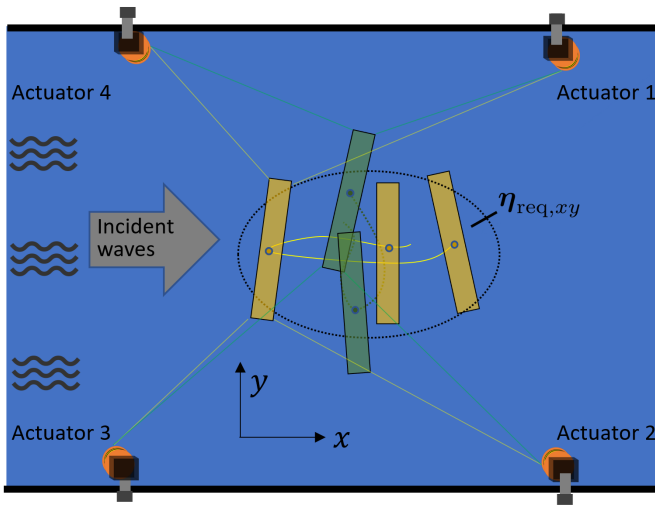


Figure 3.7: Moored barge in various poses and with the horizontal required workspace indicated.

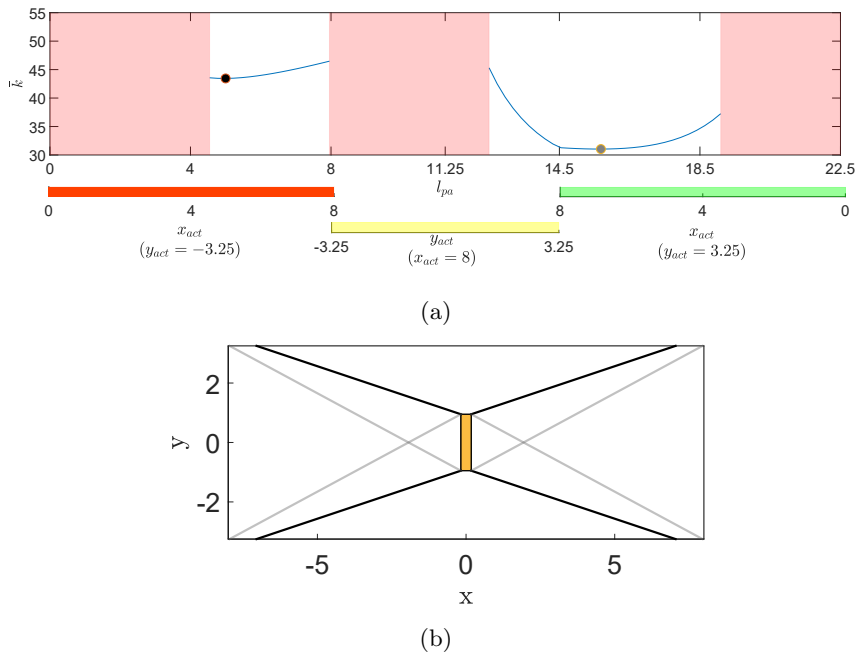


Figure 3.8: Optimal actuator placement minimising the cost function. (a) Global performance measure as a function of actuator placement (parameterised by the variable l_{pa} which refers to actuator placement along the basin wall). (b) Optimal actuator placement for the barge test case. Grey lines: crossed cables allowed. Black lines: crossed cables not allowed.

3.4 Improvements in Cable Force Control

[J-3] – Target Force Tracking using Position Controlled Motors, Added Compliance and an Adaptive Feedforward Controller –with Application to CDPR

Problem Description and Novelty This paper considers the problem of accurate force control using actuated winches¹, intended for use in ReaTHM testing and relevant for CDPRs that use force control in an inner control loop. The paper demonstrates how a load actuation system based on a position controlled servomotor fitted with a clockspring, a drum, and a force sensor at the end effector may be used for accurate cable force control on a moving object.

To ensure high-performance force control, methods are proposed to deal with time delay, model disturbances, and slowly varying actuator spring characteristics. If not compensated for, these lead to force errors that correlate with end effector motions, actuator dynamics and actuator spring deflection.

Force control using actuated winches has traditionally been achieved using servomotors controlled in torque mode. In contrast, this paper considers the much less studied strategy of force control using position controlled servomotors. Although the actuator’s basic design idea is simple, we have not managed to find similar designs in the CDPR literature. In this context, the paper is significant both due to the force control design’s novelty and due to the force control performance achieved with the proposed control strategies.

Although the primary motivation of this work was ReaTHM testing, developments towards accurate force control using actuated winches are significant for a number of CDPR applications using force control in an inner loop for kinematic control.

Methodology The paper discusses how, under some assumptions, the control of each actuator in a CDPR configuration can be treated as an independent control problem. Force tracking for a single cable is then investigated, assuming that the results are applicable to multiple cables in parallel topology.

To better understand the setup and facilitate control design, the study develops the actuator force model illustrated in Figure 3.9. Three different feedforward controllers are proposed with increasing complexity:

1. The simple feedforward controller that employs position and force feedforward control, based on the spiral torsion spring stiffness model.
2. The predictive feedforward controller, which also compensates for delay-induced errors by using the forward predicted drum angle as input to the feedforward position term.
3. The model correcting predictive feedforward controller, which, in addition to compensating for delays, also corrects for modelled actuator dynamics.

¹The considered actuator has been developed by the ReaTHM testing research team at NTNU and Sintef Ocean over time. See for example [60] for an earlier iteration of it.

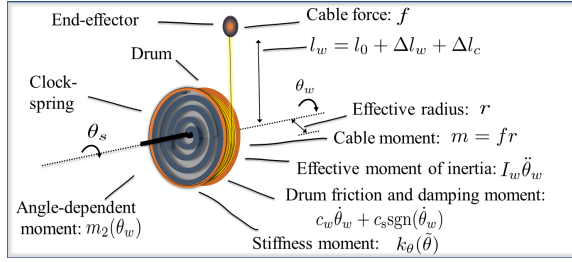


Figure 3.9: Actuator transmission system model developed in [J-3].

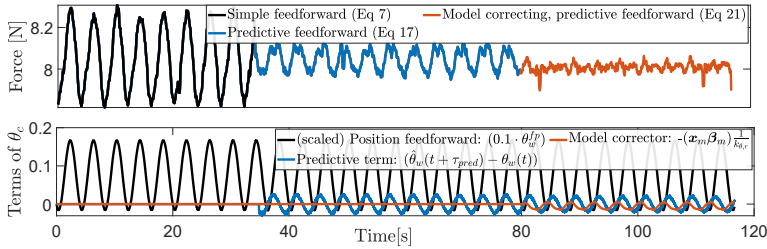


Figure 3.10: Force tracking with moving end effector and a constant target force $f_c=8N$. θ_c is the commanded servomotor shaft.

The proposed methods include online and adaptive estimation of the controller parameters using least-squares fitting and forward delay estimation methods. Using the experimental platform shown in Figure 2.13, experiments are extensively performed to validate the proposed methods.

Results Although a direct comparison was not made, the performance of force tracking appears promising compared to references using torque-controlled servomotors. See, for example [97].

Figure 3.10 shows how compensating for the delay and actuator dynamics in the proposed feedforward controller enhances force tracking performance. A number of other results are similarly demonstrated experimentally, including time-delay compensation, parameter estimation, and online adaptation of feedforward control parameters.

[Suggested Extension to [J-3], not previously published elsewhere]

A Design for an Actuated Winch with a Voice Coil End Effector

In this section, we propose and describe a conceptual new actuator design for force control that combines the actuator winch described in [J-3] with a voice coil actuator [98], as illustrated in Figure 3.11. Key advantages of voice coil actuators include high reliability, zero backlash, low friction, low hysteresis, a low electrical time constant (enabling fast responses), proportional current-to-force ratio (enabling high force resolution), and high force precision capabilities [99, 98]. By connecting the voice coil actuator to the end effector, the goal is to take advantage of the voice coil superior force control capabilities while retaining the position tracking capabilities of the actuated winch. To the best of our knowledge, the proposed actuator configuration for force control on CDPR setups is novel.

Voice Coil Actuator Force Model

The voice coil actuator consists of a current-carrying conductor (coil) contained in a housing with a magnetic field; see Figure 3.11b.

Let the mass of the voice coil be $m_c = m_{vc} + m_{ch}$, where m_{vc} is the mass of the coil, and m_{ch} is the mass of the voice coil housing attached to the platform; see Figure 3.12. The coil is free to move in the axial direction, with relative displacement denoted $x_e = x_2 - x_1$, where x_1 and x_2 are the displacements of the cable-attached coil and the platform-fixed housing, respectively. x_e is measured with built-in high precision encoders and is restricted by bearings to within the strokelength s_l . That is, $x_e \in \{-s_l/2, s_l/2\}$

When a current I flows through the conductor, a force f_v proportional and perpendicular to the current and the magnetic field is induced (Lorentz force), according to

$$f_v = IkBLN \quad (3.1)$$

where k is a constant, B is the magnetic flux density, L is the length of the conductor, and N is the number of conductors [98].

For practical purposes, $kBLN$ depends only on x_e , described by the mapping;

$$k_v(x_e) = kBLN, \quad x_e \in \{-s_l/2, s_l/2\}. \quad (3.2)$$

By design, the curve $k_v(x_e)$ is typically nearly constant over the stroke x_e . This results in the simple equation for the interface force

$$f_v = k_v(x_e)I. \quad (3.3)$$

Changing the direction of the current I , switches between push and pull force.

Actuated Winch Force Model

The following section describes the actuated winch dynamic model as a slightly simplified version of the model derived in [J-3].

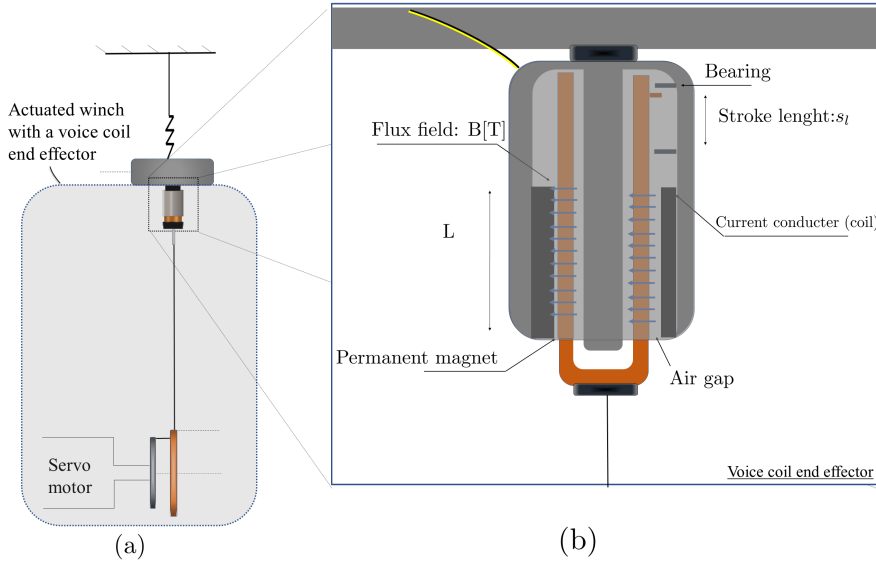


Figure 3.11: Proposed new actuator configuration combining the actuated winch with a voice coil actuator.

The cable-force resulting from compression of the clockspring is described by

$$f_w = (\theta_s - \theta_w - \theta_0) k_{\theta,r}, \quad (3.4)$$

where, $k_{\theta,r}$ is the clockspring stiffness, θ_0 is the spring equilibrium offset, θ_s is the motor shaft angular position, and θ_w is the drum angular position.

The servomotor is controlled in position-mode, with a pure delay τ_{cs} modelling the transient phase between the control input θ_c and the motor shaft angle θ_s :

$$\theta_s(t) = \theta_c(t + \tau_{cs}) \quad (3.5)$$

Let $x_w = -\theta_w r$ be the unwound cable-length due to change of θ_w , and the drum inertia with respect to x_w be $I_{w,x}$. Assuming that the cable is infinitely stiff and never goes slack, then x_1 and x_w are rigidly connected, with a common effective mass $m_v = m_{vc} + I_{w,x}$.

The voice coil force f_v acts onto m_v in one direction, and the actuator transmission force f_w , acts in the other. This results in the kinematic model

$$m_v \ddot{x}_w = f_v - f_w. \quad (3.6)$$

The cable-elongation is modelled by $\zeta(t)$:

$$\zeta = x_1 - x_w \quad (3.7)$$

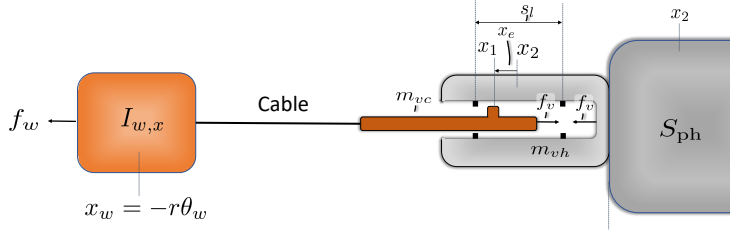


Figure 3.12: Voice coil actuator model, highlighting variables related to the dynamical model.

Control Problem

We divide the resulting control problem into two subproblems;

Control problem 1 (end effector force control): *Use control input I to regulate f_v such that it tracks $f_c(t)$.*

Assuming that I is accurately controlled using high performing current drives, and that $-s_l/2 \leq x_e \leq s_l/2$, setting

$$I = \frac{f_c}{k_v(x_e)} \quad (3.8)$$

should by (3.3) track the desired forces accurately.

Control problem 2 (end effector position control): *Use control input θ_c to regulate x_e such it is always within the stroke length $-s_l/2 \leq x_e \leq s_l/2$.*

Control problem 2 depends on whether or not the actuated winch has a clockspring between the motor shaft and the pulley or not, as described next.

With clockspring This is the original configuration described in [J-3]. In this case, we propose combining the simple feedforward controller of [J-3] with a classical PID controller as follows

$$\theta_c = \theta_w + \frac{f_c}{k_{\theta,r}} - \frac{x_e}{r} - k_p x_e - k_d \dot{x}_e - k_i \int x_e. \quad (3.9)$$

Without Clockspring The clockspring was initially installed to provide compliance and feedforward force control capabilities. This should no longer be necessary since the voice coil now introduces compliance, and the feedforward force control can be achieved using (3.3). This implies that the pulley can be mounted directly on the motor shaft. In this configuration, we propose a simple controller that let x_w track x_2 using

$$\theta_c = \theta_w - \frac{x_e}{r} - k_i \int (x_e). \quad (3.10)$$

Importantly, in this case, \dot{x}_e is no longer used in feedback, such that velocity estimates are not needed.

Simulations

In this section, we assess control performance using simulations, in which we model the actuator connected to a linear oscillator, described by:

$$\underbrace{2\ddot{x}_2+0.5\dot{x}_2+10x_2}_{\text{mass-damper-spring dynamics}} = \sin(t) - f_v, \quad (3.11)$$

where f_v is the actuated force that should track f_c , and $\sin(t)$ is an excitation force acting on the system. For the actuator winch model, described in (3.4)-(3.7), $r=0.06\text{m}$, $m_v=0.5\text{kg}$, $\tau_{cs}=15\text{ms}$, $\zeta(t)=-0.04\sin(0.04t)$, and $\theta_0(t)=0.05\sin(0.05t)$ are used. Finally, the target force trajectory is set to $f_c=\sin(2\pi\cdot 6t)+\sin(2\pi\cdot t)$.

If *Control problem 2* is satisfied, we assume that *Control problem 1* is directly satisfiable. That is, if x_e is within the stroke length, then f_v tracks f_c with sufficient accuracy using (3.9). We assume a stroke length of $s_l=2\text{cm}$, so that $-0.01\text{m}\leq x_e\leq 0.01\text{m}$ is required for Control problem 2 to be satisfied.

With Clockspring In this simulation, the clockspring is modelled using $k_{\theta,r}=8\text{rads}^{-1}\text{N/rad}$, and it is assumed that \dot{x}_e can be obtained with high accuracy using a lowpass filter with a cutoff frequency of 10 Hz. Furthermore, controller (3.9) is used with the gains $k_p=35$, $k_i=30$ and $k_d=2$.

Figures 3.13a-3.13b show the resulting trajectories of x_e and x_2 . Although x_e oscillates rapidly, it is always within the stroke length, such that both control problems are satisfied.

Without Clockspring In this simulation, the clockspring is modelled using $k_{\theta,r}=1500\text{Nrad}^{-1}$ (representing a very stiff interface between the motor shaft and x_1) and $\theta_0(t)$ is set to 0. Furthermore, controller (3.10) is used with gain $k_i=0.05$.

Figures 3.13c-3.13d show the resulting trajectories of x_e and x_2 . x_e is within the stroke length such that both control problems are satisfied. Overall, the system now oscillates much less, which is intuitively desirable. Therefore, for future investigation, we will prefer this configuration.

In Summary and for use in ReaTHM Testing

In this section, we have proposed and assessed a new actuator design for use in ReaTHM testing. If the proposed configuration is successfully implemented on a ReaTHM testing setup, it is envisioned that it would significantly enhance load tracking accuracy and the frequency range of applicable loads. Although the simple simulations presented in this section were successful, we recognize that all issues may not be adequately captured and that real-world testing is required to verify the feasibility of the setup. For example, it may be that transverse cable vibrations are detrimental to performance or that (3.8) is difficult to satisfy in practice. For further assessment, the configuration should be tested experimentally. First on a single degree of freedom setup, then on more complex setups. This is left open for future work.

ReaTHM testing applications with high frequency numerical load components and where the cable attack angle does not change significantly during the testing

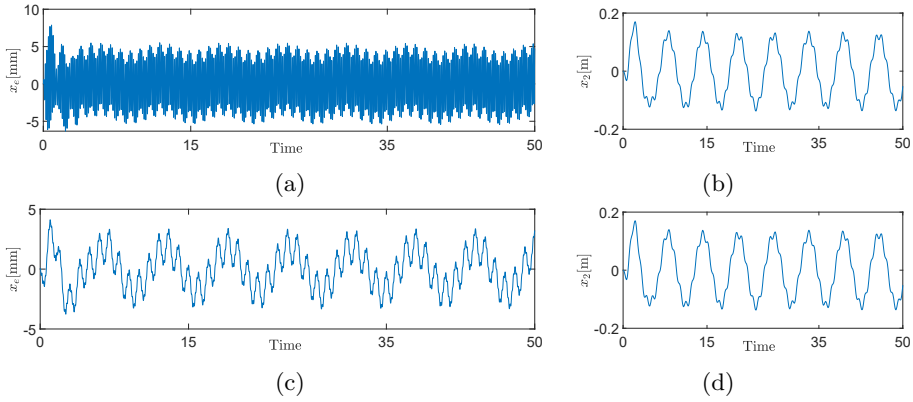


Figure 3.13: Simulated trajectories with simulations described in Section 3.4. (a-b) With clockspring. (c-d) Without clockspring.

campaign seem to be particularly suitable for the proposed actuator. This is typically the case for ReaTHM testing of offshore wind turbines. The hardware sensors and are then proposed for installation on the platform, as shown in Figure 3.14.

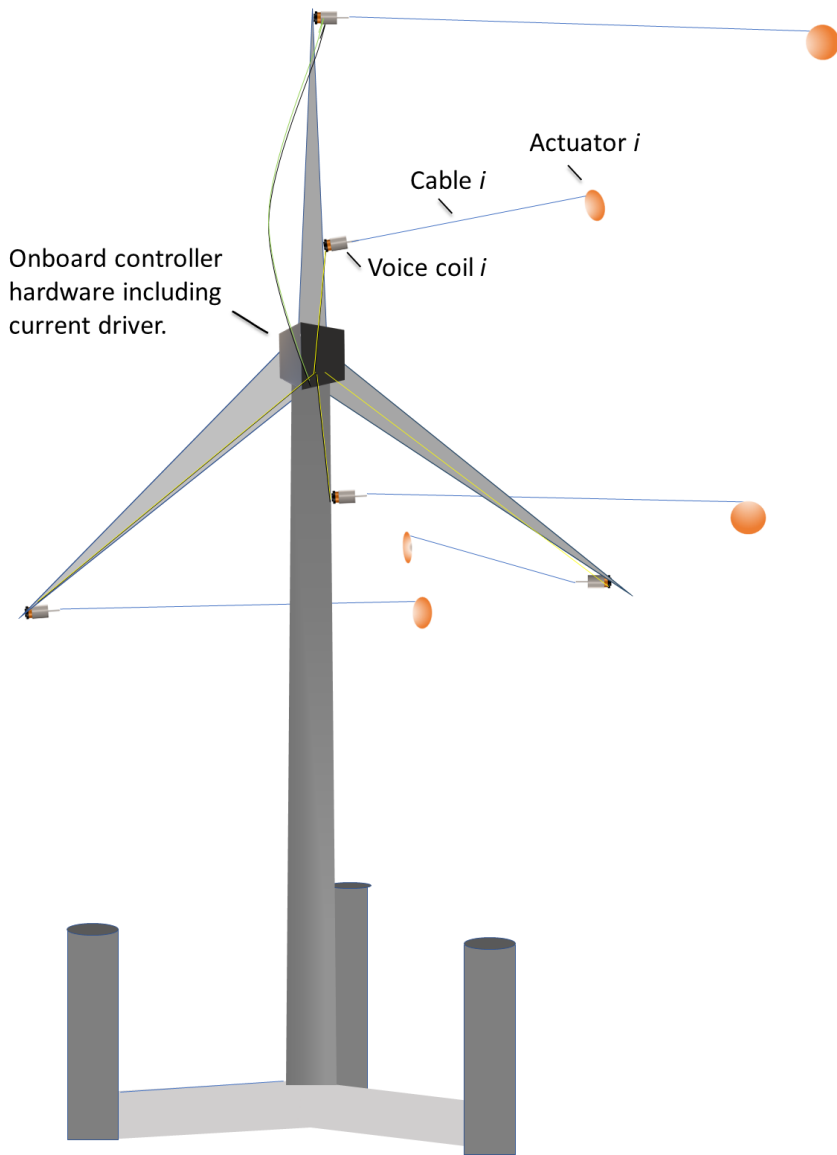


Figure 3.14: Conceptual design of a ReaTHM testing bed installed with proposed actuators. Set up for ReaTHM testing of an offshore wind turbine.

Chapter 4

Conclusions and Recommended Future Work

4.1 Conclusions

In this thesis, we have developed methods and tools for ReaTHM testing using CDPR. This has been done through experiments, theoretical analysis, and numerical simulations – with an emphasis on accurate and robust load actuation.

We have developed an advantageous framework for force allocation for CDPR setups that robustly generates differentiable cable forces in real-time. The results are beneficial for ReaTHM testing due to the method flexibility and since smoother cable force trajectories are expected to be more precisely tracked by the actuators. Moreover, the slack formulation may increase the applicability and robustness of basin specific standardised ReaTHM testing setups, by allowing errors in low-priority DOFs, when this does not cause loss of fidelity.

We have developed a framework for optimal placement of actuators that prioritises load actuation accuracy and ensures that the numerically calculated loads can always be applied according to predefined workspace specifications. No other such guidelines are found for ReaTHM testing.

We have developed and demonstrated an actuator control system design that accurately tracks forces on moving objects using actuated winches. This study emphasises ReaTHM testing by focusing on relevant use cases, force magnitudes, and frequency ranges. We have also proposed a new actuator solution for force control combining actuated winches and voice coil actuators, particularly suited for force-control with high-frequency end effector motions. Although considerable work remains, we see a promising potential for this new solution if further developed.

We have used experimental testing to identify and understand practical challenges, to enable and validate developments, and to maximize the practical relevance of the work. Experiments with the 1-DOF setup, enabled improvement of the actuator force controller. ReaTHM testing of the moored barge enabled us to identify and study sources of errors, and was used for an experimental demonstration of a complete ReaTHM setup of a ship-shaped vessel.

With that, we conclude that the thesis has achieved the intended research ob-

jectives and has enabled more accurate and robust load control for ReaTHM testing using CDPR. Since accurate load control is one of the major challenges for ReaTHM testing, we believe that the presented developments constitute a valuable step towards making ReaTHM testing a documented, accepted, and valued practice that accurately identifies and predicts the behaviour of ocean structures in realistic marine environments.

The thesis work is valuable also beyond ReaTHM testing. For example, both the contributions of [J-1] and [J-3] are generally relevant for CDPR applications that use cable force control.

Results from the thesis are currently being applied in commercial projects by SINTEF Ocean. This demonstrates how the presented methods have advanced the state of the art and had a real impact. For example, shortly after they had been adequately assessed, colleagues in the research team successfully applied the developments on force tracking presented in [J-3] for ReaTHM testing of a bottom fixed offshore wind turbine subjected to wave and wind loads; see Figure 4.1

4.2 Recommended Future Work

To further improve on the actuator force tracking procedures presented in [J-3], we recommend investigating the use of neural networks to determine the relationship between the actuator motor shaft, drum angle, and the resulting end effector force. The intent is to then use this model inversely as a feedforward control term to determine the appropriate motor shaft angle based on the preceding time-window of motor shaft angles, drum angles and target forces. To ensure robustness, we would consider implementing this as a saturated, rate limited correction term to the original controller presented in [J-3], to capture and compensate for additional systematic force variations. We believe this approach may be suitable since 1) the state of the actuator's transmission system and the response variable (e.g., the applied force) are measured with high accuracy. 2) large data sets for training can be obtained relatively quickly through automated experimental testing.

The actuator proposed in Chapter 3.4 is another interesting approach that has the potential to further improve force tracking capabilities – particularly when the motions of the physical substructure are high-frequent. We recommend an experimental implementation to evaluate its practical feasibility.

[J-2] served as a starting point for robust and well-performing actuator placement for ReaTHM testing. We recommend further developing the presented ideas, including their application to more complex cases and further refinement of the problem specification guidelines.

We believe that the thesis choice of using a simplified numerical substructure was appropriate given the thesis research objectives. However, future studies should incorporate realistic numerical models. Efforts should also be made to enable the actuation system to actuate vertical load components in a practical manner.

The preceding recommendations relate to load actuation in ReaTHM testing using CDPR. To ensure the eventual adaptation of ReaTHM testing as a new best practice for validating ocean structures, and to promote the overall development of the method, the authors also recommend the following:

- Improve numerical efficiency – to ensure that moderately complex numerical models can be run in real-time without compromising fidelity.
- Ensure that popular numerical solvers are ReaTHM testing compatible – to improve performance and robustness and ease industry acceptance of the method.
- Perform benchmark ReaTHM testing of ocean structures with known behaviour – for method validation and industry acceptance. The benchmark data can be obtained from full-scale testing or using cases where the target structure is well emulated either fully experimentally or fully numerically.
- Establish rigorous practices for testing, monitoring, verification, and deployment of new ReaTHM test setups – to ensure robust and cost-efficient use of the method. This includes automated integration testing of software, hardware, sensors, numerical models, actuators and the ReaTHM test loop as a whole.

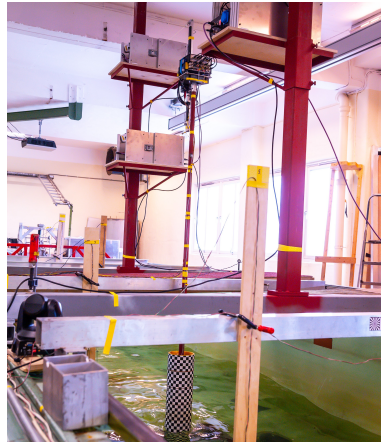


Figure 4.1: ReaTHM testing performed by research partners in SINTEF Ocean in June 2020 in the small wave tank at NTNU. Courtesy SINTEF Ocean.

References

- [1] iLaks. Salmar får åtte utviklingstillatelser for sin nye gigantmerd (in norwegian). <https://ilaks.no/salmar-far-atte-utviklingstillatelser-for-sin-nye-gigantmerd/>, Accessed at 15.05.2020.
- [2] Equinor and SSE Renewables. Doggerbank, 2020. <https://doggerbank.com/>, Accessed at 15.05.2020.
- [3] Equinor. Base selected for world's largest offshore wind farm, 2020. <https://www.equinor.com/en/news/2020-05-13-port-tyne-base.html> Accessed at 15.05.2020.
- [4] Oljedirektoratet. Faktasider: Johan Sverdrup, 2020. <https://factpages.npd.no/nb-no/field/pageview/all/26376286>, Accessed at 15.05.2020.
- [5] Statistisk sentralbyrå (Norwegian statistics bureau). Statistics Norway, Aquaculture, 2019. <https://www.ssb.no/en/jord-skog-jakt-og-fiskeri/statistikker/fiskeoppdrett>, Accessed at 15.05.2020.
- [6] Hans V Bjelland, Martin Føre, Pål Lader, David Kristiansen, Ingunn M Holmen, Arne Fredheim, Esten I Grøtli, Dariusz E Fathi, Frode Oppedal, Ingrid B Utne, et al. Exposed aquaculture in Norway. In *OCEANS 2015-MTS/IEEE Washington*. IEEE, 2015.
- [7] Statistisk sentralbyrå (Norwegian statistics bureau). Statistics norway, inntekter fra olje og gass (in norwegian), 2019. <https://www.ssb.no/energi-og-industri/faktaside/olje-og-energi>, Accessed at 15.05.2020.
- [8] Norwegian petroleum directorate. Petroleum related research and development, 2020. <https://www.norskpetroleum.no/en/environment-and-technology/petroleum-related-research-and-development/>, Accessed at 15.05.2020.
- [9] C Walsh et al. Offshore Wind in Europe – key trends and statistics 2019. *Wind Europe, Brussels*, 2019.
- [10] European commission. Onshore and offshore wind. https://ec.europa.eu/energy/topics/renewable-energy/onshore-and-offshore-wind_en, Accessed at 15.05.2020.

- [11] Subrata Chakrabarti. Physical model testing of floating offshore structures. In *Dynamic positioning conference*. Citeseer, 1998.
- [12] DNV GL. Recommended practice, environmental conditions and environmental loads. DNV-RP-C205, 2010. URL <https://rules.dnvgl.com/docs/pdf/dnv/codes/docs/2010-10/rp-c205.pdf>.
- [13] International Towing Tank Conference. Recommended procedures and guidelines – guide to the expression of uncertainty in experimental hydrodynamics (7.5-02-01-01). 2014.
- [14] John Nicholas Newman. *Marine hydrodynamics*. The MIT press, 2018.
- [15] Subrata Chakrabarti. *Handbook of Offshore Engineering (2-volume set)*. Elsevier, 2005.
- [16] Dominique Roddier, Tim Finnigan, and Stergios Liapis. Influence of the reynolds number on spar vortex induced motions (vim): multiple scale model test comparisons. In *International Conference on Offshore Mechanics and Arctic Engineering*, 2009.
- [17] International Towing Tank Conference. Recommended procedures and guidelines – model tests for offshore wind turbines (7.5-02-07-03.8). 2017.
- [18] Oleg Zikanov. *Essential computational fluid dynamics*. John Wiley & Sons, 2019.
- [19] Roger Temam. *Navier-Stokes equations: theory and numerical analysis*, volume 343. American Mathematical Soc., 2001.
- [20] Daniel Fonseca de Carvalho e Silva. Ride the wave. <https://www.ansys.com/about-ansys/advantage-magazine/volume-xi-issue-1-2017/ride-the-wave>, Accessed at 15.05.2020.
- [21] OpenFOAM Foundation Inc. About OpenFOAM, 2020. <https://www.openfoam.com/>, Accessed at 15.05.2020.
- [22] Jiyuan Tu, Guan Heng Yeoh, and Chaoqun Liu. *Computational fluid dynamics: a practical approach*. Butterworth-Heinemann, 2018.
- [23] Tahsin Tezdogan. *Potential flow and CFD-based hydrodynamic analyses of mono-and multi-hull vessels*. PhD thesis, University of Strathclyde, 2015.
- [24] Odd Faltinsen. *Sea loads on ships and offshore structures*. Cambridge university press, 1993.
- [25] WAMIT, Inc., Chestnut Hill, MA, USA. Wamit® user manual, version 7.3.
- [26] Ove T Gudmestad and Geir Moe. Hydrodynamic coefficients for calculation of hydrodynamic loads on offshore truss structures. *Marine Structures*, 1996.
- [27] Andreas Pott. *Cable-Driven Parallel Robots: Theory and Application*. Springer, 2018.

-
- [28] Clément Gosselin and Martin Grenier. On the determination of the force distribution in overconstrained cable-driven parallel mechanisms. *M*, 2011.
- [29] Sen Qian, Bin Zi, Wei-Wei Shang, and Qing-Song Xu. A review on cable-driven parallel robots. *Chinese Journal of Mechanical Engineering*, 31(1):66, 2018.
- [30] Werner Kraus. *Force control of cable-driven parallel robots*. PhD thesis, 2016.
- [31] Tobias Bruckmann, Christian Sturm, and Wildan Lalo. Wire robot suspension systems for wind tunnels. *Wind tunnels and experimental fluid dynamics research*, pages 29–50, 2010.
- [32] Robohub / Max Planck Institute for Biological Cybernetics. Cable-driven parallel robots: Motion simulation in a new dimension. Access ed on 2020.15.05.
- [33] Thomas Sauder. *Fidelity of Cyber-Physical Empirical Methods Application to the active truncation of slender marine structures*. PhD thesis, 2018.
- [34] International Towing Tank Conference. Recommended procedures and guidelines – free running model tests (7.5-02-06-01).
- [35] S.A Vilsen. *Method for real-time hybrid model testing of ocean structures : case study on slender marine systems*. PhD thesis, Norwegian University of Science and Technology, 2019.
- [36] Thomas Sauder, Valentin Chabaud, Maxime Thys, Erin E Bachynski, and Lars Ove Sæther. Real-time hybrid model testing of a braceless semi-submersible wind turbine: Part i—the hybrid approach. In *ASME 2016 35th International Conference on Ocean, Offshore and Arctic Engineering*. American Society of Mechanical Engineers Digital Collection, 2016.
- [37] Matthew Hall, Javier Moreno, and Krish Thiagarajan. Performance specifications for real-time hybrid testing of 1: 50-scale floating wind turbine models. In *ASME 2014 33rd International Conference on Ocean, Offshore and Arctic Engineering*. American Society of Mechanical Engineers Digital Collection, 2014.
- [38] International Towing Tank Conference. Recommended procedures and guidelines – active hybrid model tests of floating offshore structures with mooring lines (7.5-02-07-03.4). 2017.
- [39] Puishum B Shing and Stephen A Mahin. Experimental error effects in pseudodynamic testing. *Journal of Engineering Mechanics*, 1990.
- [40] Motohiko Hakuno, Masatoshi Shidawara, and Tsukasa Hara. Dynamic destructive test of a cantilever beam, controlled by an analog-computer. In *Proceedings of the Japan Society of Civil Engineers*. Japan Society of Civil Engineers, 1969.

- [41] Christopher Robin Thewalt and Stephen A Mahin. *Hybrid solution techniques for generalized pseudodynamic testing*. PhD thesis, University of California, Berkeley, 1987.
- [42] Hiroshi Nakai, Toshiyuki Kitada, and Katsuyoshi Nakanishi. Hybrid test for simulating seismic behavior of steel and composite bridge piers. *Memoirs faculty of engineering osaka city university*, 1996.
- [43] Juan E Carrion and Billie F Spencer Jr. Model-based strategies for real-time hybrid testing. Technical report, Newmark Structural Engineering Laboratory. University of Illinois at Urbana . . . , 2007.
- [44] Masayoshi Nakashima, Hiroto Kato, and Eiji Takaoka. Development of real-time pseudo dynamic testing. *Earthquake Engineering & Structural Dynamics*, 1992.
- [45] AP Darby, A Blakeborough, and MS Williams. Real-time substructure tests using hydraulic actuator. *Journal of Engineering Mechanics*, 1999.
- [46] A Blakeborough, MS Williams, AP Darby, and DM Williams. The development of real-time substructure testing. *Philosophical Transactions of the Royal Society of London A: Mathematical, Physical and Engineering Sciences*, 2001.
- [47] B Wu, H Bao, J Ou, and S Tian. Stability and accuracy analysis of the central difference method for real-time substructure testing. *Earthquake engineering & structural dynamics*, 2005.
- [48] YN Kyrychko, KB Blyuss, A Gonzalez-Buelga, SJ Hogan, and DJ Wagg. Real-time dynamic substructuring in a coupled oscillator-pendulum system. *Proceedings of the Royal Society A: Mathematical, Physical and Engineering Sciences*, 2006.
- [49] Andrew R Plummer. Model-in-the-loop testing. *Proceedings of the Institution of Mechanical Engineers, Part I: Journal of Systems and Control Engineering*, 2006.
- [50] Thomas Sauder, Stefano Marelli, and Asgeir J Sørensen. Probabilistic robust design of control systems for high-fidelity cyber-physical testing. *Automatica*, 2019.
- [51] Dennis de Klerk, Daniel J Rixen, and SN Voormeeren. General framework for dynamic substructuring: history, review and classification of techniques. *AIAA journal*, 2008.
- [52] D De Klerk and S Voormeeren. Uncertainty propagation in experimental dynamic substructuring. In *Proceedings of the Twenty Sixth International Modal Analysis Conference, Orlando, FL*. Society for Experimental Mechanics Bethel, CT, 2008.

-
- [53] DP McCrum and MS Williams. An overview of seismic hybrid testing of engineering structures. *Engineering Structures*, 2016.
- [54] Cheng Chen and James M Ricles. Tracking error-based servohydraulic actuator adaptive compensation for real-time hybrid simulation. *Journal of Structural Engineering*, 2010.
- [55] T Horiuchi, M Inoue, T Konno, and Y Namita. Real-time hybrid experimental system with actuator delay compensation and its application to a piping system with energy absorber. *Earthquake Engineering & Structural Dynamics*, 1999.
- [56] David P Stoten and Eduardo G Gómez. Adaptive control of shaking tables using the minimal control synthesis algorithm. *Philosophical Transactions of the Royal Society of London. Series A: Mathematical, Physical and Engineering Sciences*, 2001.
- [57] SA Neild, DP Stoten, D Drury, and DJ Wagg. Control issues relating to real-time substructuring experiments using a shaking table. *Earthquake engineering & structural dynamics*, 2005.
- [58] Akira Igarashi, Hirokazu Iemura, and Takanori Suwa. Development of substructured shaking table test method. In *Proceedings of the 12th World Conference on Earthquake Engineering*, 2000.
- [59] Andrei Reinhorn, M Sivaselvan, Scot Weinreber, and Xiaoyun Shao. Real-time dynamic hybrid testing of structural systems. 2004.
- [60] Valentin Chabaud. *Real-Time Hybrid Model Testing of Floating Wind Turbines*. PhD thesis, Norwegian University of Science and Technology, 2016.
- [61] Valentin Bruno Chabaud, Lene Eliassen, Maxime Thys, and Thomas Michel Sauder. Multiple-degree-of-freedom actuation of rotor loads in model testing of floating wind turbines using cable-driven parallel robots. 2018.
- [62] Sehoon Oh and Kyoungchul Kong. High-precision robust force control of a series elastic actuator. *IEEE/ASME Transactions on mechatronics*, 22(1): 71–80, 2016.
- [63] Rolf Isermann, Jochen Schaffnit, and Stefan Sinsel. Hardware-in-the-loop simulation for the design and testing of engine-control systems. *Control Engineering Practice*, 1999.
- [64] Hosam K Fathy, Zoran S Filipi, Jonathan Hagena, and Jeffrey L Stein. Review of hardware-in-the-loop simulation and its prospects in the automotive area. In *Modeling and simulation for military applications*. International Society for Optics and Photonics, 2006.
- [65] Roger Skjetne and Olav Egeland. Hardware-in-the-loop testing of marine control system. 2006.

- [66] I Bayati, A Facchinetti, ALESSANDRO FONTANELLA, H Giberti, and M Belloli. A wind tunnel/hil setup for integrated tests of floating offshore wind turbines. In *7th Science of Making Torque from Wind, TORQUE 2018*. Institute of Physics Publishing, 2018.
- [67] Cláudio Gomes, Casper Thule, David Broman, Peter Gorm Larsen, and Hans Vangheluwe. Co-simulation: State of the art. *arXiv preprint arXiv:1702.00686*, 2017.
- [68] Bernhard Schweizer, Pu Li, and Daixing Lu. Explicit and implicit cosimulation methods: stability and convergence analysis for different solver coupling approaches. *Journal of Computational and Nonlinear Dynamics*, 2015.
- [69] S Watts. Hybrid hydrodynamic modelling. *Offshore technology*, 1999.
- [70] B Buchner, JEW Wichers, JJ De Wilde, et al. Features of the state-of-the-art deepwater offshore basin. In *Offshore Technology Conference*, 1999.
- [71] Carl Trygve Stansberg, Harald Ormberg, and Ola Oritsland. Challenges in deep water experiments: hybrid approach. *J. Offshore Mech. Arct. Eng.*, 2002.
- [72] Stefan A Vilsen, Thomas Sauder, and Asgeir J Sørensen. Real-time hybrid model testing of moored floating structures using nonlinear finite element simulations. In *Dynamics of Coupled Structures, Volume 4*. Springer, 2017.
- [73] Yusong Cao and Galin Tahchiev. A study on an active hybrid decomposed mooring system for model testing in ocean basin for offshore platforms. In *ASME 2013 32nd International Conference on Ocean, Offshore and Arctic Engineering*. American Society of Mechanical Engineers Digital Collection, 2013.
- [74] Erin E Bachynski, Maxime Thys, Thomas Sauder, Valentin Chabaud, and Lars Ove Sæther. Real-time hybrid model testing of a braceless semi-submersible wind turbine: Part II—experimental results. In *ASME 2016 35th International Conference on Ocean, Offshore and Arctic Engineering*. American Society of Mechanical Engineers Digital Collection, 2016.
- [75] Raffaello Antonutti, Jean-Charles Poirier, Sébastien Gueydon, et al. Coupled testing of floating wind turbines in waves and wind using winches and software-in-the-loop. In *Offshore Technology Conference*, 2020.
- [76] CENER. Offshore wind energy - hybrid testing. <https://www.cener.com/en/offshore-wind-resource/>, Accessed at 28.10.2020.
- [77] Stefan Arenfeldt Vilsen, T Sauder, Asgeir Johan Sørensen, and Martin Føre. Method for real-time hybrid model testing of ocean structures: Case study on horizontal mooring systems. *Ocean Engineering*, 2019.
- [78] Maxime Thys, Valentin Chabaud, Thomas Sauder, Lene Eliassen, Lars O Sæther, and Øyvind B Magnussen. Real-time hybrid model testing of a semi-submersible 10mw floating wind turbine and advances in the test method. In

- International Conference on Offshore Mechanics and Arctic Engineering*, volume 51975, page V001T01A013. American Society of Mechanical Engineers, 2018.
- [79] Jose Azcona, Henrik Bredmose, Filippo Campagnolo, A Manjock, R Pereira, and F Sandner. D4. 22: Methods for performing scale-tests for method and model validation of floating wind turbines. 2014.
- [80] Thomas Sauder, Stefano Marelli, Kjell Larsen, and Asgeir J Sørensen. Active truncation of slender marine structures: Influence of the control system on fidelity. *Applied Ocean Research*, 2018.
- [81] Ingvil Snøfugl. Testing tomorrow’s offshore wind technology. <https://lifes50plus.eu/tag/real-time-hybrid-model-test/>, Accessed at 15.05.2020.
- [82] Gemini.no. Denne testmetoden gir oss mer vindkraft til havs, 2020. <https://gemini.no/2020/10/denne-testmetoden-gir-oss-mer-vindkraft-til-havs/> Accessed at 15.12.2020.
- [83] Thomas Sauder, Asgeir J Sørensen, and Kjell Larsen. Real-time hybrid model testing of a top tensioned riser: A numerical case study on interface time-delays and truncation ratio. In *ASME 2017 36th International Conference on Ocean, Offshore and Arctic Engineering*. American Society of Mechanical Engineers.
- [84] NTNU, SINTEF. Ocean Space Centre, 2020. <https://oceanspacecentre.no/>, Accessed at 15.05.2020.
- [85] Jacob Fraden. *Handbook of modern sensors: physics, designs, and applications*. Springer Science & Business Media, 2010.
- [86] BECHOFF. Basic principles of strain gauge technology. <https://infosys.beckhoff.com/english.php?content=../content/1033/e13356/1499036171.html&id=>, Accessed at 15.05.2020.
- [87] Einar S Ueland and Roger Skjetne. Effect of time delays and sampling in force actuated real-time hybrid testing; a case study. In *OCEANS–Anchorage, 2017*. IEEE, 2017.
- [88] Einar S Ueland, Roger Skjetne, and Stefan A Vilsen. Force actuated real-time hybrid model testing of a moored vessel: A case study investigating force errors. *IFAC-CAMS*, 2018.
- [89] Einar Ueland, Thomas Sauder, and Roger Skjetne. Optimal force allocation for overconstrained cable-driven parallel robots: Continuously differentiable solutions with assessment of computational efficiency. *IEEE Transactions on Robotics*, 2020.
- [90] Einar Ueland, Thomas Sauder, and Roger Skjetne. Optimal actuator placement for real-time hybrid model testing using cable-driven parallel robots. *Journal of Marine Science and Engineering*, 9(2), 2021. ISSN 2077-1312. doi: 10.3390/jmse9020191. URL <https://www.mdpi.com/2077-1312/9/2/191>.

- [91] Einar Ueland, Thomas Sauder, and Roger Skjetne. Force tracking using actuated winches with position controlled motors for use in hydrodynamic model testing. *Submitted for publication (under review)*, 2021.
- [92] SINTEF Ocean. Reflex user manual 4.8.0. Technical report, 2016.
- [93] Patrick J Moriarty and A Craig Hansen. Aerodyn theory manual. Technical report, National Renewable Energy Lab., Golden, CO (US), 2005.
- [94] Qualisys. Qualisys track manager. URL <https://www.qualisys.com/software/qualisys-track-manager/>. Accessed on 15.05.2020.
- [95] Thor I Fossen. *Handbook of marine craft hydrodynamics and motion control*. John Wiley & Sons, 2011.
- [96] Randal W Beard and Timothy W McLain. *Small unmanned aircraft: Theory and practice*. Princeton university press, 2012.
- [97] Christopher Reichert, Katharina Müller, and Tobias Bruckmann. Robust internal force-based impedance control for cable-driven parallel robots. In *Cable-Driven Parallel Robots*. Springer, 2015.
- [98] Robert Van Rooyen, Andrew Schloss, and George Tzanetakis. Voice coil actuators for percussion robotics. In *NIME*, 2017.
- [99] Akribis. Voice coil motors-17.1.1. [http://www.akribis-sys.co.kr/download/0104/Voice%20Coil%20Motors%20\(EN\)-17.1.1.pdf](http://www.akribis-sys.co.kr/download/0104/Voice%20Coil%20Motors%20(EN)-17.1.1.pdf), Accessed at 15.05.2020.

Part II

Collection of Articles

Article 1 – C-1

Effect of Time Delays and Sampling in Force Actuated Real-Time Hybrid Testing; A Case Study

Einar S. Ueland, Roger Skjetne

In Proceedings of OCEANS 2017 MTS/IEEE Anchorage

<https://ieeexplore.ieee.org/abstract/document/8232196>

This article is not included due to copyright

Article 2 – C-2

Force Actuated Real-time Hybrid Model Testing of a Moored Vessel; A Case Study Investigating Force Errors

Einar S. Ueland, Roger Skjetne, Stefan A. Vilsen
In the 11th IFAC Conference on Control Applications in Marine Systems,
Robotics, and Vehicles
[10.1016/j.ifacol.2018.09.472](https://doi.org/10.1016/j.ifacol.2018.09.472)

Force Actuated Real-Time Hybrid Model Testing of a Moored Vessel: A Case Study Investigating Force Errors ^{*}

Einar S. Ueland^{*} Roger Skjetne^{**} Stefan A. Vilsen ^{***}

^{*/**/**} Centre for Autonomous Marine Operations and Systems;
Norwegian University of Science and Technology (NTNU AMOS);
Department of Marine Technology; NO-7491 Trondheim, Norway

^{*}Corresponding author: einars.ueland@ntnu.no

^{***}SINTEF Ocean, NO-7465 Trondheim, Norway

Abstract: This paper presents a study where real-time hybrid testing is used to emulate a moored barge. The barge is modelled physically while the mooring forces are simulated numerically and actuated onto the physical substructure. Assuming no errors in modelling of the numerical substructure, we investigate what separates the instantaneous forces acting on the physical substructure, from the forces that would be acting on it in the ideal, non-substructured case that we are trying to replicate. Four different types of errors are identified, discussed, and partly quantified.

© 2018, IFAC (International Federation of Automatic Control) Hosting by Elsevier Ltd. All rights reserved.

Keywords: Force control, Hybrid Testing, Error analysis, Sub-structuring, Mooring systems.

1. INTRODUCTION

Real-time hybrid model testing (or *ReaTHM*[®] testing¹) is an experimental method for performing hydrodynamic model-scale testing, where systems/structures are partitioned into physical and numerical substructures. The physical substructure is then modelled physically in a laboratory facility, while the numerical substructure is modelled numerically using simulation software. The two are then coupled in real-time using a measurement and control-system interface. In general, we want to perform model-scale testing to identify the characteristics and responses of structures. This is motivated by the fact that complex hydrodynamic phenomena are difficult to model numerically or analytically. Real-time hybrid model testing is an extension to conventional model-scale testing, in that it enables the inclusion of numerically simulated components, into the classical experimental regime. As such the method can address some of the challenges and limitations of traditional model testing, which due to the complexity of structures, limitations of facilities, demand for rapid prototyping, or conflicts from differences in scaling effects, is not always feasible or practical to perform on the whole structure.

One application of *ReaTHM*, hereafter simply referred to as hybrid testing, is to use it in the testing of moored systems, where (in particular for deep-water structures) the spacial limitation of the basin-infrastructure is identified as a major challenge (Stansberg et al., 2002). In Cao and Tahchiev (2013) and Sauder et al. (2018) the use of

hybrid testing for active mooring line truncation has been studied through numerical simulations. In these cases, the flexibility of the mooring lines means that imposing target displacements on the physical substructure is an alternative. This is what is typically done in seismic engineering, where hybrid testing has been studied extensively (Carrion, 2007).

In the approach seen in this paper, as also studied by Vilsen et al. (2017), the entirety of the mooring lines are modelled numerically, meaning that sub-structuring is performed at the fairled point connecting the mooring system to the floating structure. Since the interface of the numerically calculated effort, in this case, is directly on the rigid body under study, we need to (in order to maintain flexibility) actuate target-forces, rather than displacements, on the floating test structure.

In this paper, a ship-shaped vessel is tested using the hybrid testing strategy. To the author's knowledge, this is the first time hybrid testing has been applied to ship-shaped vessels. In the present work, the focus is on developing the hybrid testing concept, rather than quantifying the responses of the moored structure. If the goal, instead, were to reproduce the real-world mooring system accurately, one would typically use a model of a full-scale vessel, in combination with a high fidelity numerical simulation tool for the mooring system. See for example Vilsen et al. (2017).

The main focus is on the investigation of issues relating to force control. In a broader sense, the objective of the presented work is to further develop the experimental framework of hybrid testing (building of the work of Vilsen et al. (2018)). The long-term goal is for hybrid testing to become a qualified method, which is accepted and valued by industrial stakeholders.

^{*} This work was supported by the Research Council of Norway through the Centre of Excellence AMOS, project no. 223254, and through grant No. 254845/O80 "Real-Time Hybrid Model Testing for Extreme Marine Environments".

¹ *ReaTHM*[®] testing is a registered trademark of SINTEF Ocean.

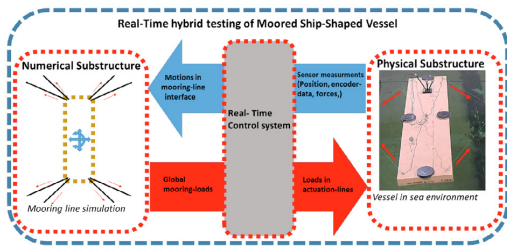


Fig. 1. The real-time hybrid test loop for hybrid testing of a ship-shaped vessel, where mooring lines are numerically simulated. Right image is from the actual test setup.

1.1 Real-Time Hybrid Test-Loop

The numerical and physical substructures are coupled through the real-time hybrid test loop as illustrated in Figure 1. The goal is to replicate the responses of the ideal non-structured system in terms of relevant performance measures (often referred to as key performance indicators), when exposed to relevant loads. Based on measured responses of the physical structure, the numerical substructure calculates and outputs target forces to be applied to the physical substructure.

1.2 Problem Statement

Assuming no modeling errors of the numerical substructure, we are asking the following question: what distinguish the loads acting on the physical substructure in a hybrid test setup from the ideal loads that would be acting on it in the real non-structured system that we try to replicate?

We aim to identify (and partly quantify) discrepancies related to force control in a real-time hybrid test setup. Using experiences from the test-case, we identify four error sources that are studied and discussed:

- (1) Force allocation errors.
- (2) Force estimation errors.
- (3) Target-force tracking errors
- (4) Delay-induced force errors.

2. EXPERIMENTAL SETUP AND METHODS

2.1 Experimental Setup

A ship-shaped structure in the form of a barge was set up in an experiment to test various objectives related to hybrid model testing; see Figure 1. The tests were performed in a basin laboratory at NTNU (MC-Lab). This is equipped with a camera tracking system that measures the local position and attitude of the vessel.

Physical Substructure For geometric simplicity and being easy to handle, the barge seen in Figure 2 was chosen as the physical substructure. Relevant dimensions are listed in Table 1. Ballasted with weights, the mass of the barge was about 15.35 kg

Numerical Substructure A linear mooring model with target-forces proportional to the excursion in position

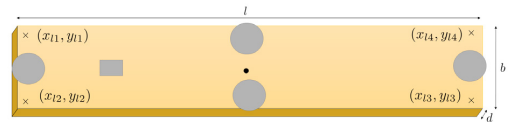


Fig. 2. Barge dimensions. Corresponding data in Table 1.

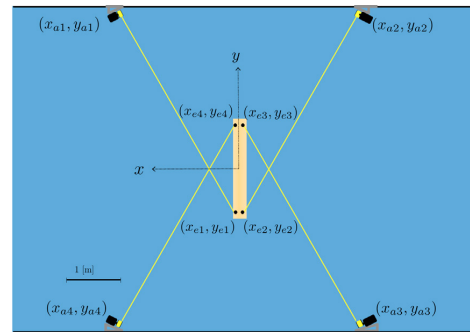


Fig. 3. Barge and actuator configuration when barge is centred in origo.

Table 1. Test-dimensions and placements

	Distance/Position [m]
l, b, d	(2.0, 0.45, 0.085)
$\mathbf{x}_{a1}, \mathbf{x}_{a2}, \mathbf{x}_{a3}, \mathbf{x}_{a4}$	$(x, y) : (\pm 3.25, \pm 2.6)$
$\mathbf{x}_{l1}, \mathbf{x}_{l2}, \mathbf{x}_{l3}, \mathbf{x}_{l4}$	$(x, y) : (\pm 0.175, \pm 0.95)$

and heading (i.e., x, y, ψ) was chosen as the numerical substructure. This means that the numerical substructure is a linear approximation to a horizontal mooring model:

$$F_t = -[k_x x \ k_y y \ k_\psi \psi]^T + \omega, \quad (1)$$

where F_t is the target interface force-vector, k_x, k_y and k_ψ are linear stiffness coefficients, and $\omega = [\omega_x \ \omega_y \ \omega_\psi]^T$ represents additional artificial environmental loads we may subject the structure to.

Actuators, Placement, and Control Forces are actuated using four separate actuators connected to the floating structure through thin braided lines. The actuators are similar to those described by Ueland and Skjetne (2017), consisting of a DC-motor connected, via a clock spring and a line, to the end-effector on the physical structure. The basin walls where the actuators could be placed, is of limited dimensions. Therefore, in order to have a flexible system, capable of applying relevant loads, the symmetric cross configuration illustrated in Figure 3 was chosen. The positions of the actuators and end-effectors are listed in Table 1.

The control system is similar to that of Vilsen et al. (2018). Important modifications include additional moment control and the use of encoders on the actuator-line-pulleys.

2.2 Configuration

Force allocation In this section two coordinates frames are used: $\{n\}$ is the local Earth-fixed basin frame defined in x, y and z direction, assumed inertial, while $\{b\}$ is the moving coordinate system fixed to the vessel body. Transformation from $\{n\}$ to $\{b\}$ is performed using the

rotation matrix $\mathbf{R}(\Theta)$, parameterized by the attitude vector $\Theta = [\phi, \theta, \psi]^T$. See Fossen (2011). Unless otherwise specified, vectors in this paper are in $\{n\}$.

The position of end-effector i , denoted (x_{ei}, y_{ei}, z_{ei}) , is given by

$$\begin{bmatrix} x_{ei} \\ y_{ei} \\ z_{ei} \end{bmatrix} = \mathbf{R}(\Theta) \underbrace{\begin{bmatrix} x_{li}^b \\ y_{li}^b \\ z_{li}^b \end{bmatrix}}_{\mathbf{x}_{li}} + \underbrace{\begin{bmatrix} x \\ y \\ z \end{bmatrix}}_{\boldsymbol{\eta}} \quad (2)$$

where (x, y, z) is the position of the barge body frame in $\{n\}$ and $(x_{li}^b, y_{li}^b, z_{li}^b)$ is the local lever arm to end effector i in $\{b\}$.

The position of the point where the actuator-line connects to the actuator-pulley i is (x_{ai}, y_{ai}, z_{ai}) . The relative distance between end-effector and actuator is then

$$\Delta x_i = x_{ai} - x_{ei}, \Delta y_i = y_{ai} - y_{ei}, \Delta z_i = z_{ai} - z_{ei} \quad (3)$$

The forces in x, y and z direction of line i now becomes:

$$[F_{x,i} \ F_{y,i} \ F_{z,i}]^T = \begin{pmatrix} F_i \\ R_i \end{pmatrix} [\Delta x_i \ \Delta y_i \ \Delta z_i]^T, \quad (4)$$

where $R_i = \sqrt{\Delta x_i^2 + \Delta y_i^2 + \Delta z_i^2}$ is the line length of actuator i .

We aim at controlling the force in the three degrees of freedom of surge, sway, and yaw (i.e., position and heading). The force components induced in the other degrees of freedom are assumed negligible. The global load vector $\mathbf{F} = [F_x, F_y, M_{\psi}]^T$ for n actuation lines is a function of the individual line forces according to

$$\mathbf{F} = \underbrace{\begin{bmatrix} \frac{\Delta x_1}{R_1} & \frac{\Delta x_2}{R_2} & \dots & \frac{\Delta x_n}{R_n} \\ \frac{\Delta y_1}{R_1} & \frac{\Delta y_2}{R_2} & \dots & \frac{\Delta y_n}{R_n} \\ \frac{\Delta y_1 r_{x1} - \Delta x_1 r_{y1}}{R_1} & \frac{\Delta y_2 r_{x2} - \Delta x_2 r_{y2}}{R_2} & \dots & \frac{\Delta y_n r_{xn} - \Delta x_n r_{yn}}{R_n} \end{bmatrix}}_{\mathbf{T}} \begin{bmatrix} F_1 \\ F_2 \\ \vdots \\ F_n \end{bmatrix}, \quad (5)$$

where $r_{xi} = x_{ei} - x$ and $r_{yi} = y_{ei} - y$ are the lever arms in $\{n\}$.

Equation (5) can be used to find the desired line tensions \mathbf{F}_l , given a global target force \mathbf{F}_t . It is generally subject to constraints, such as a minimum and maximum tension. The studied system was sufficiently actuated by using the pseudoinverse (about the desired pretension line forces) to find a least squares values for \mathbf{F}_l , without violating these constraints.

Hydrodynamic Parameter Estimation The hybrid test setup was also used to identify the hydrodynamic properties of the vessel. A simplified vessels model in free decay is:

$$(M_A + M_{rb})\ddot{x} + D_q \dot{x} |\dot{x}| + D_l \dot{x} = F \quad (6)$$

wherein the performed decay tests, F is given by (1), under the assumption of perfect actuation and $\boldsymbol{\omega} = 0$.

Faltinsen (1993, p. 252), suggests a method for estimating the nonlinear decay. However, identifying the nonlinear decay term was not found feasible for the given case.

Assuming only linear damping (setting $D_q = 0$), the motions of a decay test can be described as a damped sine

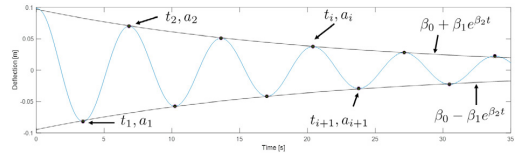


Fig. 4. Identification of decay-rate from decay tests.

wave. The amplitudes, which are the data-points we wish to fit the experimental data to, can be expressed as:

$$\beta_0 + \text{Sign}(a_i) \beta_1 e^{-\beta_2 t}, \quad (7)$$

where β_0 is the offset from the circular reference position caused by biases in the experimental setup, β_1 is the initial offset, β_2 is the decay rate of the system, and a_i is the amplitude, alternating between positive and negative.

Hydrodynamic parameters can then be extracted by:

$$\begin{aligned} T &= \frac{2(t_n - t_0)}{n} & w_d &= \frac{2\pi}{T} \\ M &= \frac{K}{w_d^2 + \beta_2^2} & D &= -2M\beta_2 \end{aligned} \quad (8)$$

where $M = M_a + M_{rb}$ includes added mass and β_2 is found using an NLP-solver to minimise least square error of (7) onto the amplitudes from each test points; see Figure 4.

3. ANALYSIS

The experiments presented in this paper are all from decay-tests in still water, where the floating barge is released from an initial offset, and allowed to decay to its equilibrium point.

3.1 Target-Force Tracking Errors

We are not able to perfectly track the desired target-forces that are output from the numerical substructure. This causes an error which in Figure 5a can be recognized as the difference between the target and measured force.

Figure 5b illustrates how such errors affect the system in a decay test in sway-direction, and how the effect accumulates. The power-error seen in the figure was estimated by multiplying the end-effector velocity by the force-error of each actuator line, and the estimated energy-error is the power integrated with respect to time. In addition to lower frequency oscillations, three force error components are evident: 1) a high-frequency measurement noise component present at about 50 Hz, 2) large error amplitudes when the velocity changes direction, and 3) the applied force is, on average, ahead of the desired force (possibly due to overcompensation of delay).

Of the three mentioned issues, the first has little effect on the dynamics, since the noise frequency is much higher than the system eigenfrequency. The dynamic effect of the second is hypothesized to be reduced by the low power errors associated with the low velocity. The last issue is the most problematic, as it is continuously damping energy from the system.

The mean-average force tracking errors for decay tests with varying mooring stiffness are presented in Figure 6. The overall force tracking errors in these tests can be characterized as low. The figures also show good repeatability in that there are low variations within each test type.

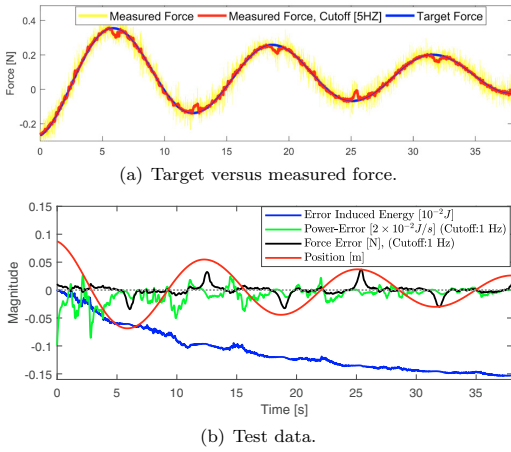


Fig. 5. Trajectory and errors for decay-test in x-direction. ($k_x=4N/m$)

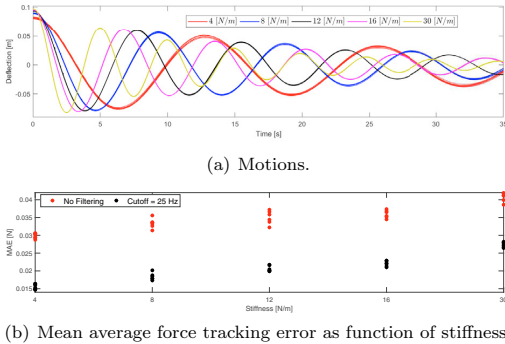


Fig. 6. Trajectories (a) and mean-average force tracking errors (b) for decay tests in x-direction with varying numerical mooring stiffness.

Generally, experimental factors such as actuator dynamics, together with imperfections in the communication flow between the actuator and the real-time control-system will affect the applied forces and cause systematic errors that can accumulate over time if not properly handled. The tracking force errors occurring around velocity direction change, which was due to slack between transmission gears between the actuators and the encoders, serves as an example of this (this was later fixed).

Steps that can be taken to improve force tracking include improvements in communication flow (to reduce delays and jitter), improvements of the actuators (to reduce the effect of actuator dynamics), compensation of delays and dynamics, and better control design (to increase the responsiveness to more accurately track the target forces).

3.2 Force Allocation Errors

The accuracy of force allocation as given by (5), depends on how accurately we estimate the relative distances of (3). Here we separate between three types of errors. In the

following, for a quantity κ , the estimation error is denoted $\delta(\kappa)=\hat{\kappa}-\kappa$, (i.e., the estimated value minus the true value):

- (1) Error in position estimate of the vessel ($\boldsymbol{\eta}$ and $\boldsymbol{\Theta}$): $(\delta_x, \delta_y, \delta_z, \delta_\phi, \delta_\theta, \delta_\psi)$. This is a result of errors in the position tracking system, as well as errors induced when calibrating the vessel in the basin frame with respect to the markers on the vessel. These are reduced by a high quality tracking system, and precise alignment of the vessel in the basin frame.
- (2) Error in actuator positioning (\boldsymbol{x}_{ia}): $(\delta_{xai}, \delta_{yai}, \delta_{zai})$. As these are defined in the basin frame, it is important to know accurately how the basin coordinate frame is aligned relative to the basin walls.
- (3) Error in lever arm estimation (\boldsymbol{x}_{li}): $(\delta_{xli}, \delta_{yli}, \delta_{zli})$. These errors are relative to the body frame, and expected to be relatively simple to keep low.

The linearized error on the global force, given tension F_i in actuator i , and small errors δ_{κ} is obtained by multiplying the resulting perturbations $(\delta_{\Delta x_i}, \delta_{\Delta y_i}, \delta_{\Delta z_i})$ with the derivative of (4) with respect to $\Delta x, \Delta y$, and Δz :

$$\begin{bmatrix} \delta F_x \\ \delta F_y \\ \delta F_z \end{bmatrix} \Big|_{\delta=0} = \frac{1}{R_i^3} \begin{bmatrix} (\Delta y_i^2 + \Delta z_i^2) & -(\Delta x_i \Delta y_i) & -(\Delta x_i \Delta z_i) \\ -(\Delta x_i \Delta y_i) & (\Delta x_i^2 + \Delta z_i^2) & -(\Delta y_i \Delta z_i) \\ -(\Delta x_i \Delta z_i) & -(\Delta y_i \Delta z_i) & (\Delta y_i^2 + \Delta z_i^2) \end{bmatrix} \begin{bmatrix} \delta_{\Delta x_i} \\ \delta_{\Delta y_i} \\ \delta_{\Delta z_i} \end{bmatrix} [F_i], \quad (9)$$

where,

$$\begin{bmatrix} \delta_{\Delta x} \\ \delta_{\Delta y} \\ \delta_{\Delta z} \end{bmatrix} = \begin{bmatrix} \delta_x - \delta_{xai} \\ \delta_y - \delta_{yai} \\ \delta_z - \delta_{zai} \end{bmatrix} + [R(\boldsymbol{\Theta})] \begin{bmatrix} \delta_{xli} \\ \delta_{yli} \\ \delta_{zli} \end{bmatrix} + \begin{bmatrix} 0 & r_{zi} & -r_{yi} \\ -r_{zi} & 0 & r_{xi} \\ r_{yi} & -r_{xi} & 0 \end{bmatrix} \begin{bmatrix} \delta_\phi \\ \delta_\theta \\ \delta_\psi \end{bmatrix} \quad (10)$$

Using (10) it can further be shown that the linearized absolute force allocation error is bounded by:

$$\|\delta \mathbf{F}_i\| \leq \frac{1}{R_i} \|\delta \Delta \mathbf{x}\| F_{li}, \quad (11)$$

where $\|\delta \Delta \mathbf{x}\|$ is the euclidean norm of $[\Delta x, \Delta y, \Delta z]^T$.

From (9)-(11) it is clear that allocation errors due to inaccurate estimation of distances reduce rapidly with increased length of the actuator lines. Thus, not surprising, actuators placed far from the structure is much more robust in terms of avoiding allocation errors.

For the reviewed setup, a rough estimate suggests that the estimation errors of $\boldsymbol{\eta}$, \boldsymbol{x}_{li} , and \boldsymbol{x}_{ia} are lower than 2cm, 0.5cm and 5cm, respectively, in any direction, while δ_ψ is estimated to be lower than two degrees. Using (9) on the resulting trajectories from the experimental data, it was estimated (always using the sign that increase errors), that in worst case, maximal decomposition error, of a line force F_i was lower than $0.032F_i$ [N] and $0.017F_i$ [N] in x- and y-direction, respectively.

Other sources of errors relating to force-allocation include basin coordinate system inaccuracies, deflection of actuator lines, and delayed measurements. For the presented tests, a guide was needed to ensure that the line stayed on the actuator pulley, resulting in some deflection of the line, causing minor additional decomposition errors.

In the presented case, the test-setup was installed in the laboratory for this particular testing campaign. It is expected that larger basin facilities, combined with standardized and careful positioning of actuators can reduce decomposition errors to an insignificant level.

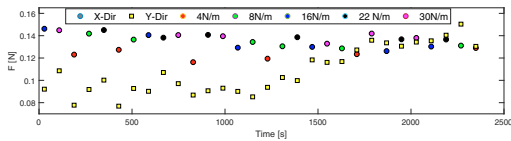


Fig. 7. Estimated bias. Samples were taken at start of each decay test in Figure 6(a). The tests were run consecutively without recalibrating

3.3 Force-Estimation Errors

As the estimated forces are used in feedback when applying target-forces on the physical substructure, any inaccuracies in the estimates will affect the applied forces.

The forces are measured by strain-gauge cells connecting the actuator lines to the physical substructure. Two types of errors are associated with these measurements: systematic errors and random errors.

Random Errors These are noise on the measurements signal, which can be identified in the steady state when vibrations have died out. Noting that the high-frequency oscillations observed in Figure 5(a) are mostly due to vibrations of the actuator interface, the observed random errors are small.

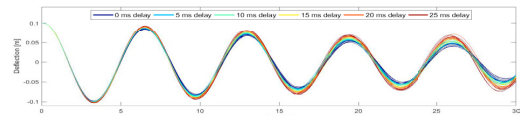
Systematic Errors These are bias-like errors between the measured and real force, typically caused by inaccurate (or no longer valid) calibrations and sensor drift (dominated by temperature-dependent drift). As opposed to the high-frequency random errors (which are filtered out), the effect of biases on the dynamics of the test-structure typically accumulates over time.

In the performed testing, the following measures were taken to reduce the systematic force measurement errors:

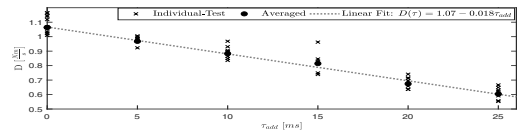
- (1) Force sensors were routinely re-calibrated to zero.
- (2) In the initialisation phase, a high linear stiffness was applied using the numerical substructure, forcing the vessel to the origin. When the system was stabilized at the pre-tensioned equilibrium point, the force sensors were resynchronized, ensuring minimal relative biases between the force-sensors.

The estimated applied force acting on the vessel before releasing the barge at the start of the tests of Figure 6(a) was recorded and is presented in Figure 7. As the vessel at this point is at rest, we know that the sum of forces should be zero. Thus, these forces provide an estimate of the systematic errors in the given configuration as they evolve over time. In retrospect, given the small dimensions of setup, the described procedure of re-synchronization could have been performed more often to reduce the systematic errors.

Both biases and random noise is to some degree independent of the magnitude of the applied forces. Thus, testing using larger scales and forces is expected to result in a relatively lower effect of biases and noise.



(a) Trajectories for varying added delay.



(b) Damping fitted to linear polynomial.

Fig. 8. Effect of added delay on decay test in surge direction. ($k_y=16\text{N/m}$)

3.4 Delay-Induced Force Errors

Due to communication delays, sampling, and processing time, there is a delay between the actual states of the system (which are measured inputs to the numerical substructure), and. This means that the forces we are tracking, in reality, are delayed relative to the ideal forces.

Theoretically, the instantaneous effect of a delay of a linear stiffness term, given sufficiently small delays, is the introduction of a negative linear damping coefficient proportional to the stiffness (Ueland and Skjetne, 2017):

$$D_{\text{induced}} = -K\tau, \quad (12)$$

where K is a linear stiffness coefficient, and τ is the delay between the actuated and ideal force.

The force delays were not known accurately for the test-case (but roughly estimated to be about 15 ms). In order to assess their effect, decay tests were performed where an extra delay was added to the target forces.

Figure 8(a) shows the resulting trajectories for introduced added delay ranging from 0 to 5 samples (0 to 25 ms) in decay in y-direction, with stiffness of $k_y=16\frac{\text{N}}{\text{m}}$. Although some internal variations between test sets are present, it is clear that the added delay introduces negative damping to the system.

The amplitudes are now fitted to (7) and (8), and subsequently fitted to a linear polynomial as a function of added delay. See Figure 8(b). It was hypothesised that we might observe a similar trend as (12); however, due to the presence of nonlinearities, test-variance, and imperfect actuation we should not expect an exact match to the instantaneous effect. The experimentally estimated, induced negative delay coefficient is found to be $18.8\frac{\text{N}}{\text{s}}$. As such the experimental data are according to the expected trend.

As delays may have a profound effect on the system, it is advised to take measures to counteract it. For small delays, extrapolating data using least-square regression is found to be an effective countermeasure. See for example Wallace et al. (2005). The challenge is that it is difficult to estimate the delays accurately. Time-stamping measurement data, in a synchronised setup, is one means of obtaining delay estimates.

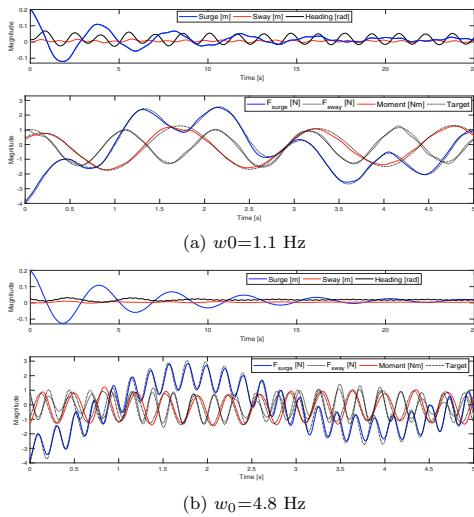


Fig. 9. Decay tests in x-direction. Excitation force defined by (13) using $[k_x, k_y, k_\psi] = [16 \frac{N}{m}, 30 \frac{N}{M}, 12 \frac{Nm}{rad}]$

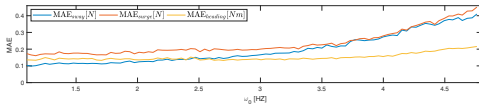


Fig. 10. Mean average force tracking error as function of excitation frequency.

4. TEST SETUP DISCUSSION

We have now illustrated issues that may affect the force actuation accuracy in a hybrid test setup. In this section, the test-setup, and its performance is further explored.

To demonstrate the flexibility of the setup, decay tests of the moored barge was combined with the introduction of numerically calculated harmonic forces. In these test, the additional external forces, to be actuated by the control system were given by:

$$\mathbf{w} = [\sin(2\pi\omega_0 t + \phi_1) \quad \sin(1.8\pi\omega_0 t + \phi_2) \quad \sin(1.2\pi\omega_0 t + \phi_3)]^T, \quad (13)$$

where the phase angles ϕ_i may vary from test to test.

In Figure 4 the resulting response and the systems ability to apply forces are shown for two cases of ω_0 . Figure 10 illustrates how the mean average error of the target tracking errors increases with the frequency of the harmonic force. Although the error increases with frequency, the tests indicate that the system was able to apply forces and moments quite well.

5. CONCLUDING REMARKS AND FURTHER WORK

In this paper we have, using a hybrid test setup, identified and discussed four sources of errors that affect the applied force from the ideal, non-sub-structured setup. Reducing these errors is of importance in ensuring realistic emulation of the original test case. Overall, testing shows promising potential of the method in the application to ship-shaped vessels.



Fig. 11. Test setup used on model-scale vessel.

In addition to response identification, hybrid testing of a moored vessel opens up for a wide arrange of flexible test opportunities. This may for example be relevant if the goal is to verify a DP-system, or snap loads in the mooring lines. The possibility of rapid changes and prototyping of the numerical substructure further means that tests can be performed in an efficient manner.

Future plans include a more in-depth review of the issues presented in this paper and the use a similar test-setup for identification of responses on a realistic model scenario. This may involve scaling considerations, more sophisticated numerical models, and a series of realistic waves spectrums. Figure 11 provides an image from initial testing.

REFERENCES

- Cao, Y. and Tahchiev, G. (2013). A study on an active hybrid decomposed mooring system for model testing in ocean basin for offshore platforms. In *ASME 2013 32nd International Conference on Ocean, Offshore and Arctic Engineering*.
- Carrion, J.E. (2007). *Model-based strategies for real-time hybrid testing*. University of Illinois at Urbana-Champaign.
- Faltinsen, O. (1993). *Sea loads on ships and offshore structures*, volume 1. Cambridge university press.
- Fossen, T.I. (2011). *Handbook of marine craft hydrodynamics and motion control*. John Wiley & Sons.
- Sauder, T., Marelli, S., Larsen, K., and Sørensen, A.J. (2018). Active truncation of slender marine structures: Influence of the control system on fidelity. *Applied Ocean Research*, 74, 154–169.
- Stansberg, C.T., Ormberg, H., and Oritsland, O. (2002). Challenges in deep water experiments: hybrid approach. *Journal of Offshore Mechanics and Arctic Engineering*, 124(2), 90–96.
- Ueland, E.S. and Skjetne, R. (2017). Effect of time delays and sampling in force actuated real-time hybrid testing; a case study. In *OCEANS-Anchorage, 2017*, 1–10. IEEE.
- Vilsen, S., Sauder, T., Sørensen, A.J., and Føre, M. (2018). Method for real-time hybrid model testing of ocean structures: Case study on horizontal mooring systems. *Submitted for Publication, January 2018*.
- Vilsen, S.A., Sauder, T., and Sørensen, A.J. (2017). Real-time hybrid model testing of moored floating structures using nonlinear finite element simulations. In *Dynamics of Coupled Structures, Volume 4*, 79–92. Springer.
- Wallace, M., Wagg, D., and Neild, S. (2005). An adaptive polynomial based forward prediction algorithm for multi-actuator real-time dynamic substructuring. In *Proceedings of the Royal Society of London A: Mathematical, Physical and Engineering Sciences*, volume 461.

Article 3 – J-1

**Optimal Force Allocation for Overconstrained Cable-Driven
Parallel Robots: Continuously Differentiable Solutions with
Assessment of Computational Efficiency**

Einar S. Ueland, Thomas Sauder, Roger Skjetne
IEEE Transactions on Robotics
<https://doi.org/10.1109/TRO.2020.3020747>




This article is not included due to copyright

Article 4 – J-2
**Optimal Actuator Placement for Real-time Hybrid Model
Testing using Cable-driven Parallel Robots**

Einar S. Ueland, Thomas Sauder, Roger Skjetne
Journal of Marine Science and Engineering
[10.3390/jmse9020191](https://doi.org/10.3390/jmse9020191)

Article

Optimal Actuator Placement for Real-Time Hybrid Model Testing Using Cable-Driven Parallel Robots

Einar Ueland ^{1,*}, Thomas Sauder ^{1,2} and Roger Skjetne ¹

¹ Centre for Autonomous Marine Operations and Systems (NTNU AMOS), Department of Marine Technology, Norwegian University of Science and Technology, NO-7491 Trondheim, Norway; Thomas.Sauder@sintef.no (T.S.); roger.skjetne@ntnu.no (R.S.)

² SINTEF Ocean, NO-7465 Trondheim, Norway

* Correspondence: einar.s.ueland@ntnu.no

Abstract: In real-time hybrid model testing, complex ocean structures are emulated by fusing numerical modelling with traditional hydrodynamic model testing. This is done by partitioning the ocean structure under consideration into a numerical and a physical substructure, coupled in real time via a measurement and control interface. The numerically computed load vector is applied to the physical substructure by means of multiple actuated winches so that the resulting experimental platform becomes a type of cable-driven parallel robot. In this context, the placement of the actuated winches is important to ensure that the loads can be accurately and robustly transferred to the physical substructure. This paper addresses this problem by proposing a performance measure and an associated actuator placement procedure that enables accurate force tracking and ensures that the numerically calculated loads can be actuated throughout the testing campaign. To clarify the application of the proposed procedure, it is applied to the design of a test setup for a moored barge. Overall, the paper represents a guideline for robust and beneficial actuator placement for real-time hybrid model testing using cable-driven parallel robots for load-actuation.



Citation: Ueland, E.; Sauder, T.; Skjetne, R. Optimal Actuator Placement for Real-Time Hybrid Model Testing Using Cable-Driven Parallel Robots. *J. Mar. Sci. Eng.* **2021**, *9*, 191. <https://doi.org/10.3390/jmse9020191>

Academic Editor: Jaw-Fang Lee
Received: 11 January 2021
Accepted: 8 February 2021
Published: 12 February 2021

Publisher's Note: MDPI stays neutral with regard to jurisdictional claims in published maps and institutional affiliations.



Copyright: © 2021 by the authors. Licensee MDPI, Basel, Switzerland. This article is an open access article distributed under the terms and conditions of the Creative Commons Attribution (CC BY) license (<https://creativecommons.org/licenses/by/4.0/>).

Keywords: real-time hybrid model testing; hybrid testing; actuator placement; CDPR; ocean engineering; marine control systems

1. Introduction

Real-time hybrid model testing (ReaTHM testing) is a cyber-physical empirical method for emulating complex ocean structures that combines numerical models with traditional hydrodynamic model testing [1,2]. This is done by partitioning the ocean structure under consideration into a numerical substructure and a physical substructure that are coupled in real time through a measurement and control interface. See Figure 1. The method enables emulation of ocean systems where neither a purely numerical simulation nor a purely physical model test is feasible within satisfactory performance levels.

Applications of the method include testing of offshore wind turbines [3]—to overcome the Froude-Reynolds scaling conflict [4], seakeeping tests of floating structures [5]—to overcome limitations of soft horizontal mooring systems, and testing of moored structures [6]—to overcome spacial limitations of ocean basin laboratories (see Figure 2). In the above-cited applications, and in line with the present publication, the numerically calculated load vector is transferred to the physical substructure using multiple actuated winches. Thus, the resulting experimental substructure becomes a type of cable-driven parallel robot (CDPR), which is a setup characterised by a mobile platform being actuated by cabled winches configured in a parallel topology [7]. See Figure 3. From each cabled actuator, the actuated load is a function of the cable-tension and its two cable endpoints. Due to actuator limitations and to avoid slack cables, lower and upper constraints are enforced on the cable-tensions. The cable endpoints of all connected actuators, together with the platform pose, constitute the platform configuration of a CDPR.

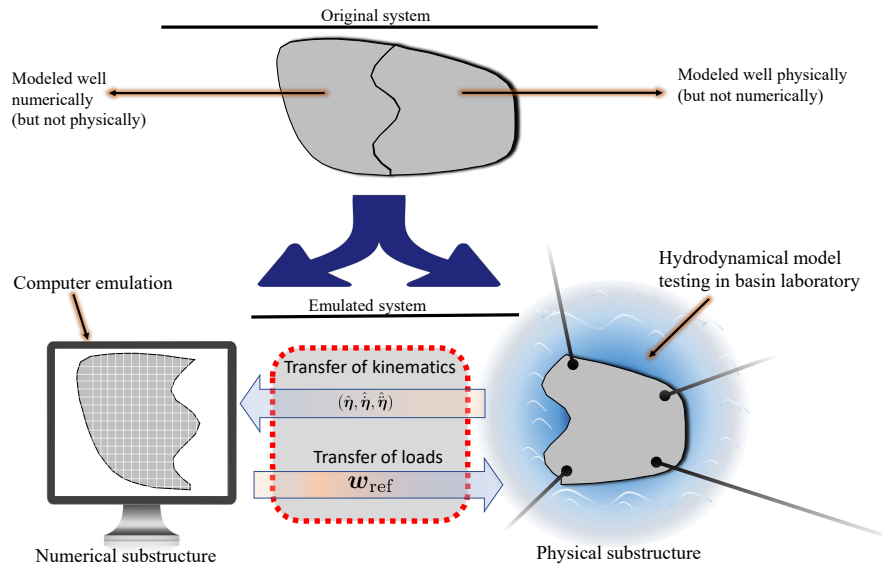


Figure 1. ReaTHM testing of an ocean structure. $\omega_{(c)}$ represents environmental loads acting on the structure.

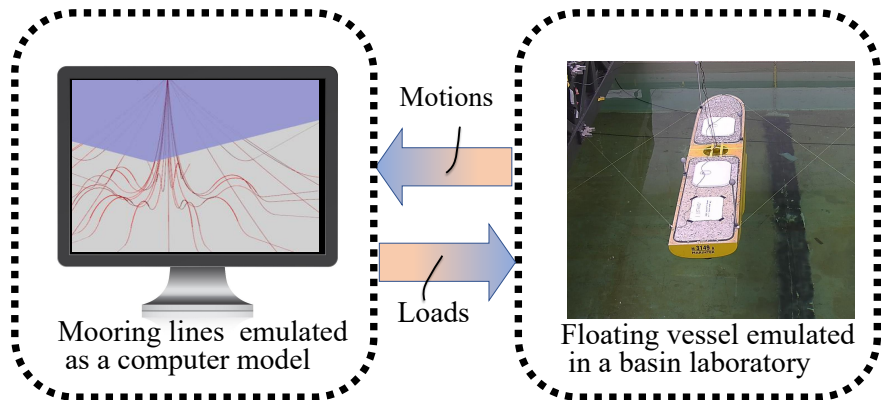


Figure 2. ReaTHM testing of a moored ship. Notice the four nylon strings used to apply the numerically calculated mooring loads onto the ship. See [6,8].

Beyond their use for ReaTHM testing, CDPRs have received considerable attention in recent decades [9,10] for diverse applications, including aerial cameras [11], manufacturing [12], agriculture [13], and ocean engineering [14]. They are recognised for their large workspace coverage, lightweight structure, fast dynamics, and reconfigurability [15–17].

In our experience, placement of actuators in previous ReaTHM testing CDPR setups, such as [3,6,8], has mostly been determined using a practical and heuristic approach, i.e., for a given ReaTHM testing scenario, the actuators have been placed based on simplified analysis, experiential experience and intuitive understanding – with limited systematic analysis. At the time of this publication, no guidelines exist for actuator placement for ReaTHM testing using CDPR.

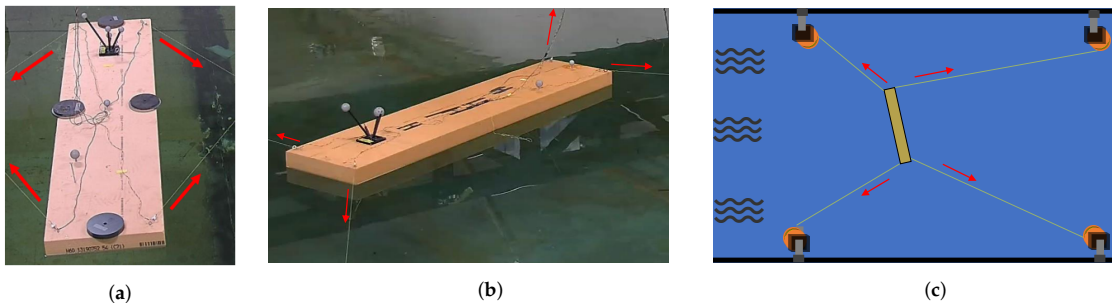


Figure 3. ReaTHM testing of a moored barge using a planar CDPR. Red arrows mark the direction of the actuated force, passed axially through each cable. (a–b) Image from laboratory setup of the authors [8]. (a) Crossed configuration. (b) Uncrossed configuration. (c) Schematic overview.

Conversely, for other CDPR applications, the minimization of performance measures evaluating the quality of platform configurations are commonly used to determine the optimal placement of actuators ([10] [Ch 8]). Reference [18] suggests using a controllability measure based on eigenvectors, which is a popular measure when considering the control of linear systems [19]. Also related to controllability, [20–22] uses a conditioning number referred to as the platform dexterity measure. Several references [22–24] use performance measures related to the CDPR’s stiffness, with the goal of either maximising the stiffness or ensuring that the stiffness distribution is uniform. Reference ([10] [Ch 8]) lists several additional performance measures including quality of tension distribution, accuracy, energy considerations, closeness to singularities, and proximity to cable collision. Other popular performance measures relate to optimising workspace coverage. These performance measures can for example be to maximise the range of poses in which certain prescribed loads can be actuated [25,26] (wrench-feasible workspace), or the range of poses for which any load can be actuated given no upper cable-tension constraints [27] (wrench-closure workspace).

In some cases, the performance measure is minimised subject to specific requirements being satisfied. See for example [28] in which actuator placement is determined by minimising cable tensions subject to the condition that wrench-closure workspace requirements are satisfied. In [29] the search for optimal actuator placement is divided into an exploration phase, in which promising CDPR geometries are identified, and a subsequent optimisation phase, in which the optimal actuator placement is determined by minimising the proposed performance measure for the selected geometries.

In ReaTHM testing, precisely applying the calculated loads onto the marine platform is particularly important to achieve high fidelity in replicating the non-structured ocean structure’s behaviour [8,30,31]. Although there are many performance measures for CDPR setups, these are in our opinion, not appropriate for ReaTHM testing—as this application requires a different set of priorities, as elaborated next.

Table 1 lists characteristic differences between CDPR used in ReaTHM testing [2,6,8] and typical¹ CDPR setups used for other applications ([10] [Ch 2.4]). The practical implications of these differences are as follows:

1. Whereas there is some margin for load (forces and moments) tracking errors in typical CDPR applications, accurate load tracking is paramount to ensure high-fidelity ReaTHM testing [31]. Therefore, the relative focus on accurate load control is considerably higher for the latter.
2. For typical CDPR applications, a higher stiffness throughout the workspace may be preferable to minimise undesired perturbations from external disturbances [24]. Con-

¹ What constitutes a typical CDPR application has been inferred based on the trends observed by examining a large number of references. Being trends only, there exist counterexamples for each statement in Table 1.

- versely, for ReaTHM testing, a lower stiffness is preferable, to make the setup less sensitive to platform motions (this relates to delay-induced errors, as discussed in [32]).
3. Given similar platform dimensions, the actuation system in typical CDPR applications carries larger loads than in ReaTHM testing and must be designed accordingly.
 4. In ReaTHM testing, the platform design is fixed to the emulation target, whereas in typical CDPR applications multiple platform designs may serve the same purpose.

Table 1. Differences between CDPR in typical applications and CDPR in ReaTHM testing.

	Typical CDPR Applications.	CDPR for ReaTHM Testing (Using Load Control)
(1) Control objective	A target pose is the control objective. Force/tension control may be used in an inner control loop to achieve the desired pose. See discussion in [32].	A target load vector is the control objective, with pose trajectories following consequently [6].
(2) External forces	The cabled actuators help ensure that the platform remains close to the desired pose in the presence of external excitations [33].	The loads applied by the cabled actuators are in addition to other external loads (typically hydrodynamic) acting on the platform. The applied loads should not be disturbed by the external loads, nor the platform’s movements [8].
(3) Platform weight	The platform is suspended in air, and the platform weight is carried by the cabled actuators. See Figure 4.	The platform is located in a water basin, and the cabled actuators do not carry its weight. See Figure 3.
(4) Design considerations	The CDPR setup is designed for the specific objectives of the application. Typical objectives include to carry a payload or to sense or interact with the environment in a specific way ([10] [Ch 2.4]).	The platform is designed to achieve similarity to the target ocean substructure it models (typically using Froude scaling). The objective is for the actuated load vector to track the reference load vector with high accuracy [7].

These items imply a different focus when determining the actuator placement for the two cases. For ReaTHM testing, we propose using a procedure that aims at accurate load actuation—while ensuring that the target load vector is always achievable. Conversely, actuator placement for typical CDPR applications is not based on load actuation accuracy, but on other measures [10,20–22,25,26], as discussed earlier.

In this paper, we seek to develop a procedure for placement of actuators for CDPR setups that is suitable for use in ReaTHM testing. Specifically, we seek a procedure for placement of actuators that: (1) facilitates accurate load tracking—which is important to ensure high fidelity ReaTHM testing that accurately predicts the behaviour of the target ocean structure, and (2) ensures that the actuators can always actuate the numerically calculated loads according to specified workspace requirements—which is a prerequisite to carry out a successful ReaTHM testing campaign. The resulting procedure shall be optimal in the sense that it minimises the proposed performance measure.

The remainder of the paper is structured as follows. Section 2 outlines the preliminary background. Section 3 presents the proposed procedure for actuator placement. Section 4 demonstrates the procedure for ReaTHM testing of a moored barge.

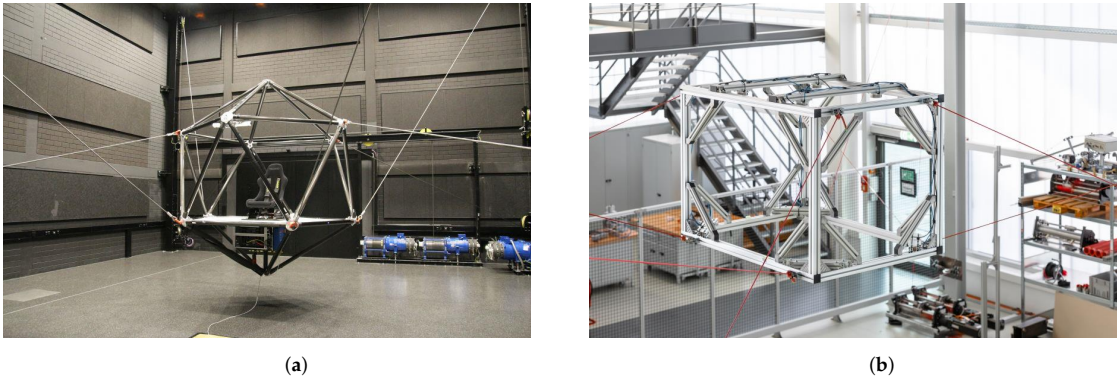


Figure 4. Two CDRP setups. (a) The CableRobot Simulator [34]. Reproduced with permission from Max Planck Institute for Biological Cybernetics ©2015. (b) The IPAnema 3 CDRP [35]. Reproduced with permission from Fraunhofer IPA © 2019.

2. Problem Formulation

2.1. Force Allocation

Force allocation for CDRP is the problem of finding the optimal cable tensions $\mathbf{f}^* = (f_1^*, f_2^*, \dots, f_n^*)$ on an overconstrained CDRP setup such that they sum up to the reference load vector $\mathbf{w}_{\text{ref}} \in \mathbb{R}^m$, where n is the number of connected cabled actuators and m is the number of controlled degrees of freedom (DOF) in which the load \mathbf{w}_{ref} shall be actuated. We typically consider the physical platform to be described in 6 DOF, in which case $m \leq 6$. In the case of ReaTHM testing \mathbf{w}_{ref} corresponds to the numerically calculated load vector that is to be actuated onto the physical substructure. See Figure 1.

We next express the force allocation problem as an optimisation problem, similar to [36]. When considering the experimental setup, we refer to two reference frames, $\{a\}$ and $\{b\}$; O^a is the local Earth-fixed coordinate frame’s stationary origin $\{a\}$, and O^b is the platform’s body-fixed frame’s moving origin $\{b\}$. See Figure 5. Accordingly, vectors decomposed in $\{a\}$ or $\{b\}$ are given superscripts a or b , respectively. If the superscript is omitted, and the vector has not been previously defined, then it is decomposed in $\{a\}$.

The position and orientation (pose) of the body frame $\{b\}$ relative to $\{a\}$ are denoted $\mathbf{p} := \mathbf{p}^a = (x, y, z) \in \mathbb{R}^3$ and $\Theta := (\phi, \theta, \psi) \in \mathcal{S}_1^3$, where $\mathcal{S}_1 \in [-\pi, \pi]$ (this paper represents orientation by the zyx Euler angle convention ([37] [Ch 2.2.1])). These are combined in the body’s pose vector $\boldsymbol{\eta} := (\mathbf{p}, \Theta) \in \mathbb{R}^3 \times \mathcal{S}_1^3$. For each actuator $i \in \{1, \dots, n\}$, let $\mathbf{p}_{ai} := \mathbf{p}_{ai}^a$ be the fixed position of the i^{th} cable exit point A_i . Similarly, let the constant body-fixed lever arm from O^b to the i^{th} cable attachment anchor E_i (on the platform) be denoted \mathbf{r}_i^b .

The Euler angle rotation matrix $\mathbf{R}(\Theta)$ maps vectors from $\{b\}$ to $\{a\}$:

$$\mathbf{R}(\Theta) = \mathbf{R}_z(\psi)\mathbf{R}_y(\theta)\mathbf{R}_x(\phi), \tag{1}$$

with,

$$\mathbf{R}_x = \begin{bmatrix} 1 & 0 & 0 \\ 0 & \cos(\phi) & -\sin(\phi) \\ 0 & \sin(\phi) & \cos(\phi) \end{bmatrix}, \quad \mathbf{R}_y = \begin{bmatrix} \cos(\theta) & 0 & \sin(\theta) \\ 0 & 1 & 0 \\ -\sin(\theta) & 0 & \cos(\theta) \end{bmatrix}, \quad \mathbf{R}_z = \begin{bmatrix} \cos(\psi) & -\sin(\psi) & 0 \\ \sin(\psi) & \cos(\psi) & 0 \\ 0 & 0 & 1 \end{bmatrix}. \tag{2}$$

Accordingly, $\mathbf{r}_i^a = \mathbf{R}(\Theta)\mathbf{r}_i^b$.

It follows that the absolute position of E_i is $\mathbf{p}_{ei} := \mathbf{p}_{ei}^a = \mathbf{p} + \mathbf{R}(\Theta)\mathbf{r}_i^b$. From each actuator i , a force f_i directed along the straight line $\mathbf{p}_{ai} - \mathbf{p}_{ei}$, with direction denoted by the unit vector $\mathbf{u}_i := \frac{\mathbf{p}_{ai} - \mathbf{p}_{ei}}{\|\mathbf{p}_{ai} - \mathbf{p}_{ei}\|}$ is actuated on the platform at E_i . The relationship between the

cable tensions $f = (f_1, f_2, \dots, f_n)$ and the resulting load vector w generated by the cables is described by $w = Wf$, where

$$W = [q_1 \quad q_2 \quad \dots \quad q_n], \text{ with } q_i = \begin{bmatrix} u_i \\ r_i^a \times u_i \end{bmatrix}, \tag{3}$$

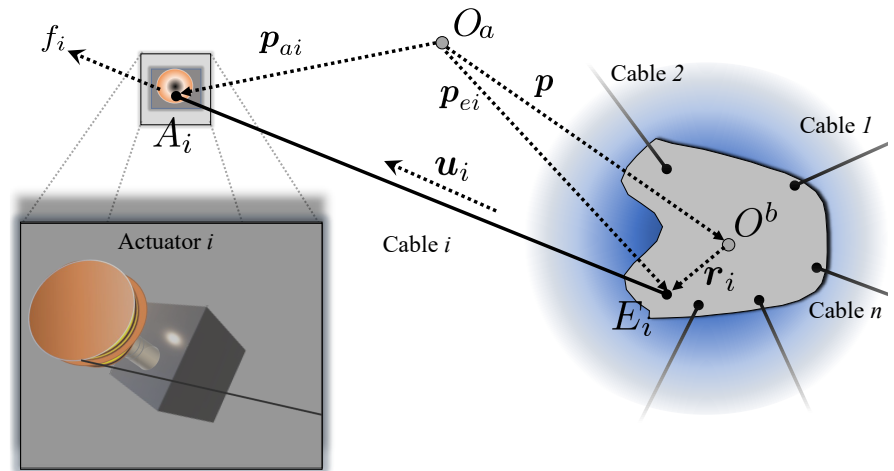


Figure 5. Reference frames and the experimental test setup with the platform (down-scaled physical substructure) connected to n actuated cables. One of the actuators is sketched and annotated.

The set of cable attachment points $\{p_a\} := (p_{a1}, p_{a2}, \dots, p_{an})$ combined with the body-fixed lever arms $\{r^b\} := (r_1^b, r_2^b, \dots, r_n^b)$ are referred to as the *actuator configuration* of the CDPR. The *platform configuration* of the CDPR refers to the *actuator configuration* combined with the platform pose η , and thus describes the cable endpoints for all actuator cables.

In solving the force allocation problem as an optimisation problem, we find f^* as the cable tensions f that minimise a cost function $g(f)$ subject to cable constraints $f_{\min} \preceq f \preceq f_{\max}$ and kinematic mapping,

$$f^* = \arg \min_{f'} \{g(f') : f' \in \mathbb{R}^n, Wf' = w_{\text{ref}}, f_{\min} \preceq f' \preceq f_{\max}\} \tag{4}$$

where f' is any cable tension vector f satisfying the constraints.

In this paper, we will use the following cost function:

$$g(f) = \sum_{i=1}^n \left(\frac{|f_i - f_{0,i}|^2}{\alpha^2} - c_1 \log(f_i - f_{i,\min}) - c_2 \log(f_{i,\max} - f_i) \right), \tag{5}$$

where α , c_1 and c_2 are scaling parameters and $f_0 = (f_{0,1}, f_{0,2}, \dots, f_{0,n})$ is the preferred load vector dependent on application specific factors such as actuator technology, cable properties, safety concerns, and operating conditions. The cost function has beneficial properties, as shown in [36].

2.2. The ReaTHM Testing Loop

Figure 6 shows the resulting ReaTHM testing loop coupling the two substructures. Some additional notes on its components are:

- Hydrodynamic loads act on both the numerical and physical substructure throughout the test.

- The numerical substructure is driven by the pose estimate $\hat{\eta}$. This generally deviates from the true pose η due to delays and estimation errors.
- For the actuator control system, the goal is for the applied cables tensions f to track the optimal cable tensions f^* closely. In our research group work, we consider the control of each actuator independently. See for example [6].
- The resulting load vector w generally deviates from the reference load vector w_{ref} due to delays, mischaracterisation of W , force estimation errors, and target force tracking errors [8]. In this paper, accurate load tracking refers to w tracking w_{ref} closely.

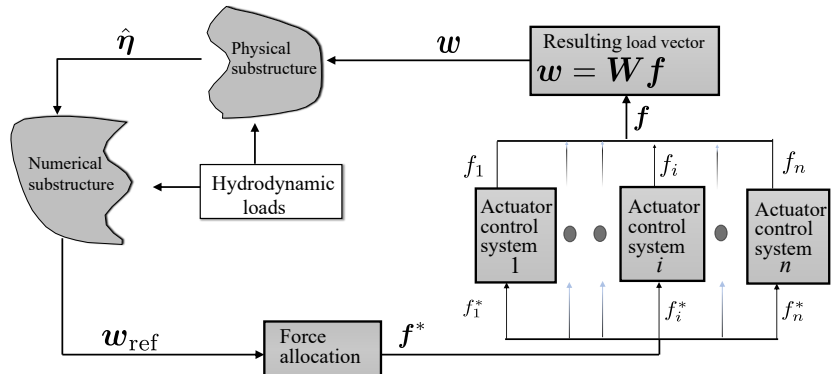


Figure 6. The ReaTHM testing loop

2.3. Wrench Feasible Workspace

In ReaTHM testing, it is crucial to ensure that the cabled actuators can apply the reference load vector onto the physical substructure throughout the testing campaign. To this end, we adopt the notion of *wrench feasibility* [38–40] to specify the workspace where this can be guaranteed (in the CDPR literature, the term *wrench* is commonly used to denote the load vector w):

Definition 1 (Definitions of Wrench Feasibility and Workspaces). Let the set of *feasible wrenches* $\mathcal{W}_{fe}(\eta) = \{w \in \mathbb{R}^m : w = W(\eta)f, f_{min} \preceq f \preceq f_{max}\}$ be the set of loads that is feasible at a given pose η . Furthermore, let the *wrench feasibility requirement* $\mathcal{W}_{req}(\eta)$ be the set of all loads that, per requirements, should be feasible at a given pose η . A pose η is said to be *wrench feasible* if $\mathcal{W}_{req}(\eta) \subseteq \mathcal{W}_{fe}(\eta)$. Let the *wrench feasible workspace* be the set of poses that are *wrench feasible*, i.e., $\mathcal{N} = \{\eta \in \mathbb{R}^m : \mathcal{W}_{req}(\eta) \subseteq \mathcal{W}_{fe}(\eta)\}$. Finally, let the *wrench feasible workspace requirement* \mathcal{N}_{req} be the set of poses in which wrench feasibility is required. We say that the CDPR fulfils wrench feasibility requirements if $\mathcal{N}_{req} \subseteq \mathcal{N}$.

Several authors addressed wrench feasibility analytically by constructing geometric bounds of \mathcal{N} . See, for example [39]. Although continuous expressions for \mathcal{N} can be found for simple geometries, and promising approaches using interval-analysis exist [40], discretisation and subsequent exhaustive numerical evaluation remain popular in the relevant literature due to the complexity of alternative approaches. See the discussion in ([10] [Ch 5]).

In this paper, wrench feasibility is checked using the following proposition:

Proposition 1. (Adapted from [41].) If $\mathcal{W}_{req}(\eta)$ is enclosed by the polyhedron formed by I vertices $v_i \in \mathbb{R}^m$ with $v_i \subseteq \mathcal{W}_{fe}(\eta)$ for $i = \{1, 2, \dots, I\}$, then $\mathcal{W}_{req}(\eta) \subseteq \mathcal{W}_{fe}(\eta)$.

This follows simply from the total feasible workspace $\mathcal{W}_{fe}(\boldsymbol{\eta})$ being a convex hull [41] (specifically, it is a zonotope [42]). Due to its simplicity, we suggest using pose dependent box constraints,

$$\mathcal{W}_{req}(\boldsymbol{\eta}) = \{w \in \mathbb{R}^m : w_{min}(\boldsymbol{\eta}) \preceq w \preceq w_{max}(\boldsymbol{\eta})\}, \tag{6}$$

where $w_{min}(\boldsymbol{\eta})$ and $w_{max}(\boldsymbol{\eta})$ are the required minimum and maximum load vector constraints for each controlled DOF. Using Proposition 1, with box constraints, there are 2^m vertices to check for each platform (the use of Proposition 1 is later exemplified in Section 4).

An alternative framework for checking of wrench feasibility of a *platform configuration*, in which the set of feasible loads are described as a linear inequality system is presented in [42,43].

2.4. Cable Collision

To ensure that the platform can move freely within \mathcal{N}_{req} , the cables should not collide with each other or with the platform during operation [44]. This is especially relevant if cables cross each other as in [8]. Some sources determine collision-free workspaces using analytical approaches [45]. Since this quickly becomes complex, we suggest assessing cable collisions numerically for each pose using Algorithm 1.

In brief, this algorithm considers the distance between line segments in the workspace. In this process, if needed, the platform shapes can be transformed into a simpler convex shape enclosing the platform hull [46]. Let there be n_k straight platform line segments enclosing the platform hull and n straight cable line segments. Then, there are a total of $(n-1)!$ cable to cable line segments and $n \times n_k$ cable to platform line segments that the algorithm needs to check for collision. Finding the shortest distance between two line segments is a simple well-known mathematical problem with relatively low computational cost. See for example [47].

Algorithm 1 Cable Collision

$\delta_{lim} \leftarrow$ Critical collision distance.

for each *pose* in the *grid* **do**

for each *cable*, find minimum distances {d} to all other line segments.

if (*any*({d}) < δ_{lim}) **then** define as collision (or refine search).

end if

end for

2.5. Configuration Performance Measure

As described generally for CDPR setups in ([10] [Ch 8]) and discussed in the paper introduction, each platform configuration can be associated with a performance measure $c_p(\boldsymbol{\eta})$. A global performance measure \bar{k} is obtained by integrating the cost over the entire volume of interest $V(\mathcal{N}_{req})$ using

$$\bar{k} = \frac{1}{V(\mathcal{N}_{req})} \int_{\mathcal{N}_{req}} c_p(\boldsymbol{\eta}) d\mathcal{N}_{req} \approx \frac{1}{K} \sum_{i=1}^K c_p(\boldsymbol{\eta}_i), \tag{7}$$

where the latter is the corresponding approximation summing over \mathcal{N}_{req} , which is discretised into K cells.

3. Procedure for Optimal Actuator Placement in ReaTHM Testing

3.1. Performance Measure

In this paper and for use in ReaTHM testing applications we propose using the following platform configuration performance measure given n actuators and a fixed cost function $g(\mathbf{f})$:

$$c_p(\boldsymbol{\eta}) = \underbrace{\kappa_g(g(\mathbf{f}^*) - g(\mathbf{f}_0))}_{c_{pg}} + \underbrace{\sum_{i=1}^{i=m} \left| \kappa_1[i] \left(\nabla_{\mathbf{w}_{ref}[i]}(\mathbf{f}^*) \right) \right|_1}_{c_{p1}} + \underbrace{\sum_{i=1}^{i=m} \left| \kappa_2[i] \left(\nabla_{\boldsymbol{\eta}[i]}(\mathbf{f}^*) \right) \right|_1}_{c_{p2}} + \underbrace{\sum_{i=1}^{i=m} \left| \kappa_3[i] \left(\nabla_{\boldsymbol{\eta}[i]}(\mathbf{W}) \right) \mathbf{f}^* \right|_1}_{c_{p3}} \quad (8)$$

where $\kappa_g \in \mathbb{R}_{\geq 0}^1$, $\kappa_1 \in \mathbb{R}_{\geq 0}^m$, $\kappa_2 \in \mathbb{R}_{\geq 0}^m$, and $\kappa_3 \in \mathbb{R}_{\geq 0}^m$ are constant scaling parameters that determine the relative weighting of each term. Further $\kappa_{(\cdot)}[i]$, $\mathbf{w}_{ref}[i]$ and $\boldsymbol{\eta}[i]$ are the i th components of $\kappa_{(\cdot)}$, \mathbf{w}_{ref} , and $\boldsymbol{\eta}$, respectively (for example $\boldsymbol{\eta}[1]$ denotes x). The notation ∇ denotes partial derivatives. For example, $\left(\nabla_{\boldsymbol{\eta}[i]}(\mathbf{f}^*) \right)$ denotes the partial derivative of (\mathbf{f}^*) with respect to the variable $\boldsymbol{\eta}[i]$. The terms of (8) are expressed mathematically in Appendix A. Finally, \mathbf{f}^* is the solution \mathbf{f}^* to (4) given $\mathbf{w}_{ref} = \mathbf{0}$. The latter means that the performance for each pose is only evaluated around the static equilibrium point ($\mathbf{w} = 0$) and is a choice made to limit computation times (we expect the performance near $\mathbf{w} = 0$ to be the most important).

Although not done in this work, if computation times are of no concern, it is straightforward to extend (8) such that it for a given pose sums over a weighted version of the wrench feasibility requirement. Another straightforward extension would be multiplying $c_p(\boldsymbol{\eta})$ with a pose-dependent weight. The latter would allow increasing the prioritisation of performance in poses that are particularly important.

The reasoning for each component of (8) is as follows:

- c_{pg} —(quality of tension distribution) associates the cable tensions with the cost captured by the cost function. The cost function is assumed to be designed such that the actuated cables operate at higher performance when $g(\mathbf{f}^*)$ is low.
- c_{p1} —(load vector sensitivity) is a measure of the sensitivity of the optimal cable tensions to a change in the reference load vector. Since \mathbf{f}^* is the minimiser of the optimisation problem, the term can also be interpreted as a controllability measure that takes the cost function and constraints into account – as opposed to simpler controllability measures based on eigenvectors [22].
- c_{p2} —(motion sensitivity) is a measure of the optimal cable tensions sensitivity to platform motions. The intent is to limit the sensitivity of the optimal cable tensions to motions – to generate smoother trajectories that are easier to track.
- c_{p3} —(kinematic mapping sensitivity) quantifies the actual load vector’s sensitivity to changes in $\boldsymbol{\eta}$, given fixed cable tensions \mathbf{f}^* . Keeping c_{p3} low reduces force allocation errors by making the load vector less sensitive to small errors in the pose estimates $\hat{\boldsymbol{\eta}}$. See discussion on force allocation errors in [8]. The term also reduces the stiffness in the weighted degrees of freedom (specifically it reduces stiffness induced from internal forces, which is one of two components of the overall stiffness of a CDPR mechanism [48]).

3.2. Procedure Description

Using the performance measure (8), we formulate the following procedure:

Procedure 1. *Optimal actuator placement for ReaTHM testing using CDPR*

1. (*Problem specification*) Specify the number of actuators n , the cable cost function $g(f)$, the cable tension constraints f_{\min} and f_{\max} , the workspace requirements \mathcal{N}_{req} and \mathcal{W}_{req} , the performance measure weights κ_g , κ_1 , κ_2 , and κ_3 , and the constraints in the placement of actuators.
2. (*Determination of optimal actuator placement*) Given the above specifications, with \bar{k} and $c(\eta)$ given by and (7) and (8), respectively, then determine the optimal actuator placement that minimises \bar{k} subject to: 1) $\mathcal{N}_{\text{req}} \subseteq \mathcal{N}$, 2) no cable collisions, and 3) constraints in the placement of actuators.

By using a performance measure that is a linear combination of terms that all target accurate actuation of forces (that is, quality of force distribution, load vector sensitivity, motion sensitivity, and kinematic mapping sensitivity), Procedure 1 is designed to: (1) increase load tracking accuracy and (2) ensure that the expected numerical loads are always feasible. As such, it is suitable for ReaTHM testing, where load inaccuracies may jeopardize fidelity. Conversely, traditional optimality measures for CDPR applications such as maximising workspaces or minimising the effect of external forces on the platform (by increasing stiffness) are not part of the cost function. This reflects the different prioritisation when considering ReaTHM testing compared to other typical CDPR applications, as discussed in the paper introduction.

3.3. *General Guidelines for Problem Specification in Procedure 1*

3.3.1. *Controlled Degrees of Freedom and the Number of Actuators*

Although a higher number of actuators can increase actuation capabilities and the extent of \mathcal{N} , each actuator increases the setup’s complexity and is associated with acquisition, installation, and maintenance costs. In the literature on CDPR, it appears to be most common to have either one (for planar CDPR) or two (for 6-DOF CDPR) more actuators than controlled DOFs [49].

For ReaTHM testing, there may be several reasons to have fewer than six controlled DOFs (e.g., $m < 6$). Uncontrolled DOFs are characterized by being self-stabilizing, with the corresponding numerical load component having a negligible impact on the quantities of interest compared to hydrostatic and hydrodynamic loads. See the following examples:

1. In ReaTHM testing of a floating offshore wind turbine reported in [3,7,50], leaving out the vertical component of w_{ref} is shown to have negligible effect on the motions of the wind turbine, mooring force and internal loads. The physical platform is actuated in five DOFs ($m = 5$), using six cabled actuators ($n = 6$).
2. In ReaTHM testing of a moored buoy reported in [51] it is argued that out-of-plane numerical load components can be neglected. Due to the circular, symmetrical shape of the buoy, the yaw moment is also neglected. The physical platform is actuated in two DOFs ($m = 2$), using three cabled actuators ($n = 3$).
3. Similarly, for the ReaTHM testing of the ship-shaped vessel reported in [8], out-of-plane numerical load components are neglected (see also [5]). Unlike [51], however, the yaw moment is considered important. The physical platform is actuated in three DOFs ($m = 3$), using four cabled actuators ($n = 4$).

3.3.2. *Actuator Tension Constraints and Cost function*

The actuator cable tension constraints are highly dependent on the characteristics of the actuators in use. A minimum admissible tension $f_{\min} = (f_{\min,1}, f_{\min,2}, \dots, f_{\min,n})$ is set to prevent the cable from going slack, whereas a maximum admissible tension $f_{\max} = (f_{\max,1}, f_{\max,2}, \dots, f_{\max,n})$ is set due to actuator and cable limitations.

Although Procedure 1 is not restricted to a specific cost function, as stated earlier, we propose to reuse the cost function presented in (5). See [36], for guidelines on determining its parameters.

3.3.3. Workspace Requirements

For ReaTHM testing, we recommend adjusting \mathcal{W}_{req} and \mathcal{N}_{req} based on the expected outputs of the numerical substructure and based on the expected excursions/motions of the model in the basin. These can either be derived from simulation studies or determined heuristically based on simplified analysis, experience, intuitive understanding, and case assessment. If the plan is to reuse the setup in several different testing campaigns, this should be reflected in \mathcal{N}_{req} and \mathcal{W}_{req} .

3.3.4. Constraints in Placement of Actuators

The actuators will typically be mounted onto existing basin infrastructure (such as along the basin walls), which imposes natural constraints on the placement of the actuators. Other important factors include ease of access for installation and maintenance, including cabling for communication, power, and control.

Enforcing symmetry constraints on the placement of actuators simplifies the design process and increases robustness by alleviating some biases. A symmetric design also conforms to standards for typical CDPR applications. See for example ([10,12,17,21] (Ch 2.3)).

3.3.5. Performance Weights

We suggest the following approach to determine the weights κ_g , κ_1 , κ_2 , and κ_3 :

1. Since κ_1 and κ_2 both relate to target force tracking, they are scaled relative to each other and in proportion to the expected variation in $\boldsymbol{\eta}$ and $\boldsymbol{w}_{\text{ref}}$ – under the assumption that it is easier to track target forces that vary less.
2. Next κ_3 is determined by considering the importance of force allocation errors relative to force tracking errors. If the expected accuracy of $\dot{\boldsymbol{\eta}}$ is high, κ_3 can be reduced relative to κ_1 and κ_2 , and increased in the opposite case.
3. Next, the entries of κ_1 , κ_2 , and κ_3 are determined in proportion to the expected dynamic range and the variations of $\boldsymbol{\eta}$ and $\boldsymbol{w}_{\text{ref}}$. For example, an expectation of large variations in $\boldsymbol{\eta}[1]$, corresponds to an increase in $\kappa_2[1]$ and $\kappa_3[1]$, as these scaling parameters capture sensitivity to changes in $\boldsymbol{\eta}[1]$. Conversely, an expectation of large variations of $\boldsymbol{w}_{\text{ref}}[1]$ corresponds to an increase in $\kappa_1[1]$, since this scaling parameter captures sensitivity to $\boldsymbol{w}_{\text{ref}}[1]$.
4. Finally, the cost vector gain κ_g is chosen according to the importance of having a low cost function value relative to keeping the other terms low. This gain will be highly dependent on the selected cost function.

4. Optimal Placement of Actuators for ReaTHM Testing of a Barge

This section demonstrates Procedure 1 by applying it to an example test case closely resembling that of Figure 3, studied by the authors in [8]. Specifically, it considers a case where a moored barge is to be tested in a small basin facility with dimensions 16.2 m \times 6.7 m with its side against the incident waves as illustrated in Figure 7. The body-fixed cable lever arms $\{r_i^b\}$ are specified in Table 2 (a). Procedure 1 is used to determine the actuator placement $\{p_a\}$ along the basin wall.

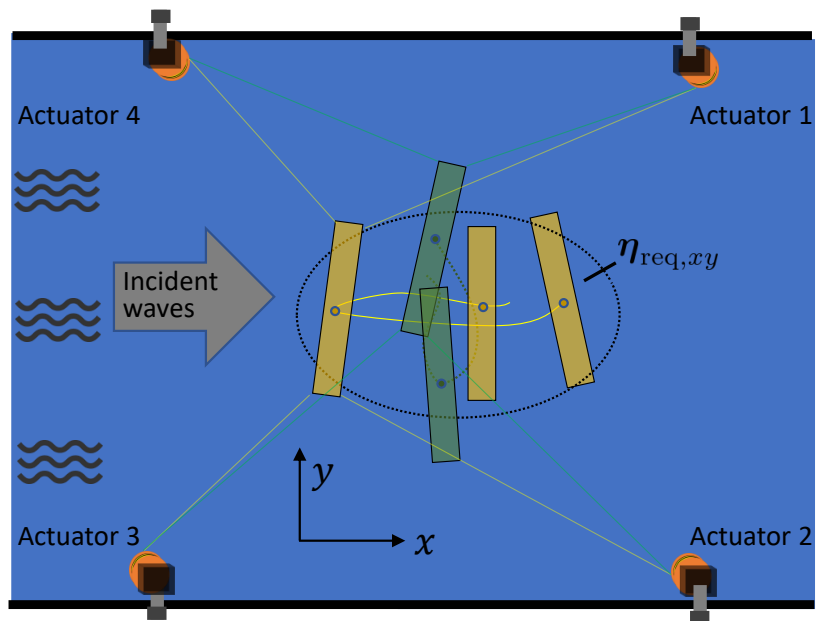


Figure 7. The moored barge in various poses and with the horizontal required workspace $\eta_{req, xy}$ indicated. Green and yellow colours indicate trajectories in two different test runs.

Table 2. Sample actuator and platform configurations used in Section 4.

(a) $\{r_b\}$ used throughout Section 4.									
	1	2	3	4					
x	0.175	0.175	-0.175	-0.175					
y	0.95	-0.95	-0.95	0.95					
z	0	0	0	0					
(b) Sample actuator configurations.									
	$\{p_a\}$				$\{r_b\}$				
Actuator configuration 1	Table 2 (a)				Table 2 (d)				
Actuator configuration 2	Table 2 (a)				Table 2 (e)				
(c) Sample platform configurations									
Platform configuration 1	Actuator configuration 1 with $\eta_3 = (0, 0, 0)^T$								
Platform configuration 2	Actuator configuration 1 with $\eta_3 = (1.9, -0.7, -0.15)^T$								
(d) $\{p_a\}$ uncrossed configuration				(e) $\{p_a\}$ crossed configuration					
	1	2	3	4	1	2	3	4	
x	3.25	3.25	-3.25	-3.25	x	3.25	3.25	-3.25	-3.25
y	3.25	-3.25	-3.25	3.25	y	-3.25	3.25	3.25	-3.25
z	0	0	0	0	z	-0.025	0.025	-0.025	0.025

4.1. Problem Specification

4.1.1. Controlled Degrees of Freedom and the Number Of Actuators

The numerical substructure is composed of a horizontal model of the barge’s mooring system, with only planar load components transmitted across the partitioning interface, i.e., out-of-plane loads of the mooring system are neglected. This implies that the numerically calculated load vector is to be actuated in the three degrees of freedom surge, sway, and yaw (x, y, ψ) . Accordingly, we specify the case with $\eta_3 := (x, y, \psi)$ in place of η , $w := (w_x, w_y, w_\psi)$, and $m = 3$.

To not use more actuators than necessary, the case is specified with four actuators ($n = 4$) which is sufficient to ensure that the system is overconstrained.

4.1.2. Constraints in Placement of Actuators

The case is specified with the following constraints on the actuator placement along the basin walls:

- Each actuator protrudes 10 cm out from the basin wall.
- The actuators shall be symmetrically placed along the basin walls.
- Cable 1 may cross Cable 2, and Cable 3 may cross Cable 4 (as in [8]). In case of cable crossing, the cables are raised or lowered by 2.5 centimetres to avoid cable collision. It is assumed that the effect that the introduced z-component of the force has on the emulated system is negligible compared to hydrostatic and hydrodynamic loads.

Mathematically, the four cable exit points $(p_{a1}, p_{a2}, p_{a3},$ and $p_{a4})$ are constrained by:

$$p_{a1} = [x_{act} \ y_{act} \ -z_c], \ p_{a2} = [x_{act} \ -y_{act} \ z_c], \tag{9a}$$

$$p_{a3} = [-x_{act} \ -y_{act} \ -z_c], \ p_{a4} = [-x_{act} \ y_{act} \ z_c], \tag{9b}$$

with,

$$(x_{act}, y_{act}) \in \bigcup_{i=1}^3 \Lambda_i, \tag{10}$$

where

$$\Lambda_1 = \{(x, 3.25) | 0 \leq x \leq 8\}, \ \Lambda_2 = \{(8, y) | -3.25 \leq y \leq 3.25\}, \ \Lambda_3 = \{(x, -3.25) | 0 \leq x \leq 8\} \tag{11}$$

and

$$z_c = \begin{cases} 0.025, & \text{if } y_{act} \leq 0 \\ 0, & \text{if } y_{act} > 0. \end{cases} \tag{12}$$

With the given constraints and symmetry considerations, there is effectively only one optimisation variable, which denotes distance along the three walls $(\Lambda_1, \Lambda_2, \Lambda_3)$, parameterised by the variable l_{pa} :

$$l_{pa} = \begin{cases} x_{act}, & \text{if } y_{act} = 3.25 & (\Lambda_1) \\ 11.25 - y_{act}, & \text{if } x_{act} = 8 & (\Lambda_2) \\ 22.5 - x_{act}, & \text{if } y_{act} = -3.25 & (\Lambda_3) \end{cases} \tag{13}$$

See also Figure 8, which outlines l_{pa} along the basin wall for Actuator 1.

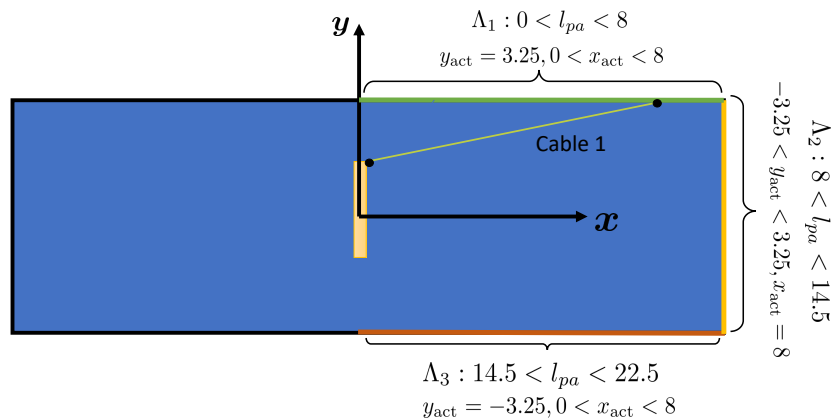


Figure 8. Moored barge in the basin, highlighting allowed placement of cable exit point for Cable 1.

4.1.3. Wrench Feasibility and Workspace Requirements

The intended use of the setup is system identification and estimation of responses to nonlinear wave loads, similar to [5]. Among the important tests for this purpose are decay tests [8], where the vessel is released from an initial offset from the mooring line equilibrium point, as shown in Figure 7. Most of the excitations are expected to be directed along the incident waves coming from the negative x-direction. Also expecting some variations in heading, the workspace requirement is specified as:

$$\mathcal{N}_{req} := \begin{cases} x^2 + 2y^2 < 3 \\ \left(-20 + 10\frac{x^2+2y^2}{3}\right)\frac{\pi}{180} \leq \psi \leq \left(20 - 10\frac{x^2+2y^2}{3}\right)\frac{\pi}{180} \end{cases} \quad (\mathcal{N}_{req,xy}) \quad (14)$$

where $\mathcal{N}_{req,xy}$ specify the workspace requirement in the x-y plane with (x,y,ψ) having units $[m, m, \text{rad}]$

The numerically calculated load vector emulates mooring forces that are expected to restore toward the mooring equilibrium $(x, y, \psi)^T = \mathbf{0}$. Taking this into account, incorporating some load vector flexibility and expecting larger loads in x-direction, the wrench feasibility requirement is specified by the following box constraints:

$$\mathcal{W}_{req}(\eta_3) := \left\{ [-12 - 2x \quad -8 - y \quad -2 - \psi]^T \leq w \leq [+12 - 2x \quad +8 - y \quad 2 - \psi]^T \right\}, \quad (15)$$

where w has units $[N,N,Nm]$.

To verify $\mathcal{N}_{req} \subseteq \mathcal{N}$, Proposition 1 is applied to each cell in the discretised workspace. See Figures 9 and 10 that demonstrate the proposition for the two platform configurations of Table 2. Figure 11 outlines \mathcal{N} for the two actuator configurations of Table 2. While both cases satisfy $\mathcal{N}_{req} \subseteq \mathcal{N}$, the cross configuration has a significantly larger wrench feasible workspace.

4.1.4. Cost Function

The designated actuators are similar to those we described in [32], and are specified with the minimum and maximum admission tensions $1[N]$ and $50[N]$, respectively.

For the cost function, we reuse (5) configured with the following parameters:

$$c_1 = 0.1, \quad c_2 = 0.1,$$

$$\alpha_i = 20 \quad f_{min,i} = 1, \quad f_{max,i} = 50, \quad f_{0,i} = 10 \quad \text{for } i = 1, 2, \dots, n.$$

Example 1. Wrench feasibility for two sample poses.

In this example Proposition 1 is applied to the two platform configurations of Table 2, given (15). In Platform configuration 1, $\mathcal{W}_{fe}(\eta_3)$ encloses all vertices (red dots), such that $\mathcal{W}_{req}(\eta_3) \subseteq \mathcal{W}_{fe}(\eta_3)$, and the pose is wrench feasible. In Platform configuration 2, three vertices (blue dots) are not enclosed by $\mathcal{W}_{fe}(\eta_3)$ such that the platform configuration is not wrench feasible. See Figure 10.

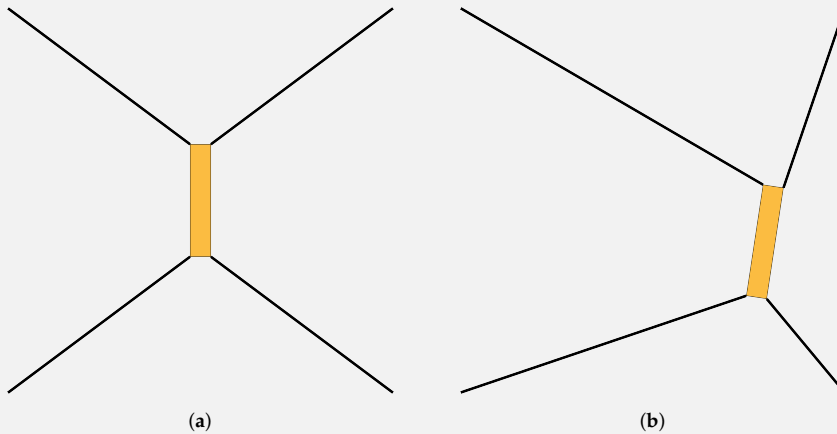


Figure 9. The platform configurations of Table 2. (a) Platform configuration 1 (b) Platform configuration 2.

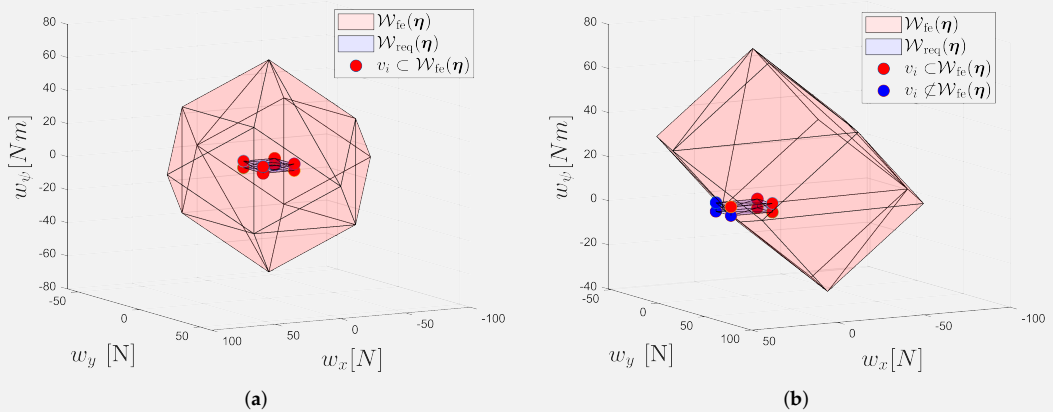


Figure 10. Box load vector requirement \mathcal{W}_{req} (blue cuboid), relative to feasible loads \mathcal{W}_{fe} (red polyhedron), given (15) for the platform configuration of Table 2. \mathcal{W}_{fe} is found by the method described in [42] and computed for illustrative purpose only. (a) Platform configuration 1. (b) Platform configuration 2.

4.1.5. Performance Measure Weights

The following performance measure weights are chosen:

$$\kappa_g = 10, \quad \kappa_1 = 5 [\kappa_x \quad \kappa_y \quad 0.5] \quad \kappa_2 = 1 [\kappa_x \quad \kappa_y \quad 0.1] \quad \kappa_3 = 0.2 [\kappa_x \quad \kappa_y \quad 0.1]. \quad (17)$$

These are determined as follows: (1) over the testing campaign, we expect the numerical variations in w_{ref} , to be about five times larger than η_3 (this is also reflected in (14) and (15)), and put a five times larger gain for κ_1 than that of κ_2 . (2) Based on experimental experience, we expect that the accuracy of the estimates $\hat{\eta}_3$ is high and that force tracking errors are more critical to performance than errors in $\hat{\eta}_3$. We therefore scale κ_3 with a

lower gain of 0.2. (3) Since $\dot{\psi}$ [rad/s] is expected to be significantly smaller in magnitude than (\dot{x}, \dot{y}) [m/s], the gains associated with changes in ψ are scaled with a gain of 0.1 (applies to κ_2 and κ_3). For similar reasons, we scale moments with gain of 0.5 relative to translational forces (applies to κ_1). We leave $\kappa_{(\cdot)}$ [1] and $\kappa_{(\cdot)}$ [2] as priority parameters κ_x and κ_y . (4) Considering that the cost function value is typically low (due to division by α^2), we set $\kappa_g = 10$, which ensures that the term has a moderately smaller impact on the global performance measure function than the other terms.

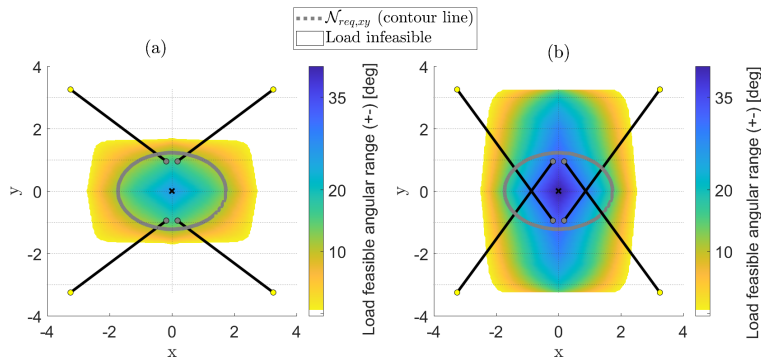


Figure 11. Visual representation of the wrench feasible workspace \mathcal{N} for the two actuator configurations of Table 2. The black lines represent cables configuration at $\eta_3 = 0$. The colour is a measure of wrench feasibility as a function of ψ (in degrees). For example, if the colour of a cell indicates a value of 20, it is wrench feasible with $-20 < \psi < 20$ [deg]. (a) Actuator configuration 1 (uncrossed). (b) Actuator configuration 2 (crossed).

For more insight, and to further support the choice of κ values, Table 3 presents the terms of (8) for the two platform configurations of Table 2 and Figure 12 shows the resulting cost terms of (8) over $\mathcal{N}_{req,xy}$ for the two actuator configurations of Table 2. Table 3 demonstrates how the terms of (8) are significantly more sensitive to rotational than translational motions—as also reflected in the chosen weights. Also, since Platform configuration 2 is farther from the centre of the workspace, it is associated with more variation in cable tensions and less controllability—resulting in significantly higher costs than in Platform configuration 1. Figure 12 shows how the cost increases toward the edges of the workspace and how the crossed configuration is associated with significantly lower costs than the uncrossed configuration. When considering Figure 12, it should be noted that constant common offsets have no effect on the optimisation procedure. Instead, the variations of each term between different platform configurations should be considered.

Table 3. Terms of (8), for the two platform configurations of Figure 9/ Table 2.

	$(\nabla_{w_{ref}[i]}(f'^*))$	$(\nabla_{w_{ref}[i]}(f'^*))$	$(\nabla_{\eta[i]}(W))f'^*$	$g(f'^*) - g(f_0)$
Platform configuration 1	$\begin{bmatrix} 0.31 & 0.42 & -0.38 \\ 0.31 & -0.42 & 0.38 \\ -0.31 & -0.42 & -0.38 \\ -0.31 & 0.42 & 0.38 \end{bmatrix}$	$\begin{bmatrix} 1.33 & 3.18 & -14.61 \\ 1.33 & -3.18 & 14.61 \\ -1.33 & -3.18 & -14.61 \\ -1.33 & 3.18 & 14.61 \end{bmatrix}$	$\begin{bmatrix} -4.26 & 0 & 0 \\ 0 & -7.62 & 0 \\ 0 & 0 & -38.32 \end{bmatrix}$	-2.3784
Platform configuration 2	$\begin{bmatrix} 1.02 & 0.39 & -1.08 \\ 0.89 & -0.6 & -0.51 \\ 0.26 & -0.36 & -1.17 \\ -0.4 & 0.1 & 0.5 \end{bmatrix}$	$\begin{bmatrix} 5.42 & 1.44 & -22.7 \\ 3.4 & -2.38 & -4.26 \\ -1.08 & -3.91 & -31.05 \\ -3.31 & 1.68 & 22.24 \end{bmatrix}$	$\begin{bmatrix} -7.81 & -1.2 & -0.15 \\ -1.2 & -5.29 & -2.95 \\ -0.15 & -2.95 & -39.31 \end{bmatrix}$	-1.9314

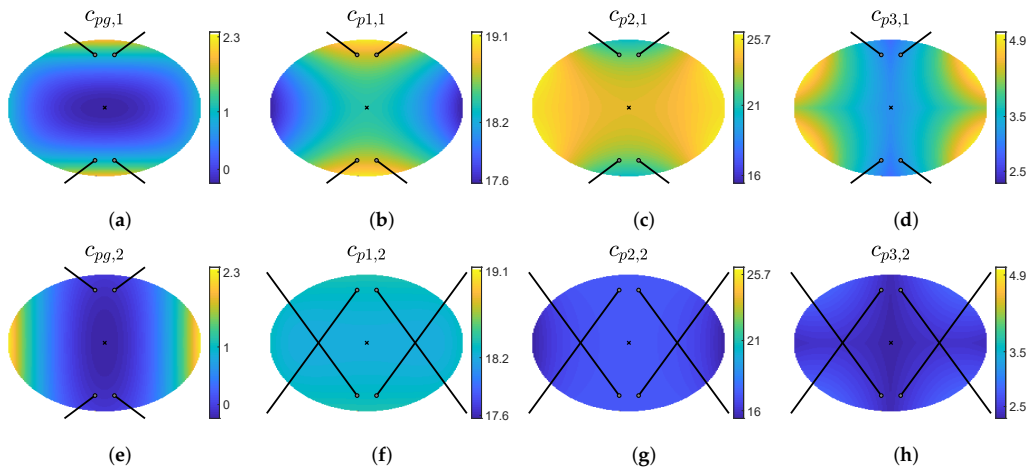


Figure 12. Cost maps for the terms of (8) for the two actuator configurations of Table 2 using (17) with $\kappa_x = 1$ and $\kappa_y = 1$. The black lines represent cables configuration at $\eta_3 = 0$. Coloured area is $N_{req,xy}$. (a–d) Actuator configuration 1. (e–h) Actuator configuration 2.

4.2. Determination of Optimal Actuator Placement

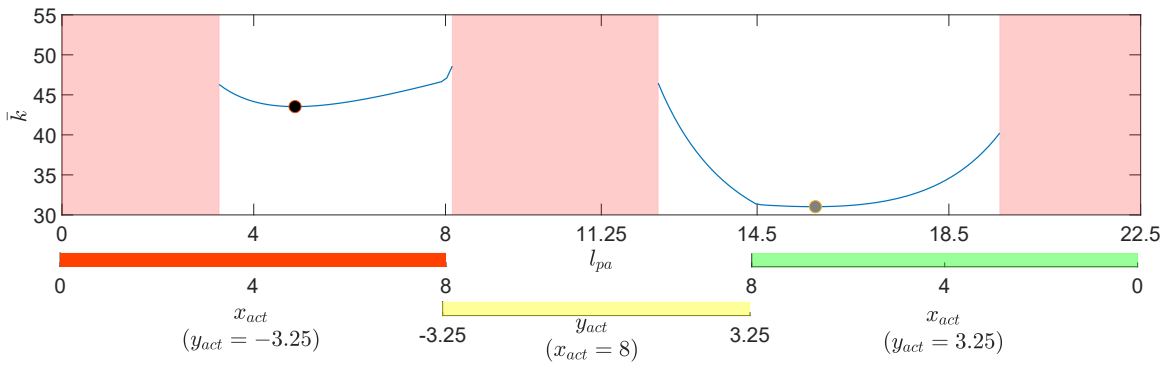
In this section, the actuator placement is determined for the given case, i.e., Procedure 1 is used with the actuator constraints given by (9)–(13), the cable cost function given by (5), the wrench feasible workspace requirements given by (14) and (15), and the performance measure weights given by (17).

The procedure is considered for three different sets of κ_x and κ_y : *Prioritisation 1*) $\kappa_x = 1$ and $\kappa_y = 1$, *Prioritisation 2*) $\kappa_x = 4$ and $\kappa_y = 1$, and *Prioritisation 3*) $\kappa_x = 1$ and $\kappa_y = 4$. Whereas *Prioritisation 1* represents a base case with equal weighting in x and y direction, *Prioritisation 2* is in line with the considered test case that expects most movement and loads to be directed in x-direction. Finally, *Prioritisation 3*, where the weight in y-direction is the highest, is included for comparison reasons.

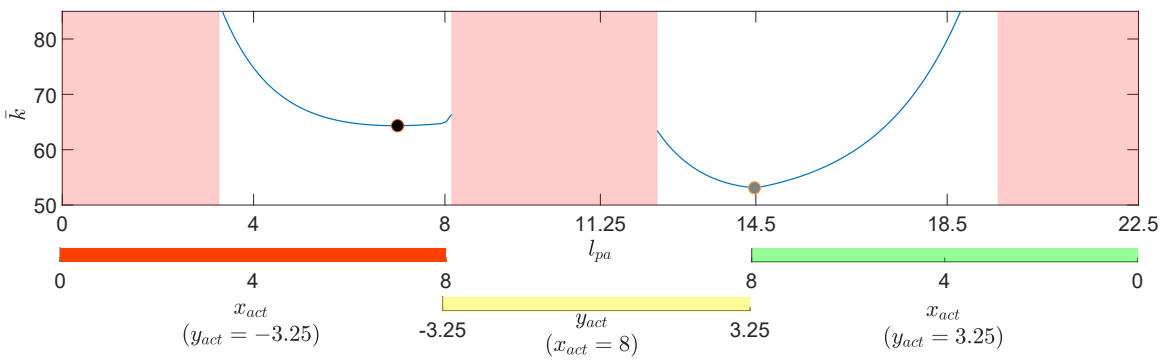
Figure 13 shows the resulting global performance measure \bar{k} as a function of l_{pa} for each of the three cases. The optimal placement is indicated in the figure both with uncrossed cable configuration (black mark) and with crossing cables (grey mark). The corresponding actuator placements are detailed in Table 4 and shown geometrically in Figure 14.

We note that for all three cases, the crossed configuration yields significantly lower cost \bar{k} – and thus represent a higher performing actuator configuration. Given the smaller basin dimensions of the test case, this can be explained by the cross-configuration enabling longer cable lengths and higher controllability. Crossed cable configuration yielding better performance is in line with previous work. See for example ([10] [Ch 8]). It also conforms with the author’s experiences with earlier testing campaigns on the experimental setup shown in Figure 3.

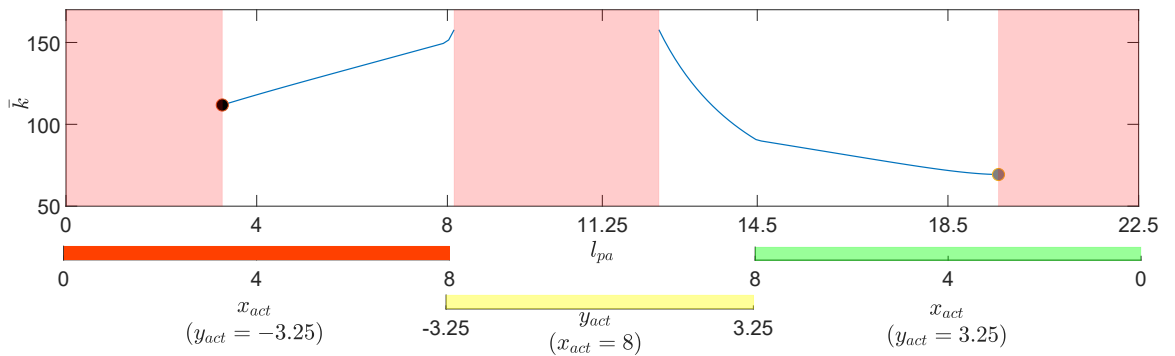
While there are multiple trade-offs, captured by the global performance measure, we observe that the procedure tends to account for the change of prioritisation by aligning the cable attack angles in the direction of the higher weighted DOF. For *Prioritisation 2*, which corresponds to the considered test case, the actuators are placed quite far in x-direction from the origin (see Figure 14b), which should allow high performance for the specified case, where most of the expected movements and loads are in the x-direction.



(a)



(b)



(c)

Figure 13. Performance measure cost function as a function of actuator placement, highlighting minimum for both crossed and uncrossed cable configuration. Cables are in crossed configuration when $l_{pa} > 11.25$ (a) $\kappa_x = 1, \kappa_y = 1$. (b) $\kappa_x = 4, \kappa_y = 1$. (c) $\kappa_x = 1, \kappa_y = 4$.

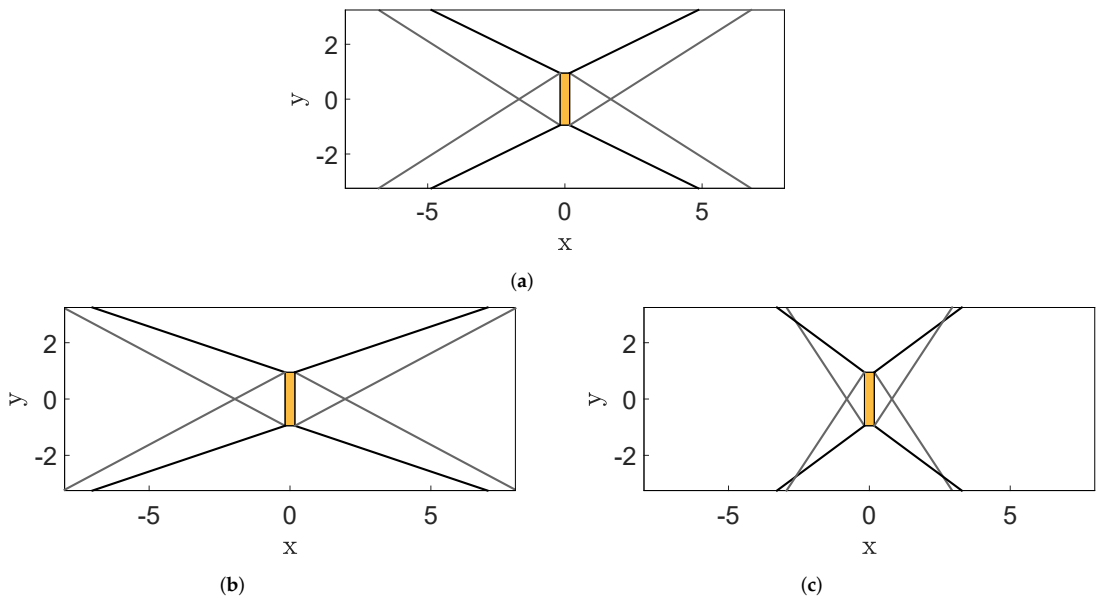


Figure 14. Resulting optimal actuator placement. Black lines are optimal placement with uncrossed cable configuration, and grey lines are optimal placement if crossed configuration is used. (a) $\kappa_x = 1, \kappa_y = 1$. (b) $\kappa_x = 4, \kappa_y = 1$. (c) $\kappa_x = 1, \kappa_y = 4$.

Table 4. Test case resulting optimal actuator placement as defined in (9).

	Uncrossed Configuration (x_{act}, y_{act})	Crossed Configuration (x_{act}, y_{act})
Prioritisation 1	(4.86, 3.25)	(6.78, -3.25)
Prioritisation 2	(7.01, 3.25)	(8, -3.22)
Prioritisation 3	(3.28, 3.25)	(2.94, -3.25)

4.3. A Delimiting Note

As discussed at a general level for CDPR setups in ([10] [Ch 8]), platform configuration performance measures are typically not complete in the sense that there is usually some ambiguity and uncertainty in the choice of performance measure design parameters. Moreover, it can be challenging to prove that the actuator placement that minimises the cost function corresponds to a practically optimal CDPR design. These considerations also apply for Procedure 1. As such, the proposed procedure should be considered to be a tool that aids the laboratory-engineer in determining actuator placement.

5. Conclusions

In this paper, we presented a procedure for placement of actuators on CDPR setups, particularly suitable for ReaTHM testing. The procedure incorporates performance measures that maximise load tracking accuracy, while ensuring that the numerically calculated loads are always applicable according to specified workspace requirements. In this sense, the present work contributes to robust and well-performing actuator placement in ReaTHM testing, for which no other such guidelines exist.

Future work on the method includes application to more complex cases, in-depth analysis of the impact that each term of (8) has on load tracking accuracy, and refinement of the guidelines for selecting the performance measure weights.

Author Contributions: Conceptualization, E.U.; methodology, E.U.; software, E.U.; validation, E.U., T.S. and R.S.; formal analysis, E.U.; investigation, E.U., T.S. and R.S.; writing—original draft

preparation, E.U.; writing–review and editing, E.U., T.S. and R.S.; visualization, E.U.; supervision, T.S. and R.S.; project administration, R.S.; funding acquisition, R.S. and T.S. All authors have read and agreed to the published version of the manuscript.

Funding: This work was supported by grant No. 254845 ReaTHM testing for Extreme Marine Environments and the Research Council of Norway through the Centre of Excellence NTNU AMOS, project no. 223254.

Institutional Review Board Statement: Not applicable.

Informed Consent Statement: Not applicable.

Data Availability Statement: Not applicable.

Conflicts of Interest: The authors declare no conflict of interest.

Abbreviations

The following abbreviations are used in this manuscript:

CDPR	Cable-driven parallel robot
ReaTHM testing *	Real-time hybrid model testing
DOF	Degrees of freedom

*ReaTHM® testing is a registered trademark of SINTEF Ocean.

Appendix A. Expression for the Terms of (8)

This section writes out the terms of (8). For conciseness, the ∇ notation denotes partial derivatives. For example $\nabla_{\eta[i]} \mathbf{W}(\eta)$ denotes $\frac{d\mathbf{W}(\eta)}{d\eta[i]}$.

As elaborated in [36], given some necessary assumptions, at the solution to (8), the following conditions are satisfied.

$$\mathbf{C}(\mathbf{z}) = \begin{bmatrix} \nabla_f g(\mathbf{f}^*) + \mathbf{W}^\top \lambda \\ \mathbf{W} \mathbf{f}^* - \mathbf{w}_{\text{ref}} \end{bmatrix} = \mathbf{0}, \text{ where } \mathbf{z} = \begin{bmatrix} \mathbf{f}^{*\top} & \lambda^\top \end{bmatrix}. \quad (\text{A1})$$

The underlying solver described in [36] finds \mathbf{z} using Newtons iterations. Once \mathbf{z} is found, it is numerically cheap to find the terms of (8) as outlined next.

The partial derivative of \mathbf{z} with respect a parameter p is

$$\frac{\partial \mathbf{z}}{\partial p} = - \left(\frac{\partial \mathbf{C}}{\partial \mathbf{z}} \right)^{-1} \frac{\partial \mathbf{C}}{\partial p} = \mathbf{H}^{-1} \frac{\partial \mathbf{C}}{\partial p}, \text{ where } \mathbf{H} = \begin{bmatrix} \nabla_f^2 g(\mathbf{f}) & \mathbf{W}^\top \\ \mathbf{W} & \mathbf{0} \end{bmatrix}. \quad (\text{A2})$$

Furthermore, the partial derivatives of \mathbf{R} with respect to $\mathbf{w}_{\text{ref}}[i]$ and $\eta[i]$ is

$$\frac{\partial \mathbf{C}}{\partial \mathbf{w}_{\text{ref}}[i]} = \begin{bmatrix} \mathbf{0} \in \mathbb{R}^{n \times 1} \\ -\mathbf{d}_i \in \mathbb{R}^{m \times 1} \end{bmatrix}, \quad \frac{\partial \mathbf{C}}{\partial \eta[i]} = \begin{bmatrix} \nabla_{\eta[i]} (\mathbf{W}^\top(\eta)) \lambda \\ \nabla_{\eta[i]} (\mathbf{W}(\eta)) \mathbf{f}^* \end{bmatrix}, \quad (\text{A3})$$

where $\mathbf{d}_i \in \mathbb{R}^m$ is a vector that has all zero-entries except the i th entry which equals -1 and

$$\nabla_{\eta[i]} \mathbf{W}(\eta) = \begin{bmatrix} \nabla_{\eta[i]} j_1 & \nabla_{\eta[i]} j_2 & \dots & \nabla_{\eta[i]} j_n \end{bmatrix}, \text{ with } \nabla_{\eta[i]} j_i = \begin{bmatrix} \nabla_{\eta[i]}(\mathbf{u}_i) \\ \mathbf{r}_i^a \times \nabla_{\eta[i]}(\mathbf{u}_i) + \nabla_{\eta[i]}(\mathbf{r}_i^a) \times \mathbf{u}_i \end{bmatrix}. \quad (\text{A4})$$

The components of (A4), written out for each i in $\eta[i]$ are

$$\nabla_x \mathbf{r}_i^a = \mathbf{0}, \quad \nabla_y \mathbf{r}_i^a = \mathbf{0}, \quad \nabla_z \mathbf{r}_i^a = \mathbf{0}, \quad \nabla_\theta \mathbf{r}_i^a = \mathbf{R}_z(\psi) \mathbf{R}_y(\phi) \mathbf{R}_x(\theta) \mathbf{S}_x \mathbf{r}_i^b \quad (\text{A5a})$$

$$\nabla_\phi \mathbf{r}_i^a = \mathbf{R}_z(\psi) \mathbf{R}_y(\phi) \mathbf{S}_y \mathbf{R}_x(\theta) \mathbf{r}_i^b, \quad \nabla_\psi \mathbf{r}_i^a = \mathbf{R}_z(\psi) \mathbf{S}_z \mathbf{R}_y(\phi) \mathbf{R}_x(\theta) \mathbf{r}_i^b \quad (\text{A5b})$$

$$\nabla_x \mathbf{u}_i = (1/l_{c,i}^3) [(-\Delta y^2 - \Delta z^2) \quad (\Delta x \Delta y) \quad (\Delta x \Delta z)]^\top \quad (\text{A5c})$$

$$\nabla_y \mathbf{u}_i = (1/l_{c,i}^3) [(\Delta x \Delta y) \quad (-\Delta x^2 - \Delta z^2) \quad (\Delta y \Delta z)]^\top \quad (\text{A5d})$$

$$\nabla_z \mathbf{u}_i = (1/l_{c,i}^3) [(\Delta x \Delta z) \quad (\Delta y \Delta z) \quad (-\Delta x^2 - \Delta y^2)]^T \tag{A5e}$$

$$\nabla_{\theta} \mathbf{u}_i = [\nabla_x \mathbf{u}_i \quad \nabla_y \mathbf{u}_i \quad \nabla_z \mathbf{u}_i] [\nabla_{\theta}(\mathbf{r})] \tag{A5f}$$

$$\nabla_{\phi} \mathbf{u}_i = [\nabla_x \mathbf{u}_i \quad \nabla_y \mathbf{u}_i \quad \nabla_z \mathbf{u}_i] [\nabla_{\phi}(\mathbf{r})] \tag{A5g}$$

$$\nabla_{\psi} \mathbf{u}_i = [\nabla_x \mathbf{u}_i \quad \nabla_y \mathbf{u}_i \quad \nabla_z \mathbf{u}_i] [\nabla_{\psi}(\mathbf{r})], \tag{A5h}$$

$$\text{where } S_x = \begin{bmatrix} 0 & 0 & 0 \\ 0 & 0 & -1 \\ 0 & 1 & 0 \end{bmatrix}, S_y = \begin{bmatrix} 0 & 0 & 1 \\ 0 & 0 & 0 \\ -1 & 0 & 0 \end{bmatrix}, S_z = \begin{bmatrix} 0 & -1 & 0 \\ 1 & 0 & 0 \\ 0 & 0 & 0 \end{bmatrix},$$

$$[\Delta x \quad \Delta y \quad \Delta z]^T = (\mathbf{p}_{ai} - \mathbf{p}_{ei}), \text{ and } l_{c,i} = |\mathbf{p}_{ai} - \mathbf{p}_{ei}|_2.$$

The first term of (8) is given directly by the cost function, whereas inserting (A3) into (A2) and substituting p with $w_{ref}[i]$ and $\eta[i]$ gives the second and third term of (8), respectively. Finally, the last term of (8) is found using (A4) directly.

As (A5)(a–h) indicates, larger basins and cable distances, tend to reduce the cost c_p . This is especially the case for c_{p2} and c_{p3} , as evident by the factor $1/l_{c,i}^3$ in (A5)(a–h). In cases where longer cable length is expected to have detrimental effects, this can be accounted for in the cost function.

References

- Sauder, T. Fidelity of Cyber-Physical Empirical Methods: A Control System Perspective. In *Experimental Techniques*; Springer: Berlin/Heidelberg, Germany, 2020; pp. 1–17.
- Chabaud, V. Real-Time Hybrid Model Testing of Floating Wind Turbines. Ph.D. Thesis, Norwegian University of Science and Technology, Trondheim, Norway, 2016.
- Sauder, T.; Chabaud, V.; Thys, M.; Bachynski, E.E.; Sæther, L.O. Real-time hybrid model testing of a braceless semi-submersible wind turbine: Part I—The hybrid approach. In Proceedings of the ASME 2016 35th International Conference on Ocean, Offshore and Arctic Engineering. American Society of Mechanical Engineers Digital Collection, Busan, Korea, 19–24 June 2016.
- Chakrabarti, S. Physical model testing of floating offshore structures. In Proceedings of the Dynamic Positioning Conference, Citeseer, Houston, USA, 13–14 October 1998.
- Sauder, T.; Tahchiev, G. From soft mooring to active positioning in laboratory experiments. In Proceedings of the 39th International Conference on Ocean, Offshore and Arctic Engineering. American Society of Mechanical Engineers Digital Collection, Virtual, Online, 3–7 August 2020.
- Vilsen, S.A.; Sauder, T.; Sørensen, A.J.; Føre, M. Method for Real-Time Hybrid Model Testing of ocean structures: Case study on horizontal mooring systems. *Ocean. Eng.* **2019**, *172*, 46–58.
- Chabaud, V.B.; Eliassen, L.; Thys, M.; Sauder, T.M. Multiple-degree-of-freedom actuation of rotor loads in model testing of floating wind turbines using cable-driven parallel robots. *J. Phys. Conf. Ser.* **2018**, *1104*, 012021.
- Ueland, E.S.; Skjetne, R.; Vilsen, S.A. Force Actuated Real-Time Hybrid Model Testing of a Moored Vessel: A Case Study Investigating Force Errors. *FAC-PapersOnLine* **2018**, *51*, 74–79.
- Gosselin, C.; Grenier, M. On the determination of the force distribution in overconstrained cable-driven parallel mechanisms. *Meccanica* **2011**, *46*, 3–15.
- Pott, A. *Cable-Driven Parallel Robots: Theory and Application*; Springer: Berlin/Heidelberg, Germany, 2018.
- Rodnunsky, J.; Bayliss, T. Aerial Cableway and Method for Filming Subjects in Motion. U.S. Patent 5,224,426, 6 July 1993.
- Pott, A.; Mütterich, H.; Kraus, W.; Schmidt, V.; Miermeister, P.; Verl, A. IPAnema: A family of cable-driven parallel robots for industrial applications. In *Cable-Driven Parallel Robots*; Springer: Berlin/Heidelberg, Germany, 2013.
- Newman, M.; Zygjelbaum, A.; Terry, B. Static analysis and dimensional optimization of a cable-driven parallel robot. In *Cable-Driven Parallel Robots*; Springer: Berlin/Heidelberg, Germany, 2018.
- Horoub, M.; Hawwa, M. Influence of cables layout on the dynamic workspace of a six-DOF parallel marine manipulator. *Mech. Mach. Theory* **2018**, *129*, 191–201.
- Kraus, W.; Schmidt, V.; Rajendra, P.; Pott, A. System identification and cable force control for a cable-driven parallel robot with industrial servo drives. In Proceedings of the 2014 IEEE International Conference on Robotics and Automation (ICRA), Hong Kong, China, 31 May–7 June 2014.
- Oh, S.R.; Agrawal, S.K. Cable suspended planar robots with redundant cables: Controllers with positive tensions. *IEEE Trans. Robot.* **2005**, *21*, 457–465.
- Lamaury, J.; Gouttefarde, M. A tension distribution method with improved computational efficiency. In *CDPRs*; Springer: Berlin/Heidelberg, Germany, 2013.
- Rushton, M.; Khajepour, A. Optimal actuator placement for vibration control of a planar cable-driven robotic manipulator. In Proceedings of the 2016 American Control Conference (ACC), Boston, MA, USA, 6–8 July 2016.
- Kim, Y.; Junkins, J.L. Measure of controllability for actuator placement. *J. Guid. Control. Dyn.* **1991**, *14*, 895–902.

20. Pusey, J.; Fattah, A.; Agrawal, S.; Messina, E. Design and workspace analysis of a 6–6 cable-suspended parallel robot. *Mech. Mach. Theory* **2004**, *39*, 761–778.
21. Aref, M.M.; Taghirad, H.D.; Barissi, S. Optimal design of dexterous cable driven parallel manipulators. *Int. J. Robot.* **2009**, *1*, 29–47.
22. Abdolshah, S.; Zanotto, D.; Rosati, G.; Agrawal, S.K. Optimizing stiffness and dexterity of planar adaptive cable-driven parallel robots. *J. Mech. Robot.* **2017**, *9*, 031004.
23. Anson, M.; Alamdari, A.; Krovi, V. Orientation workspace and stiffness optimization of cable-driven parallel manipulators with base mobility. *J. Mech. Robot.* **2017**, *9*, 031011.
24. Jamshidifar, H.; Khajepour, A.; Fidan, B.; Rushton, M. Kinematically-constrained redundant cable-driven parallel robots: modeling, redundancy analysis, and stiffness optimization. *IEEE/ASME Trans. Mechatron.* **2016**, *22*, 921–930.
25. Ouyang, B.; Shang, W. Wrench-feasible workspace based optimization of the fixed and moving platforms for cable-driven parallel manipulators. *Robot. Comput. Integr. Manuf.* **2014**, *30*, 629–635.
26. Song, D.; Zhang, L.; Xue, F. Configuration optimization and a tension distribution algorithm for cable-driven parallel robots. *IEEE Access* **2018**, *6*, 33928–33940.
27. Azizian, K.; Cardou, P. The dimensional synthesis of planar parallel cable-driven mechanisms through convex relaxations. *J. Mech. Robot.* **2012**, *4*, 031011.
28. Bryson, J.T.; Jin, X.; Agrawal, S.K. Optimal design of cable-driven manipulators using particle swarm optimization. *J. Mech. Robot.* **2016**, *8*, 041003.
29. Gouttefarde, M.; Collard, J.F.; Riehl, N.; Baradat, C. Geometry selection of a redundantly actuated cable-suspended parallel robot. *IEEE Trans. Robot.* **2015**, *31*, 501–510.
30. Sauder, T.; Marelli, S.; Sørensen, A.J. Probabilistic robust design of control systems for high-fidelity cyber-physical testing. *Automatica* **2019**, *101*, 111–119.
31. Sauder, T.; Marelli, S.; Larsen, K.; Sørensen, A.J. Active truncation of slender marine structures: Influence of the control system on fidelity. *Appl. Ocean. Res.* **2018**, *74*, 154–169.
32. Ueland, E.; Sauder, T.; Skjetne, R. Force Tracking Using Actuated Winches with Position Controlled Motors for Use in Hydrodynamic Model Testing. *IEEE Access* **2021**, submitted for publication.
33. Hussein, H.; Santos, J.C.; Gouttefarde, M. Geometric optimization of a large scale CDPR operating on a building facade. In Proceedings of the 2018 IEEE/RSJ International Conference on Intelligent Robots and Systems (IROS), Madrid, Spain, 1–5 October 2018.
34. Robohub/Max Planck Institute for Biological Cybernetics. Cable-Driven Parallel Robots: Motion Simulation in a New Dimension. Available online: <https://robohub.org/cable-driven-parallel-robots-motion-simulation-in-a-new-dimension> (accessed on 15 May 2020).
35. Fraunhofer IPA. Cable-Driven Parallel Robots. Available online: <https://www.ipa.fraunhofer.de/en/expertise/robot-and-assistive-systems/intralogistics-and-material-flow/cable-driven-parallel-robot.html> (accessed on 4 January 2021).
36. Ueland, E.; Sauder, T.; Skjetne, R. Optimal Force Allocation for Overconstrained Cable-Driven Parallel Robots: Continuously Differentiable Solutions With Assessment of Computational Efficiency. *IEEE Trans. Robot.* **2020**, doi:10.1109/TRO.2020.3020747.
37. Fossen, T.I. *Handbook of Marine Craft Hydrodynamics and Motion Control*; John Wiley & Sons: Hoboken, NJ, USA, 2011.
38. Ebert-Uphoff, I.; Voglewede, P.A. On the connections between cable-driven robots, parallel manipulators and grasping. In Proceedings of the IEEE International Conference on Robotics and Automation (ICRA '04), New Orleans, LA, USA, 26 April–1 May 2004.
39. Bosscher, P.M. Disturbance Robustness Measures and Wrench-Feasible Workspace Generation Techniques for Cable-driven Robots. Ph.D. Thesis, Georgia Institute of Technology, Atlanta, GA, USA, 2004.
40. Gouttefarde, M.; Daney, D.; Merlet, J.P. Interval-analysis-based determination of the wrench-feasible workspace of parallel cable-driven robots. *IEEE Trans. Robot.* **2011**, *27*, 1–13.
41. Bosscher, P.; Riechel, A.T.; Ebert-Uphoff, I. Wrench-feasible workspace generation for cable-driven robots. *IEEE Trans. Robot.* **2006**, *22*, 890–902.
42. Bouchard, S.; Gosselin, C.; Moore, B. On the ability of a cable-driven robot to generate a prescribed set of wrenches. *J. Mech. Robot.* **2010**, *2*, 011010.
43. Gouttefarde, M.; Krut, S. Characterization of parallel manipulator available wrench set facets. In *Advances in Robot Kinematics: Motion in Man and Machine*; Springer: Berlin/Heidelberg, Germany, 2010; pp. 475–482.
44. Lahouar, S.; Ottaviano, E.; Zeghoul, S.; Romdhane, L.; Ceccarelli, M. Collision free path-planning for cable-driven parallel robots. *Robot. Auton. Syst.* **2009**, *57*, 1083–1093.
45. Perreault, S.; Cardou, P.; Gosselin, C.M.; Otis, M.J.D. Geometric determination of the interference-free constant-orientation workspace of parallel cable-driven mechanisms. *J. Mech. Robot.* **2010**, *2*, 031016.
46. Nguyen, D.Q.; Gouttefarde, M. On the improvement of cable collision detection algorithms. In *Cable-Driven Parallel Robots*; Springer: Berlin/Heidelberg, Germany, 2015.
47. Sunday, D. Distance between 3D Lines and Segments. Available online: https://geomalgorithms.com/a07-_distance.html (accessed on 15 May 2020).
48. Bolboli, J.; Khosravi, M.A.; Abdollahi, F. Stiffness feasible workspace of cable-driven parallel robots with application to optimal design of a planar cable robot. *Robot. Auton. Syst.* **2019**, *114*, 19–28.

49. Gouttefarde, M.; Lamaury, J.; Reichert, C.; Bruckmann, T. A Versatile Tension Distribution Algorithm for n -DOF Parallel Robots Driven by $n + 2$ Cables. *IEEE Trans. Robot.* **2015**, *31*, 1444–1457.
50. Bachynski, E.E.; Chabaud, V.; Sauder, T. Real-time hybrid model testing of floating wind turbines: Sensitivity to limited actuation. *Energy Procedia* **2015**, *80*, 2–12.
51. Vilsen, S.A.; Sauder, T.; Sørensen, A.J. Real-Time Hybrid Model Testing of Moored Floating Structures Using Nonlinear Finite Element Simulations. In *Dynamics of Coupled Structures*; Springer: Berlin/Heidelberg, Germany, 2017; Volume 4.

Article 5 – J-3
**Force Tracking using Actuated Winches with
Position-controlled Motors for use in Hydrodynamical
Model Testing**

Einar S. Ueland, Thomas Sauder, Roger Skjetne
IEEE Access [10.1109/ACCESS.2021.3083539](https://doi.org/10.1109/ACCESS.2021.3083539)

Received April 19, 2021, accepted May 10, 2021. Date of publication xxxx 00, 0000, date of current version xxxx 00, 0000.

Digital Object Identifier 10.1109/ACCESS.2021.3083539

Force Tracking Using Actuated Winches With Position-Controlled Motors for Use in Hydrodynamical Model Testing

EINAR UELAND¹, THOMAS SAUDER^{1,2}, AND ROGER SKJETNE¹, (Senior Member, IEEE)

¹Centre for Autonomous Marine Operations and Systems (AMOS), Department of Marine Technology, Norwegian University of Science and Technology (NTNU), 7491 Trondheim, Norway

²SINTEF Ocean, 7465 Trondheim, Norway

Corresponding author: Einar Ueland (einar.s.ueland@gmail.com)

This work was supported in part by the Research Council of Norway (RCN) Real-Time Hybrid Model Testing for Extreme Marine Environments under Grant 254845, and in part by the Centre of Excellence NTNU AMOS, RCN Project, under Grant 223254.

ABSTRACT In this paper, we consider the problem of accurate force control using actuated winches, intended for use in real-time hybrid hydrodynamic model testing. The paper is also relevant to other cable-driven parallel robot applications that use force control in an inner control loop. For this problem, conventional strategies typically use actuated winches with torque-controlled servomotors directly connected to the cabled drum. In contrast, we propose using actuated winches with position-controlled servomotors that connect to the cabled drum via a clockspring. The servomotors are position controlled at drive-level and are rapid, accurate, robust, and simple to install. We show how this, combined with an accurate estimate of the clockspring deflection and stiffness, can yield fast and precise force tracking on moving objects. This includes proposing associated feedforward force-controllers that compensates for damping, angle-dependent force variations, delays, and non-constant clockspring characteristics. Extensive experimental testing on a 1 degree of freedom actuated mass-spring system supports the work.

INDEX TERMS Actuated winches, cable-driven parallel robots, force tracking, force control, hydrodynamic model testing, real-time hybrid model testing.

I. INTRODUCTION

Accurate force control using actuated winches equipped with servomotors is a key problem for cable-driven parallel robots (CDPR) that use cable force control [1]–[3]. The prime motivation of this paper is real-time hybrid model testing [4], [5], in which complex ocean structures are emulated by combining numerical models with traditional hydrodynamic model testing; see Figure 1. In such a setting, the structure under study is partitioned into a numerical substructure and a physical substructure that are coupled through real-time measurement and load control interfaces; see Figure 2. We refer to these as the kinematic interface (measurements and estimation of kinematic variables) and the kinetic interface (actuation of forces). The numerically calculated reference load vector is applied on the physical substructure through actuated winches, such that the resulting experimental

The associate editor coordinating the review of this manuscript and approving it for publication was Giambattista Gruosso ¹.

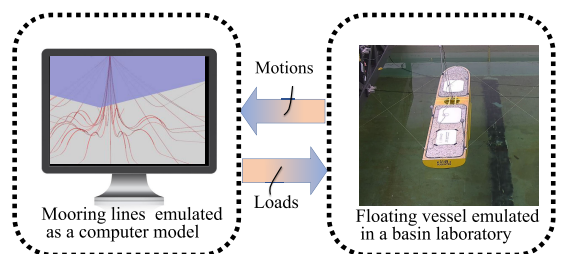


FIGURE 1. Real time hybrid model testing of a moored ship. Notice the four cables used to impose the numerically calculated mooring loads on the ship.

platform becomes a type of CDPR. Significant platform motions are expected throughout a typical testing campaign. Precisely applying the reference loads onto the marine platform, despite significant end-effector motions, is important to achieve high fidelity and to accurately emulate the behaviour

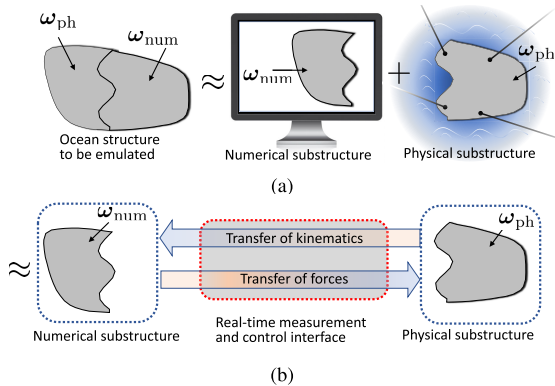


FIGURE 2. Real time hybrid model testing. $\omega_{(i)}$ represents environmental forces acting on the structure. (a) Partitioning of a target structure. (b) The recoupled system emulating the target ocean structure.

of the non-substructured ocean structure [6], [7]. See [8] for a discussion on CDRP used for real-time hydrodynamic model testing in relation to other typical CDRP applications.

For force control with actuated winches, the servomotor is typically controlled in *torque mode* [9, ch 6] by altering the motor current. In this paper, we consider the less studied strategy of force control using position-controlled servomotors [2], [10], [11]. Assuming compliance in the actuator transmission system, the resulting force will, in this case, be a function of the transmission system deflection and stiffness. This enables the use of industrial servomotors with integrated internal encoders, drive-level position-control, and associated electronics. These are easy to install, allow high bandwidth, are rapid and accurate, and have robust internal control software. With good knowledge of the deflection and stiffness of the actuator transmission system, this can yield robust and accurate force control properties. A challenge, however, is that the actuator needs to compensate for the dynamic motion of the end effector, to keep the transmission system deflection at the target values. To achieve this, an accurate real-time position estimate, delay compensation, and fast motor reaction are useful to limit the transient disturbances. In this paper, we handle delays using polynomial prediction, which is convenient due to the short delays, frequent sampling, and not relying on a dynamic model of the end-effector trajectories. An alternative approach would be to use model-based prediction methods as described in [12, Ch 5].

In earlier works considering force control using position-controlled servomotors [2], [11], the actuator transmission system has typically been defined between the two endpoints of the stretched cable, with stiffness being the specific cable stiffness over cable length. This causes challenges for feedforward control purposes because: 1) the elongation to force relationship in synthetic cables is nonlinear and hysteretic [2], and 2) the end effector position needs to be accurately measured or estimated. Reference [11] proposes to estimate the

end effector position using a camera system, whereas [2] uses forward/inverse kinematics to estimate the pose (and thus end effector positions). In this paper, we apply a clockspring between the motor shaft and the drum, as well as rotational encoders for accurate angular position measurements, to overcome the two aforementioned challenges. The resulting actuators have been developed by the research team over time, where the works [4], [6], [13] use earlier iterations of the same type of actuators. Although the basic design idea behind the actuator is simple, we have not managed to find similar designs reported in the CDRP literature.

Good models of the actuators are advantageous for accurate force control. The cable is typically made of polymer with a high strength to weight characteristic [14]. This is modelled as a linear spring in [15] and by nonlinear cable models in [10]. The drum may be modelled using friction, damping, and inertia models [1], [16]. Effects such as ovalization, manufacturing accuracy, and uneven cable settling cause time, force, and angle-dependent variations in the drum effective radius [17]. Other effects often considered (which are not relevant in this paper) include effects associated with cable guides and motor gearboxes [3]. Several authors compensate for drum friction, damping, or drum-inertia in the cable force controller [1], [3], [16], [18]. In practice, compensation of inertia forces may be challenging due to inaccurate acceleration feedback [3].

The actuator and control designs depend on application-specific requirements, such as precision, expected bandwidth, force rates, accelerations, and expected tension levels. The latter can vary dramatically depending on the application [19]–[21]. In this paper, we focus on lower tension levels of 2 N to 15 N, accuracies in the range of 0.2 N, and bandwidth up to 1.4 Hz, intended for use in high accuracy real-time hybrid model testing.

Force sensors can either be integrated as part of the winch/drum system [1], [22] or attached directly at or near the end effector [6], [20], [23], [24]. As discussed in [16], advantages with the former include stationary force sensors, whereas the latter has the highest precision since the force measurements intrinsically capture pulley and cable force-effects. The force measurements can be used in some combination of proportional-integral-derivative (PID) feedback [2], [3], [25].

In this paper, we design and demonstrate a force actuation system based on a position-controlled servomotor fitted with a clockspring, a drum, and a force sensor at the end effector. Moreover, we propose a feedforward force control term based on an online estimate of the clockspring characteristics to handle time-dependent changes of the spring parameters. Methods are further presented to compensate for damping, angle-dependent force variations, and time delays, which, unless compensated for, introduce force errors that correlate with end effector motions. Finally, extensive experimental results are presented to support the research. While the general purpose of the research is to improve force control in real-time hybrid model testing, the results should

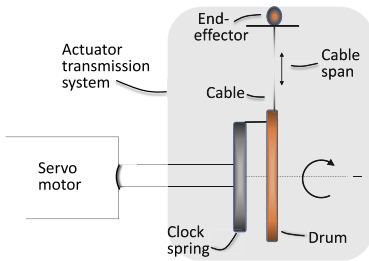


FIGURE 3. Schematic overview of actuator setup.

also be applicable to other CDPR setups that use force control.

II. FORCE TRACKING PROBLEM STATEMENT

A. FORCE ACTUATION SYSTEM DESIGN AND MODELLING

The actuators used in this paper are integrated servomotors controlled in position mode, where the motor shaft is connected to a cable drum via a clockspring, as illustrated in Figure 3. This has several advantages, such as: 1) it reduces the transmission stiffness such that the resulting force is less sensitive to end effector motions, 2) it increases compliance that hinders antagonistic actuator behaviour [26], 3) the rotational encoders measure the deflection of the actuator transmission system with high accuracy (which is useful for position feedforward purposes), and 4) the clockspring has close to linear force to deflection properties (which is useful for force feedforward purposes). We next describe each component of the system, including its modelling, in detail. This model is useful for the subsequent feedforward control design and as a reference for further studies employing similar setups and strategies.

1) SERVO MOTOR

Due to the internal dynamics of the motor, there is a transient phase between the commanded shaft angle θ_c and the resulting shaft angle θ_s . In the Laplace-domain this can conveniently be modelled as a combination of a pure time delay $e^{-\tau_{cs}s}$ and a transfer function $h(s)$ according to

$$\frac{\theta_s(s)}{\theta_c(s)} = H(s) := h(s)e^{-\tau_{cs}s} \quad (1)$$

For servomotors in closed-loop position-control, [27, Ch. 3.5] suggests using a second-order process to model $h(s)$.

In our setup, for the frequencies of interest, we consistently find the transient phase to be well approximated by a pure delay, as shown in Figure 4, so that $h(s) = 1$ and $H(s) = e^{-\tau_{cs}s}$. An underlying assumption here is that the commanded motor-shaft trajectories are always within the servomotor's capabilities such that the motor dynamics is well described by a pure delay. Due to the high-performance of the industrial servomotor used (see Figure 4), this is in practice not a very restrictive assumption for our use-cases.

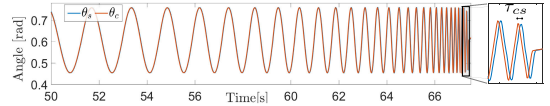


FIGURE 4. Harmonic sweep test. Commanded shaft angle θ_c versus achieved shaft angle θ_s .

2) CABLE DRUM

The drum has cable wound in multiple layers with the cable being free to wind onto any part of the drum-track. A ball bearing is used between the drum and its axis of rotation. θ_w denotes the drum's angular position. θ_w , θ_c , and θ_s are all defined positive in the direction that winds the cable onto the drum.

An important drum parameter is the effective radius r , which is the distance from the drum centre of rotation to the attack point of the tensioned cable, as illustrated in Figure 5. This is modelled as

$$r = r_0 + k_r \theta_w + \delta_f + \delta_s, \quad (2)$$

where r_0 is the radius at initialization ($\theta_w = 0$), and $k_r \theta_w$ represents the change of cable-layer thickness due to spooling. Here, $k_r = d_c / (2\pi n_w)$, where d_c is the cable-layer thickness, and n_w is the average number of parallel cables per cable-layer. δ_s is an unmodelled radius uncertainty, dependent on how the cable settled as it was wound in, and δ_f is a force-dependent radius uncertainty. The latter is due to reshaping/tightening of the cable-layers and the fact that the cable tends to dig itself into the cable-layers under tension.

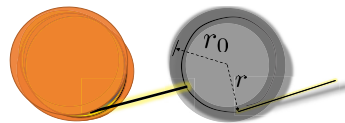


FIGURE 5. Drum from the side, illustrating the effective radius.

I_{wd} denotes the drum inertia. For simplicity, we lump all damping (mainly due to bearing, encoder, and cable friction) into two components: $c_w \dot{\theta}_w + c_s \text{sgn}(\dot{\theta}_w)$. A more detailed model could, for example, include force-dependent cable friction as well as the Dahl model [16] for bearing friction.

3) CLOCKSING

The clockspring is a flat spiral spring that has its inner end fixed to the motor shaft and the outer end fixed to the drum. We model the spring characteristics by the mapping $m_1 = k_\theta(\tilde{\theta})$, where m_1 is the resulting moment, and $\tilde{\theta} = \theta_s - \theta_w - \theta_0$ is the spring deflection. Here, θ_0 is the equilibrium offset such that $k_\theta(\tilde{\theta}) = 0$ when $m_1 = 0$.

The coils of the clockspring are assumed not to touch under compression. By design, this results in low friction and close to linear deflection to moment characteristics: $m_1 \approx k_\theta \tilde{\theta}$.

I_s denotes the clockspring inertia. We model a weight-induced moment $m_g(\theta_w, \theta_s) \approx m_g(\theta_w)$ due to the non-symmetric mass distribution of the clockspring.

Depending on the spring properties, the clockspring characteristics (θ_0 and k_θ) may be slowly varying with time and under stress due to factors such as material creep, material deformations, and material warm up.

4) CABLE

The cable is a thin braided polymer line, mass-produced for high-performance fishing applications. We model the stretched cable length as:

$$l_w = l_0 + \Delta l_w + \Delta l_c, \quad (3)$$

where l_0 is the initial cable length, Δl_w is the unwound cable length, and Δl_c is the elongation of the cable due to stretching.

The change in cable length due to spooling is modelled as $\Delta l_w = -r_0\theta_w - 0.5 k_r\theta_w^2 + \zeta_s + \zeta_f$ where ζ_s is an uncertainty due to uneven settling of the cable (dependent on the spooling-tension history of the cable) and ζ_f is a force-dependent uncertainty (similarly to δ_f , more cable length is pulled out under tension). The cable elongation is modelled as: $\Delta l_c = \zeta_k + \zeta_c$, where ζ_k is a force-dependent elongation, often modelled by Hook's law ($\zeta_k = fl_w/k_0$), and ζ_c is the cable creep [28].

We assume that both transverse and axial cable vibrations have a negligible effect on both the drum angle θ_w and on the applied force. This assumption is consistent with experimental experience and is reasonable due to 1) the high cable stiffness relative to the drum mass (little axial vibrations), and 2) the low mass of the cable relative to its tension ensures that it tends to form a straight line and not vibrate transversely.

5) END EFFECTOR AND MEASUREMENTS

The end effector consists of the cable attached to an electrically wired strain gauge, itself attached to the platform. The resulting force measurements are, in general, subject to bias and noise, but not at a level that is significant for the present application.

B. ACTUATOR FORCE MODEL

We assume that the stretched cable is mass-less, such that the force on the end effector is equal to the force in the drum-end of the stretched cable. This means that cable elongation effects (such as creep) do not affect the force model, and the end effector force can conveniently be modelled based on the motor-shaft, clockspring, and drum configuration. Combining the model for each component seen in Figure 6, we get the end effector force,

$$f = \frac{1}{r} \left(\underbrace{k_\theta \tilde{\theta}}_{m_1} + m_2(\theta_w) - \underbrace{(I_w \ddot{\theta}_w + c_w \dot{\theta}_w + c_s \text{sgn}(\dot{\theta}_w))}_{m_3} + m_4 \right) \quad (4)$$

where we have separated between: m_1 - the dominating static restoring term, m_2 - the angle-dependent moment variations

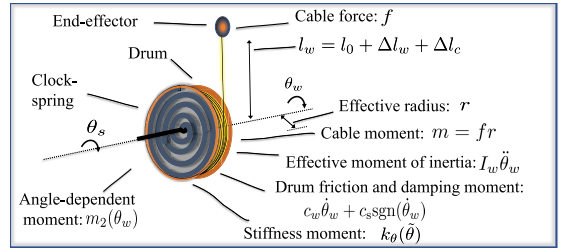


FIGURE 6. Actuator transmission system modelling.

(including m_g), m_3 - the transmission system damping and inertia, and m_4 - the lumped unmodelled disturbances and uncertainties such as, clockspring dynamics, inertia, and non-linear effects. The term $I_w \ddot{\theta}_w$ is the effective moment induced by inertial effects, which in addition to the drum inertia I_{wd} and the clockspring inertia I_s includes inertia effects from the layered cable.

For simplicity, we transform moments to forces using the subscript $(\cdot)_r$ to mean $\frac{(\cdot)}{r}$:

$$f = k_{\theta,r} \tilde{\theta} - (I_{w,r} \ddot{\theta}_w + c_{w,r} \dot{\theta}_w + c_{s,r} \text{sgn}(\dot{\theta}_w)) + f_2(\theta_w) + f_4, \quad (5)$$

where $f_2(\theta_w) = m_2(\theta_w)/r$ and $f_4 = m_4/r$.

We emphasise that even small variations of r can have a significant effect on the force (in our case $r_0 = 60\text{mm}$, such that a 0.6mm change in r corresponds to about 1 percent change in applied force).

C. CONTROL LOOPS AND CONTROL PROBLEM

CDPR control systems that use force control typically consists of a higher level outer loop and a lower level inner loop. This is illustrated for real-time hybrid model testing in Figure 7.

Broadly, the outer loop control objective using CDPR setups is either pose control [1], [2] or load control [6], [29]. In the former, the objective real-time for the platform to track the target pose trajectories – despite external excitations.

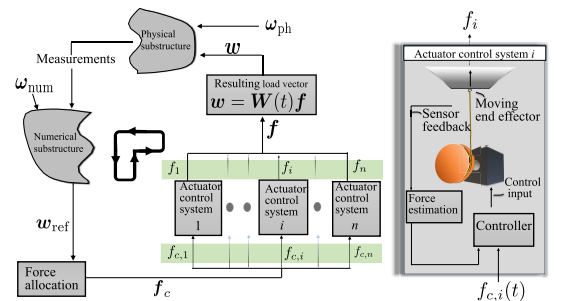


FIGURE 7. Real-time hybrid model testing control loop. An outer loop outputs the commanded cable forces f_c , and an inner loop performs cable force tracking.

In the latter, the objective real-time to actuate the correct loads onto the platform – despite platform motions. Although the present study was performed with load-control in mind (e.g., real-time hybrid model testing), the paper results are relevant for both – since both might use cable-force control in the inner loop to achieve the outer loop control objective.

1) OUTER LOOP

Common for the frameworks considered in this work is that the outer loop continuously outputs a set of commanded cable forces $\mathbf{f}_c = (f_{c1}, f_{c2}, \dots, f_{cn})$. These are found by first determining the reference load vector \mathbf{w}_{ref} , according to the outer loop control objective. In real-time hybrid model testing, \mathbf{w}_{ref} is a numerically calculated load vector to be actuated onto the experimental platform. By solving the force allocation problem subject to actuator constraints, geometric mapping, and optimization criteria, the corresponding commanded cable forces \mathbf{f}_c are found [30]. Based on the results in [30], we find it reasonable to assume that \mathbf{f}_c is continuously differentiable and within the actuator constraints.

2) INNER LOOP

In the inner control loop, the goal is for the actuators to track the forces \mathbf{f}_c , under the following assumption

A.1. *The servomotor bandwidth is at least 5-10 times higher than that of the outer loop. Moreover, cross-talk between the actuators are negligible.*

A.2. *From the inner loop perspective, the cable drum angular positions θ_w (and its derivatives $\dot{\theta}_w, \ddot{\theta}_w$), target force \mathbf{f}_c , and effective radius r are considered external inputs.*

A.1 is reasonable since we use fast, high-performing industrial servomotors, while the outer loop is significantly slower due to the relatively higher mass of the platform; see also [11], [20], [21]. Moreover, with compliance, the actuators only affect each other via movement of the slower platform (they are not antagonistic [26]).

We use the concept of successive loop closure [31, Ch 6], based on A.1. The inner loop is first closed. Assuming high inner loop performance, the outer loop can then be designed with the inner loop approximated as a unity gain. Correspondingly, we consider the inner loop and the outer loop control independently and treat the control of each actuator as an independent control problem.

It follows that the signals θ_w , r , and \mathbf{f}_c are external inputs to the inner loop (coming from the outer loop). That is, 1) θ_w follows from the end-effector positions and non-controlled uncertainties related to spooling and cable-elongation, 2) r follow from θ_w and non-controllable radius uncertainties, and 3) \mathbf{f}_c follows from \mathbf{w}_{ref} and the force-allocation procedure.

3) CONTROL PROBLEM

We consider force control of a single actuator, assuming that the results are applicable for multiple cables in parallel topology. The problem under consideration is to control the actuated force $f(t)$ applied by the end effector on a moving object

such that it tracks the commanded force $f_c(t)$ accurately. That is, we want to minimize the tracking error $\tilde{f}(t) = f(t) - f_c(t)$ for an individual actuator despite significant end effector motions, whose frequencies are, for our applications, in the range of 0.1 Hz to 1.4 Hz.

The problem, including the associated controller and force model, is illustrated in a block diagram representation in Figure 8. Note how we treat the end effector and target force as external inputs to the inner loop force model in accordance with A.2. Since the clockspring is fixed at both ends (one part to the motor-shaft, and the other part to the cable-attached drum), there are no modeled dynamical states in the transmission system. That is, the force depends only on signals from the outer loop, uncertainties, disturbances, and the actuator transmission system mapping from control input to force (which vary slowly in time due to parameter uncertainties and drift/creep). The control problem under consideration is, therefore, in practice to: 1) identify the force transmission system mapping, and 2) use this mapping in feedforward control designs to ensure accurate force-tracking.

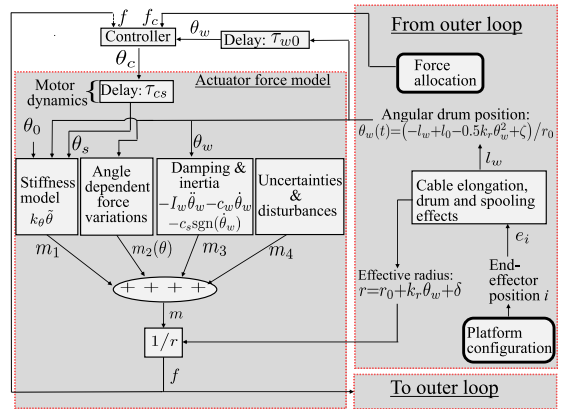


FIGURE 8. Force model for one actuator in the inner loop. Trajectories and target force are given by the outer loop.

The system's dynamical states (e.g. platform motions) are considered as part of the outer loop, which is not a focus in this paper. One should note, however, that for the case of real-time hybrid hydrodynamic testing, significant hydrodynamic damping typically ensures that unwanted oscillations do not occur and that the system as a whole (the outer loop) is stable. For other applications, and depending on the system design, other measures such as active vibration suppression [32] and dynamical system analysis [33], [34] might be needed in the outer loop control design to ensure overall stability and robustness.

D. EXPERIMENTAL SETUP

Figure 9(a) shows the experimental setup developed for the present study, with installed sensors and corresponding

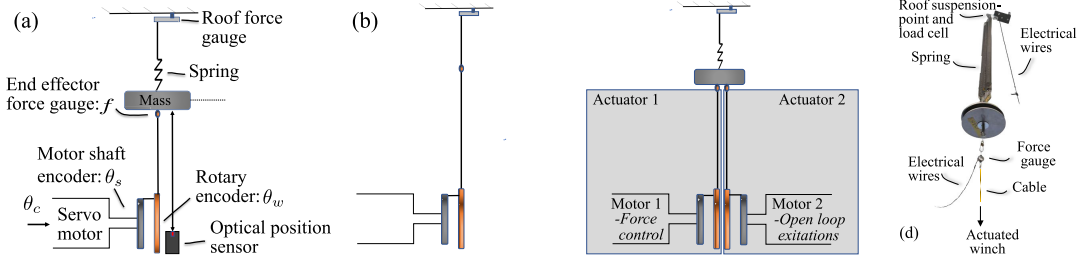


FIGURE 9. Experimental setup and configurations. (a) Sensors and measurements (b) Configuration 1 (c) Configuration 2 (d) Image from laboratory setup.

measurements.¹ It consists of a mass connected via linear springs to a suspension point. The cable forces are actuated onto the mass from below along the same vertical axis, effectively constituting a 1 degree of freedom system. The setup is chosen since it is simple to model, monitor, install, reconfigure, and perform tests with. Additionally, it can provide wide-ranging force and end effector trajectories.

The control system is implemented in MATLAB and LabView and compiled on high-performance National Instrument industrial hardware. An industrial data acquisition system from HBM provides high-performance sampling and routing of data in the loop. Communication between computers, sensors, and motors is configured using a combination of CanBus, Ethercat, and electrical wires.

We use the setup in two different actuator configurations:

Configuration 1, as illustrated in Figure 9(b). The end effector is attached directly to the fixed roof suspension point, allowing force control with a constant end effector position.

Configuration 2, as illustrated in Figure 9(c). The motions of the mass are excited by a second actuator (Actuator 2) controlled such as to track a predetermined shaft angle trajectory. The primary actuator (Actuator 1) is run in force control mode as before. This allows force tracking tests with dynamic end effector trajectories.

E. PERFORMANCE INDICATORS

To assess performance, we use the bias-adjusted mean absolute force tracking error:

$$\begin{aligned} \text{MAE}_f^* &:= \frac{1}{M} \sum_{k=1}^M |f'(t_k) - f_c(t_k) - b_0|, \text{ with } b_0 \\ &= \frac{1}{M} \sum_{k=1}^M (f'(t_k) - f_c(t_k)) \end{aligned} \quad (6)$$

where f' is f filtered in post-processing using a lowpass filter of 10 Hz, M is the number of discrete sample points t_k in the considered time window, and b_0 is the tracking error bias.

¹For validation and calibration, an extra force sensor is installed in the spring suspension point, and an extra optical position sensor measures the mass position (their measurements are not discussed further in this paper).

III. DELAYS AND PREDICTION

1) MEASUREMENTS, SAMPLING, AND DELAY IN THE CONTROL LOOP

Figure 10 illustrates the flow of signals in the loop. We control the actuator using a discrete control system with cycle times $T_d = 5$ ms. At the start of each control cycle, measurements are input to the control system from the data acquisition system (DAQ), whereas at the end of each control cycle, the motor control command θ_c is output. This means that there is a control cycle delay $\tau_{cc} = T_d$. A system for logging data is set up both in the DAQ and in the control system cycle. The force measurements are sampled at 1200 Hz and filtered by Butterworth anti-aliasing filter of cutoff frequency 200 Hz before the controller samples the signal. Although the sampled force signal still exhibits high-frequency noise, further filtering is not deemed necessary since the force measurements will not be used directly in feedback control.

Consider now the simple feedforward control

$$\theta_c = \underbrace{\theta_w}_{\theta_c^{fp}} + \underbrace{\frac{f_c}{k_{\theta,r}}}_{\theta_c^{ff}} + \theta_0 \quad (7)$$

where the position and force-feedforward terms are labelled by θ_c^{fp} and θ_c^{ff} , respectively. Communication, sampling, motor dynamics, and cycle times delay the feedforward signals, as illustrated in Figure 10. The relative position feedforward delays are denoted by τ_{wc} , τ_{ws} , and τ_{cs} such that $\theta_s^{fp}(t) = \theta_c^{fp}(t - \tau_{cs}) = \theta_w(t - \tau_{ws})$ and $\theta_c^{fp}(t) = \theta_w(t - \tau_{wc} - \tau_{w0})$. Here, τ_{w0} represents the small unknown delay until the drum angle has been sampled. τ_{fs} is the force-feedforward delay such that $\theta_s^{ff}(t) = f_c(t - \tau_{fs})/k_{\theta,r}$. In this paper, f_c is constructed at the

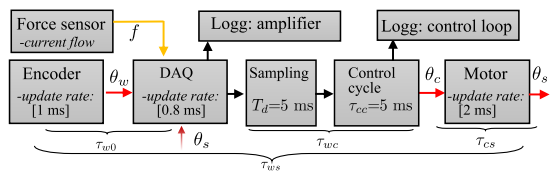


FIGURE 10. Flow of signals, sampling and delays in the control loop.

end of the control cycle such that $\tau_{fs} = \tau_{cs}$. However, this is not always the case. For example, [35] calculates f_c using another control-loop with separate characteristic delays.

As illustrated in Figure 10, the different components in our control system have varying update frequency, and they were not further synchronised. Due to varying phase between measurement, we expect a varying time delay in the interval ± 3 ms from test to test.

2) EFFECT OF TIME DELAYS

A delayed signal can be approximated through a Taylor series expansion of the delayed term τ about zero [36]:

$$x(t - \tau) = \sum_{q=0}^Q \frac{x^{(q)}(t)}{q!} (-\tau)^q + \mathcal{O}(\tau^{Q+1}), \quad (8)$$

where $x^{(q)}(t)$ denotes the q th derivative, and $\mathcal{O}(\tau^{Q+1})$ denotes higher-order terms. For sufficiently small delays, higher-order terms can be neglected to get

$$x(t - \tau) \approx x(t) - \tau \dot{x}(t) \quad (9)$$

If θ_s is delayed by τ , we get from (9) that the first-order delay-dependent error of (5) is

$$(\theta_s(t - \tau) - \theta_s(t))k_{\theta,r} \approx -\tau \dot{\theta}_s k_{\theta,r}, \quad (10)$$

Considering that the two have different delays, the first-order position feedforward delay-induced error is

$$k_{\theta,r}(\theta_w(t - \tau_{ws}) - \theta_w(t)) \approx -k_{\theta,r} \tau_{ws} \dot{\theta}_w, \quad (11)$$

whereas the first-order force feedforward delay-induced error is

$$f_c(t - \tau_{fs}) - f_c(t) \approx -\tau_{fs} \dot{f}_c. \quad (12)$$

In our applications $k_{\theta,r} \dot{\theta}_w \gg \dot{f}_c$ and $\tau_{ws} > \tau_{fs}$ such that the effect of (11) is typically much greater than (12). We highlight this in the following remark.

Remark 1. For force control using winched actuators with the servomotor in position mode, the position feedforward term is sensitive to time delays. Given a pure position feedforward time delay τ , the first-order error is given by the damping term $\tilde{f} = -k_x \dot{x}_e \tau$, where x_e is the feedforwarded position (in the pull direction) and k_x is the transmission stiffness.

It is difficult to separate the effect of (11) from the damping force $c_{w,r} \dot{\theta}_w$. We therefore, hereafter, lump $c_{w,r}$ into the effective time delay τ_{ws} .

3) LEAST SQUARES PARAMETER ESTIMATION

For identification and for prediction purposes, we will use least squares parameter estimation [37] to fit a set of state variables x_1, x_2, \dots, x_l to a response variable y assumed described by the linear mapping

$$y = \beta_0 + \beta_1 x_1 + \beta_2 x_2 + \dots + \beta_l x_l + \epsilon, \quad (13)$$

where ϵ is a zero-mean random error. We denote a dataset with m observations by $\mathbf{y} = (y_1, y_2 \dots y_m)^\top$ and

$\mathbf{X} = (\mathbf{x}_0, \mathbf{x}_1, \dots, \mathbf{x}_l)$ where $\mathbf{x}_0 = \mathbf{1}_{m \times 1}$ and $\mathbf{x}_i = (x_{i1}, x_{i2} \dots x_{im})^\top$ for $i = \{1, 2, \dots, l\}$.

Let $\hat{\mathbf{y}}_k := [x_{1k}, x_{2k}, \dots, x_{lk}] \boldsymbol{\beta}$. The set of coefficients $\boldsymbol{\beta}$, minimising the weighted least square estimation error $\sum_{k=1}^{k=m} w_k (\hat{y}_k - y_k)^2$ is

$$\boldsymbol{\beta} = \left((\mathbf{W}\mathbf{X})^\top (\mathbf{W}\mathbf{X}) \right)^{-1} \mathbf{W}\mathbf{X}^\top \mathbf{W}\mathbf{y}, \quad (14)$$

where $\boldsymbol{\beta} = (\beta_0, \beta_1, \beta_2 \dots, \beta_l)^\top$ and $\mathbf{W} = \text{diag}(w_1, w_2, \dots, w_m)$. Hereafter, when not specified, we use the non-weighted version of (14), that is, $w_k = 1$ for $i \in \{1, \dots, m\}$. Later, we continue to use bold notation to refer to sampled sets when referencing (14). For example, we write $\boldsymbol{\theta}_w$ to mean $(\theta_{w,1}, \theta_{w,2}, \dots, \theta_{w,m})^\top$ and $\text{sgn}(\boldsymbol{\theta}_w)$ to mean $(\text{sgn}(\theta_{w,1}), \text{sgn}(\theta_{w,2}), \dots, \text{sgn}(\theta_{w,m}))^\top$.

4) POLYNOMIAL PREDICTION

We can predict the drum angle θ_w an interval τ_{pred} forward in time using polynomial prediction [38] as follows. At time t_N , let $\boldsymbol{\theta}_w$ be a vector of the N past measured drum angles, sampled at the past N time instances: $\{t_1, t_2, \dots, t_N\}$. Expecting trajectories to be smooth, we assume that $\theta_w(t_k)$ in the interval $t = [t_1, (t_N + \tau_{\text{pred}})]$ can be described by a p -th order polynomial model: $\theta_w(t_k) = \mathbf{x}_r(t - t_N) \boldsymbol{\beta}_r$, where

$$\mathbf{x}_r(\tau) = [1 \ \tau \ \tau^2 \ \dots \ \tau^p]. \quad (15)$$

Assuming values that are close to the query point provide more information, we now find $\boldsymbol{\beta}_r$ using the weighted least square (14) with $\mathbf{y} = \boldsymbol{\theta}_w$ and $\mathbf{X} = [1 \ t^{i'o1} \ t^{i'o2} \ \dots \ t^{i'op}]$, where $t^{i'oi} = [(t_1 - t_N)^i (t_2 - t_N)^i \dots (t_N - t_N)^i]^\top$ for $i = \{1, \dots, p\}$. Inspired by [39], we choose a Gaussian-like weighting, $w_k = e^{-(0.015 + (t_N - t_k))^2 / 0.02}$. We then express the predicted drum angle by²

$$\hat{\theta}_w(t + \tau_{\text{pred}}) = \mathbf{x}_r(\tau_{\text{pred}}) \boldsymbol{\beta}_r \quad (16)$$

The frequency to magnitude response of polynomial predictive filters may be difficult to characterize, and extrapolation with polynomials may generally be hazardous and prone to errors [40]. In this paper, we assume that (16) gives satisfactory prediction performance. By this, we mean that the force errors due to inaccurate prediction $\hat{\theta}_w(t + \tau_{\text{pred}}) - \theta_w(t + \tau_{\text{pred}})$ are small compared to the overall force tracking error. This assumption is reasonable due to a short prediction horizon, frequent sampling, smooth end-effector trajectories, and low cable vibrations. We verify this experimentally in Section V, where we use prediction parameters $N = 23$ and $p = 3$.

Similar methods for actuator position prediction have been applied with success in other fields. See, for example [38]. For more on polynomial prediction, we refer to [39]–[41].

²When used in online prediction, to limit computational demand, we compute the term $\mathbf{H} = \left((\mathbf{W}\mathbf{X})^\top (\mathbf{W}\mathbf{X}) \right)^{-1} \mathbf{W}\mathbf{X}^\top \mathbf{W}$ offline and $\hat{\theta}_w(t + \tau_{\text{pred}}) = \mathbf{x}_r(\tau_{\text{pred}}) \mathbf{H} \boldsymbol{\theta}_w$ online.

We estimate predicted derivatives using $\hat{\theta}_w(t + \tau_{\text{pred}}) = \dot{\mathbf{x}}_t(\tau_{\text{pred}})\boldsymbol{\beta}_t$ and $\hat{\ddot{\theta}}_w(t + \tau_{\text{pred}}) = \ddot{\mathbf{x}}_t(\tau_{\text{pred}})\boldsymbol{\beta}_t$, where $\dot{\mathbf{x}}_t$ and $\ddot{\mathbf{x}}_t$ are element-wise derivatives of (15). For each step of differentiation, noise and prediction errors are amplified.

IV. CONTROL DESIGN

Consider now the feedforward control (7). We expect this to be associated with: 1) motion-induced errors associated with damping, inertia, and angle-dependent force variations modelled in (5), 2) force feedforward-induced errors associated with inaccuracies in the linear deflection-to-force model, and 3) delay-induced errors as outlined in Section III-2. In this section, we extend the feedforward control to overcome most of these errors.

A. DELAY COMPENSATION

We now introduce *the predictive feedforward controller*, which compensates for delays by predicting the drum angle θ_w an interval τ_{pred} forward in time:

$$\theta_c(t) = \hat{\theta}_w(t + \tau_{\text{pred}}) + \frac{f_c}{k_{\theta,r}} + \theta_0, \quad (17)$$

where $\hat{\theta}_w(t + \tau_{\text{pred}})$ is the predicted position, found using (16).

We should with this achieve the feedforward position term $\theta_s^{\text{ff}}(t) = \hat{\theta}_w(t - \tau_{ws} + \tau_{\text{pred}})$, which for $\tau_{\text{pred}} = \tau_{ws}$ should compensate for delay if the extrapolation procedure is accurate.

1) DELAY ESTIMATION

To use (17), we must estimate τ_{ws} . We can use (9) as an efficient method to estimate the delays between θ_w , θ_c , and θ_s as follows. Let the signals θ_1 and θ_2 be characterized by $\theta_1(t - \tau) \approx b_0 + b_1\theta_2(t)$. Solving (14) with $\boldsymbol{\beta} = [\beta_{\theta,0} \ \beta_{\theta,1} \ \beta_{\dot{\theta},1}]$, $\mathbf{X} = [\mathbf{1} \ \theta_1 \ \dot{\theta}_1]$ and $\mathbf{y} = \theta_2$, the delay between the two signals is found using:

$$\hat{\tau} \approx -\frac{\beta_{\dot{\theta},1}}{\beta_{\theta,1}}, \quad (18)$$

which is used to determine $\hat{\tau}_{ws}$, $\hat{\tau}_{wc}$, and $\hat{\tau}_{cs}$.

Assuming that damping is dominated by the position feedforward delay-induced damping (11), a redundant and independent method to identify delays uses (14) with $\boldsymbol{\beta} = [\beta_0 \ \beta_{\dot{\theta}_w}]$, $\mathbf{X} = [\mathbf{1} \ \dot{\theta}_w]$, and $\mathbf{y} = \dot{f}$. The delay between the two signals is then estimated by:

$$\check{\tau}_{ws} \approx -\frac{\beta_{\dot{\theta}_w}}{k_{\theta,r}}, \quad (19)$$

where we have used the notation $\check{\tau}_{ws}$ to differentiate the estimates from that of (18).

Recall now the force model (5). We have already lumped the damping $c_{w,r}\dot{\theta}_w$ into the effective time delay. However, $c_{s,r}\text{sgn}(\dot{\theta}_w)$ also correlates with the angular speed. Therefore, if the estimate of $c_{s,r}$ is available, then using $\mathbf{y} = \dot{f} - c_{s,r}\text{sgn}(\dot{\theta})$ to find $\beta_{\dot{\theta}}$ is expected to increase the accuracy of (19).

We expect $\check{\tau}_{ws}$ estimated from (19) to be less accurate and noisier than $\hat{\tau}_{ws}$ estimated from (18) with $\theta_1 = \theta_s$ and $\theta_2 = \theta_w$. However, it has the advantage of incorporating both τ_{w0} and the effective delay from damping, as well as not being affected by delays associated with sampling.

2) ADAPTIVE DELAY PREDICTION

Whereas (18) and (19) find $\tau_{\text{pred}} = \tau_{ws}$ offline, we next present a method that adaptively estimates τ_{pred} online:

1. We allow the predicted error to drift by:

$$\dot{\tau}_{\text{pred},0} = -k_{\tau}\tilde{f}\text{sgn}^*(\dot{\theta}_w), \quad (20)$$

where $\text{sgn}^*(\dot{\theta}_w) := \{0, \ \forall |\dot{\theta}_w| < \theta_{\text{trunc}}; \ \pm 1, \ \text{otherwise}\}$, k_{τ} is an integral gain, and $\theta_{\text{trunc}} = 0.05$ rad/s truncates the signal for low velocities.

2. $\tau_{\text{pred},0}$ is saturated such it is always in the interval $\{0, \tau_{\text{max}}\}$, where τ_{max} is the expected upper limit on the delay, imposed for robustness.

3. We set $\tau_{\text{pred}} = \text{LPF}(\tau_{\text{pred},0})$, where LPF is a lowpass filter applied to smoothen the variations of τ_{pred} .

The procedure has the advantage of being able to capture time-dependent variations in delay as well as not depending on exact delay identification. It assumes that the components of \tilde{f} that correlate with angular velocity (e.g., $c_{s,r}\text{sgn}(\dot{\theta}_w)$ and $k_{\theta,r}\dot{\theta}_w(\tau_{ws} - \tau_{\text{pred}})$) dominate the integrated term $\int \tilde{f}\text{sgn}^*(\dot{\theta}_w)$. The contribution from other components of \tilde{f} are expected to cancel out as $\text{sgn}^*(\dot{\theta}_w)$ attains approximately equally many negative and positive values over time.

Since the integrated term correlates with both $c_{s,r}\text{sgn}(\dot{\theta}_w)$ and $k_{\theta,r}\dot{\theta}_w\tau_{ws}$, increased accuracy is expected in the estimation of τ_{ws} if one first corrects for $c_{s,r}\text{sgn}(\dot{\theta}_w)$ in the feedforward controller.

Although used with success in this paper, caution must be taken if the procedure is combined with broad-banded trajectories with varying target forces. Concretely, when $\tau_{\text{pred}} \neq \tau_{ws}$ the term $\int \tilde{f}\text{sgn}^*(\dot{\theta}_w)$ should be dominated by $k_{\theta,r}\dot{\theta}_w(\tau_{ws} - \tau_{\text{pred}})$ for the method to work effectively. Even so, one can also use the method to tune τ_{pred} in the initialization phase, when motions and target forces are highly controlled.

B. MODEL COMPENSATION

We now introduce *the model correcting, predictive feedforward controller* which includes a term $\mathbf{x}_m\boldsymbol{\beta}_m/k_{\theta,r}$ that aims at compensating for actuator damping and angle-dependent force variations:

$$\theta_c = \hat{\theta}_w(t + \tau_{\text{pred}}) + \frac{f_c}{k_{\theta,r}} + \theta_0 - \frac{\mathbf{x}_m\boldsymbol{\beta}_m}{k_{\theta,r}}, \quad (21)$$

where $\mathbf{x}_m = [1 \ \sin(\theta) \ \cos(\theta) \ \text{sat}(\dot{\theta}_w/\mu)]$ and $\boldsymbol{\beta}_m = [\beta_0 \ \beta_{\sin} \ \beta_{\cos} \ \beta_{\text{sgn}}]$. To avoid chattering, we have here replaced $\text{sgn}(\dot{\theta}_w)$ with $\text{sat}(\dot{\theta}_w/\mu) := \{\theta_w/\mu, \ \text{for } -1 < (\dot{\theta}_w/\mu) < 1; \ \text{sgn}(\dot{\theta}_w/\mu), \ \text{otherwise}\}$. The choice of $\mathbf{x}_m\boldsymbol{\beta}_m$ is explained as follows. We deduce experimentally in Section V-B that the mapping $k_1\sin(\theta_w) + k_2\cos(\theta_w)$ fits the angle-dependent force variations f_2 quite well (if needed,

this could easily be extended to more complex mappings). For transmission system damping and inertia, we note that the damping term $c_{w,r}\dot{\theta}_w$ is incorporated by the predictive feedforward delay compensation, whereas $c_{s,r}\text{sgn}(\dot{\theta}_w)$ is compensated through (21). We would ideally like to compensate for $I_{w,r}\ddot{\theta}_w$. However, in Section V-B we show that the use of acceleration feedback is not feasible with our setup.

C. ADAPTATION OF PARAMETERS

In this section, we describe how we identify parameters for use in the feedforward controller. Generally, this can be performed adaptively online or through offline identification.

1) ESTIMATION OF SPRING CHARACTERISTICS

As discussed earlier, the clockspring characteristics may be slowly varying with time. To take this into account, we estimate $k_{\theta,r}$ and θ_0 online during operation as follows³:

1. Every time interval t_0 , we sample θ_w , θ_s , and f to a buffer (θ_w, θ_s, f) containing the last K sampled data points.
2. The buffered data are then used to solve (14) with $\beta = \beta_k = [\beta_0 \ \beta_{k,\theta}]$, $X = X_k = [\mathbf{1} \ (\theta_s - \theta_w)]$ and $y = f$.
3. $\hat{\theta}_0 = -\frac{\beta_0}{\beta_{k,\theta}}$ and $\hat{k}_{r,\theta} = \beta_{k,\theta}$ are now the online estimated input parameters to the feedforward controller.

By allowing variations in $k_{\theta,r}$, note that one may also capture some of the effects of unmodelled slowly-varying changes of the effective radius r . For the procedure outlined above to be accurate, the buffered data must capture a dataset with sufficiently rich variation in deflection (it cannot be used if f_c is constant). Moreover, sampling should be done over a long enough time window such that local trends and spring characteristics that do not correlate with deflection average out.

2) OTHER MODEL PARAMETERS

For estimating the other model parameters, (14) is solved with $\beta = \beta_m = [\beta_0 \ \beta_{\sin} \ \beta_{\cos} \ \beta_{\text{sgn}}]$, $y = \tilde{f}$, and $X = X_m = [\mathbf{1} \ \sin(\theta_w) \ \cos(\theta_w) \ \text{sgn}(\dot{\theta}_w)]$. To capture variations and for practical purposes, this identification can be performed by estimating the parameters offline or online by sampling data to a buffer similarly as above. For both cases, the data should be acquired during time-windows with significant actuator and end effector motions.

D. CONTROL SUMMARY AND DISCUSSION

We have now presented three feedforward controllers of increasing complexity. That is, (7), (17), and (21). Figure 11 features the implementation of (21). In the following, we elaborate on some practical implementation details and considerations.

- a. *Sampling and buffering*: For robustness, the measurements used for parameter estimation should cover a

³While this work has implemented least squares estimation using a windowed approach, we note that for reasons of computational efficiency similar results can be obtained using recursive least squares implementations, such as described in for example [42].

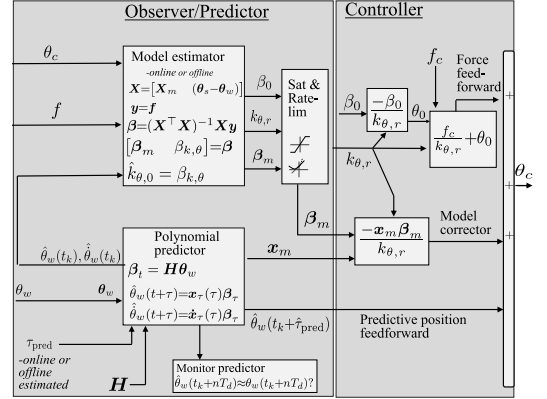


FIGURE 11. Full control loop using (21) including prediction, estimation and controller terms.

sufficiently rich test dataset. If a windowed least squares implementation is used, the buffer and sampling should be configured to cover a sufficiently large number of samples (we use $K = 1000$ and $t_0 = 0.04$ s for buffer sampling). Similarly, for a recursive least squares implementation, the forgetting factor should be configured to sufficiently prioritize earlier samples.

- b. *Rate limitation and saturation*: These are for robustness imposed on the estimated β -values. The rate limiter matches the expectation of slowly varying changes, and the saturation block provides robustness by limiting the parameters to within expected bounds.
- c. *Adaptive model estimation*: The control system is set up such that it is simple to switch between: 1) updating β -values based on estimation, 2) fixing the β -values (while monitoring the estimated β -values), and 3) switching to offline estimated values. If the β -values are calculated online, we can find β_m and β_k individually as above or collectively using $X = [X_m \ (\theta_s - \theta_w)]$, $y = f$, and $\beta = [\beta_m \ \beta_{k,\theta}]$. Due to frequent sampling, assumption of slow variations, saturations, and rate limitations, we expect to be able to adaptively handle the parameter variations effectively (this is later demonstrated experimentally). Although not implemented in this work, we note that there are least squares variants that further emphasise robustness [43], [44].

As described in Section II-C3, there are no internal states in the considered inner loop transmission system. Since the control input depends only on feedforward control terms (with rate-limited saturated adaptation), there are no variables that can become unstable. Since force errors are not used in direct feedback control and θ_w follows from the slower platform dynamics, force errors and disturbances are generally not amplified by the controller. High-performance force tracking thus relies on the feedforward controller's ability to accurately capture the force transmission system mapping. If the actual transmission system properties were perfectly known,

TABLE 1. Experimental tests overview.

Test	Description/Test goal	Target force	EE-trajectory	Controller	Config	Section	Figure
1	Online estimation of spring characteristic	Harmonic	Fixed	(7)	1	V-A	12
2	Online estimation of spring characteristic	Sweeping	Fixed	(7)	1	V-A	13
3	Identification of angle-dependent force variations under low velocities	Fixed	Slow	(7)	2	V-B	14
4,5	Demonstration of time delay estimation and the effect of time delays	8 N	Fast	(7)	2	V-B	15, 16
6	Model identification with sweeping end effector trajectory	8 N	Sweeping	(7)	2	V-B	17-19
7,8	Demonstration of the adaptive delay prediction procedure	8 N	Fast	(17)	2	V-B	20, 21
9	Force error comparison with varying controllers	8 N	Fast	(7,17,21)	2	V-B	22
6,10,11	MAE _r ⁴ as function of period with varying controllers	8 N	Sweeping	(7,17,21)	2	V-B	23
12	Force tracking with moving end effector and variable target force	Sweeping	Sweeping	(21)	2	V-C	24

TABLE 2. End effector and target force trajectories.

(a) End effector trajectory*			
Case	T_2	$\Delta\theta_{e2}$	End effector amplitude
Slow trajectory	600 s	$\frac{10}{3}\pi$	≈ 63 cm
Fast trajectory	4 s	$\frac{2}{3}\pi$	≈ 12 cm
Sweeping trajectory**	10 s to 1 s	$\frac{3}{2}\pi$	≈ 12 cm

(b) Target force trajectory	
Case	f_c [N]
Harmonic force	$9 + 7\sin(2\pi t/10)$
Sweeping force***	$8 + 2\sin(2\pi t/T_c)$

* Motor 2 drive the system by tracking the harmonic target shaft angle $\theta_{e2} = \Delta_0 + \Delta\theta_{e2}\cos(2\pi/T_2)$.
 ** $T_2 =$ increases discretely every 10th period over 75 steps.
 *** T_c decreases discretely after each period.

the force tracking error could be expressed according to (5) and Remark 1. In the next chapter, we study the performance experimentally.

V. EXPERIMENTAL TESTING

Experimental testing has been performed for system identification purposes, method validation, and investigation of controller performance. In brief, we have separated the experimental study into three parts; 1) Section V-A covers the problem of tracking a variable cable force onto a fixed end effector (Test 1-2), 2) Section V-B covers the problem of regulating a fixed cable force onto a moving end effector (Test 3-11), and 3) Section V-C covers the coupled problem of tracking a variable target force onto a moving end effector (Test 12). A summary of the tests is presented in Table 1, together with their objectives and test characteristics. Table 2 details the corresponding test trajectories.

Unless specified otherwise, figures display experimental data that has been smoothed in post-processing using phase-free lowpass filters with a cutoff frequency of 5 Hz.

A. VARIABLE CABLE FORCE WITH FIXED END EFFECTOR POSITION

TEST 1-2: ONLINE ESTIMATION OF SPRING CHARACTERISTICS (θ_0 AND $k_{\theta,r}$) USING CONTROLLER (7)

Figure 12(a) shows the resulting force tracking performance and online estimated spring characteristics⁴ from Test 1. As

⁴We verified that the online estimated values closely matched the results obtained in offline post-processing.

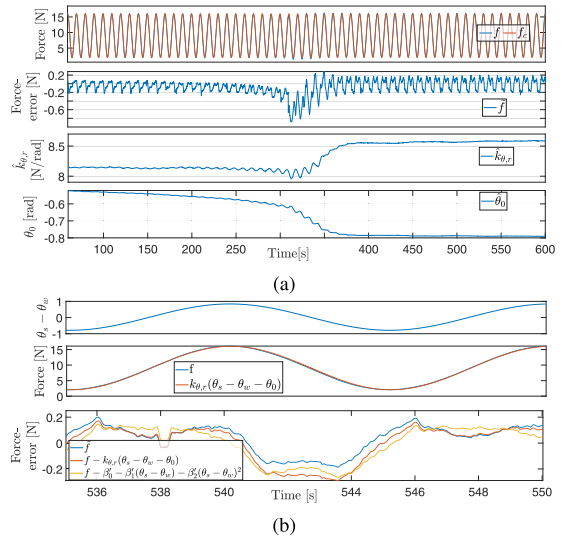


FIGURE 12. (From Test 1) Force tracking with adaptive spring characteristics with fixed end effector (a) Full interval. (b) Sample interval.

illustrated, the spring characteristic alters significantly after about 300 seconds, which initially leads to increased force error. However, once the estimated spring characteristics settle at a new level, the adaptivity ensures that the feedforward errors again are small. Note the integral effect of the term θ_0 .

Figure 12(b) highlights force tracking and corresponding spring deflection on a specific time interval. It also shows the remaining error after subtracting the modelled force for the chosen linear mapping as well as when a second-order mapping $f' = \beta'_0 + \beta'_1(\theta_s - \theta_w) + \beta'_2(\theta_s - \theta_w)^2$ is used. The resulting estimation error is similar for the linear and the second-order model, indicating that the linear deflection-to-force model is sufficient. We believe the remaining error is due to damping, inertia, backlash, and weight induced forces. Although not detailed in this paper, we observe that the error is partly systematic (for example, there appears to be one term proportional to $\text{sgn}(\dot{\theta})$), and thus presumably could be modelled as part of the feedforward controller.

Figure 13(a) shows the resulting forces for Test 2, illustrating how the force-feedforward term behaves well. As indicated in the highlighted segment, high-performance force tracking is also achieved for higher frequencies. The increase

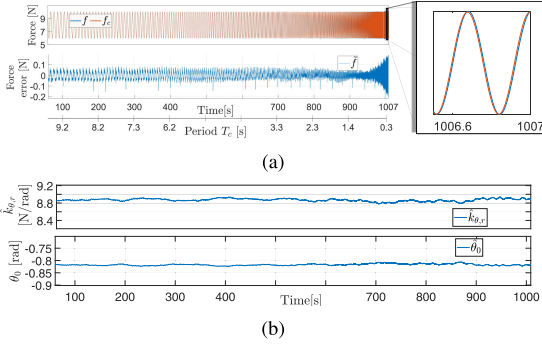


FIGURE 13. (From Test 2) Force tracking with adaptive spring characteristics and harmonic sweeping target force. (a) Force performance (\tilde{f} filtered at 10 Hz). (b) Online spring characteristics estimation.

of \tilde{f} at high frequencies is mostly due to the phase lag (from the feedforward time delay τ_{fs}).

Test 1 serves as an example where the change in spring characteristics were greater than typical (see Figure 12(a)) and Test 2 serves as an example of a case where the spring characteristics were more stable (see Figure 13(b)). The online stiffness estimation handles both cases well.

B. FIXED FORCE WITH A MOVING END EFFECTOR

In this section, we use actuator Configuration 2 with a fixed target force to assess the effects of end effector motions on the control performance.

1) TEST 3: IDENTIFICATION OF $f_2(\theta_w)$ AND $c_{s,r}$ USING CONTROLLER (7)

Figure 14 shows the resulting force errors as a function of θ_w for Test 3 for a set of different fixed target forces. The black arrows in the figure indicate the direction in time, with one full revolution corresponding to 600 seconds. Due to low velocities, we expect forces proportional to velocity and acceleration to be negligible.

We can roughly divide the force error in Figure 14 into a directional component and an angle-dependent component (e.g., $c_{s,r} \text{sgn}(\dot{\theta}_w)$ and $f_2(\theta_w) \approx f_0 + k_1 \sin(\theta_w) + k_2 \cos(\theta_w)$). We believe the majority of $f_2(\theta_w)$ to be related to the unsymmetrical mass distribution of the spring. However, some may come from systematic errors in the servomotor's internal position-controller, encoders, or cable-layering.

We now use (14) to fit a model for the slow-speed variations using $\beta_m = [\beta_0 \beta_{\sin} \beta_{\cos} \beta_{\text{sgn}}]$ and $X_m = [1 \sin(\theta_w) \cos(\theta_w) \text{sgn}(\dot{\theta}_w)]$. The resulting model is shown in grey in Figure 14 and appears to follow the trend quite well.

2) TEST 4-5: IDENTIFICATION OF DELAYS ($\hat{\tau}_{ws}$, $\hat{\tau}_{ws}$, $\hat{\tau}_{wc}$, $\hat{\tau}_{cs}$) AND THEIR EFFECT ON FORCE TRACKING PERFORMANCE USING CONTROLLER (7)

Figure 15 shows the resulting forces and the corresponding estimated delays of Test 4. In this test, we increased the

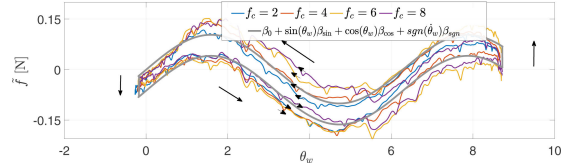


FIGURE 14. (From Test 3) Resulting forces with slow end effector trajectory and regression model. \tilde{f} filtered at 1 Hz.

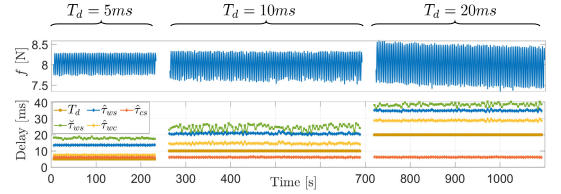


FIGURE 15. (From Test 4) Delay estimation with fast end effector trajectory and $f_c = 8$ N. Increasing control cycle times T_d .

control cycle times T_d in two steps. The effective delay from sample rate T_d , is expected to be $T_d/2$ [45]. Since it captures both the effective sampling delay and the control cycle delay τ_{cc} , we expect $\tau_{wc} = \frac{3}{2}T_d$, which holds experimentally as T_d increases.

In Test 5, we repeated the experiment (for $T_d = 5$ ms only), but we now artificially increased the control cycle delay τ_{cc} by one sample (e.g., 5 ms) every 10th period, as shown in Figure 16. Noting that the velocity amplitude $a_{\dot{\theta}}$, indicated in the figure is 1.36 rad s^{-1} , we expect per Remark 1, an increase in τ_{ws} of $\Delta\tau_{ws} = 5$ ms to result in an increase in force amplitude of $\Delta F = \Delta\tau_{ws} a_{\dot{\theta}} k_{\theta,r} = 0.056 \text{ N}$ (also indicated in the figure). Further, the resulting estimated delays $\hat{\tau}_{ws}$, $\hat{\tau}_{ws}$, $\hat{\tau}_{wc}$, $\hat{\tau}_{cs}$ should all increase by 5 ms. As seen in the figure, this holds closely, thus experimentally verifying the results of Section III-2.

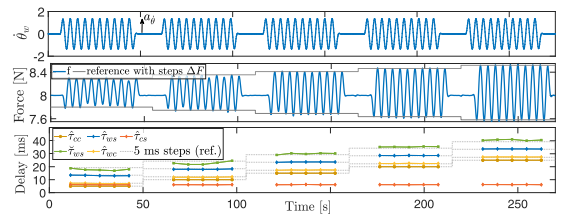


FIGURE 16. (From Test 5) Delay estimation with fast end effector trajectory and $f_c = 8$ N. Artificial delay increases by 5 ms every 10th period. \tilde{f} is filtered at 1 Hz.

The identified delays (for $T_d = 5$ ms) are presented in Table 3. To calculate $\hat{\tau}_{ws}$, we used (19) with $y = \tilde{f} - c_{s,r} \text{sgn}(\dot{\theta}_w)$, where $c_{s,r} = -\beta_{\text{sgn}}$, as identified in Figure 14. Note how the estimates $\hat{\tau}_{ws}$ and $\hat{\tau}_{ws}$ differ due to the reasons previously discussed.

TABLE 3. Identified delays in loop (from Test 4-5).

$\hat{\tau}_{ws}$	$\hat{\tau}_{us}$	$\hat{\tau}_{wc}$	$\hat{\tau}_{cs}$
17.5 ms	13.5 ms	7.3 ms	6.2 ms

3) TEST 6: ACTUATOR MODEL IDENTIFICATION AND ASSESSMENT OF PREDICTOR PERFORMANCE USING CONTROLLER (7)

To investigate the underlying model, we now fit all data-points from Test 6 using $\beta = [\beta_0 \ \beta_{\sin} \ \beta_{\cos} \ \beta_{\text{sgn}} \ \beta_{\dot{\theta}_w} \ \beta_{\ddot{\theta}_w}]$, $y = \hat{f}$, and $X = [1 \ \sin(\theta_w) \ \cos(\theta_w) \ \text{sgn}(\theta_w) \ \theta_w \ \dot{\theta}_w]$. Table 4 presents the resulting coefficients. Figure 17(a) shows the resulting force error components for three sample periods, illustrating how the force error exhibit similar trends for varying T_2 . Figure 17(b) presents MAE_f^* as a function of the period, showing how the model explains most of the resulting error.

TABLE 4. Identified model parameters (from Test 6).

β_0	β_{\sin}	β_{\cos}	β_{sgn}	$\beta_{\dot{\theta}_w}$	$\beta_{\ddot{\theta}_w}$
0.002	-0.02	-0.1	-0.03	-0.1	-0.006

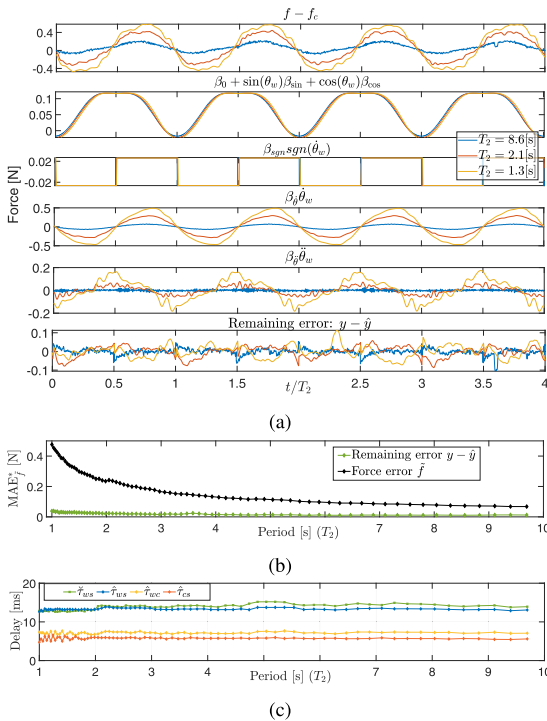


FIGURE 17. (From Test 6) Force tracking with sweeping end effector trajectory and $f_c = 8$ N. f is filtered at 10 Hz. (a) Force error separated into components for three sample periods. (b) MAE_f^* as function of period T_2 . (c) Estimated delays over the trajectory.

The estimated delays (see Figure 17(c)) remains relatively stable, and τ_{ws} is mostly independent of the period, which indicates that to model the effects of internal motor dynamics, delays, communication, and sampling as a pure time delay is an appropriate choice.

Figure 18 shows prediction performance for a sample from Test 6 where $T_2 = 1$ s, demonstrating how the predictor estimates θ_w 15 ms forward in time well (prediction was only monitored and not used in the control input in Test 6).

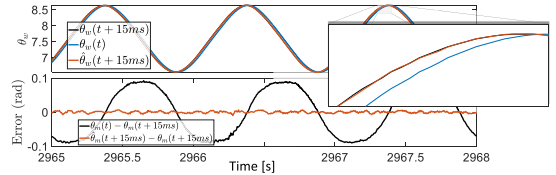


FIGURE 18. (From Test 6) Prediction performance for θ_w with $T_2 = 1$ s.

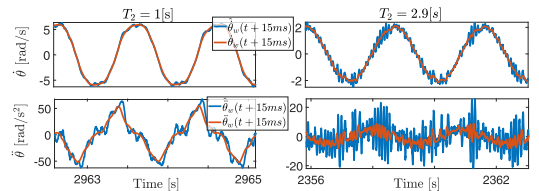


FIGURE 19. (From Test 6) Prediction performance for $\dot{\theta}_w$ and $\ddot{\theta}_w$ for two sample periods.

Figure 19 compares the predicted derivatives ($\hat{\dot{\theta}}_w$ and $\hat{\ddot{\theta}}_w$) to the benchmark estimates (that is $\dot{\theta}_w$ and $\ddot{\theta}_w$ obtained by lowpass smoothing in post-processing) for two values of T_2 . As indicated in the figure, the relative proportion of noise increases with lower velocities and accelerations.

Whereas velocities are estimated quite well, the acceleration estimates from polynomial prediction are noisier. Conversely, traditional filtering techniques would yield non-acceptable delays. This explains why we do not compensate for the inertia effects in (21).

4) TEST 7-8: ADAPTIVE DELAY PREDICTION PROCEDURE USING THE PREDICTIVE FEEDFORWARD CONTROL (17)

In this section, we use (17) with the adaptive delay prediction procedure of Section IV-A2. In Test 7 we start the prediction procedure after 50 seconds with $k_\tau = 2 \cdot 10^{-3}$. Figure 20 shows the resulting estimated delays, as well as the resulting forces and MAE_f^* for each period. While the estimated delay τ_{pred} increases until it stabilises at around 15.5 ms, the estimations for τ_{ws} behaves inversely, ending up close to zero. The position feedforward-induced errors are significantly reduced.

In Test 8 (Figure 21) we have repeated the experiment, (with $k_\tau = 2 \cdot 10^{-2}$) and added an artificial delay of one sample (5 ms) to the control loop every 80 seconds. This helps

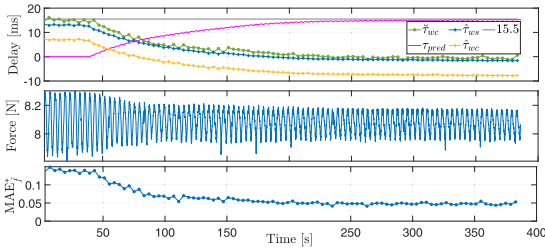


FIGURE 20. (From Test 7) Force tracking performance and time delay estimation with adaptive τ_{pred} .

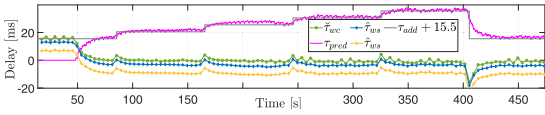


FIGURE 21. (From Test 8) Force tracking performance and time delay estimation with adaptive τ_{pred} . Artificial delay τ_{add} increases by 5 ms every 80 second.

validate that the adaptive delay prediction procedure performs accurately and adaptively.

5) TEST 9 AND TEST 6,10 AND 11: COMPARING THE PERFORMANCE OF CONTROLLERS (7), (17), AND (21)

Figure 22 shows the resulting forces from *Test 9*, where we progressively changed the controller from (7) to (17) to (21). Figure 23 compares MAE_f^* for the three controllers (*Test 6*, *Test 10*, *Test 11*) with the *sweeping end effector trajectory*. As the figures show, we reduce force errors significantly as the physical model used in the feedforward controller becomes more advanced.

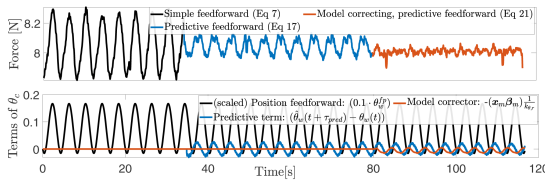


FIGURE 22. (From Test 9) Force tracking with fast end effector trajectory and $f_c = 8$ N. Progressively changing controller.

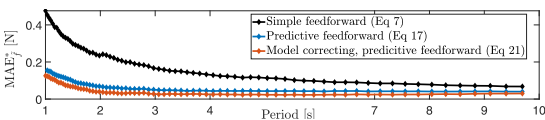
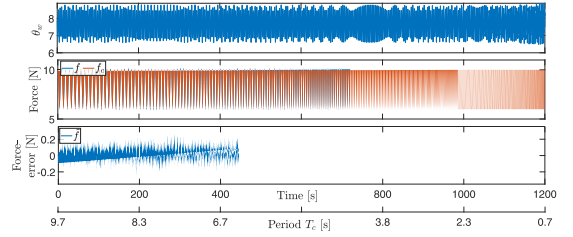


FIGURE 23. (From Test 6,10 and 11) MAE_f^* for sweeping trajectory with different controllers.

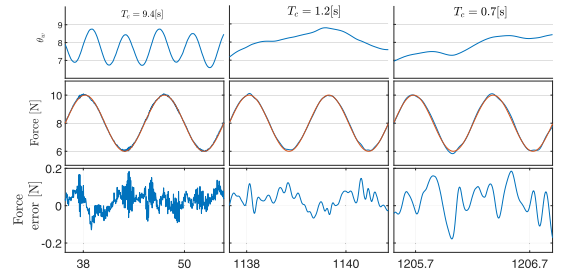
C. MOVING END EFFECTOR, VARIABLE CABLE FORCE

TEST 12: PERFORMANCE WITH CONTROLLER (21)

We have thus far considered force tracking with either fixed end effector or fixed target forces. In *Test 12*, we vary both.



(a)



(b)

FIGURE 24. (From Test 12) Tracking a variable target force with a moving end effector. f is filtered at 10 Hz. (a) Full test. (b) Three sample periods highlighted (when comparing the three samples, the difference in time scale should be kept in mind).

Figure 24 presents the resulting force tracking performance on moving objects with varying target force. Note that the end effector trajectories are not purely harmonic, since both Actuator 1 and Actuator 2 affects the end effector position, resulting in faster accelerations that further challenge the controller. The errors remain below about 0.2 N throughout the test, indicating that the proposed controller performs well.

D. SUMMARY AND KEY FINDINGS FROM EXPERIMENTAL TESTING

We have shown experimentally how force tracking accuracy is sensitive to time delays (figures 15 and 16) and how the presented actuator model can describe most of the applied force (figures 14 and 17). Moreover, we have demonstrated predictor performance (figures 18 and 19) and the adaptive delay estimation procedure (figures 20 and 21).

For accurate force control, we recommend controlling the motor shaft position θ_c using (21) – as this eliminates a large portion of the error associated with the simple feedforward control (7) (demonstrated in figures 22 and 23). We further recommend adaptively estimating and updating the spring characteristics online – to capture their time-dependent variations (demonstrated in figures 12 and 13).

Although the overall trend is that higher-frequency end-effector and target force trajectories correlate with increased force tracking errors, the errors remain low throughout the tests (figures 13, 23, and 24). This indicates that the proposed controller performs well despite significant end-effector

motions and variable target forces. This is particularly advantageous for real-time hybrid model testing – since the emulated ocean structure (and thus the attached end-effectors) typically undergo significant motions that should not disturb the cable-actuated loads.

Although a direct comparison is difficult due to variations in setup properties, objective, and non-disclosed details, the demonstrated performance of the complete control system (see Figure 24) appears promising when compared to force errors seen in relevant literature using torque-controlled servomotors.

VI. CONCLUSION

In this paper, we have studied and demonstrated how position-controlled servomotors connected to cabled drums via clocksprings might be used for force control with an accuracy of 0.2 N and bandwidth up to 1.4 Hz. The suggested control law compensates for both delays and motion-induced forces. The controller also employs online parameter estimation to improve control performance further. Through experimental testing, we conclude on good force-tracking performance on moving objects. The results are valuable for CPDR setups that use force control and, in particular, for real-time hybrid model testing of ocean structures, where accurate force control, despite significant platform motions, is of utmost importance.

APPENDIX NOMENCLATURE AND VARIABLE LIST

For simplicity, we transformed moments to forces using subscript $(\cdot)_r$ to mean $\frac{(\cdot)}{r}$. (e.g., $c_{w,r} = c_w/r$). We use bold notation to refer to sampled sets when referencing (14).

ANGULAR POSITIONS

θ_c	Commanded motor shaft angle
θ_s	Resulting motor shaft angle
θ_w	Cable drum shaft angle
θ_0	Spring equilibrium offset
$\tilde{\theta}$	Spring deflection ($\tilde{\theta} = \theta_s - \theta_w - \theta_0$)
$\dot{\theta}_w$	Drum angular velocity
$\ddot{\theta}_w$	Drum angular acceleration
θ_{c2}	Commanded shaft angle of Motor 2
$\Delta\theta_{c2}$	Amplitude of harmonic motions of θ_{c2}
$\hat{\theta}_w$	Estimate of θ_w using predictive polynomial filter
θ_c^{ff}	Force feedforward
θ_c^{fp}	Position feedforward

DELAY AND TIME INTERVALS

τ_{cs}	Feedforward delay from θ_c to θ_s
τ_{ws}	Feedforward delay from θ_w to θ_s
τ_{wc}	Feedforward delay from θ_w to θ_c
τ_{w0}	Delay in sampling of the drum shaft angle
τ_{cc}	Control cycle delay

τ_{fs}	Force feedforward delay
$\hat{\tau}$	Estimated delay using (18)
$\tilde{\tau}_{ws}$	Estimated delay using (19)
τ_{pred}	Time interval for forward prediction
T_2	Period of end-effector trajectory (controlled by Motor 2)
T_c	Period of harmonic target force
T_d	Control cycle time

ESTIMATION AND PREDICTOR VARIABLES

t_k	Time instance at the discrete sample k
$\beta_{(\cdot)}$	Coefficient corresponding to variable (\cdot)
k_τ	Integral gain for delay time estimator
MAE_f^*	Bias adjusted mean absolute force tracking error
b_0	Constant force tracking bias
M	Total number of discrete points in an interval
$(\mathbf{y}, \boldsymbol{\beta}, \mathbf{X}, \mathbf{W}, w_k, \hat{y}, m,)$	Coefficients and variables used for multiple linear regression; see Section III-3
$(\boldsymbol{\beta}_r, \mathbf{x}_r, \mathbf{H}, N, p)$	Coefficients and variables used for polynomial prediction; see Section III-4
$(\boldsymbol{\beta}_k, \mathbf{X}_k)$	Coefficients and variables corresponding to identification of spring characteristics; see Section IV-A1
$(\boldsymbol{\beta}_m, \mathbf{X}_m)$	Coefficients and variables corresponding to identification of the actuator model; see Section IV-A2

FORCES AND MOMENTS

m	Cable moment about drum centre of rotation
m_g	Weight induced moment
m_1	Static stiffness moment
m_2	Angle dependent moment ($f_2 = m_2/r$)
m_3	Moment due to transmission system damping and inertia
m_4	Moment from lumped unmodelled dynamics ($f_4 = m_4/r$)
f	Cable force
f'	Cable force filtered in post processing
f_c	Commanded cable force
\tilde{f}	Force tracking error; $\tilde{f} = f - f_c$

PROPERTIES OF THE ACTUATOR SYSTEM

r	Effective drum radius
r_0	Effective drum radius at initialization
k_r	Change of effective radius (ratio) due to winding
d_c	Cable layer thickness
n_w	Average number of parallel cables per cable layer
$\delta_{(\cdot)}$	Uncertainties in effective radius model

l_w	Stretched cable length
l_0	Stretched cable length at initialization
Δl_w	Unwound cable length
Δl_c	Cable elongation
l_0	Initial cable length
e_i	End-effector position
$\zeta_{(\cdot)}$	Uncertainties in cable length model
k_0	Hooks law constant
c_w	Linear damping coefficient
c_s	Directional damping coefficient
k_θ	Spring deflection to moment mapping
I_w	Effective inertia (drum, spring and cable)
I_s	Clockspring inertia
I_{wd}	Drum inertia

OTHER

w_{ref}	Desired cable wrench (load vector)
w	Cable wrench applied on the platform
W	Kinematic mapping from forces to wrench
$\omega_{num}, \omega_{ph}$	Environmental loads (typically hydrodynamic)
$sgn(\cdot)$	The sign function.

REFERENCES

- [1] S. Fang, D. Franitza, M. Torlo, F. Bekes, and M. Hiller, "Motion control of a tendon-based parallel manipulator using optimal tension distribution," *IEEE/ASME Trans. Mechatronics*, vol. 9, no. 3, pp. 561–568, Sep. 2004.
- [2] W. Kraus, V. Schmidt, P. Rajendra, and A. Pott, "System identification and cable force control for a cable-driven parallel robot with industrial servo drives," in *Proc. IEEE Int. Conf. Robot. Autom. (ICRA)*, May 2014, pp. 5921–5926.
- [3] M. J.-D. Otis, T.-L. Nguyen-Dang, T. Laliberte, D. Ouellet, D. Laurendeau, and C. Gosselin, "Cable tension control and analysis of reel transparency for 6-dof haptic foot platform on a cable-driven locomotion interface," *Int. J. Electr. Electron. Eng.*, vol. 3, no. 1, pp. 16–29, 2009.
- [4] V. Chabaud, "Real-time hybrid model testing of floating wind turbines," Ph.D. dissertation, NTNU, Trondheim, Norway, 2016.
- [5] T. Sauder, V. Chabaud, M. Thys, E. E. Bachynski, and L. O. S  ther, "Real-time hybrid model testing of a braceless semi-submersible wind turbine: Part I—The hybrid approach," in *Proc. Ocean Space Utilization, Ocean Renew. Energy*, Jun. 2016. [Online]. Available: <https://asmedigitalcollection.asme.org/OMAE/proceedings-abstract/OMAE2016/V006T09A039/281288>
- [6] E. S. Ueland, R. Skjetne, and S. A. Vilsen, "Force actuated real-time hybrid model testing of a moored vessel: A case study investigating force errors," *IFAC-Papers Line*, vol. 51, no. 29, pp. 74–79, 2018.
- [7] T. Sauder, S. Marelli, and A. J. S  rensen, "Probabilistic robust design of control systems for high-fidelity cyber-physical testing," *Automatica*, vol. 101, pp. 111–119, Mar. 2019.
- [8] E. Ueland, T. Sauder, and R. Skjetne, "Optimal actuator placement for real-time hybrid model testing using cable-driven parallel robots," *J. Mar. Sci. Eng.*, vol. 9, no. 2, p. 191, Feb. 2021.
- [9] A. Pott, *Cable-Driven Parallel Robots: Theory Application*, vol. 120. Cham, Switzerland: Springer, 2018.
- [10] W. Kraus, "Force control cable-driven parallel robots," Ph.D. dissertation, Fakult  t f  r Konstruktions-, Produktions- und Fahrzeugtechnik, Universit  t Stuttgart, Stuttgart, Germany, 2016.
- [11] J. Begey, L. Cuvillon, M. Lesellier, M. Gouttefarde, and J. Gangloff, "Dynamic control of parallel robots driven by flexible cables and actuated by position-controlled winches," *IEEE Trans. Robot.*, vol. 35, no. 1, pp. 286–293, Feb. 2019.
- [12] J. E. Carrion and B. F. Spencer, Jr., "Model-based strategies for real-time hybrid testing," Newmark Struct. Eng. Lab., Univ. Illinois at Urbana, Champaign, IL, USA, Tech. Rep. NSEL-006, 2007.
- [13] S. A. Vilsen, T. Sauder, A. J. S  rensen, and M. F  re, "Method for real-time hybrid model testing of ocean structures: Case study on horizontal mooring systems," *Ocean Eng.*, vol. 172, pp. 46–58, Jan. 2019.
- [14] V. Schmidt and A. Pott, "Bending cycles and cable properties of polymer fiber cables for fully constrained cable-driven parallel robots," in *Cable-Driven Parallel Robots*. Cham, Switzerland: Springer, 2018, pp. 85–94.
- [15] R. Verhoeven, "Analysis workspace tendon-based stewart platforms," Ph.D. dissertation, Fakult  t f  r Ingenieurwissenschaften, Univ. Duisburg-Essen, Duisburg, Germany, 2004.
- [16] W. Kraus, M. Kessler, and A. Pott, "Pulley friction compensation for winch-integrated cable force measurement and verification on a cable-driven parallel robot," in *Proc. IEEE Int. Conf. Robot. Autom. (ICRA)*, May 2015, pp. 1627–1632.
- [17] V. Schmidt, A. Mall, and A. Pott, "Investigating the effect of cable force on winch winding accuracy for cable-driven parallel robots," in *New Trends Mechanism Machine Science*. Cham, Switzerland: Springer, 2015, pp. 315–323.
- [18] E. Picard, S. Caro, F. Claveau, and F. Plestan, "Pulleys and force sensors influence on payload estimation of cable-driven parallel robots," in *Proc. IEEE/RSJ Int. Conf. Intell. Robots Syst. (IROS)*, Oct. 2018, pp. 1429–1436.
- [19] E. Laroche, R. Chellal, L. Cuvillon, and J. Gangloff, "A preliminary study for h_∞ control of parallel cable-driven manipulators," in *Cable-Driven Parallel Robots*. Berlin, Germany: Springer, 2013, pp. 353–369.
- [20] R. Babaghasabha, M. A. Khosravi, and H. D. Taghirad, "Adaptive robust control of fully-constrained cable driven parallel robots," *Mechatronics*, vol. 25, pp. 27–36, Feb. 2015.
- [21] G. Meunier, B. Boulet, and M. Nahon, "Control of an overactuated cable-driven parallel mechanism for a radio telescope application," *IEEE Trans. Control Syst. Technol.*, vol. 17, no. 5, pp. 1043–1054, Sep. 2009.
- [22] E. Ottaviano, G. Castelli, and G. Cannella, "A cable-based system for aiding elderly people in Sit-to-Stand Transfer," *Mech. Based Des. Struct. Mach.*, vol. 36, no. 4, pp. 310–329, Nov. 2008.
- [23] D. Mayhew, B. Bachrach, W. Z. Rymer, and R. F. Beer, "Development of the MACARM—a novel cable robot for upper limb neurorehabilitation," in *Proc. 9th Int. Conf. Rehabil. Robot.*, 2005, pp. 299–302.
- [24] T. Morizono, K. Kurahashi, and S. Kawamura, "Analysis and control of a force display system driven by parallel wire mechanism," *Robotica*, vol. 16, no. 5, pp. 551–563, Sep. 1998.
- [25] Y. Zou, H. Ma, Z. Han, Y. Song, and K. Liu, "Force control of wire driving lower limb rehabilitation robot," *Technol. Health Care*, vol. 26, pp. 399–408, May 2018.
- [26] C. Reichert, K. M  ller, and T. Bruckmann, "Robust internal force-based impedance control for cable-driven parallel robots," in *Cable-Driven Parallel Robots*. Cham, Switzerland: Springer, 2015, pp. 131–143.
- [27] O. Egeland and J. T. Gravdahl, *Modeling Simulation for Automation Control*, vol. 76. Oslo, Norway: Marine Cybernetics Trondheim, 2002.
- [28] J.-P. Merlet, "Analysis of wire elasticity for wire-driven parallel robots," in *Proc. EUCOMES*. Dordrecht, The Netherlands: Springer, 2009, pp. 471–478.
- [29] A. F. Cote, P. Cardou, and C. Gosselin, "A tension distribution algorithm for cable-driven parallel robots operating beyond their wrench-feasible workspace," in *Proc. 16th Int. Conf. Control, Autom. Syst. (ICCAS)*, Oct. 2016, pp. 68–73.
- [30] E. Ueland, T. Sauder, and R. Skjetne, "Optimal force allocation for over-constrained cable-driven parallel robots: Continuously differentiable solutions with assessment of computational efficiency," *IEEE Trans. Robot.*, vol. 37, no. 2, pp. 659–666, Apr. 2020.
- [31] R. W. Beard and T. W. McLain, *Small Unmanned Aircraft: Theory Practics*. Princeton, NJ, USA: Princeton Univ. Press, 2012.
- [32] X. Weber, L. Cuvillon, and J. Gangloff, "Active vibration canceling of a cable-driven parallel robot in modal space," in *Proc. IEEE Int. Conf. Robot. Autom. (ICRA)*, May 2015, pp. 1599–1604.
- [33] W. Deng, J. Yao, and D. Ma, "Time-varying input delay compensation for nonlinear systems with additive disturbance: An output feedback approach," *Int. J. Robust Nonlinear Control*, vol. 28, no. 1, pp. 31–52, Jan. 2018.
- [34] M. Krstic, "Input delay compensation for forward complete and strict-feedforward nonlinear systems," *IEEE Trans. Autom. Control*, vol. 55, no. 2, pp. 287–303, Feb. 2010.
- [35] S. A. Vilsen, T. Sauder, and A. J. S  rensen, "Real-time hybrid model testing of moored floating structures using nonlinear finite element simulations," in *Dynamics of Coupled Structures*, vol. 4. Cham, Switzerland: Springer, 2017, pp. 79–92.

- [36] T. Insperger, "On the approximation of delayed systems by Taylor series expansion," *J. Comput. Nonlinear Dyn.*, vol. 10, no. 2, Mar. 2015.
- [37] D. A. Freedman, *Statistical Models: Theory and Practice*. Cambridge, U.K.: Cambridge Univ. Press, 2009.
- [38] M. I. Wallace, D. J. Wagg, and S. A. Neild, "An adaptive polynomial based forward prediction algorithm for multi-actuator real-time dynamic substructuring," *Proc. Roy. Soc. A, Math., Phys. Eng. Sci.*, vol. 461, no. 2064, pp. 3807–3826, Dec. 2005.
- [39] A. W. Moore, J. G. Schneider, and K. Deng, "Efficient locally weighted polynomial regression predictions," in *Proc. Int. Mach. Learn. Conf.* Burlington, MA, USA: Morgan Kaufmann, 1997, pp. 1–5.
- [40] D. C. Montgomery, E. A. Peck, and G. G. Vining, *Introduction to Linear Regression Analysis*, vol. 821. Hoboken, NJ, USA: Wiley, 2012.
- [41] S. Valiivita, S. J. Ovaska, and O. Vainio, "Polynomial predictive filtering in control instrumentation: A review," *IEEE Trans. Ind. Electron.*, vol. 46, no. 5, pp. 876–888, 1999.
- [42] J. Jiang and Y. Zhang, "A revisit to block and recursive least squares for parameter estimation," *Comput. Electr. Eng.*, vol. 30, no. 5, pp. 403–416, Jul. 2004.
- [43] M. Z. A. Bhotto and A. Antoniou, "Robust recursive least-squares adaptive-filtering algorithm for impulsive-noise environments," *IEEE Signal Process. Lett.*, vol. 18, no. 3, pp. 185–188, Mar. 2011.
- [44] L. R. Vega, H. Rey, J. Benesty, and S. Tressens, "A fast robust recursive least-squares algorithm," *IEEE Trans. Signal Process.*, vol. 57, no. 3, pp. 1209–1216, Mar. 2009.
- [45] E. S. Ueland and R. Skjetne, "Effect of time delays and sampling in force actuated real-time hybrid testing: A case study," in *Proc. OCEANS*, Sep. 2017, pp. 1–10.



EINAR UELAND received the M.Sc. degree in marine technology from NTNU, in 2016, with a focus on marine cybernetics and robotics. He is currently finalizing of his Ph.D. fellowship with the Center of Excellence on Autonomous Marine Operations and Systems (AMOS), Department of Marine Technology, NTNU. His Ph.D. topic is on real-time hybrid model testing, which includes the use and study of cable-driven parallel robots.



THOMAS SAUDER received the joint M.Sc. degree from the Ecole Centrale de Lyon and from the Department of Marine Technology, NTNU, in 2007, and the Ph.D. degree in marine cybernetics from NTNU, in 2018. Since 2013, he has played a central role in the development of cyber-physical aempirical methods in this field. He has occupied several research and management positions with SINTEF Ocean AS, where he is currently a Senior Researcher. He is also an Associate Professor with the Department of Marine Technology, NTNU. His research interests include numerical and experimental methods in marine hydrodynamics.



ROGER SKJETNE (Senior Member, IEEE) received the M.Sc. degree from the University of California at Santa Barbara (UCSB), in 2000, and the Ph.D. degree in control engineering from NTNU, in 2005. From 2004 to 2009, he worked in Marine Cybernetics on Hardware-In-the-Loop verification of marine control systems. Since August 2009, he has held the Kongsberg Maritime Chair of Professor in marine control engineering with the Department of Marine Technology, NTNU. His research interests include dynamic positioning of ships, control of marine hybrid electric power systems, and nonlinear and autonomous motion control of ships and marine structures.

• • •

Part III

Previous PhD theses published at the Department of Marine Technology

**Previous PhD theses published at the Department of Marine Technology
(earlier: Faculty of Marine Technology)
NORWEGIAN UNIVERSITY OF SCIENCE AND TECHNOLOGY**

Report No.	Author	Title
	Kavlie, Dag	Optimization of Plane Elastic Grillages, 1967
	Hansen, Hans R.	Man-Machine Communication and Data-Storage Methods in Ship Structural Design, 1971
	Gisvold, Kaare M.	A Method for non-linear mixed -integer programming and its Application to Design Problems, 1971
	Lund, Sverre	Tanker Frame Optimalization by means of SUMT-Transformation and Behaviour Models, 1971
	Vinje, Tor	On Vibration of Spherical Shells Interacting with Fluid, 1972
	Lorentz, Jan D.	Tank Arrangement for Crude Oil Carriers in Accordance with the new Anti-Pollution Regulations, 1975
	Carlsen, Carl A.	Computer-Aided Design of Tanker Structures, 1975
	Larsen, Carl M.	Static and Dynamic Analysis of Offshore Pipelines during Installation, 1976
UR-79-01	Brigt Hatlestad, MK	The finite element method used in a fatigue evaluation of fixed offshore platforms. (Dr.Ing. Thesis)
UR-79-02	Erik Pettersen, MK	Analysis and design of cellular structures. (Dr.Ing. Thesis)
UR-79-03	Sverre Valsgård, MK	Finite difference and finite element methods applied to nonlinear analysis of plated structures. (Dr.Ing. Thesis)
UR-79-04	Nils T. Nordsve, MK	Finite element collapse analysis of structural members considering imperfections and stresses due to fabrication. (Dr.Ing. Thesis)
UR-79-05	Ivar J. Fylling, MK	Analysis of towline forces in ocean towing systems. (Dr.Ing. Thesis)
UR-80-06	Nils Sandsmark, MM	Analysis of Stationary and Transient Heat Conduction by the Use of the Finite Element Method. (Dr.Ing. Thesis)
UR-80-09	Sverre Haver, MK	Analysis of uncertainties related to the stochastic modeling of ocean waves. (Dr.Ing. Thesis)
UR-81-15	Odland, Jonas	On the Strength of welded Ring stiffened cylindrical Shells primarily subjected to axial Compression
UR-82-17	Engesvik, Knut	Analysis of Uncertainties in the fatigue Capacity of

Welded Joints

UR-82-18	Rye, Henrik	Ocean wave groups
UR-83-30	Eide, Oddvar Inge	On Cumulative Fatigue Damage in Steel Welded Joints
UR-83-33	Mo, Olav	Stochastic Time Domain Analysis of Slender Offshore Structures
UR-83-34	Amdahl, Jørgen	Energy absorption in Ship-platform impacts
UR-84-37	Mørch, Morten	Motions and mooring forces of semi submersibles as determined by full-scale measurements and theoretical analysis
UR-84-38	Soares, C. Guedes	Probabilistic models for load effects in ship structures
UR-84-39	Aarsnes, Jan V.	Current forces on ships
UR-84-40	Czujko, Jerzy	Collapse Analysis of Plates subjected to Biaxial Compression and Lateral Load
UR-85-46	Alf G. Engseth, MK	Finite element collapse analysis of tubular steel offshore structures. (Dr.Ing. Thesis)
UR-86-47	Dengody Sheshappa, MP	A Computer Design Model for Optimizing Fishing Vessel Designs Based on Techno-Economic Analysis. (Dr.Ing. Thesis)
UR-86-48	Vidar Aanesland, MH	A Theoretical and Numerical Study of Ship Wave Resistance. (Dr.Ing. Thesis)
UR-86-49	Heinz-Joachim Wessel, MK	Fracture Mechanics Analysis of Crack Growth in Plate Girders. (Dr.Ing. Thesis)
UR-86-50	Jon Taby, MK	Ultimate and Post-ultimate Strength of Dented Tubular Members. (Dr.Ing. Thesis)
UR-86-51	Walter Lian, MH	A Numerical Study of Two-Dimensional Separated Flow Past Bluff Bodies at Moderate KC-Numbers. (Dr.Ing. Thesis)
UR-86-52	Bjørn Sortland, MH	Force Measurements in Oscillating Flow on Ship Sections and Circular Cylinders in a U-Tube Water Tank. (Dr.Ing. Thesis)
UR-86-53	Kurt Strand, MM	A System Dynamic Approach to One-dimensional Fluid Flow. (Dr.Ing. Thesis)
UR-86-54	Arne Edvin Løken, MH	Three Dimensional Second Order Hydrodynamic Effects on Ocean Structures in Waves. (Dr.Ing. Thesis)
UR-86-55	Sigurd Falch, MH	A Numerical Study of Slamming of Two-Dimensional Bodies. (Dr.Ing. Thesis)
UR-87-56	Arne Braathen, MH	Application of a Vortex Tracking Method to the Prediction of Roll Damping of a Two-Dimension Floating Body. (Dr.Ing. Thesis)

UR-87-57	Bernt Leira, MK	Gaussian Vector Processes for Reliability Analysis involving Wave-Induced Load Effects. (Dr.Ing. Thesis)
UR-87-58	Magnus Småvik, MM	Thermal Load and Process Characteristics in a Two-Stroke Diesel Engine with Thermal Barriers (in Norwegian). (Dr.Ing. Thesis)
MTA-88-59	Bernt Arild Bremdal, MP	An Investigation of Marine Installation Processes – A Knowledge - Based Planning Approach. (Dr.Ing. Thesis)
MTA-88-60	Xu Jun, MK	Non-linear Dynamic Analysis of Space-framed Offshore Structures. (Dr.Ing. Thesis)
MTA-89-61	Gang Miao, MH	Hydrodynamic Forces and Dynamic Responses of Circular Cylinders in Wave Zones. (Dr.Ing. Thesis)
MTA-89-62	Martin Greenhow, MH	Linear and Non-Linear Studies of Waves and Floating Bodies. Part I and Part II. (Dr.Techn. Thesis)
MTA-89-63	Chang Li, MH	Force Coefficients of Spheres and Cubes in Oscillatory Flow with and without Current. (Dr.Ing. Thesis)
MTA-89-64	Hu Ying, MP	A Study of Marketing and Design in Development of Marine Transport Systems. (Dr.Ing. Thesis)
MTA-89-65	Arild Jæger, MH	Seakeeping, Dynamic Stability and Performance of a Wedge Shaped Planing Hull. (Dr.Ing. Thesis)
MTA-89-66	Chan Siu Hung, MM	The dynamic characteristics of tilting-pad bearings
MTA-89-67	Kim Wikstrøm, MP	Analysis av projekteringen for ett offshore projekt. (Licenciat-avhandling)
MTA-89-68	Jiao Guoyang, MK	Reliability Analysis of Crack Growth under Random Loading, considering Model Updating. (Dr.Ing. Thesis)
MTA-89-69	Arnt Olufsen, MK	Uncertainty and Reliability Analysis of Fixed Offshore Structures. (Dr.Ing. Thesis)
MTA-89-70	Wu Yu-Lin, MR	System Reliability Analyses of Offshore Structures using improved Truss and Beam Models. (Dr.Ing. Thesis)
MTA-90-71	Jan Roger Hoff, MH	Three-dimensional Green function of a vessel with forward speed in waves. (Dr.Ing. Thesis)
MTA-90-72	Rong Zhao, MH	Slow-Drift Motions of a Moored Two-Dimensional Body in Irregular Waves. (Dr.Ing. Thesis)
MTA-90-73	Atle Minsaas, MP	Economical Risk Analysis. (Dr.Ing. Thesis)
MTA-90-74	Knut-Aril Farnes, MK	Long-term Statistics of Response in Non-linear Marine Structures. (Dr.Ing. Thesis)
MTA-90-75	Torbjørn Sotberg, MK	Application of Reliability Methods for Safety Assessment of Submarine Pipelines. (Dr.Ing. Thesis)

		Thesis)
MTA-90-76	Zeuthen, Steffen, MP	SEAMAID. A computational model of the design process in a constraint-based logic programming environment. An example from the offshore domain. (Dr.Ing. Thesis)
MTA-91-77	Haagensen, Sven, MM	Fuel Dependant Cyclic Variability in a Spark Ignition Engine - An Optical Approach. (Dr.Ing. Thesis)
MTA-91-78	Løland, Geir, MH	Current forces on and flow through fish farms. (Dr.Ing. Thesis)
MTA-91-79	Hoen, Christopher, MK	System Identification of Structures Excited by Stochastic Load Processes. (Dr.Ing. Thesis)
MTA-91-80	Haugen, Stein, MK	Probabilistic Evaluation of Frequency of Collision between Ships and Offshore Platforms. (Dr.Ing. Thesis)
MTA-91-81	Sødahl, Nils, MK	Methods for Design and Analysis of Flexible Risers. (Dr.Ing. Thesis)
MTA-91-82	Ormberg, Harald, MK	Non-linear Response Analysis of Floating Fish Farm Systems. (Dr.Ing. Thesis)
MTA-91-83	Marley, Mark J., MK	Time Variant Reliability under Fatigue Degradation. (Dr.Ing. Thesis)
MTA-91-84	Krokstad, Jørgen R., MH	Second-order Loads in Multidirectional Seas. (Dr.Ing. Thesis)
MTA-91-85	Molteberg, Gunnar A., MM	The Application of System Identification Techniques to Performance Monitoring of Four Stroke Turbocharged Diesel Engines. (Dr.Ing. Thesis)
MTA-92-86	Mørch, Hans Jørgen Bjelke, MH	Aspects of Hydrofoil Design: with Emphasis on Hydrofoil Interaction in Calm Water. (Dr.Ing. Thesis)
MTA-92-87	Chan Siu Hung, MM	Nonlinear Analysis of Rotordynamic Instabilities in Highspeed Turbomachinery. (Dr.Ing. Thesis)
MTA-92-88	Bessason, Bjarni, MK	Assessment of Earthquake Loading and Response of Seismically Isolated Bridges. (Dr.Ing. Thesis)
MTA-92-89	Langli, Geir, MP	Improving Operational Safety through exploitation of Design Knowledge - an investigation of offshore platform safety. (Dr.Ing. Thesis)
MTA-92-90	Sævik, Svein, MK	On Stresses and Fatigue in Flexible Pipes. (Dr.Ing. Thesis)
MTA-92-91	Ask, Tor Ø., MM	Ignition and Flame Growth in Lean Gas-Air Mixtures. An Experimental Study with a Schlieren System. (Dr.Ing. Thesis)
MTA-86-92	Hessen, Gunnar, MK	Fracture Mechanics Analysis of Stiffened Tubular Members. (Dr.Ing. Thesis)

MTA-93-93	Steinebach, Christian, MM	Knowledge Based Systems for Diagnosis of Rotating Machinery. (Dr.Ing. Thesis)
MTA-93-94	Dalane, Jan Inge, MK	System Reliability in Design and Maintenance of Fixed Offshore Structures. (Dr.Ing. Thesis)
MTA-93-95	Steen, Sverre, MH	Cobblestone Effect on SES. (Dr.Ing. Thesis)
MTA-93-96	Karunakaran, Daniel, MK	Nonlinear Dynamic Response and Reliability Analysis of Drag-dominated Offshore Platforms. (Dr.Ing. Thesis)
MTA-93-97	Hagen, Arnulf, MP	The Framework of a Design Process Language. (Dr.Ing. Thesis)
MTA-93-98	Nordrik, Rune, MM	Investigation of Spark Ignition and Autoignition in Methane and Air Using Computational Fluid Dynamics and Chemical Reaction Kinetics. A Numerical Study of Ignition Processes in Internal Combustion Engines. (Dr.Ing. Thesis)
MTA-94-99	Passano, Elizabeth, MK	Efficient Analysis of Nonlinear Slender Marine Structures. (Dr.Ing. Thesis)
MTA-94-100	Kvålsvold, Jan, MH	Hydroelastic Modelling of Wetdeck Slamming on Multihull Vessels. (Dr.Ing. Thesis)
MTA-94-102	Bech, Sidsel M., MK	Experimental and Numerical Determination of Stiffness and Strength of GRP/PVC Sandwich Structures. (Dr.Ing. Thesis)
MTA-95-103	Paulsen, Hallvard, MM	A Study of Transient Jet and Spray using a Schlieren Method and Digital Image Processing. (Dr.Ing. Thesis)
MTA-95-104	Hovde, Geir Olav, MK	Fatigue and Overload Reliability of Offshore Structural Systems, Considering the Effect of Inspection and Repair. (Dr.Ing. Thesis)
MTA-95-105	Wang, Xiaozhi, MK	Reliability Analysis of Production Ships with Emphasis on Load Combination and Ultimate Strength. (Dr.Ing. Thesis)
MTA-95-106	Ulstein, Tore, MH	Nonlinear Effects of a Flexible Stern Seal Bag on Cobblestone Oscillations of an SES. (Dr.Ing. Thesis)
MTA-95-107	Solaas, Frøydis, MH	Analytical and Numerical Studies of Sloshing in Tanks. (Dr.Ing. Thesis)
MTA-95-108	Hellan, Øyvind, MK	Nonlinear Pushover and Cyclic Analyses in Ultimate Limit State Design and Reassessment of Tubular Steel Offshore Structures. (Dr.Ing. Thesis)
MTA-95-109	Hermundstad, Ole A., MK	Theoretical and Experimental Hydroelastic Analysis of High Speed Vessels. (Dr.Ing. Thesis)
MTA-96-110	Bratland, Anne K., MH	Wave-Current Interaction Effects on Large-Volume Bodies in Water of Finite Depth. (Dr.Ing. Thesis)
MTA-96-111	Herfjord, Kjell, MH	A Study of Two-dimensional Separated Flow by a Combination of the Finite Element Method and

		Navier-Stokes Equations. (Dr.Ing. Thesis)
MTA-96-112	Æsøy, Vilmar, MM	Hot Surface Assisted Compression Ignition in a Direct Injection Natural Gas Engine. (Dr.Ing. Thesis)
MTA-96-113	Eknes, Monika L., MK	Escalation Scenarios Initiated by Gas Explosions on Offshore Installations. (Dr.Ing. Thesis)
MTA-96-114	Erikstad, Stein O., MP	A Decision Support Model for Preliminary Ship Design. (Dr.Ing. Thesis)
MTA-96-115	Pedersen, Egil, MH	A Nautical Study of Towed Marine Seismic Streamer Cable Configurations. (Dr.Ing. Thesis)
MTA-97-116	Moksnes, Paul O., MM	Modelling Two-Phase Thermo-Fluid Systems Using Bond Graphs. (Dr.Ing. Thesis)
MTA-97-117	Halse, Karl H., MK	On Vortex Shedding and Prediction of Vortex-Induced Vibrations of Circular Cylinders. (Dr.Ing. Thesis)
MTA-97-118	Igland, Ragnar T., MK	Reliability Analysis of Pipelines during Laying, considering Ultimate Strength under Combined Loads. (Dr.Ing. Thesis)
MTA-97-119	Pedersen, Hans-P., MP	Levendefiskteknologi for fiskefartøy. (Dr.Ing. Thesis)
MTA-98-120	Vikestad, Kyrre, MK	Multi-Frequency Response of a Cylinder Subjected to Vortex Shedding and Support Motions. (Dr.Ing. Thesis)
MTA-98-121	Azadi, Mohammad R. E., MK	Analysis of Static and Dynamic Pile-Soil-Jacket Behaviour. (Dr.Ing. Thesis)
MTA-98-122	Ulltang, Terje, MP	A Communication Model for Product Information. (Dr.Ing. Thesis)
MTA-98-123	Torbergsen, Erik, MM	Impeller/Diffuser Interaction Forces in Centrifugal Pumps. (Dr.Ing. Thesis)
MTA-98-124	Hansen, Edmond, MH	A Discrete Element Model to Study Marginal Ice Zone Dynamics and the Behaviour of Vessels Moored in Broken Ice. (Dr.Ing. Thesis)
MTA-98-125	Videiro, Paulo M., MK	Reliability Based Design of Marine Structures. (Dr.Ing. Thesis)
MTA-99-126	Mainçon, Philippe, MK	Fatigue Reliability of Long Welds Application to Titanium Risers. (Dr.Ing. Thesis)
MTA-99-127	Haugen, Elin M., MH	Hydroelastic Analysis of Slamming on Stiffened Plates with Application to Catamaran Wetdecks. (Dr.Ing. Thesis)
MTA-99-128	Langhelle, Nina K., MK	Experimental Validation and Calibration of Nonlinear Finite Element Models for Use in Design of Aluminium Structures Exposed to Fire. (Dr.Ing. Thesis)
MTA-99-	Berstad, Are J., MK	Calculation of Fatigue Damage in Ship Structures.

129		(Dr.Ing. Thesis)
MTA-99-130	Andersen, Trond M., MM	Short Term Maintenance Planning. (Dr.Ing. Thesis)
MTA-99-131	Tveiten, Bård Wathne, MK	Fatigue Assessment of Welded Aluminium Ship Details. (Dr.Ing. Thesis)
MTA-99-132	Søreide, Fredrik, MP	Applications of underwater technology in deep water archaeology. Principles and practice. (Dr.Ing. Thesis)
MTA-99-133	Tønnessen, Rune, MH	A Finite Element Method Applied to Unsteady Viscous Flow Around 2D Blunt Bodies With Sharp Corners. (Dr.Ing. Thesis)
MTA-99-134	Elvekrok, Dag R., MP	Engineering Integration in Field Development Projects in the Norwegian Oil and Gas Industry. The Supplier Management of Norne. (Dr.Ing. Thesis)
MTA-99-135	Fagerholt, Kjetil, MP	Optimeringsbaserte Metoder for Ruteplanlegging innen skipsfart. (Dr.Ing. Thesis)
MTA-99-136	Bysveen, Marie, MM	Visualization in Two Directions on a Dynamic Combustion Rig for Studies of Fuel Quality. (Dr.Ing. Thesis)
MTA-2000-137	Storteig, Eskild, MM	Dynamic characteristics and leakage performance of liquid annular seals in centrifugal pumps. (Dr.Ing. Thesis)
MTA-2000-138	Sagli, Gro, MK	Model uncertainty and simplified estimates of long term extremes of hull girder loads in ships. (Dr.Ing. Thesis)
MTA-2000-139	Tronstad, Harald, MK	Nonlinear analysis and design of cable net structures like fishing gear based on the finite element method. (Dr.Ing. Thesis)
MTA-2000-140	Kroneberg, André, MP	Innovation in shipping by using scenarios. (Dr.Ing. Thesis)
MTA-2000-141	Haslum, Herbjørn Alf, MH	Simplified methods applied to nonlinear motion of spar platforms. (Dr.Ing. Thesis)
MTA-2001-142	Samdal, Ole Johan, MM	Modelling of Degradation Mechanisms and Stressor Interaction on Static Mechanical Equipment Residual Lifetime. (Dr.Ing. Thesis)
MTA-2001-143	Baarholm, Rolf Jarle, MH	Theoretical and experimental studies of wave impact underneath decks of offshore platforms. (Dr.Ing. Thesis)
MTA-2001-144	Wang, Lihua, MK	Probabilistic Analysis of Nonlinear Wave-induced Loads on Ships. (Dr.Ing. Thesis)
MTA-2001-145	Kristensen, Odd H. Holt, MK	Ultimate Capacity of Aluminium Plates under Multiple Loads, Considering HAZ Properties. (Dr.Ing. Thesis)
MTA-2001-146	Greco, Marilena, MH	A Two-Dimensional Study of Green-Water

			Loading. (Dr.Ing. Thesis)
MTA-2001-147	Heggelund, Svein E., MK		Calculation of Global Design Loads and Load Effects in Large High Speed Catamarans. (Dr.Ing. Thesis)
MTA-2001-148	Babalola, Olusegun T., MK		Fatigue Strength of Titanium Risers – Defect Sensitivity. (Dr.Ing. Thesis)
MTA-2001-149	Mohammed, Abuu K., MK		Nonlinear Shell Finite Elements for Ultimate Strength and Collapse Analysis of Ship Structures. (Dr.Ing. Thesis)
MTA-2002-150	Holmedal, Lars E., MH		Wave-current interactions in the vicinity of the sea bed. (Dr.Ing. Thesis)
MTA-2002-151	Rognebakke, Olav F., MH		Sloshing in rectangular tanks and interaction with ship motions. (Dr.Ing. Thesis)
MTA-2002-152	Lader, Pål Furset, MH		Geometry and Kinematics of Breaking Waves. (Dr.Ing. Thesis)
MTA-2002-153	Yang, Qinzheng, MH		Wash and wave resistance of ships in finite water depth. (Dr.Ing. Thesis)
MTA-2002-154	Melhus, Øyvinn, MM		Utilization of VOC in Diesel Engines. Ignition and combustion of VOC released by crude oil tankers. (Dr.Ing. Thesis)
MTA-2002-155	Ronæss, Marit, MH		Wave Induced Motions of Two Ships Advancing on Parallel Course. (Dr.Ing. Thesis)
MTA-2002-156	Økland, Ole D., MK		Numerical and experimental investigation of whipping in twin hull vessels exposed to severe wet deck slamming. (Dr.Ing. Thesis)
MTA-2002-157	Ge, Chunhua, MK		Global Hydroelastic Response of Catamarans due to Wet Deck Slamming. (Dr.Ing. Thesis)
MTA-2002-158	Byklum, Eirik, MK		Nonlinear Shell Finite Elements for Ultimate Strength and Collapse Analysis of Ship Structures. (Dr.Ing. Thesis)
IMT-2003-1	Chen, Haibo, MK		Probabilistic Evaluation of FPSO-Tanker Collision in Tandem Offloading Operation. (Dr.Ing. Thesis)
IMT-2003-2	Skaugset, Kjetil Bjørn, MK		On the Suppression of Vortex Induced Vibrations of Circular Cylinders by Radial Water Jets. (Dr.Ing. Thesis)
IMT-2003-3	Chezhan, Muthu		Three-Dimensional Analysis of Slamming. (Dr.Ing. Thesis)
IMT-2003-4	Buhaug, Øyvind		Deposit Formation on Cylinder Liner Surfaces in Medium Speed Engines. (Dr.Ing. Thesis)
IMT-2003-5	Tregde, Vidar		Aspects of Ship Design: Optimization of Aft Hull with Inverse Geometry Design. (Dr.Ing. Thesis)
IMT-	Wist, Hanne Therese		Statistical Properties of Successive Ocean Wave

2003-6		Parameters. (Dr.Ing. Thesis)
IMT-2004-7	Ransau, Samuel	Numerical Methods for Flows with Evolving Interfaces. (Dr.Ing. Thesis)
IMT-2004-8	Soma, Torkel	Blue-Chip or Sub-Standard. A data interrogation approach of identity safety characteristics of shipping organization. (Dr.Ing. Thesis)
IMT-2004-9	Ersdal, Svein	An experimental study of hydrodynamic forces on cylinders and cables in near axial flow. (Dr.Ing. Thesis)
IMT-2005-10	Brodtkorb, Per Andreas	The Probability of Occurrence of Dangerous Wave Situations at Sea. (Dr.Ing. Thesis)
IMT-2005-11	Yttervik, Rune	Ocean current variability in relation to offshore engineering. (Dr.Ing. Thesis)
IMT-2005-12	Fredheim, Arne	Current Forces on Net-Structures. (Dr.Ing. Thesis)
IMT-2005-13	Heggemes, Kjetil	Flow around marine structures. (Dr.Ing. Thesis)
IMT-2005-14	Fouques, Sebastien	Lagrangian Modelling of Ocean Surface Waves and Synthetic Aperture Radar Wave Measurements. (Dr.Ing. Thesis)
IMT-2006-15	Holm, Håvard	Numerical calculation of viscous free surface flow around marine structures. (Dr.Ing. Thesis)
IMT-2006-16	Bjørheim, Lars G.	Failure Assessment of Long Through Thickness Fatigue Cracks in Ship Hulls. (Dr.Ing. Thesis)
IMT-2006-17	Hansson, Lisbeth	Safety Management for Prevention of Occupational Accidents. (Dr.Ing. Thesis)
IMT-2006-18	Zhu, Xinying	Application of the CIP Method to Strongly Nonlinear Wave-Body Interaction Problems. (Dr.Ing. Thesis)
IMT-2006-19	Reite, Karl Johan	Modelling and Control of Trawl Systems. (Dr.Ing. Thesis)
IMT-2006-20	Smogeli, Øyvind Notland	Control of Marine Propellers. From Normal to Extreme Conditions. (Dr.Ing. Thesis)
IMT-2007-21	Storhaug, Gaute	Experimental Investigation of Wave Induced Vibrations and Their Effect on the Fatigue Loading of Ships. (Dr.Ing. Thesis)
IMT-2007-22	Sun, Hui	A Boundary Element Method Applied to Strongly Nonlinear Wave-Body Interaction Problems. (PhD Thesis, CeSOS)
IMT-2007-23	Rustad, Anne Marthine	Modelling and Control of Top Tensioned Risers. (PhD Thesis, CeSOS)
IMT-2007-24	Johansen, Vegar	Modelling flexible slender system for real-time simulations and control applications
IMT-2007-25	Wroldsen, Anders Sunde	Modelling and control of tensegrity structures.

(PhD Thesis, CeSOS)

IMT-2007-26	Aronsen, Kristoffer Høye	An experimental investigation of in-line and combined inline and cross flow vortex induced vibrations. (Dr. avhandling, IMT)
IMT-2007-27	Gao, Zhen	Stochastic Response Analysis of Mooring Systems with Emphasis on Frequency-domain Analysis of Fatigue due to Wide-band Response Processes (PhD Thesis, CeSOS)
IMT-2007-28	Thorstensen, Tom Anders	Lifetime Profit Modelling of Ageing Systems Utilizing Information about Technical Condition. (Dr.ing. thesis, IMT)
IMT-2008-29	Refsnes, Jon Erling Gorset	Nonlinear Model-Based Control of Slender Body AUVs (PhD Thesis, IMT)
IMT-2008-30	Berntsen, Per Ivar B.	Structural Reliability Based Position Mooring. (PhD-Thesis, IMT)
IMT-2008-31	Ye, Naiquan	Fatigue Assessment of Aluminium Welded Box-stiffener Joints in Ships (Dr.ing. thesis, IMT)
IMT-2008-32	Radan, Damir	Integrated Control of Marine Electrical Power Systems. (PhD-Thesis, IMT)
IMT-2008-33	Thomassen, Paul	Methods for Dynamic Response Analysis and Fatigue Life Estimation of Floating Fish Cages. (Dr.ing. thesis, IMT)
IMT-2008-34	Pákozdi, Csaba	A Smoothed Particle Hydrodynamics Study of Two-dimensional Nonlinear Sloshing in Rectangular Tanks. (Dr.ing.thesis, IMT/ CeSOS)
IMT-2007-35	Grytøyr, Guttorm	A Higher-Order Boundary Element Method and Applications to Marine Hydrodynamics. (Dr.ing.thesis, IMT)
IMT-2008-36	Drummen, Ingo	Experimental and Numerical Investigation of Nonlinear Wave-Induced Load Effects in Containerships considering Hydroelasticity. (PhD thesis, CeSOS)
IMT-2008-37	Skejic, Renato	Maneuvering and Seakeeping of a Singel Ship and of Two Ships in Interaction. (PhD-Thesis, CeSOS)
IMT-2008-38	Harlem, Alf	An Age-Based Replacement Model for Repairable Systems with Attention to High-Speed Marine Diesel Engines. (PhD-Thesis, IMT)
IMT-2008-39	Alsos, Hagbart S.	Ship Grounding. Analysis of Ductile Fracture, Bottom Damage and Hull Girder Response. (PhD-thesis, IMT)
IMT-2008-40	Graczyk, Mateusz	Experimental Investigation of Sloshing Loading and Load Effects in Membrane LNG Tanks Subjected to Random Excitation. (PhD-thesis, CeSOS)
IMT-2008-41	Taghypour, Reza	Efficient Prediction of Dynamic Response for Flexible amd Multi-body Marine Structures. (PhD-

		thesis, CeSOS)
IMT-2008-42	Ruth, Eivind	Propulsion control and thrust allocation on marine vessels. (PhD thesis, CeSOS)
IMT-2008-43	Nystad, Bent Helge	Technical Condition Indexes and Remaining Useful Life of Aggregated Systems. PhD thesis, IMT
IMT-2008-44	Soni, Prashant Kumar	Hydrodynamic Coefficients for Vortex Induced Vibrations of Flexible Beams, PhD thesis, CeSOS
IMT-2009-45	Amlashi, Hadi K.K.	Ultimate Strength and Reliability-based Design of Ship Hulls with Emphasis on Combined Global and Local Loads. PhD Thesis, IMT
IMT-2009-46	Pedersen, Tom Arne	Bond Graph Modelling of Marine Power Systems. PhD Thesis, IMT
IMT-2009-47	Kristiansen, Trygve	Two-Dimensional Numerical and Experimental Studies of Piston-Mode Resonance. PhD-Thesis, CeSOS
IMT-2009-48	Ong, Muk Chen	Applications of a Standard High Reynolds Number Model and a Stochastic Scour Prediction Model for Marine Structures. PhD-thesis, IMT
IMT-2009-49	Hong, Lin	Simplified Analysis and Design of Ships subjected to Collision and Grounding. PhD-thesis, IMT
IMT-2009-50	Koushan, Kamran	Vortex Induced Vibrations of Free Span Pipelines, PhD thesis, IMT
IMT-2009-51	Korsvik, Jarl Eirik	Heuristic Methods for Ship Routing and Scheduling. PhD-thesis, IMT
IMT-2009-52	Lee, Jihoon	Experimental Investigation and Numerical in Analyzing the Ocean Current Displacement of Longlines. Ph.d.-Thesis, IMT.
IMT-2009-53	Vestbøstad, Tone Gran	A Numerical Study of Wave-in-Deck Impact using a Two-Dimensional Constrained Interpolation Profile Method, Ph.d.thesis, CeSOS.
IMT-2009-54	Bruun, Kristine	Bond Graph Modelling of Fuel Cells for Marine Power Plants. Ph.d.-thesis, IMT
IMT 2009-55	Holstad, Anders	Numerical Investigation of Turbulence in a Sekwed Three-Dimensional Channel Flow, Ph.d.-thesis, IMT.
IMT 2009-56	Ayala-Uraga, Efen	Reliability-Based Assessment of Deteriorating Ship-shaped Offshore Structures, Ph.d.-thesis, IMT
IMT 2009-57	Kong, Xiangjun	A Numerical Study of a Damaged Ship in Beam Sea Waves. Ph.d.-thesis, IMT/CeSOS.
IMT 2010-58	Kristiansen, David	Wave Induced Effects on Floaters of Aquaculture Plants, Ph.d.-thesis, CeSOS.

IMT 2010-59	Ludvigsen, Martin	An ROV-Toolbox for Optical and Acoustic Scientific Seabed Investigation. Ph.d.-thesis IMT.
IMT 2010-60	Hals, Jørgen	Modelling and Phase Control of Wave-Energy Converters. Ph.d.thesis, CeSOS.
IMT 2010- 61	Shu, Zhi	Uncertainty Assessment of Wave Loads and Ultimate Strength of Tankers and Bulk Carriers in a Reliability Framework. Ph.d. Thesis, IMT/ CeSOS
IMT 2010-62	Shao, Yanlin	Numerical Potential-Flow Studies on Weakly-Nonlinear Wave-Body Interactions with/without Small Forward Speed, Ph.d.thesis,CeSOS.
IMT 2010-63	Califano, Andrea	Dynamic Loads on Marine Propellers due to Intermittent Ventilation. Ph.d.thesis, IMT.
IMT 2010-64	El Khoury, George	Numerical Simulations of Massively Separated Turbulent Flows, Ph.d.-thesis, IMT
IMT 2010-65	Seim, Knut Sponheim	Mixing Process in Dense Overflows with Emphasis on the Faroe Bank Channel Overflow. Ph.d.thesis, IMT
IMT 2010-66	Jia, Huirong	Structural Analysis of Intact and Damaged Ships in a Collision Risk Analysis Perspective. Ph.d.thesis CeSoS.
IMT 2010-67	Jiao, Linlin	Wave-Induced Effects on a Pontoon-type Very Large Floating Structures (VLFS). Ph.D.-thesis, CeSOS.
IMT 2010-68	Abrahamsen, Bjørn Christian	Sloshing Induced Tank Roof with Entrapped Air Pocket. Ph.d.thesis, CeSOS.
IMT 2011-69	Karimirad, Madjid	Stochastic Dynamic Response Analysis of Spar-Type Wind Turbines with Catenary or Taut Mooring Systems. Ph.d.-thesis, CeSOS.
IMT - 2011-70	Erlend Meland	Condition Monitoring of Safety Critical Valves. Ph.d.-thesis, IMT.
IMT – 2011-71	Yang, Limin	Stochastic Dynamic System Analysis of Wave Energy Converter with Hydraulic Power Take-Off, with Particular Reference to Wear Damage Analysis, Ph.d. Thesis, CeSOS.
IMT – 2011-72	Visscher, Jan	Application of Particle Image Velocimetry on Turbulent Marine Flows, Ph.d.Thesis, IMT.
IMT – 2011-73	Su, Biao	Numerical Predictions of Global and Local Ice Loads on Ships. Ph.d.Thesis, CeSOS.
IMT – 2011-74	Liu, Zhenhui	Analytical and Numerical Analysis of Iceberg Collision with Ship Structures. Ph.d.Thesis, IMT.
IMT – 2011-75	Aarsæther, Karl Gunnar	Modeling and Analysis of Ship Traffic by Observation and Numerical Simulation. Ph.d.Thesis, IMT.

Imt – 2011-76	Wu, Jie	Hydrodynamic Force Identification from Stochastic Vortex Induced Vibration Experiments with Slender Beams. Ph.d.Thesis, IMT.
Imt – 2011-77	Amini, Hamid	Azimuth Propulsors in Off-design Conditions. Ph.d.Thesis, IMT.
IMT – 2011-78	Nguyen, Tan-Hoi	Toward a System of Real-Time Prediction and Monitoring of Bottom Damage Conditions During Ship Grounding. Ph.d.thesis, IMT.
IMT- 2011-79	Tavakoli, Mohammad T.	Assessment of Oil Spill in Ship Collision and Grounding, Ph.d.thesis, IMT.
IMT- 2011-80	Guo, Bingjie	Numerical and Experimental Investigation of Added Resistance in Waves. Ph.d.Thesis, IMT.
IMT- 2011-81	Chen, Qiaofeng	Ultimate Strength of Aluminium Panels, considering HAZ Effects, IMT
IMT- 2012-82	Kota, Ravikiran S.	Wave Loads on Decks of Offshore Structures in Random Seas, CeSOS.
IMT- 2012-83	Sten, Ronny	Dynamic Simulation of Deep Water Drilling Risers with Heave Compensating System, IMT.
IMT- 2012-84	Berle, Øyvind	Risk and resilience in global maritime supply chains, IMT.
IMT- 2012-85	Fang, Shaoji	Fault Tolerant Position Mooring Control Based on Structural Reliability, CeSOS.
IMT- 2012-86	You, Jikun	Numerical studies on wave forces and moored ship motions in intermediate and shallow water, CeSOS.
IMT- 2012-87	Xiang ,Xu	Maneuvering of two interacting ships in waves, CeSOS
IMT- 2012-88	Dong, Wenbin	Time-domain fatigue response and reliability analysis of offshore wind turbines with emphasis on welded tubular joints and gear components, CeSOS
IMT- 2012-89	Zhu, Suji	Investigation of Wave-Induced Nonlinear Load Effects in Open Ships considering Hull Girder Vibrations in Bending and Torsion, CeSOS
IMT- 2012-90	Zhou, Li	Numerical and Experimental Investigation of Station-keeping in Level Ice, CeSOS
IMT- 2012-91	Ushakov, Sergey	Particulate matter emission characteristics from diesel engines operating on conventional and alternative marine fuels, IMT
IMT- 2013-1	Yin, Decao	Experimental and Numerical Analysis of Combined In-line and Cross-flow Vortex Induced Vibrations, CeSOS

IMT-2013-2	Kurniawan, Adi	Modelling and geometry optimisation of wave energy converters, CeSOS
IMT-2013-3	Al Ryati, Nabil	Technical condition indexes doe auxiliary marine diesel engines, IMT
IMT-2013-4	Firoozkoohi, Reza	Experimental, numerical and analytical investigation of the effect of screens on sloshing, CeSOS
IMT-2013-5	Ommani, Babak	Potential-Flow Predictions of a Semi-Displacement Vessel Including Applications to Calm Water Broaching, CeSOS
IMT-2013-6	Xing, Yihan	Modelling and analysis of the gearbox in a floating spar-type wind turbine, CeSOS
IMT-7-2013	Balland, Océane	Optimization models for reducing air emissions from ships, IMT
IMT-8-2013	Yang, Dan	Transitional wake flow behind an inclined flat plate----Computation and analysis, IMT
IMT-9-2013	Abdillah, Suyuthi	Prediction of Extreme Loads and Fatigue Damage for a Ship Hull due to Ice Action, IMT
IMT-10-2013	Ramirez, Pedro Agustin Pérez	Ageing management and life extension of technical systems- Concepts and methods applied to oil and gas facilities, IMT
IMT-11-2013	Chuang, Zhenju	Experimental and Numerical Investigation of Speed Loss due to Seakeeping and Maneuvering. IMT
IMT-12-2013	Etemaddar, Mahmoud	Load and Response Analysis of Wind Turbines under Atmospheric Icing and Controller System Faults with Emphasis on Spar Type Floating Wind Turbines, IMT
IMT-13-2013	Lindstad, Haakon	Strategies and measures for reducing maritime CO2 emissons, IMT
IMT-14-2013	Haris, Sabril	Damage interaction analysis of ship collisions, IMT
IMT-15-2013	Shainee, Mohamed	Conceptual Design, Numerical and Experimental Investigation of a SPM Cage Concept for Offshore Mariculture, IMT
IMT-16-2013	Gansel, Lars	Flow past porous cylinders and effects of biofouling and fish behavior on the flow in and around Atlantic salmon net cages, IMT
IMT-17-2013	Gaspar, Henrique	Handling Aspects of Complexity in Conceptual Ship Design, IMT
IMT-18-2013	Thys, Maxime	Theoretical and Experimental Investigation of a Free Running Fishing Vessel at Small Frequency of Encounter, CeSOS
IMT-19-2013	Aglen, Ida	VIV in Free Spanning Pipelines, CeSOS

IMT-1-2014	Song, An	Theoretical and experimental studies of wave diffraction and radiation loads on a horizontally submerged perforated plate, CeSOS
IMT-2-2014	Rogne, Øyvind Ygre	Numerical and Experimental Investigation of a Hinged 5-body Wave Energy Converter, CeSOS
IMT-3-2014	Dai, Lijuan	Safe and efficient operation and maintenance of offshore wind farms ,IMT
IMT-4-2014	Bachynski, Erin Elizabeth	Design and Dynamic Analysis of Tension Leg Platform Wind Turbines, CeSOS
IMT-5-2014	Wang, Jingbo	Water Entry of Freefall Wedged – Wedge motions and Cavity Dynamics, CeSOS
IMT-6-2014	Kim, Ekaterina	Experimental and numerical studies related to the coupled behavior of ice mass and steel structures during accidental collisions, IMT
IMT-7-2014	Tan, Xiang	Numerical investigation of ship's continuous- mode icebreaking in level ice, CeSOS
IMT-8-2014	Muliawan, Made Jaya	Design and Analysis of Combined Floating Wave and Wind Power Facilities, with Emphasis on Extreme Load Effects of the Mooring System, CeSOS
IMT-9-2014	Jiang, Zhiyu	Long-term response analysis of wind turbines with an emphasis on fault and shutdown conditions, IMT
IMT-10-2014	Dukan, Fredrik	ROV Motion Control Systems, IMT
IMT-11-2014	Grimsmo, Nils I.	Dynamic simulations of hydraulic cylinder for heave compensation of deep water drilling risers, IMT
IMT-12-2014	Kvittem, Marit I.	Modelling and response analysis for fatigue design of a semisubmersible wind turbine, CeSOS
IMT-13-2014	Akhtar, Juned	The Effects of Human Fatigue on Risk at Sea, IMT
IMT-14-2014	Syahroni, Nur	Fatigue Assessment of Welded Joints Taking into Account Effects of Residual Stress, IMT
IMT-1-2015	Böckmann, Eirik	Wave Propulsion of ships, IMT
IMT-2-2015	Wang, Kai	Modelling and dynamic analysis of a semi-submersible floating vertical axis wind turbine, CeSOS
IMT-3-2015	Fredriksen, Arnt Gunvald	A numerical and experimental study of a two-dimensional body with moonpool in waves and current, CeSOS
IMT-4-2015	Jose Patricio Gallardo Canabes	Numerical studies of viscous flow around bluff bodies, IMT

IMT-5-2015	Vegard Longva	Formulation and application of finite element techniques for slender marine structures subjected to contact interactions, IMT
IMT-6-2015	Jacobus De Vaal	Aerodynamic modelling of floating wind turbines, CeSOS
IMT-7-2015	Fachri Nasution	Fatigue Performance of Copper Power Conductors, IMT
IMT-8-2015	Oleh I Karpa	Development of bivariate extreme value distributions for applications in marine technology, CeSOS
IMT-9-2015	Daniel de Almeida Fernandes	An output feedback motion control system for ROVs, AMOS
IMT-10-2015	Bo Zhao	Particle Filter for Fault Diagnosis: Application to Dynamic Positioning Vessel and Underwater Robotics, CeSOS
IMT-11-2015	Wenting Zhu	Impact of emission allocation in maritime transportation, IMT
IMT-12-2015	Amir Rasekhi Nejad	Dynamic Analysis and Design of Gearboxes in Offshore Wind Turbines in a Structural Reliability Perspective, CeSOS
IMT-13-2015	Arturo Jesús Ortega Malca	Dynamic Response of Flexibles Risers due to Unsteady Slug Flow, CeSOS
IMT-14-2015	Dagfinn Husjord	Guidance and decision-support system for safe navigation of ships operating in close proximity, IMT
IMT-15-2015	Anirban Bhattacharyya	Ducted Propellers: Behaviour in Waves and Scale Effects, IMT
IMT-16-2015	Qin Zhang	Image Processing for Ice Parameter Identification in Ice Management, IMT
IMT-1-2016	Vincentius Rumawas	Human Factors in Ship Design and Operation: An Experiential Learning, IMT
IMT-2-2016	Martin Storheim	Structural response in ship-platform and ship-ice collisions, IMT
IMT-3-2016	Mia Abrahamsen Prsic	Numerical Simulations of the Flow around single and Tandem Circular Cylinders Close to a Plane Wall, IMT
IMT-4-2016	Tufan Arslan	Large-eddy simulations of cross-flow around ship sections, IMT

IMT-5-2016	Pierre Yves-Henry	Parametrisation of aquatic vegetation in hydraulic and coastal research,IMT
IMT-6-2016	Lin Li	Dynamic Analysis of the Instalation of Monopiles for Offshore Wind Turbines, CeSOS
IMT-7-2016	Øivind Kåre Kjerstad	Dynamic Positioning of Marine Vessels in Ice, IMT
IMT-8-2016	Xiaopeng Wu	Numerical Analysis of Anchor Handling and Fish Trawling Operations in a Safety Perspective, CeSOS
IMT-9-2016	Zhengshun Cheng	Integrated Dynamic Analysis of Floating Vertical Axis Wind Turbines, CeSOS
IMT-10-2016	Ling Wan	Experimental and Numerical Study of a Combined Offshore Wind and Wave Energy Converter Concept
IMT-11-2016	Wei Chai	Stochastic dynamic analysis and reliability evaluation of the roll motion for ships in random seas, CeSOS
IMT-12-2016	Øyvind Selnes Patricksson	Decision support for conceptual ship design with focus on a changing life cycle and future uncertainty, IMT
IMT-13-2016	Mats Jørgen Thorsen	Time domain analysis of vortex-induced vibrations, IMT
IMT-14-2016	Edgar McGuinness	Safety in the Norwegian Fishing Fleet – Analysis and measures for improvement, IMT
IMT-15-2016	Sepideh Jafarzadeh	Energy efficiency and emission abatement in the fishing fleet, IMT
IMT-16-2016	Wilson Ivan Guachamin Acero	Assessment of marine operations for offshore wind turbine installation with emphasis on response-based operational limits, IMT
IMT-17-2016	Mauro Candeloro	Tools and Methods for Autonomous Operations on Seabed and Water Coumn using Underwater Vehicles, IMT
IMT-18-2016	Valentin Chabaud	Real-Time Hybrid Model Testing of Floating Wind Tubines, IMT
IMT-1-2017	Mohammad Saud Afzal	Three-dimensional streaming in a sea bed boundary layer
IMT-2-2017	Peng Li	A Theoretical and Experimental Study of Wave-induced Hydroelastic Response of a Circular Floating Collar
IMT-3-2017	Martin Bergström	A simulation-based design method for arctic maritime transport systems

IMT-4-2017	Bhushan Taskar	The effect of waves on marine propellers and propulsion
IMT-5-2017	Mohsen Bardestani	A two-dimensional numerical and experimental study of a floater with net and sinker tube in waves and current
IMT-6-2017	Fatemeh Hoseini Dadmarzi	Direct Numerical Simulation of turbulent wakes behind different plate configurations
IMT-7-2017	Michel R. Miyazaki	Modeling and control of hybrid marine power plants
IMT-8-2017	Giri Rajasekhar Gunnu	Safety and efficiency enhancement of anchor handling operations with particular emphasis on the stability of anchor handling vessels
IMT-9-2017	Kevin Koosup Yum	Transient Performance and Emissions of a Turbocharged Diesel Engine for Marine Power Plants
IMT-10-2017	Zhaolong Yu	Hydrodynamic and structural aspects of ship collisions
IMT-11-2017	Martin Hassel	Risk Analysis and Modelling of Allisions between Passing Vessels and Offshore Installations
IMT-12-2017	Astrid H. Brodtkorb	Hybrid Control of Marine Vessels – Dynamic Positioning in Varying Conditions
IMT-13-2017	Kjersti Bruslerud	Simultaneous stochastic model of waves and current for prediction of structural design loads
IMT-14-2017	Finn-Idar Grøtta Giske	Long-Term Extreme Response Analysis of Marine Structures Using Inverse Reliability Methods
IMT-15-2017	Stian Skjong	Modeling and Simulation of Maritime Systems and Operations for Virtual Prototyping using co-Simulations
IMT-1-2018	Yingguang Chu	Virtual Prototyping for Marine Crane Design and Operations
IMT-2-2018	Sergey Gavrilin	Validation of ship manoeuvring simulation models
IMT-3-2018	Jeevith Hegde	Tools and methods to manage risk in autonomous subsea inspection, maintenance and repair operations
IMT-4-2018	Ida M. Strand	Sea Loads on Closed Flexible Fish Cages
IMT-5-2018	Erlend Kvinge Jørgensen	Navigation and Control of Underwater Robotic Vehicles

IMT-6-2018	Bård Stovner	Aided Inertial Navigation of Underwater Vehicles
IMT-7-2018	Erlend Liavåg Grotle	Thermodynamic Response Enhanced by Sloshing in Marine LNG Fuel Tanks
IMT-8-2018	Børge Rokseth	Safety and Verification of Advanced Maritime Vessels
IMT-9-2018	Jan Vidar Ulveseter	Advances in Semi-Empirical Time Domain Modelling of Vortex-Induced Vibrations
IMT-10-2018	Chenyu Luan	Design and analysis for a steel braceless semi-submersible hull for supporting a 5-MW horizontal axis wind turbine
IMT-11-2018	Carl Fredrik Rehn	Ship Design under Uncertainty
IMT-12-2018	Øyvind Ødegård	Towards Autonomous Operations and Systems in Marine Archaeology
IMT-13-2018	Stein Melvær Nornes	Guidance and Control of Marine Robotics for Ocean Mapping and Monitoring
IMT-14-2018	Petter Norgren	Autonomous Underwater Vehicles in Arctic Marine Operations: Arctic marine research and ice monitoring
IMT-15-2018	Minjoo Choi	Modular Adaptable Ship Design for Handling Uncertainty in the Future Operating Context
MT-16-2018	Ole Alexander Eidsvik	Dynamics of Remotely Operated Underwater Vehicle Systems
IMT-17-2018	Mahdi Ghane	Fault Diagnosis of Floating Wind Turbine Drivetrain- Methodologies and Applications
IMT-18-2018	Christoph Alexander Thieme	Risk Analysis and Modelling of Autonomous Marine Systems
IMT-19-2018	Yugao Shen	Operational limits for floating-collar fish farms in waves and current, without and with well-boat presence
IMT-20-2018	Tianjiao Dai	Investigations of Shear Interaction and Stresses in Flexible Pipes and Umbilicals
IMT-21-2018	Sigurd Solheim Pettersen	Resilience by Latent Capabilities in Marine Systems
IMT-22-2018	Thomas Sauder	Fidelity of Cyber-physical Empirical Methods. Application to the Active Truncation of Slender Marine Structures
IMT-23-2018	Jan-Tore Horn	Statistical and Modelling Uncertainties in the Design of Offshore Wind Turbines

IMT-24-2018	Anna Swider	Data Mining Methods for the Analysis of Power Systems of Vessels
IMT-1-2019	Zhao He	Hydrodynamic study of a moored fish farming cage with fish influence
IMT-2-2019	Isar Ghamari	Numerical and Experimental Study on the Ship Parametric Roll Resonance and the Effect of Anti-Roll Tank
IMT-3-2019	Håkon Strandenes	Turbulent Flow Simulations at Higher Reynolds Numbers
IMT-4-2019	Siri Mariane Holen	Safety in Norwegian Fish Farming – Concepts and Methods for Improvement
IMT-5-2019	Ping Fu	Reliability Analysis of Wake-Induced Riser Collision
IMT-6-2019	Vladimir Krivopolianskii	Experimental Investigation of Injection and Combustion Processes in Marine Gas Engines using Constant Volume Rig
IMT-7-2019	Anna Maria Kozłowska	Hydrodynamic Loads on Marine Propellers Subject to Ventilation and out of Water Condition.
IMT-8-2019	Hans-Martin Heyn	Motion Sensing on Vessels Operating in Sea Ice: A Local Ice Monitoring System for Transit and Stationkeeping Operations under the Influence of Sea Ice
IMT-9-2019	Stefan Vilsen	Method for Real-Time Hybrid Model Testing of Ocean Structures – Case on Slender Marine Systems
IMT-10-2019	Finn-Christian W. Hanssen	Non-Linear Wave-Body Interaction in Severe Waves
IMT-11-2019	Trygve Olav Fossum	Adaptive Sampling for Marine Robotics
IMT-12-2019	Jørgen Bremnes Nielsen	Modeling and Simulation for Design Evaluation
IMT-13-2019	Yuna Zhao	Numerical modelling and dynamic analysis of offshore wind turbine blade installation
IMT-14-2019	Daniela Myland	Experimental and Theoretical Investigations on the Ship Resistance in Level Ice
IMT-15-2019	Zhengru Ren	Advanced control algorithms to support automated offshore wind turbine installation
IMT-16-2019	Drazen Polić	Ice-propeller impact analysis using an inverse propulsion machinery simulation approach
IMT-17-2019	Endre Sandvik	Sea passage scenario simulation for ship system performance evaluation

IMT-18-2019	Loup Suja-Thauvin	Response of Monopile Wind Turbines to Higher Order Wave Loads
IMT-19-2019	Emil Smilden	Structural control of offshore wind turbines – Increasing the role of control design in offshore wind farm development
IMT-20-2019	Aleksandar-Sasa Milakovic	On equivalent ice thickness and machine learning in ship ice transit simulations
IMT-1-2020	Amrit Shankar Verma	Modelling, Analysis and Response-based Operability Assessment of Offshore Wind Turbine Blade Installation with Emphasis on Impact Damages
IMT-2-2020	Bent Oddvar Arnesen Haugalokken	Autonomous Technology for Inspection, Maintenance and Repair Operations in the Norwegian Aquaculture
IMT-3-2020	Seongpil Cho	Model-based fault detection and diagnosis of a blade pitch system in floating wind turbines
IMT-4-2020	Jose Jorge Garcia Agis	Effectiveness in Decision-Making in Ship Design under Uncertainty
IMT-5-2020	Thomas H. Viuff	Uncertainty Assessment of Wave-and Current-induced Global Response of Floating Bridges
IMT-6-2020	Fredrik Mentzoni	Hydrodynamic Loads on Complex Structures in the Wave Zone
IMT-7-2020	Senthuran Ravinthrakumar	Numerical and Experimental Studies of Resonant Flow in Moonpools in Operational Conditions
IMT-8-2020	Stian Skaalvik Sandøy	Acoustic-based Probabilistic Localization and Mapping using Unmanned Underwater Vehicles for Aquaculture Operations
IMT-9-2020	Kun Xu	Design and Analysis of Mooring System for Semi-submersible Floating Wind Turbine in Shallow Water
IMT-10-2020	Jianxun Zhu	Cavity Flows and Wake Behind an Elliptic Cylinder Translating Above the Wall
IMT-11-2020	Sandra Hogenboom	Decision-making within Dynamic Positioning Operations in the Offshore Industry – A Human Factors based Approach
IMT-12-2020	Woongshik Nam	Structural Resistance of Ship and Offshore Structures Exposed to the Risk of Brittle Failure
IMT-13-2020	Svenn Are Tutturen Værnø	Transient Performance in Dynamic Positioning of Ships: Investigation of Residual Load Models and Control Methods for Effective Compensation
IMT-14-2020	Mohd Atif Siddiqui	Experimental and Numerical Hydrodynamic Analysis of a Damaged Ship in Waves
IMT-15-2020	John Marius Hegseth	Efficient Modelling and Design Optimization of Large Floating Wind Turbines

IMT-16-2020	Asle Natskår	Reliability-based Assessment of Marine Operations with Emphasis on Sea Transport on Barges
IMT-17-2020	Shi Deng	Experimental and Numerical Study of Hydrodynamic Responses of a Twin-Tube Submerged Floating Tunnel Considering Vortex-Induced Vibration
IMT-18-2020	Jone Torsvik	Dynamic Analysis in Design and Operation of Large Floating Offshore Wind Turbine Drivetrains
IMT-1-2021	Ali Ebrahimi	Handling Complexity to Improve Ship Design Competitiveness
IMT-2-2021	Davide Proserpio	Isogeometric Phase-Field Methods for Modeling Fracture in Shell Structures
IMT-3-2021	Cai Tian	Numerical Studies of Viscous Flow Around Step Cylinders
IMT-4-2021	Farid Khazaeli Moghadam	Vibration-based Condition Monitoring of Large Offshore Wind Turbines in a Digital Twin Perspective
IMT-5-2021	Shuaishuai Wang	Design and Dynamic Analysis of a 10-MW Medium-Speed Drivetrain in Offshore Wind Turbines
IMT-6-2021	Sadi Tavakoli	Ship Propulsion Dynamics and Emissions
IMT-7-2021	Haoran Li	Nonlinear wave loads, and resulting global response statics of a semi-submersible wind turbine with heave plates
IMT-8-2021	Einar Skiftestad Ueland	Load Control for Real-Time Hybrid Model Testing using Cable-Driven Parallel Robots